Spectral Element Methods
for Predicting the Flow
of Polymer Solutions and Melts

by

Roel Gerardus Maria van Os

A dissertation submitted for
the degree of Philosophi
Doctor of the University of Wales

THE UNIVERSITY OF WALES, ABERYSTWYTH
Institute of Mathematical and Physical Sciences
14 September 2004

Declaration

This work has not previously been accepted in substance for any degree and is not being concurrently submitted in candidature for any degree.

Signed ________________________ (candidate)

Date ________________________

Statement 1

This thesis is the result of my own investigations, except where otherwise stated. Other sources are acknowledged by giving explicit references. A bibliography is appended.

Signed ________________________ (candidate)

Date ________________________

Statement 2

I hereby give consent for my thesis to be available for photocopying and for inter-library loan, and for the title and summary to be made available to outside organisations.

Signed ________________________ (candidate)

Date ________________________

Acknowledgements

I would like to thank my supervisor Tim Phillips for the many insightful discussions and guidance leading to this thesis. It has been a pleasure working with him and I wish him all the best in his new position in Cardiff. I would also like to thank my examiners Ken Walters and Oliver Harlen for agreeing to take part in my Viva.

Thank you to all the postgraduate students and everyone else in the Mathematics department for making it a pleasant place to work. To Alison, Paul, Jamal, Stacy, René, Pierre and Keith I would like to say 'thank you for being great friends'! To Joe, Nest, Dylan, Dafydd, Matthew and Karen I would like say 'diolch for being great friends'! Thanks for introducing me to Aberystwyth and Shrewsbury, the many great nights out, the hours (or was it slightly more) on the football pitch, the barbeques, the skiing holidays, etc. etc. Because of you all I will always think back of these years with a big smile on my face.

I would like to thank my parents and sisters for being very supportive when I moved to Aberystwyth and for visiting me so many times! Most of all I want to say thank you to Kristien, for being o so brave to move with me to Aberystwyth three years ago, for putting up with my -sometimes work related- moods, and for making me happy in general. Without you the past couple of years would not have been half as good!

Summary

This thesis is concerned with the development of numerical methods for the prediction of flow of polymer solutions and melts. Many constitutive models are available to describe the behaviour of such fluids. The classical Oldroyd B model is used in this thesis to simulate the flow of polymer solutions. The extended pom-pom model is a model based on the recently developed pom-pom model, and is adopted to predict the flow of polymer melts. Some of the mathematical properties of this model are presented in this thesis.

The numerical algorithm that is used to simulate the fluids is based on a spectral element method. A modified interpolation function is presented that is able to deal efficiently with axisymmetric problems. The discretized set of equations are solved using iterative inversion. By using appropriate preconditioners, the efficiency of the iterative procedure is increased dramatically. Another possibility for speeding up the algorithm is to use the Schur method, which reduces the size of the discrete problem. A combination of this method with preconditioned iterative methods is shown to be an efficient way of determining solutions.

The equations in the constitutive model can be solved coupled to the conservation of mass and momentum. This means that all information about the state of the fluid is obtained simultaneously. When the equations are solved uncoupled, the stress is calculated from the velocity on the previous time level. Using this method, higher Weissenberg numbers could be reached in the numerical simulations. This number is increased even more when upwinding methods such as SUPG or LUST are used.

Solutions of the planar channel flow and flow past a confined cylinder are presented for Newtonian fluids, Oldroyd B fluids and XPP fluids. Solutions for both the transient start-up and steady flow are given. The stability of solutions of the Oldroyd B model is analyzed. Both single mode and multi-mode versions of the XPP model are used.

Contents

List of Figures

List of Tables

Chapter 1

Introduction

This thesis is concerned with the development of numerical methods for the efficient and accurate prediction of flows of viscoelastic fluids. The research is in the broad field of rheology, which can be defined as the science of the deformation and flow of matter. It involves the study of viscoelastic materials that possess characteristics of both elastic solids and viscous fluids.

This chapter starts by giving a brief historical account of the field of rheology in section 1.1. It goes on to classify the different fluids within the class of non-Newtonian fluids in section 1.2. In section 1.3 some phenomena exhibited by these fluids are described, and section 1.4 states the industrial importance of research in non-Newtonian fluid mechanics. The aim of this thesis is given in section 1.5, after which the framework in which to place this work is presented in section 1.6. Some comments about the numerical codes that have been used and developed for this research are made in section 1.7. Finally section 1.8 presents the contents of this thesis.

1.1 A Very Brief History

The first major contribution to the mechanics governing elastic solids was made by Hooke, who in 1678 proposed that *'the power of any string is in the same proportion with the tension thereof'*. In a more modern interpretation, Hooke's law reads that the stress in an elastic solid is proportional to the strain.

The interest in the dynamics of viscous fluids was first raised in the late seventeenth and early eighteenth century, by the idea that the speed of a ship was affected by the resistance of the waterflow around it. The publication of Newtons *Principia* in 1687 first provided a theoretical basis for study of fluid flow. In ideal viscous fluids, the shear stress is linearly dependent on the rate of deformation of the fluid. This law has its origin in Newton's statement that *'the resistance which arises from the lack of slipperiness originating in a fluid, other things being equal, is proportional to the velocity by which the parts of the fluid are being separated from each other'*.

The widely celebrated Navier-Stokes equations are a set of mathematical equations that describe the flow of ideal viscous fluids, like water. These were retrieved independently by both Navier and Stokes, in the first half of the nineteenth century. The fluids that are modelled by these equations are called Newtonian fluids, since they obey the above mentioned linear constitutive relation between stress and deformation. When a fluid does not obey the linear relation, it is classified as a non-Newtonian fluid. Rheology can therefore also be seen as non-Newtonian fluid mechanics.

The first known study of materials that can neither be classified as elastic solids nor as viscous fluids, was carried out by Weber (1835) on silk threads in which the stresses that are present in the thread when a load is applied to it, slowly relax on the removal of the load. In 1867 Maxwell introduced his famous empirical differential constitutive equation that relates the shear stress to deformation and stress relaxation.

To find suitable constitutive relations, which differ from fluid to fluid, is one of the main challenges in rheology. Oldroyd's study of invariance of material properties with respect to frame of reference led to the well known Oldroyd model in 1950. Since then numerous contributions have been made to constitutive modelling, resulting in so many different constitutive models, that it is sometimes said there are as many constitutive models as there are rheologists. In this thesis only a few of these constitutive models will be introduced.

Computational rheology started during the 1960s with the use of Finite Difference Methods, shortly followed during the 70s and 80s with the use of more sophisticated Finite Element, Finite Volume and Spectral Element Methods. The major challenge in this field is the tackling of the so called 'high Weissenberg number problem'. This refers to the breakdown of numerical simulations when only a limited amount of elasticity is introduced to the equations that describe the flow of the fluid.

1.2 Non-Newtonian Fluid Classification

Any material that does not obey the linear Newtonian relation between stress and deformation can be classified as a non-Newtonian fluid. Within this broad class of non-Newtonian fluids many distinct cases are identifiable on the basis of their reaction to deformation, i.e. their constitutive relations. Given here are different types of non-Newtonian fluids that are often used to classify materials.

1.2.1 Shear-thinning and shear-thickening fluids

Some fluids exhibit a decrease in viscosity when the rate of deformation acting on the fluid is increased. These fluids are said to be shear-thinning or pseudoplastic. In a shear thinning fluid, the viscosity decreases with increasing rate of deformation. The opposite is a shear-thickening fluid, where the viscosity increases with rate of deformation, i.e. the stresses increase progressively. A power law provides the simplest constitutive equation for this class of fluids. The constant viscosity in the Newtonian stress relation (2.11) is replaced by a viscosity that is a function of d_{xy},

$$\eta = \eta(d_{xy}) = k d_{xy}^{(n-1)}, \tag{1.1}$$

where k is a constant, and d_{xy} is the deformation gradient. When $n = 1$, the power law reduces to a Newtonian fluid. A shear-thinning fluid is described by $n < 1$, a shear-thickening fluid by $n > 1$. More complex relations for this class of fluids can be found in [57] or [38].

1.2.2 Yielding fluids

Some materials only start deforming after a certain amount of shear stress is exceeded. This amount is called the yield stress, and the fluids are known as yielding fluids. Of course, yielding fluids can also be shear-thinning or shear-thickening. This however is not a neccesary requirement, and an idealized material that is used in analytic investigations, the Bingham plastic, is characterized by a constant viscosity. A perfect example of a yielding fluid is toothpaste.

1.2.3 Rheopectic and Thixotropic fluids

The relation between shear stress and shear rate can also depend on the time that the fluid has undergone the shearing. In thixotropic fluids, the shear stress decreases when the fluid is sheared at a constant rate. Structure in the fluid is progressively broken down with time, resulting in a decreasing viscosity. The opposite effect is typical for rheopectic fluids. Formation of structure with time results in increasing shear stress at a constant shear rate, and the viscosity increases.

1.2.4 Viscoelastic fluids

The feature that distinguishes viscoelastic fluids from the classes named above is that they exhibit partial elastic recovery after deformation has been applied. This is a characteristic that is related to a solid rather than to a fluid, and therefore viscoleastic fluids are often said to lie between a solid and a fluid. The most important material parameter that characterises viscoelastic fluids is the relaxation time.

The relaxation time of a material is the time after which stresses that were induced by some deformation or strain relax to a certain level. Every material has a nonzero relaxation time. For fluids the relaxation time is so small (10^{-12}s for water) that stress relaxation is assumed to be instantaneous. Solids however are characterized by relaxation times of the order of years rather than seconds, and relaxation of stresses is so slow that they are assumed not to relax at all.

The relaxation times of viscoelastic fluids lie well in between these extrema. Stress relaxation is typically of the order of a few seconds. Silly putty is a good example of a viscoelastic fluid. It can bounce like a solid because the bouncing process is complete before the stresses can relax. Before human patience runs out however, silly putty can also be observed to flow like a fluid. Solvents of polymer in a viscous matrix or melts of polymer are also viscoelastic fluids.

1.3 Viscoelastic Fluid Phenomena

Viscoelastic fluids behave differently from Newtonian fluids under many circumstances. The bouncing and flowing silly putty has already been mentiond. A few of the most well known other examples are given below.

When a viscoelastic fluid is extrudated from a die, the diameter of the extrudate may swell. The extent of this swelling may be up to several times the diameter of the original die. This phenomena is known as extrudate swelling or die-swell. Newtonian fluids leaving a die show exactly the opposite behaviour and the diameter will decrease.

When a rod is rotated in a cup filled with a viscoelastic fluid, the fluid climbs up the rod. This effect is attributed to a difference in angular and radial normal stress components. This rod climbing is also known as the Weissenberg effect. Newtonian fluids on the other hand exhibit no rod climbing. Instead the fluid level of a Newtonian fluid would decrease near the rotating rod due to centrifugal forces.

A widely used benchmark problems in computational rheology is the flow through a contraction. A phenomena typical for viscoelastic fluids in this problem is that large vortices may appear in the salient corner of such a geometry. The size of this vortex can increase dramatically with increasing elasticity. The corner vortex is also present for Newtonian fluids but it is much smaller. To force a fluid through a contraction a certain pressure drop is needed. Another viscoelastic effect is that this pressure drop changes with changing elasticity. This means that to achieve the same flow rates for Newtonian and viscoelastic fluids of the same viscosity, a higher pressure drop may have to be adopted.

1.4 Industrial Importance

Non-Newtonian fluids abound in nature and industry and this accounts for the interest in their flow properties and behaviour. Ink in printers, paint dripping from our brushes before it reaches the wall, bread dough that is not mixed thoroughly enough when it should be, the molten plastics in a complex production line in a factory before it ends up in our computer screen and video player cases. Successful prediction of these flows could lead to better process control and more efficient manufacturing.

Since for most real flows, the set of mathematical equations that model the fluid is too complex to solve analytically, they are solved using a numerical scheme. The advantages of this approach is that it is cheap, parameters may be varied endlessly, and all data is instantly available, at every point in the flow. Disadvantages are that the results can only be as good as the model that simulates the flow, and that non-physical numerical artefacts may be present in the solution. It is therefore of the utmost importance that the results of a numerical simulation are sharply questioned before they can be accepted as a simulation of a real situation.

1.5 Aim of the Thesis

The major part of this work is to find numerical algorithms that are suitable to solve existing non-Newtonian fluid models. In order to do so, the efficiency and the stability of these algorithms are analyzed and enhanced if possible. Focus will be on the preconditioners to solve the systems of equations more efficiently, on upwinding methods that can be used to achieve increased stability, on the improvement of the accuracy of the iterative solving of the equations, and on the analysis of steady and transient results for both simple and complex flows.

A spectral element method is chosen to approximate the spatial dependence of the set of equations numerically, and higher order approximations will also be adopted for the temporal discretization. It is shown that different temporal discretizations lead to different sets of equations that can have a great effect on the stability of the numerical algorithm.

Theoretical analysis is performed on the recently developed pom-pom model [34] and a derivative, the extended pom-pom model [61]. The behaviour of the extensional viscosities of these models are compared, and an attempt is made to determine the type of the equations.

The spectral element method itself is also analyzed, with respect to its behaviour near symmetry boundary conditions, and to the possibility of using higher order transfinite mappings.

Apart from the pom-pom type models, attention is given to the more classical upper convected Maxwell (UCM) and Oldroyd B models. The extended pom-pom model will be conveniently nondimensionalized, in order to make it suitable for implementation into an existing solver. As will be shown later in this thesis, the UCM and the Oldroyd-B model, may be used to simulate polymer solutions, whereas the pom-pom models are suitable for simulation of polymer melts. It is not attempted in this thesis to enhance these models to obtain more realistic representations of real fluids.

1.6 Framework of this Research

After performing some calculations involving Newtonian fluids, this thesis goes on to simulate the flow of polymer solutions and polymer melts. In this sections a review is given of relevant work by other researchers in these fields.

1.6.1 Polymer solutions

Differential constitutive models such as the upper-convected Maxwell (UCM), Oldroyd B and Phan-Thien/Tanner models are nonlinear and this property has a considerable impact on the performance and stability of numerical methods. The degree of nonlinearity of the governing system of partial differential equations may be quantified in terms of a dimensionless number, We, known as the Weissenberg number which can be viewed as a measure of the memory of the fluid. As mentioned before, most numerical algorithms fail to converge above a critical value of this parameter when conventional closed form constitutive models such as the UCM or Oldroyd B models are used.

Over the last twenty years significant progress has been made in the development of reliable numerical methods for solving steady viscoelastic flow problems (see the monograph of Owens and Phillips [38], for example). On a range of benchmark problems there has been agreement across a range of numerical methods for particular models in terms of global quantities such as the drag on a sphere or cylinder in a viscoelastic medium. Stabilization techniques have been used to remove numerical instabilities in many instances in order to extend the range of Weissenberg numbers over which converged numerical solutions are obtained. One such technique is the elastic viscous split stress (EVSS) formulation, developed by Perera and Walters [43], in which a change of variables is introduced with the purpose of increasing the 'ellipticity' of the momentum equation and, therefore, the stability of the discretization. Other successful stabilization techniques are described in Owens and Phillips [38]. These methods have been shown to work well for steady problems.

In the context of spectral methods, Fiétier and Deville [15] have explored the use of stabilization techniques such as the discrete EVSS (DEVSS) method of Guénette and

Fortin [21] and the filtering method of Mullen and Fischer [36]. However, these techniques only had limited success in increasing the critical value of We. Furthermore, the authors were concerned that the use of stabilization techniques could prevent a detailed investigation into the onset and development of physical instabilities that are observed experimentally (see Smith et al. [55], for example).

Upwinding techniques are another example of stabilization methods. The Streamline Upwind/Petrov-Galerkin (SUPG) [5] technique was originally developed to achieve a stabilized finite element method. In their Locally Upwinded Spectral Technique (LUST), Owens et al. [39] extended the method for the use with spectral elements methods. The stability of the steady flow of an Oldroyd B fluid past a cylinder improved compared to the SUPG method. Higher Weissenberg numbers were achieved and the stress fields were found to be much smoother.

Much theoretical and numerical work has been performed with respect to the flow of UCM and Oldroyd B fluids in a planar channel. In the seventies, Porteous and Denn [45], Ho and Denn [23] and later Lee and Finlayson [31] and Larson [30] performed linear stability analyses of this flow.

In a more recent paper Sureshkumar and Beris [56] used an Arnoldi algorithm, which computes a group of the most unstable eigenmodes, to show that the addition of solvent viscosity considerably reduced the destabilizing effect of elasticity found by Porteous and Denn [45] for the UCM fluid in the inertial regime. They also commented on the dire consequences of inadequately resolving the continuous eigenmodes. For a given mesh the error in the approximation of these eigenmodes was shown to increase linearly with the Weissenberg number. Therefore, at relatively large values of We these modes could give rise to artificial instabilities if insufficient spatial refinement is used in the computations.

Wilson et al. [65] studied the structure of the spectrum for creeping flow of both UCM and Oldroyd B fluids. The addition of solvent viscosity is found to increase the complexity of the eigenspectrum. Although the authors were not able to prove that inertialess plane Poiseuille flow is linearly stable for all values of the Weissenberg number, no unstable eigenvalues were observed. However, poorly resolved modes of the continuous spectrum can produce spurious instabilities. The problem of under-resolution of the continuous part of the spectrum for UCM and Oldroyd B models and its impact on the generation of spurious instabilites for plane Couette flow was studied by Keiller [29]. He showed that, since the continuous part of the spectrum scales linearly with both wavenumber k_x and the order of the spectral approximation N, the critical Weissenberg number will scale with the aspect ratio of the mesh elements k_x/N when the under-resolved part of the continuous spectrum is causing the flow to appear unstable. He also showed that for calculations with the UCM model, the addition of a small amount of solvent viscosity could stabilize the spurious modes.

Atalik and Keunings [1] performed a nonlinear analysis of the evolution of two-dimensional disturbances for plane Poiseuille flow of the Giesekus fluid, which includes the UCM and Oldroyd B fluids as special cases, in the low and high Reynolds number regimes. The numerical scheme of Atalik and Keunings is based on a spectral discretization in space and a Crank-Nicolson/Adams-Bashforth discretization in time. The authors noted that the linear operator describing the time evolution of infinitesimal disturbances is non-normal for this problem. Thus, although all the eigenvalues of the two-dimensional linear operator have negative real parts, so that any infinitesimal disturbance will ultimately decay, transient growth of the disturbances is possible. If the intermediate growth is significant enough the disturbances that are misfit to the eigendirections of the linear stability operator will interact in a nonlinear fashion and eventually drive the system to a nonlinear instability. In the inertial regime they showed that finite amplitude periodic waves develop beyond a critical Reynolds number. Increasing the elasticity number has a destabilizing effect at first followed by restabilization.

Other pertinent issues such as the mathematical type of the equations, loss of evolution and the high Weissenberg number problem, for example, are discussed in Owens and Phillips [38], Renardy et al. [51] and Renardy [48, 49, 50]. More recently, Lozinski and Owens [32] have derived an energy estimate for the velocity and stress components for both inertial and creeping flows of an Oldroyd B fluid. They explained that conventional discretization schemes for the Oldroyd B model may violate the energy estimate and deliver an approximation that fails to respect important properties of the continuous problem. A novel numerical scheme that respects the energy estimate and guarantees satisfaction of key properties of the model was developed and implemented by the authors.

1.6.2 Polymer melts

In the mathematical modelling of polymer melts, significant progress has been made over the last decade. Established traditional models for polymer melts such as the Phan-Thien Tanner (PTT), Giesekus and K-BKZ models have been unsuccessful in predicting accurately the nonlinear behaviour of materials in both shear and extension. However, a new constitutive model developed by McLeish and Larson [34], known as the pom-pom model, has the facility to overcome this shortcoming.

Recent developments in constitutive modelling of polymer solutions and melts have been based on a kinetic theory approach. Models based on this approach provide a coarse-grained description of the polymer dynamics in terms of the microstructure of the fluid. A knowledge of the microstructure is necessary in order to determine the stress since the stress depends on the conformations of the model polymer molecules, viz. the orientation and degree of stretch of a molecule.

The rheological description of a polymer melt is quite distinct from that for polymer solutions in which the polymer molecules are assumed to be sufficiently disperse so as not to interact with each other. In a polymer melt the dynamics of each polymer molecule is influenced by the surrounding molecules.

Since it is impossible to describe the molecular interactions in detail, it is important to distil the crucial features of the polymer dynamics in order to derive a tractable model. Thus, Doi and Edwards [11], in the derivation of the model for linear polymers that bears their name, identified reptation as being a crucial concept. The reptation concept assumes that individual polymer molecules are constrained to move in a tube formed by neighbouring polymer molecules. Effectively, the perpendicular motion of a polymer chain is constrained within a tube of given radius generated along its backbone while parallel to the tube a linear polymer chain is free to diffuse. The snake-like motion of the chain inspired de Gennes [9] to dub this motion as reptation.

An extension of these ideas to branched polymers, for which more complicated relaxation processes are involved than for linear polymers, was developed into a constitutive model by McLeish and Larson [34]. McLeish and Larson [34] identified the topology of branched polymer molecules as a key concept in the development of a mathematical model in addition to reptation theory. The model assumes that the polymer chains are represented by a backbone segment connecting two identical sets of q arms (‘pom-poms’) at the branch points. The branch points slow down the reptation motion of the backbone section by pinning the molecule in place at the tube junctions. The free ends of the arms are still able to move however, and the polymer frees itself from the tube by 'arm-retraction'. The arms gradually work their way out of the tubes towards the branch points by diffusion. Once the arms have relaxed, the backbone can subsequently relax by moving the branch points. The backbone can then be treated as a linear polymer with two diffuse 'blobs' comprising the diffusing arms, and the chain can be modelled as a dumbbell inside a tube. A key feature of the model is therefore distinct relaxation times for these two processes, i.e. the orientation and stretch of the backbone section. Due to balance of tension in the backbone of the molecule, and in the arms, the stretch is not allowed to be greater than q. At this point, the arms are retracted into the tube and this ensures that the stretch is bounded, although retraction lengths are found to be very small.

The differential approximation of the pom-pom model has been successfully used in numerical calculations of the four-to-one contraction benchmark problem, by Bishko et al. [3], and qualitative agreement with experiments using LDPE melts was demonstrated. Inkson et al. [25] used a multi-mode pom-pom model in which the parameters are determined from the linear relaxation spectrum and the transient extensional viscosity, and found quantitative agreement between experiments and model predictions for other rheological measurements such as transient shear viscosity and transient first normal stress difference for LDPE.

The original pom-pom model suffers from three problems. First, the model predicts a zero second normal stress difference. Secondly, there is an unphysical discontinuity in the gradient of the extensional viscosity when the stretch is equal to q at steady state. Thirdly, the shear stress has a maximum. Verbeeten et al. [61] introduced a modified model, the eXtended Pom-Pom (XPP) model, to circumvent some of these problems. A modification to the stretch equation, as introduced by Blackwell [4], which allows for branch point displacement, is used to overcome the discontinuity in the gradient of the extensional viscosity. The retraction of the arms into the tube has been neglected, and thereby the constraint that the stretch cannot be larger than the number of arms is removed. A Giesekus-like term has been added to the orientation equation, to introduce a non-zero second normal stress difference. Furthermore, the orientation equation is bounded for high strain rates. Two variants of the XPP model have been developed. The double equation version of the XPP model comprises evolution equations for the orientation and the stretch, while the single equation version provides a constitutive equation in terms of the stress, and both the orientation and the stretch are directly coupled to the stress. The XPP model has been succesfully implemented in a finite element method and satisfactory quantitative agreement has been found in comparisons between experiments with LDPE melts and numerical simulations using a multi-mode XPP model (see Verbeeten et al. [62], [63]).

1.6.3 Spectral element developments

Iterative methods can be made more efficient by using of preconditioners. A much used preconditioner in spectral elements is based on local finite element discretizations of the same problem. Preconditioners of this are called overlapping Schwarz preconditioners, and they are based on the classical additive Schwarz method developed by Dryja and Widlund [12] and domain decomposition methods (see [54]). These preconditioners and have been succesfully adopted in calculations using the spectral element method by Pavarino [40], [41] and Fisher et al. [16].

The Schur complement method [46] is an alternative technique to speed up calculations. It effectively decreases the size of the discrete problem by splitting it up into a problem associated to unknowns only on the boundaries of the spectral elements and separate problem involving the internal unknowns. In a spectral element context, this method has been used for example by Couzy and Deville [8] and Pavarino and Warburton [42].

1.7 Numerical Codes

The results that are presented in chapters 5 to 7 have been generated with two separate computer codes. Parts of these codes were developed by Xavier Escriva and Marc Gerritsma, former research assistants at Aberystwyth. For the planar channel flow of polymer solutions described in chapter 6, an existing code has been extended to solve transient problems. All other results have been generated using a newly developed code, the cornerstones of which are based on the iterative methods used in the existing code. Iterative solvers provide the possibility of tackling large problems, since they do not claim much memory associated to the storage of discrete spectral element operators. For the purpose of creating geometries and meshes, the possibility to use Gambit is included. Gambit is meshing software included in the commercial fluid dynamics code Fluent. Since this is combined with an iterative solver, the new code provides great geometric flexibility. It also provides the possibility of easily incorporating other constitutive models, as long as similar non-dimensionalization is possible. All codes have been implemented in Fortran language on Unix platforms. The new code can also be compiled using the GNU Fortran compiler 'g77', which is available freely and can easily be used on Windows platforms as well as Linux platforms.

1.8 Contents of the Thesis

The contents of this thesis are as follows. In chapter 2 the continuous equations in the models that are used in this work are derived. The non-dimensionalization of the equations is given and a generic model presented. Some theoretical issues associated with constitutive models for viscoelastic fluids are analyzed and discussed as well. The different temporal discretization schemes are given in chapter 3 together with the spatial discretization using the spectral element method. Before the fully discretized equations are given for both a coupled and an uncoupled system of equations, a test function is presented that gets round the problem of a zero radial coordinate associated with the axis of symmetry in problems defined in cylindrical polar coordinates. Details of the numerical algorithm that solves the discretized equations are given in chapter 4. This involves presenting the operators that need to be inverted, the iterative methods that are used for this inversion and the preconditioners that are used to speed up the inversion. Also described in this chapter are the Schur complement method, the zero volume of pressure condition that can be used to achieve better conditioning of the Uzawa operator, and the upwinding technique LUST. Results have been generated for the flow of Newtonian fluids and these are presented in chapter 5. Simulations of the flow of polymer solutions, modelled by the UCM and Oldroyd B models, are shown in chapter 6. Although the flow past a cylinder is considered, most of this chapter involves the Poiseulle flow through a planar channel. The efficiency of the preconditioners is also tested on the channel flow problem. Chapter 7 describes the results obtained by solving the XPP model. Both planar channel flow and flow past a cylinder are dealt with. The findings and results presented in the last two chapters have been published in papers [60] and [59] and another paper is currently in preparation.

Chapter 2

Modelling Viscoelastic Fluids

2.1 Introduction

In order to be able to analyze the flow of any medium, mathematical statements are needed that 'pin down' the mediums behaviour. These mathematical equations can be formulated using the following three physical principles:

- Mass cannot be created or destroyed. This will lead to the 'conservation of mass' equation.
- Newton's second law that states $\mathbf{F} = m\mathbf{a}$ (force is mass times acceleration). This will yield the 'conservation of momentum' equation.
- Energy cannot be created or destroyed. From this principle the 'conservation of energy' equation can be derived.

The conservation of mass and momentum equations are known as the field equations, which in their most general form, are valid for any medium. Section 2.2 presents the field equations, and also explains why the energy equation can be disregarded in the framework in this thesis. The field equations are not a closed system, and that means that extra descriptions of the medium are necessary to find independent solutions to flow problems. A relation between applied deformation on a medium, and the stresses that this causes in the medium, provides that extra description. The mathematical statement that expresses it is called the constitutive equation. Unlike the field equations, the constitutive equation is medium-dependent. When this equation is coupled to the field equations, a closed form description of the medium is retrieved. In section 2.3, the constitutive models that will be used in this thesis are derived and explained, and are presented in their non-dimensional form in section 2.4. Some mathematical properties of these constitutive model will be explored in more depth in section 2.5.

2.2 The Field Equations

The derivation of the equations that satisfy the conservation of mass and momentum is given in Appendix A. All derivations are made under the assumption that the continuum hypothesis is valid. This means that the length scale of an infinitesimal element, which is used to integrate over volumes and surfaces, is still considerably larger than the largest molecular length scale. Therefore there is no need to worry about features that appear on molecular scale of the medium. The equation for the conservation of energy is briefly visited, but only to explain why it can be disregarded in the framework of this thesis.

2.2.1 Conservation of mass equation

The conservation of mass equation is the mathematical statement of the physical property of flow that no mass can be created or destroyed. It is also often referred to as the continuity equation. In its differential form the conservation of mass equation reads

$$\frac{\partial \rho}{\partial t} + \nabla \cdot (\rho \mathbf{u}) = 0, \tag{2.1}$$

where ρ is the density of the medium, and $\mathbf{u}$ is the velocity vector. In this thesis the medium is always a fluid. Since compressibility in fluids is negligible, the density does not change with time or space. The conservation of mass equation reduces to

$$\nabla \cdot \mathbf{u} = 0. \tag{2.2}$$

This reduced conservation of mass equation is often referred to as the incompressibility constraint or the divergence-free condition. In a two dimensional Cartesian coordinate system, the equation in component form reads

$$\frac{\partial u}{\partial x} + \frac{\partial v}{\partial y} = 0. \tag{2.3}$$

2.2.2 Conservation of momentum equation

The conservation of momentum equation is based on Newton's second law $\mathbf{F} = m\mathbf{a}$, where the force $\mathbf{F}$ can be split into body forces ($\mathbf{f}_b$) and surface force. Gravity is an example of a body force. The surface forces consists of a force due to pressure p, and a force due to viscous and elastic stresses. The viscous and elastic stresses are contained in the symmetric extra-stress tensor denoted by $\mathbf{T}$. In its differential form, the conservation of momentum equation reads

$$\frac{\partial(\rho\mathbf{u})}{\partial t} + \rho\mathbf{u} \cdot (\nabla\mathbf{u})^T = \nabla \cdot \boldsymbol{\sigma} + \mathbf{f}_b, \tag{2.4}$$

where the total stress tensor $\boldsymbol{\sigma}$ is related to the pressure and extra-stress tensor $\mathbf{T}$ through $\boldsymbol{\sigma} = -p\mathbf{I} + \mathbf{T}$. The convective term is written by one half of the world as $\mathbf{u} \cdot (\nabla\mathbf{u})^T$, but by the other half as $\mathbf{u} \cdot \nabla\mathbf{u}$. In this thesis we will use $\mathbf{u} \cdot \nabla\mathbf{u}$, although the velocity gradient is defined as

$$\nabla\mathbf{u} = \begin{pmatrix} \frac{\partial u}{\partial x} & \frac{\partial u}{\partial y} \\ \frac{\partial v}{\partial x} & \frac{\partial v}{\partial y} \end{pmatrix}, \tag{2.5}$$

which can be written in Einstein notation as $\mathbf{u} \cdot \nabla \mathbf{u} = u_i \frac{\partial u_j}{\partial x_i}$. So equation (2.4) will from here on be written as

$$\frac{\partial(\rho \mathbf{u})}{\partial t} + \rho \mathbf{u} \cdot \nabla \mathbf{u} = \nabla \cdot \boldsymbol{\sigma} + \mathbf{f}_b, \tag{2.6}$$

For incompressible flow, the momentum equation reads

$$\rho \left(\frac{\partial \mathbf{u}}{\partial t} + \mathbf{u} \cdot \nabla \mathbf{u} \right) = -\nabla p + \nabla \cdot \mathbf{T} + \mathbf{f}_b. \tag{2.7}$$

In a two dimensional Cartesian coordinate system, and in the absence of body forces, this is

$$\frac{\partial u}{\partial t} + u \frac{\partial u}{\partial x} + v \frac{\partial u}{\partial y} = -\frac{\partial p}{\partial x} + \frac{\partial \mathbf{T}_{xx}}{\partial x} + \frac{\partial \mathbf{T}_{xy}}{\partial y}, \tag{2.8}$$

$$\frac{\partial v}{\partial t} + u \frac{\partial v}{\partial x} + v \frac{\partial v}{\partial y} = -\frac{\partial p}{\partial y} + \frac{\partial \mathbf{T}_{xy}}{\partial x} + \frac{\partial \mathbf{T}_{yy}}{\partial y}, \tag{2.9}$$

2.2.3 Conservation of energy equation

When compressible media or temperature dependent problems are analyzed, the density and temperature are dependent variables. Together with thermodynamic equations of state, the energy equation then provides a relation between the density, the internal energy, and the temperature of the medium. Since this thesis only deals with incompressible fluids, under isothermal conditions, the energy equation need not be used.

2.3 The Constitutive Equation

As is shown above, in a two dimensional Cartesian coordinate system, there are three field equations, but six unknowns; pressure, two velocity components, and three independent extra-stress components. Apparently, a closure is needed to be able to solve the equations. This closure is called the constitutive equation, and it provides information about the stresses in the fluid.

The available constitutive models can be divided into two groups, the integral and the differential constitutive models. Integral models are highly accurate, but computationally expensive since the whole history of deformation has to be stored. A well-known example of an integral model is the K-BKZ model (Kaye - Bernstein, Kearsley and Zappas) [28], [2]. For some differential models it is possible to find an integral equivalent. In this research, only differential constitutive models are used. Since they move forward in time, there is no need for storing deformation history. This means that they are well-suited for use in numerical problems. Another advantage is that they can be used for calculating flow through complex geometries.

Constitutive equations can be derived in a number of possible ways. The approach that leads to classical models such as the UCM (Upper Convected Maxwell), the Oldroyd B and the PTT (Phan-Thien-Tanner) model [44] is based on a macroscopic definition of the fluid. For the UCM and Oldroyd B model this means that the behaviour of the fluid is modelled by a system of springs and dashpots, as is shown later in this section. The PTT model is derived from network theory. The polymer strands form a network of chains connection by junctions. The junctions allow for destruction and creation of the chains in the network. They are also allowed to slip, and to move with the fluid. The advantage of the PTT model over the Oldroyd B model is that it can predict shear thinning. The well known Giesekus model [20] contains a feature that makes it able to predict a second normal stress difference, which also lacks from the Oldroyd B model. These constitutive models are mathematical descriptions of the relation between the rate of deformation, or strain rate, that a fluid undergoes, and the resulting stresses that occur in the fluid. A derivation of the rate of deformation can be found in Appendix . In a planar flow the rate of deformation tensor **d** reads

$$\mathbf{d} = \begin{pmatrix} d_{xx} & d_{xy} \\ d_{xy} & d_{yy} \end{pmatrix} = \begin{pmatrix} \dfrac{\partial u}{\partial x} & \dfrac{1}{2}(\dfrac{\partial u}{\partial y} + \dfrac{\partial v}{\partial x}) \\ \dfrac{1}{2}(\dfrac{\partial u}{\partial y} + \dfrac{\partial v}{\partial x}) & \dfrac{\partial v}{\partial y} \end{pmatrix} = \frac{1}{2}\left(\nabla \mathbf{u} + (\nabla \mathbf{u})^T\right). \qquad (2.10)$$

The constitutive equation relates the three components of the extra-stress tensor to this deformation tensor, and thus provides three independent equations, completing the set of equations that is needed to describe fluid flow.

Other possibilities for deriving constitutive models are microscopic and mesoscopic approaches. The actual dynamics of the polymer are now modelled on a molecular level, and the macroscopic stress in then related to microscopic quantities such as orientation and stretch of the molecules, which is the case in the pom-pom model [34]. An example of a mesoscopic model is the FENE (Finitely Extensible Non-linear Elastic) model, which is derived from kinetic theory models. In the FENE model, two dumbbells connected by a spring model the dynamics of polymer chains. This leads to an expression for a configuration tensor at the microscopic level, from which the macroscopic stress can be computed.

The modelling of solutions of polymer strands in a resin, and melts of polymer is quite different. In some models the assumption is made that polymer strands do not interfere with each others dynamics. These models can be used to model solutions of polymer in a Newtonian solvent, i.e. a polymer solution. In the pom-pom model the behaviour of the individual strands do influence the surrounding strands, and therefore it is suitable to model polymer melts. For this reason, the remainder of this section and also the last three chapters of this thesis are divided into separate parts for Newtonian fluids, polymer solutions and polymer melts.

2.3.1 Newtonian fluids

In his Principia [37], Newton wrote that '*the resistance which arises from the lack of slipperiness of the parts of the fluid, other things being equal, is proportional to the velocity with which the parts of the fluid are separated from one another*'. Today this statement is interpreted as the shear stress is linearly dependent on the rate of deformation of the fluid. In a very general form, this linear Newtonian stress relation can be written as

$$\mathbf{T} = 2\eta\mathbf{d}, \tag{2.11}$$

in which η is the viscosity of the fluid, which is considered to be constant. Fluids that obey this linear dependency are called Newtonian fluids.

The relation (2.11) between stress and strain in a Newtonian fluid can be modelled by a simple dashpot, see Fig. 2.1. The time rate of change of the displacement, $\partial\gamma/\partial t$, of a dashpot is related to an applied force F through

$$\frac{\partial\gamma}{\partial t} = \frac{F}{\eta}. \tag{2.12}$$

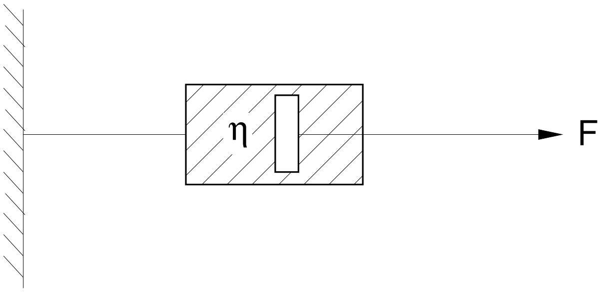

Figure 2.1: A single dashpot as a model for a Newtonian fluid.

In relation to the previous introduction to constitutive equations, the force F should be regarded as the stress in the fluid, and the rate of change of displacement as the rate of strain, or rate of deformation. The tensorial equivalent of the one dimensional equation (2.12) that the dashpot satisfies can now be written as

$$\mathbf{T} = 2\eta \mathbf{d}, \tag{2.13}$$

which is the Newtonian stress relation.

If the Newtonian stress relation (2.11) is substituted into the momentum equation (2.7) in absence of body forces, the Navier-Stokes equations can be rewritten as

$$\rho \left(\frac{\partial \mathbf{u}}{\partial t} + \mathbf{u} \cdot (\nabla \mathbf{u}) \right) = -\nabla p + \eta \Delta \mathbf{u}. \tag{2.14}$$

When the flow is considered to be creeping, the left-hand side of this equation is zero. The equation is then called the Stokes equation. Both the Stokes and the Navier-Stokes equations can be formulated in terms of either a two or a three field problem. The three field Stokes problem for example, is given by

$$\nabla \cdot \mathbf{u} = 0, \tag{2.15}$$

$$\nabla p = \nabla \cdot \mathbf{T}, \tag{2.16}$$

$$\mathbf{T} = 2\eta \mathbf{d}, \tag{2.17}$$

whereas the two field Stokes problem is defined by

$$\nabla \cdot \mathbf{u} = 0, \tag{2.18}$$

$$\nabla p = \eta \Delta \mathbf{u}. \tag{2.19}$$

2.3.2 Polymer solutions

In this thesis only Maxwell and Oldroyd models will be used to predict flow of polymer solutions. A derivation of these models is given in this section. The equations for the PTT and Giesekus model are also presented.

The UCM model

In chapter 1 it is explained that a viscoelastic fluid has characteristics of both fluids and solids. From this point of view it makes sense to model a viscoelastic material with a dashpot that models a viscous fluid, and a spring that models the elastic, solid-like behaviour. The Maxwell element (Fig. 2.2), in which a spring and a dashpot are connected in series, does just that. The dashpot, as shown before, obeys the Newtonian law for viscosity, and the spring obeys Hooke's law for solids.

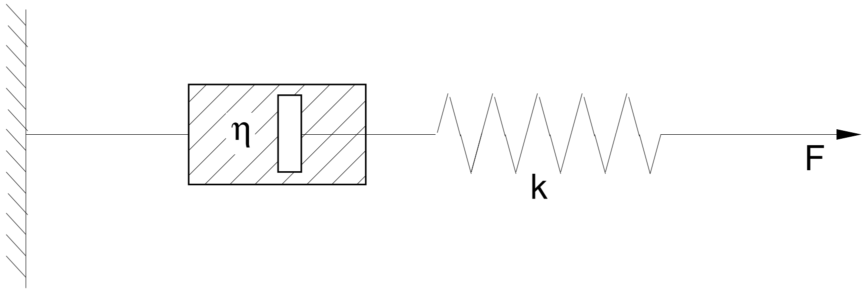

Figure 2.2: The Maxwell element: a spring-dashpot model of a Maxwell fluid.

The spring constant k is defined as the ratio of force over the displacement in a spring. Similar to the Newtonian case, the time rate of change of the total displacement can be expressed as a function of the forces in the spring and the dashpot. The same philosophy as in [26] is followed here. If the subscript 1 refers to the spring, and the subscript 2 to the dashpot, the rate of total displacement is

$$\frac{\partial \gamma}{\partial t} = \frac{\partial \gamma_1}{\partial t} + \frac{\partial \gamma_2}{\partial t} = \frac{\partial}{\partial t}\left(\frac{F_1}{k}\right) + \frac{F_2}{\eta}. \tag{2.20}$$

Since the spring and the dashpot are in series, the forces F_1 and F_2 are the same and equal F, so (2.20) reduces to

$$\frac{\partial \gamma}{\partial t} = \frac{1}{k}\frac{\partial F}{\partial t} + \frac{F}{\eta}, \tag{2.21}$$

and, with the introduction of the relaxation time $\lambda_1 = \eta/k$, we have

$$F + \lambda_1 \frac{\partial F}{\partial t} = \eta \frac{\partial \gamma}{\partial t}. \tag{2.22}$$

Again, the force F should be regarded as the stress in the fluid, and the rate of displacement $\partial\gamma/\partial t$, as the rate of deformation. The tensorial equivalent of the equation is then found to be

$$\mathbf{T} + \lambda_1 \frac{\partial \mathbf{T}}{\partial t} = 2\eta \mathbf{d}. \tag{2.23}$$

The time derivative in this equation however, is not indifferent to changes of reference frames. The Eulerian time derivative $\partial/\partial t$ is therefore replaced by an invariant derivative. The invariant derivative of a tensor $\mathbf{f}$ can be written in a general form as

$$\frac{\delta \mathbf{f}}{\delta t} = \frac{D\mathbf{f}}{Dt} - \mathbf{g} \cdot \mathbf{f} - \mathbf{f} \cdot \mathbf{g}^T, \tag{2.24}$$

where D/Dt is the material derivative, given by

$$\frac{D}{Dt} = \frac{\partial}{\partial t} + \mathbf{u} \cdot \nabla, \tag{2.25}$$

and $\mathbf{g}$ is defined as

$$\mathbf{g} = (1 - \frac{a}{2})\nabla\mathbf{u} - \frac{a}{2}(\nabla\mathbf{u})^T. \tag{2.26}$$

The upper-convected derivative is the special case of $\delta\mathbf{f}/\delta t$ with $a = 0$, and is given by

$$\overset{\nabla}{\mathbf{f}} = \frac{D\mathbf{f}}{Dt} - \nabla\mathbf{u} \cdot \mathbf{f} - \mathbf{f} \cdot (\nabla\mathbf{u})^T. \tag{2.27}$$

The terms $\nabla\mathbf{u} \cdot \mathbf{f} + \mathbf{f} \cdot (\nabla\mathbf{u})^T$ are often referred to as the deformation terms. The special cases of $\delta\mathbf{f}/\delta t$ with $a = 2$ and $a = 1$, are called the lower-convected derivative and the corotational derivative, respectively. In calculations involving viscoelastic fluids however, the upper-convected derivative is most frequently used, since it is the only derivative to produce physically relevant results for normal stress differences, as will be shown in section 2.5.3.

The UCM model is now given by (2.23), with the time derivative $\partial/\partial t$ replaced by the upper-convected derivative,

$$\mathbf{T} + \lambda_1 \overset{\nabla}{\mathbf{T}} = 2\eta \mathbf{d}. \tag{2.28}$$

The upper-convected derivate of the stress tensor $\mathbf{T}$ is given by

$$\overset{\nabla}{\mathbf{T}} = \frac{\partial \mathbf{T}}{\partial t} + \mathbf{u} \cdot \nabla \mathbf{T} - \nabla \mathbf{u} \cdot \mathbf{T} - \mathbf{T} \cdot (\nabla \mathbf{u})^T. \tag{2.29}$$

The UCM model is mathematically the simplest differential model that is available for description of the behaviour of viscoelastic models. However, it is also the hardest model to deal with numerically, because of its highly hyperbolic and nonlinear character. Together with the field equations, the UCM model is of mixed hyperbolic/elliptic type. At high Weissenberg numbers, the nonlinear upper-convected derivative becomes dominant. Although it is not within the scope of this thesis, the author believes that efficiently solving the UCM model is one of the main issues that remains open in computational rheology, since the model can be seen as a basis to which most other differential equations are extensions.

The Oldroyd model

In the Oldroyd B model, an extra term in the momentum equation adds Newtonian viscosity to the system. This overcomes part of the stability problems when trying to solve the UCM model.

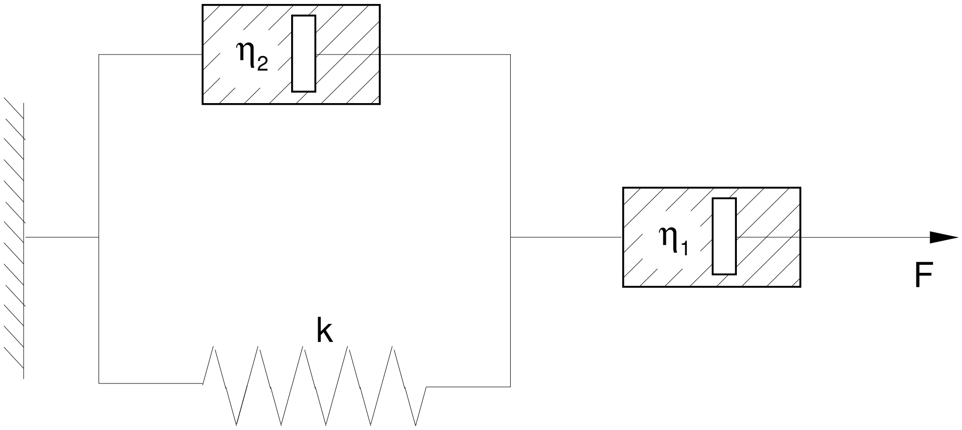

Figure 2.3: The Jeffreys model: a spring-dashpot model of an Oldroyd fluid.

The Oldroyd B model is given by

$$\mathbf{T} + \lambda_1 \overset{\nabla}{\mathbf{T}} = 2\eta(\mathbf{d} + \lambda_2 \overset{\nabla}{\mathbf{d}}). \tag{2.30}$$

The retardation time λ_2 may be seen as a measure for the time the material needs to respond to deformation. The extra-stress tensor can be split into a polymeric contribution $\boldsymbol{\tau}$ and a viscous contribution $\boldsymbol{\tau}_s$,

$$\mathbf{T} = \boldsymbol{\tau} + \boldsymbol{\tau}_s = \boldsymbol{\tau} + 2\eta_s \mathbf{d}. \tag{2.31}$$

The viscosity η is also a sum of its polymeric contribution η_p and its viscous contribution η_s, also called the solvent viscosity. The retardation and relaxation times, and the viscosity contributions are related through

$$\frac{\lambda_2}{\lambda_1} = \frac{\eta_s}{\eta_p + \eta_s}. \tag{2.32}$$

The equations can now be rewritten in terms of the polymeric contribution to the extra-stress tensor. The conservation of mass and momentum, and the constitutive equation now read

$$\nabla \cdot \mathbf{u} = 0, \tag{2.33}$$

$$\rho \left(\frac{\partial \mathbf{u}}{\partial t} + \mathbf{u} \cdot \nabla \mathbf{u} \right) = -\nabla p + \nabla \cdot \boldsymbol{\tau}_1 + \eta_s \nabla^2 \mathbf{u}, \tag{2.34}$$

$$\boldsymbol{\tau} + \lambda_1 \overset{\nabla}{\boldsymbol{\tau}} = 2\eta_p \mathbf{d}. \tag{2.35}$$

The Oldroyd B model reduces to the UCM model if λ_2 or equivalently η_s is zero. Both models predict a positive first normal stress difference and a zero second normal stress difference, which is in qualitative agreement with experimental data, in which first and second normal stress differences are found to be of opposite sign, with the first normal stress difference being an order of magnitude larger. Both models may, however, predict unbounded stress growth, as a result of the possibility of generating infinite extensional viscosity. This is, of course, an undesirable property. Moreover, they do not describe shear thinning of the fluid, so they may give a poor representation of a real fluid.

Other macroscopic models

The UCM and the Oldroyd B models are the only macroscopic models that will be used in this thesis. The PTT [44] and Giesekus [20] models will be mentioned here though, because they help to shed light on the later mentioned pom-pom model. The PTT model is given by

$$f(\lambda, \boldsymbol{\tau})\boldsymbol{\tau} + \lambda_1 \overset{\diamond}{\boldsymbol{\tau}} = 2\eta_p \mathbf{d}, \tag{2.36}$$

where the derivative $\overset{\diamond}{\boldsymbol{\tau}}$ is related to the upper-convected derivative through

$$\overset{\diamond}{\boldsymbol{\tau}} = \overset{\nabla}{\boldsymbol{\tau}} + \xi(\mathbf{d} \cdot \boldsymbol{\tau} + \boldsymbol{\tau} \cdot \mathbf{d}). \tag{2.37}$$

The parameter ξ is called the slip parameter. The PTT model can be expressed both as a linear model and as an exponential model, depending on the shape of the function $f(\lambda, \boldsymbol{\tau})$. In the linear model it has the form

$$f(\lambda_1, \boldsymbol{\tau}) = 1 + \frac{\epsilon \lambda_1}{\eta_p} I_{\boldsymbol{\tau}}, \tag{2.38}$$

and in the exponential PTT model it is of the form

$$f(\lambda_1, \boldsymbol{\tau}) = \exp\left(\frac{\epsilon \lambda_1}{\eta_p} I_{\boldsymbol{\tau}}\right). \tag{2.39}$$

The parameter ϵ is the shear thinning parameter, and it ensures that the stress growth is bounded. The parameter is usually determined by fitting of shear viscosity curves to experimental data.

The Giesekus model is given by

$$\boldsymbol{\tau} + \lambda_1 \overset{\nabla}{\boldsymbol{\tau}} + \frac{\alpha \lambda_1}{\eta_p} \boldsymbol{\tau} \cdot \boldsymbol{\tau} = 2\eta_p \mathbf{d}, \tag{2.40}$$

in which the term involving $\boldsymbol{\tau} \cdot \boldsymbol{\tau}$ introduces a second normal stress difference, the magnitude of which can be controlled by the material parameter α that can be determined by fitting to rheological data.

2.3.3 Polymer melts

As mentioned before, the modelling of polymer melts should take into account the interaction between individual molecules. Here it will be shown how the pom-pom model can be derived from the description of the dynamics of a melt at the molecular level. The derivation follows the approach used in [22]. The eXtended Pom-Pom (XPP) model [61] is based on the pom-pom model, and will also be described in this section. The philosophy behind microscopic models like these is that although it may be fine to consider the fluid as a continuum, the stress is are related to the configuration of the fluid at the molecular level. This approach leads to the following derivation of a constitutive equation.

Consider a polymer melt and a model for an average polymer molecule as a chain with N links of length b, and a certain molecular weight M_c. The molecule is described by an end-to-end vector $\mathbf{R}$. Note that the ensemble average of the end-to-end vector is $< \mathbf{R} >= 0$. Fig. 2.4 shows a volume V, in which one molecule is highlighted. The

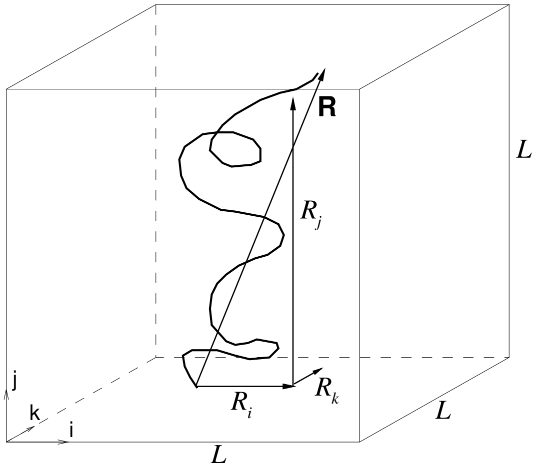

Figure 2.4: A single molecule highlighted in a volume $V = L^3$.

contribution to the stress-component σ_{ij} of the force $\mathbf{f}$ that is present in this single molecule, equals the stress that is exerted by the force in the molecule in direction i,

f_i/L^2, multiplied by the probability that the molecule cuts the j-plane of the volume V, R_j/L. Since the total number of molecules in the volume equals $L^3\rho/M_c$, the stress σ_{ij} can be expressed as

$$\sigma_{ij} = \frac{f_i}{L^2}\frac{R_j}{L}\frac{\rho}{M_c}L^3 N_A = \frac{\rho N_A}{M_c} < R_j f_i >, \tag{2.41}$$

where N_A is Avogadro's number.

The force $\mathbf{f}$ in a molecule is the force that tries to restore the molecule into its equilibrium configuration in which the end-to-end vector scales as $N^{1/2}b$. For small departures from this equilibrium, the force obeys Hooke's law and can be found to be

$$\mathbf{f} = \frac{3kT}{Nb^2}\mathbf{R}, \tag{2.42}$$

where k is Boltzmann's constant and T is the absolute temperature. With the gas constant R defined as $R = N_A k$, the expression for the stress can be found by combining (2.41) and (2.42),

$$\boldsymbol{\sigma} = \frac{\rho RT}{M_c} < 3\frac{\mathbf{RR}}{Nb^2} > . \tag{2.43}$$

When a step strain is applied to the fluid, the molecules instantaneously stretch, and then relax with a relaxation time equal to the so-called Rouse time τ_R. The Rouse time follows from the diffusivity law which states that the time of diffusion scales as the diffusion length squared over the diffusion coefficient D,

$$\tau_R \sim \frac{Nb^2}{2D}, \tag{2.44}$$

where D follows from Einsteins relation

$$D = \frac{kT}{N\zeta}, \tag{2.45}$$

in which ζ is a friction coefficient. The Rouse time can now be written as

$$\tau_R \sim \frac{N^2 b^2 \zeta}{2kT}. \tag{2.46}$$

The tube model

The derivation of the expression for the stress has not taken into account the influence of the surrounding fluid on the movement of the molecule. By neglecting this, the fluid can be physically interpreted not as a polymer melt, but as a solution of short molecules instead. When the molecular weight of the polymer is larger than some value M_e, the interactions with neighbouring molecules cannot be neglected any longer, and we are speaking of a polymer melt that is entangled. From this philosophy, de Gennes [9] and Doi and Edwards [11] developed the tube model for polymer melts of linear molecules. Such a melt would represent a High Density Poly-Ethylene (HDPE), for example. The idea is that the lateral movement of a polymer molecule is restricted by the surrounding molecules. An imaginary tube is then thought to surround the molecule (Fig. 2.5), through which the molecule is allowed to reptate, i.e. move into and out of the tube.

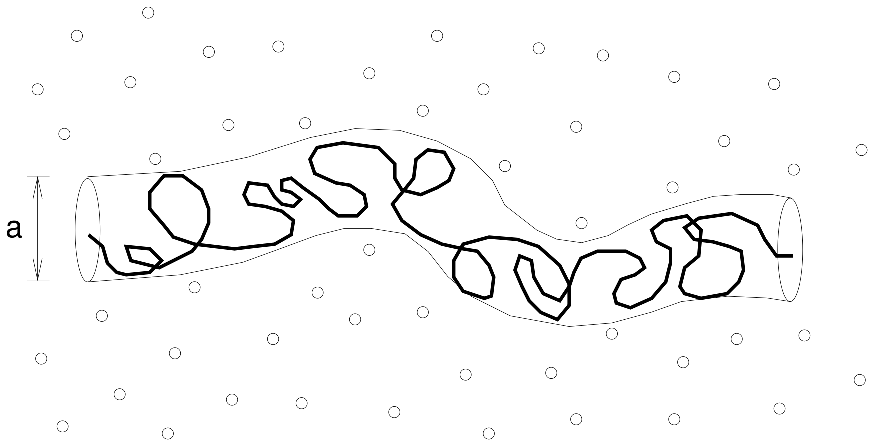

Figure 2.5: The tube model.

Since each part of the polymer molecule in Fig. 2.5 that is smaller than the entanglement molecular weight M_e will behave as an unentangled chain described before, the molecule is thought of as $s = M/M_e$ such unentangled segments. All these segments are characterized with an end-to-end vector equal to the diameter a which scales as $N_e^{1/2}b$, where N_e is the number of links in one segment, i.e. $N_e = N/s$. Equivalent to the Rouse time, the relaxation time of each of the unentangled segments is

$$\tau_e \sim \frac{a^2}{2D} \sim \frac{N_e b^2 N_e \zeta}{2kT} \sim \frac{N_e^2 b^2 \zeta}{2kT}. \tag{2.47}$$

Relaxation of the molecule in this tube model, however, is essentially different from the relaxation of the unentangled polymer. After the molecule is stretched with a step strain, the molecule first relaxes back into the tube to its original length $s \cdot a$. This relaxation happens in the Rouse time. Due to the restriction in the lateral movement, however, the molecule is not relaxed yet and tries to achieve relaxation by reptating, or diffusing, out of the tube. Again, the time this diffusion takes can be calculated with the diffusivity law

$$\tau_{\text{rep}} \sim \frac{(sa)^2}{2D} \sim \frac{s^2 a^2 N \zeta}{2kT} \sim \frac{s^2 N_e b^2 s N_e \zeta}{2kT} \sim s^3 \frac{N_e^2 b^2 \zeta}{2kT} \sim s^3 \tau_e. \tag{2.48}$$

Note that without entanglement, the Rouse time of the polymer is $\tau_R \sim s^2 \tau_e$.

The stress in a segment of the molecule with mass M_e can now be found following the same philosophy as before. The stress is written as

$$\boldsymbol{\sigma} = G_0 \mathbf{S}, \tag{2.49}$$

where $G_0 = \rho RT/M_e$ is the plateau modulus, and $\mathbf{S}$ is a tensor giving the orientation of the tube segments,

$$\mathbf{S} = \frac{< \mathbf{RR} >}{a^2/3}. \tag{2.50}$$

The orientation tensor $\mathbf{S}$ can also be expressed by the integral

$$\int_{-\infty}^{t} \frac{dt'}{\tau_{\text{rep}}} e^{-\frac{t-t'}{\tau_{\text{rep}}}} \mathbf{Q}(t', t), \tag{2.51}$$

where $\mathbf{Q}(t', t)$ is the orientatien tensor at time t, formed from an isotropic distribution of tube segments at time t', with $t > t'$.

The pom-pom molecule

When the molecule in Fig. 2.5 is provided with a number of arms, q, the pom-pom molecule is obtained. The pom-pom molecule in Fig. 2.6, for example, has $q = 3$.

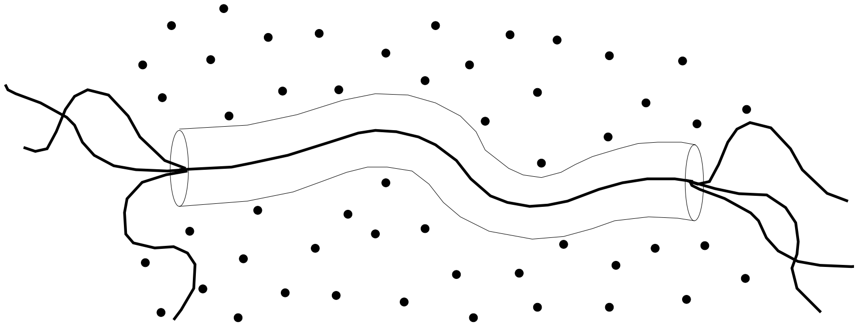

Figure 2.6: The pom-pom molecule.

Equivalent to the number of entanglements $s = s_b$ in the backbone, the number of entanglements in each of the arms is $s_a = M_a/M_e$, with M_a the molecular weight of the arm. At the two branch points, the molecule is effectively 'pinned down'. Reptation of the backbone is therefore only possible after the arms have diffused. This time of diffusion, τ_a, of the arms increases exponentially with the length of the arms,

$$\tau_a \sim \tau_e e^{s_a}. \tag{2.52}$$

In this time τ_a, the branchpoint is allowed to diffuse a length a and then the process of arm diffusion starts again (picture the image of a molecule consisting of a backbone with diffuse 'blobs' at both ends, and the name pom-pom suddenly makes sense). The Einstein relation for the branchpoint can now be written as

$$\tau_a q \sim \frac{a^2}{2D_{bp}}, \tag{2.53}$$

where the factor q reflects the fact that all arms have to diffuse before branchpoint reptation. The relaxation time of the backbone is given by

$$\tau_b \sim \frac{s_b^2 a^2}{2D_{bp}} \sim \frac{s_b^2 a^2 \tau_a q}{2a^2} \sim \frac{s_b^2 2\tau_a q}{2} \sim s_b^2 q e^{s_a} \tau_e, \tag{2.54}$$

This expression needs some correction due to differences in one- and three-dimensional diffusion coefficients and due to tube-diameter growth in the presence of arms, since the arms of neighbouring molecules do not impose the same strict constraint on lateral movement as the presence of a backbone of a neighbouring molecule. This 'dynamic dilution' makes the tube wider by a factor ϕ^{α}, where $\alpha = 1$ or $\frac{4}{3}$, and $\phi = M_b/(2qM_a + M_b)$, where M_b is the molecular weight of the backbone. The correct definition of the relaxation time of the backbone orientation is therefore given by

$$\tau_b = \frac{24\phi^{2\alpha}}{\pi^2} q s_b^2 \tau_a, \tag{2.55}$$

On the basis of the backbone relaxation time τ_b, the integral expression for the orientation tensor $\mathbf{S}$ can be defined again as

$$\int_{-\infty}^{t} \frac{dt'}{\tau_b} e^{-\frac{t-t'}{\tau_b}} \mathbf{Q}(t', t). \tag{2.56}$$

As mentioned before, integral models like these are very hard to deal with computationally, and therefore a differential approximation was sought for by McLeish and Larson [34]. This approximation is given by

$$\mathbf{S} = \frac{\mathbf{A}}{I_{\mathbf{A}}}, \tag{2.57}$$

where $I_{\mathbf{A}}$ is the trace of the tensor $\mathbf{A}$, which obeys the Maxwell model

$$\mathbf{A} + \tau_b \overset{\triangledown}{\mathbf{A}} = \mathbf{I}/3. \tag{2.58}$$

The arms that are present in the pom-pom molecule are affected by friction from the surrounding fluid. This drag force on the branch points causes the backbone to stretch, a feature that is not present in the Doi-Edwards model. Equivalent to (2.42), the tension in the backbone, characterized by the position vectors of the branch points $\mathbf{x}_1$ and $\mathbf{x}_2$, is given by

$$\mathbf{f}_b = \frac{3kT}{s_b a^2}(\mathbf{x}_2 - \mathbf{x}_1) = \frac{3kT}{a}\lambda\hat{\mathbf{n}}, \tag{2.59}$$

where $\hat{\mathbf{n}}$ is the unit vector parallel to the backbone tube, and $\lambda = \dfrac{|\mathbf{x}_2 - \mathbf{x}_1|}{s_b a}$ is the stretch of the backbone, which is the length after the stretch, relative to the length in equilibrium. The equilibrium force in the chain of $3kT/a$ needs to be subtracted from this, and then the force acting on both branch points obeys the following balances

$$\begin{aligned} \zeta_{bp}(\frac{D\mathbf{x}_1}{Dt} - \mathbf{u}_1) &= \frac{3kT}{a}(\lambda - 1)\hat{\mathbf{n}}, && (2.60) \\ \zeta_{bp}(\frac{D\mathbf{x}_2}{Dt} - \mathbf{u}_2) &= -\frac{3kT}{a}(\lambda - 1)\hat{\mathbf{n}}, && (2.61) \end{aligned}$$

where $\mathbf{u}_1$ and $\mathbf{u}_2$ are the velocities of the fluid at the branch points. Subtracting the force balances yields

$$\zeta_{bp}(\frac{D\lambda}{Dt}s_b a - \lambda s_b a \mathbf{S} : \nabla \mathbf{u}) = -\frac{6kT}{a}(\lambda - 1), \tag{2.62}$$

where $\lambda s_b a \mathbf{S} : \nabla \mathbf{u}$ replaces $\mathbf{u}_2 - \mathbf{u}_1$, and follows from a Taylor series approximation on the ensemble averaged tube orientation. The stretch equation can now be written as

$$\frac{D\lambda}{Dt} = \lambda \mathbf{S} : \nabla \mathbf{u} - \frac{\lambda - 1}{\tau_s}, \tag{2.63}$$

where the relaxation time of the stretch is given by

$$\tau_s = \frac{s_b a^2 \zeta_{bp}}{6kT}. \tag{2.64}$$

The friction coefficient of the branchpoint can be found through Einstein's relation (2.53),

$$\zeta_{bp} = \frac{kT}{D_{bp}} = kT\frac{2q\tau_a}{a^2}, \tag{2.65}$$

and with the correction factor, the stretch relaxation time is defined by

$$\tau_s = 2\phi^\alpha q s_b \tau_a. \tag{2.66}$$

The relative magnitude of the backbone relaxation time (2.55) to this stretch relaxation time is of the order $\frac{12}{\pi^2}\phi^\alpha s_b \sim s_b$. This value is typically between 2 and 5 for branched polymers. High values correspond to molecules with relatively long backbones, whereas low values correspond to melts where the dynamic dilution is high and backbones are only slightly entangled.

When the stretch becomes too large, the arms will retract into the backbone-tube. This happens when the tension in the backbone $\lambda \cdot \frac{3kT}{a}$ exceeds the tensions $q \cdot \frac{3kT}{a}$ in the arms. The value of the stretch can therefore not exceed the number of arms of the pom-pom molecule, $\lambda \leq q$.

The expression for the stress also changes as a result of the stretch of the molecule. The equilibrium length $a = N_e^{1/2} b$ after stretch changes to $\lambda a = N_e^{1/2} b$, and the stress changes from $\boldsymbol{\sigma} = G_0 \mathbf{S}$ to

$$\boldsymbol{\sigma} = 3G_0 \lambda^2 \mathbf{S}. \tag{2.67}$$

The factor 3 is incorporated to recover the correct linear viscoelastic behaviour.

The original pom-pom model

As is shown above, the differential form of the pom-pom model [34] is given by an equation for the orientation tensor of the backbone and an equation for the stretch of the molecule,

$$\mathbf{A} + \tau_b \overset{\triangledown}{\mathbf{A}} = \mathbf{I}/3, \tag{2.68}$$

$$\frac{D\lambda}{Dt} = \lambda \frac{\mathbf{A} : \nabla \mathbf{u}}{I_{\mathbf{A}}} - \frac{\lambda - 1}{\tau_s}, \qquad \lambda \leq q. \tag{2.69}$$

The stress can then be calculated from

$$\boldsymbol{\sigma} = 3G_0 \lambda^2 \frac{\mathbf{A}}{I_{\mathbf{A}}} = 3G_0 \lambda^2 \mathbf{S}. \tag{2.70}$$

The main drawback of this model is that at the point when $\lambda = q$, a discontinuity is present in the extensional viscosity, as will be shown in section 2.5. This can be overcome by not fixing the branch points, but by allowing them to move freely at distances shorter than a. Blackwell et al. [4] have shown that this results in a modification of the stretch relaxation time from τ_s to $\tau_s e^{-\nu(\lambda-1)}$. The stress equation now becomes

$$\frac{D\lambda}{Dt} = \lambda \frac{\mathbf{A} : \nabla \mathbf{u}}{I_{\mathbf{A}}} - \frac{\lambda - 1}{\tau_s} e^{\nu(\lambda-1)}, \qquad \lambda \leq q, \tag{2.71}$$

where the value of ν is found to be inversely proportional to q by fitting the model to shear-viscosity data. A commonly used value is $\nu = 2/q$.

As is mentioned in chapter 1, numerical studies by Bisko [3] and Inkson et al. [25] using the the pom-pom model have shown good agreement with a range of experiments for LDPE melts.

The extended pom-pom model

Based on the pom-pom model of McLeish and Larson [34], Verbeeten et al. [61] developed the eXtended Pom-Pom (XPP) model. The extensions overcome a few problems with the original pom-pom model. First, the original model predicts a zero second normal stress difference. Secondly, there is an unphysical discontinuity in the gradient of the extensional viscosity when the stretch is equal to q at steady state. Thirdly, the shear stress has a maximum.

In the eXtended Pom-Pom (XPP) model, two of these problems are circumvented. A modification to the stretch equation, as introduced by Blackwell [4], which allows for branch point displacement, is used to overcome the discontinuity in the gradient of the extensional viscosity. The retraction of the arms into the tube has been neglected, and thereby the constraint that the stretch cannot be larger than the number of arms is removed. A Giesekus-like term has been added to the orientation equation, to introduce a non-zero second normal stress difference. Furthermore, the orientation equation is bounded for high strain rates. To get around the problem of the maximum in the shear stress that is inherent to the original pom-pom model, so called convective constraint release (CCR) [35] can be introduced. This is, however, not incorporated in the XPP model, and will not be dealt with in this thesis.

The evolution equations for the orientation tensor $\mathbf{s}$, and the backbone stretch λ, for the eXtended Pom-Pom (XPP) model of Verbeeten et al. [61] are given by

$$\overset{\nabla}{\mathbf{s}} + f(\lambda, \mathbf{s}, \mathbf{u})\mathbf{s} + \frac{\alpha - 1}{3\lambda^2 \lambda_{0b}}\mathbf{I} + \frac{3\alpha\lambda^2}{\lambda_{0b}}\mathbf{s} \cdot \mathbf{s} = \mathbf{0}, \tag{2.72}$$

and

$$\frac{\partial \lambda}{\partial t} + \mathbf{u} \cdot \nabla \lambda = \lambda(\mathbf{d} : \mathbf{s}) - \frac{(\lambda - 1)}{\lambda_{0s}} e^{\nu(\lambda - 1)}, \tag{2.73}$$

respectively, where the function $f(\lambda, \mathbf{s}, \mathbf{u})$ is given by

$$f(\lambda, \mathbf{s}, \mathbf{u}) = 2\mathbf{d} : \mathbf{s} + \frac{1}{\lambda^2 \lambda_{0b}}(1 - \alpha - 3\alpha\lambda^4 I_{\mathbf{s}\cdot\mathbf{s}}). \tag{2.74}$$

In these equations λ_{0b} and λ_{0s} are the relaxation times of orientation and the stretch of the backbone, respectively. The evolution equation of the orientation tensor incorporates features of the Giesekus model, and for $\alpha \neq 0$ a nonzero second normal stress difference is predicted. The parameter ν is incorporated to remove the discontinuity from the gradient of the extensional viscosity. Its value is obtained by data fitting and is found to be inversely proportional to the number of arms q, viz.

$$\nu = \frac{2}{q}. \tag{2.75}$$

Finally, the extra-stress tensor can be derived from the orientation tensor through the following relation

$$\boldsymbol{\tau} = G_0(3\lambda^2 \mathbf{s} - \mathbf{I}). \tag{2.76}$$

Note that the orientation tensor exhibits a nonzero third normal stress component, even in 2D problems. The equation for this component may be eliminated from the system of equations since it is known that the trace of the orientation tensor, $I_{\mathbf{s}}$, is unity.

Equations (2.72) - (2.74) are collectively known as the double equation version of the XPP model. Equation (2.72) may be reformulated (see Appendix C) in terms of the extra-stress tensor rather than in terms of the orientation tensor. This yields the constitutive equation for the single equation version of the XPP model. It relates the polymeric stress to the rate of deformation tensor $\mathbf{d}$ through

$$f(\lambda, \boldsymbol{\tau})\boldsymbol{\tau} + \lambda_{0b} \overset{\nabla}{\boldsymbol{\tau}} + G_0(f(\lambda, \boldsymbol{\tau}) - 1)\mathbf{I} + \frac{\alpha}{G_0}\boldsymbol{\tau} \cdot \boldsymbol{\tau} = 2\lambda_{0b} G_0 \mathbf{d}, \tag{2.77}$$

in which the function $f(\lambda, \boldsymbol{\tau})$ is given by

$$f(\lambda, \boldsymbol{\tau}) = 2\frac{\lambda_{0b}}{\lambda_{0s}} e^{\nu(\lambda - 1)} \left(1 - \frac{1}{\lambda}\right) + \frac{1}{\lambda^2}\left[1 - \frac{\alpha I_{\boldsymbol{\tau}\cdot\boldsymbol{\tau}}}{3G_0^2}\right]. \tag{2.78}$$

In the single equation version, the backbone stretch λ is directly coupled to the extra-stress by taking the trace of (2.76). This yields the relation

$$\lambda = \sqrt{1 + \frac{I_{\boldsymbol{\tau}}}{3G_0}}. \tag{2.79}$$

Multimode pom-pom models

Molecules in a real polymer melt are not as simple as the pom-pom molecule depicted in Fig. 2.6. Often they consist of multiple connected backbone segments. An approximation of the relaxation of such complex molecules is achieved by considering it as a number of pom-pom molecules. Similar to the relaxation of a single pom-pom molecule, the complex molecule also relaxes from the outside inwards. In the single pom-pom molecule this is separated into relaxation of the arms, followed by relaxation of the backbone. In the complex molecule, separate pom-pom molecules need to model each of the equivalent relaxation levels. The total polymeric stress for the fluid consisting of complex molecules, is then found by adding the contributions of the stresses of the separate pom-pom molecules, i.e.

$$\boldsymbol{\tau} = \sum_{i=1}^{M} \boldsymbol{\tau}_i, \tag{2.80}$$

where M is the number of modes, or separate pom-pom molecules. The stress contributions $\boldsymbol{\tau}_i$ are found from the same constitutive equations as for single-mode models, but every mode has its own stretch λ_i and is characterized by its own set of material parameters.

2.4 Non-dimensional Equations

In this thesis all equations are used in non-dimensional form. All lengths will be non-dimensionalized with a length scale L, velocity with U, times with U/L, pressure and stress with $L/(\eta U)$,

$$\mathbf{x}^* = \frac{\mathbf{x}}{L}, \quad \mathbf{u}^* = \frac{\mathbf{u}}{U}, \quad t^* = \frac{Ut}{L}, \quad p^* = \frac{Lp}{\eta U}, \quad \boldsymbol{\tau}^* = \frac{L\boldsymbol{\tau}}{\eta U}.$$

As mentioned before, the viscosity η is the sum of its polymeric contribution η_p, and its viscous contribution η_s. The Reynolds number, Re, the Weissenberg number, We, and the viscosity ratio parameter β are defined by

$$Re = \frac{\rho U L}{\eta}, \qquad We = \frac{\lambda_1 U}{L}, \qquad \beta = \frac{\lambda_2}{\lambda_1} = \frac{\eta_s}{\eta_p + \eta_s}. \tag{2.81}$$

The constitutive equations for the XPP model are made dimensionless by suitably modifying the non-dimensionalization used for the Oldroyd B model. The motivation for doing this is to create a generic algorithm that can be used to simulate a large class of constitutive models. The polymeric viscosity η_p is defined in terms of the linear relaxation modulus G_0, which in turn can be defined as a viscosity divided by a timescale. This timescale is chosen to be λ_{0b}, so η can now be broken up into

$$\eta = \eta_s + \eta_p = \eta_s + G_0 \lambda_{0b}. \tag{2.82}$$

In this way the Weissenberg number and the parameter β become

$$We = \frac{\lambda_{0b} U}{L}, \qquad \beta = \frac{\eta_s}{\eta_s + G_0 \lambda_{0b}}. \tag{2.83}$$

This non-dimensionalization of the equations for the XPP model ensures that the conservation equations are the same for the XPP model as for the UCM and Oldroyd B models. One more non-dimensional material parameter needs to be introduced for the pom-pom model. This is the parameter ϵ, which is defined as the ratio of the two relaxation times that characterize the pom-pom molecule,

$$\varepsilon = \frac{\lambda_{0s}}{\lambda_{0b}}. \tag{2.84}$$

In a multimode model the material parameters α_i and $\nu_i = 2/q_i$ are allowed to be different for every mode i. The nondimensional parameters become

$$We_i = \frac{\lambda_{0b,i} U}{L}, \qquad \beta = \frac{\eta_s}{\eta_s + \eta_p} = \frac{\eta_s}{\eta_s + \sum_{i=1}^{M} \eta_{p,i}}, \qquad \varepsilon_i = \frac{\lambda_{0s,i}}{\lambda_{0b,i}}, \tag{2.85}$$

where M is the total number of modes, and the modal polymeric viscosities are $\eta_{p,i} = G_{0,i}\lambda_{0b,i}$. An extra viscosity ratio $\tilde{\beta}$ is now defined for every mode as

$$\tilde{\beta}_i = \frac{\eta_{p,i}}{\eta_p}. \tag{2.86}$$

2.4.1 The Navier-Stokes equations

The non-dimensional Navier-Stokes equations in the three field formulation are given by

$$\begin{aligned} \nabla \cdot \mathbf{u} &= 0, & (2.87)\\ Re\left(\frac{\partial \mathbf{u}}{\partial t} + \mathbf{u} \cdot \nabla \mathbf{u}\right) &= -\nabla p + \nabla \cdot \boldsymbol{\tau}, & (2.88)\\ \boldsymbol{\tau} &= 2\mathbf{d}, & (2.89) \end{aligned}$$

and after substituting the constitutive equation into the momentum equation, the non-dimensional two field formulation is

$$\nabla \cdot \mathbf{u} = 0, \tag{2.90}$$

$$Re\left(\frac{\partial \mathbf{u}}{\partial t} + \mathbf{u} \cdot \nabla \mathbf{u}\right) = -\nabla p + \nabla^2 \mathbf{u}. \tag{2.91}$$

In this thesis the Stokes equations will be used in a two dimensional Cartesian coordinate system with components (x, y), and in a cylindrical polar coordinate system with components (z, r, θ). Problems defined in the first system are refered to as 'planar'. There is no θ-dependence in the problems dealt with in this thesis. Therefore, problems in the latter system are called 'axisymmetric'. The three field Stokes problem is written out in component form for both coordinate systems in Appendix B (see Table B.1).

2.4.2 The UCM and Oldroyd B models

The system of non-dimensional equations for the Oldroyd B model is

$$\nabla \cdot \mathbf{u} = 0, \tag{2.92}$$

$$Re\left(\frac{\partial \mathbf{u}}{\partial t} + \mathbf{u} \cdot \nabla \mathbf{u}\right) = -\nabla p + \nabla \cdot \boldsymbol{\tau} + \beta \nabla^2 \mathbf{u}, \tag{2.93}$$

$$\boldsymbol{\tau} + We\overset{\nabla}{\boldsymbol{\tau}} = 2(1-\beta)\mathbf{d}, \tag{2.94}$$

which reduces to the UCM equations when $\beta = 0$.

2.4.3 The XPP model

The non-dimensional double equation variant of the XPP model is

$$f(\lambda, \mathbf{s}, \mathbf{u})\mathbf{s} + We\overset{\nabla}{\mathbf{s}} + \frac{\alpha - 1}{3\lambda^2}\mathbf{I} + 3\alpha\lambda^2 \mathbf{s} \cdot \mathbf{s} = 0, \tag{2.95}$$

where

$$f(\lambda, \mathbf{s}, \mathbf{u}) = 2We\mathbf{d} : \mathbf{s} + \frac{1}{\lambda^2}(1 - \alpha - 3\alpha\lambda^4 I_{\mathbf{s}\cdot\mathbf{s}}), \tag{2.96}$$

and the equation for the backbone stretch is

$$\frac{\partial \lambda}{\partial t} + \mathbf{u} \cdot \nabla \lambda = \lambda(\mathbf{d} : \mathbf{s}) - \frac{(\lambda - 1)}{\epsilon We} e^{\nu(\lambda - 1)}. \tag{2.97}$$

The extra-stress tensor can be found using the relationship

$$\boldsymbol{\tau} = \frac{(1-\beta)}{We}(3\lambda^2 \mathbf{s} - \mathbf{I}). \tag{2.98}$$

The non-dimensional single equation variant of the XPP model is given by

$$f(\lambda, \boldsymbol{\tau})\boldsymbol{\tau} + We \overset{\nabla}{\boldsymbol{\tau}} + \frac{1-\beta}{We}\left[f(\lambda, \boldsymbol{\tau}) - 1\right]\mathbf{I} + \frac{\alpha We}{1-\beta}\boldsymbol{\tau} \cdot \boldsymbol{\tau} = 2(1-\beta)\mathbf{d}, \tag{2.99}$$

where $f(\lambda, \boldsymbol{\tau})$, and λ are given by

$$f(\lambda, \boldsymbol{\tau}) = \frac{2}{\epsilon}\left(1 - \frac{1}{\lambda}\right) e^{\nu(\lambda-1)} + \frac{1}{\lambda^2}\left[1 - \left(\frac{We}{(1-\beta)}\right)^2 \frac{\alpha}{3} I_{\boldsymbol{\tau}\cdot\boldsymbol{\tau}}\right], \tag{2.100}$$

and

$$\lambda = \sqrt{1 + \frac{We}{(1-\beta)}\frac{1}{3} I_{\boldsymbol{\tau}}}. \tag{2.101}$$

The stress for the multimode version of the single equation variant of the XPP model is given by

$$\boldsymbol{\tau} = \sum_{i=1}^{M} \boldsymbol{\tau}_i, \tag{2.102}$$

where the stresses $\boldsymbol{\tau}_i$ are governed by

$$\begin{aligned} f(\lambda_i, \boldsymbol{\tau}_i)\boldsymbol{\tau}_i + We_i \overset{\nabla}{\boldsymbol{\tau}_i} + \frac{\tilde{\beta}_i(1-\beta)}{We_i}\left[f(\lambda_i, \boldsymbol{\tau}_i) - 1\right]\mathbf{I} & \\ + \frac{\alpha We_i}{\tilde{\beta}_i(1-\beta)}\boldsymbol{\tau}_i \cdot \boldsymbol{\tau}_i = 2\tilde{\beta}_i(1-\beta)\mathbf{d}, & \end{aligned} \tag{2.103}$$

where $f(\lambda_i, \boldsymbol{\tau}_i)$, and λ_i are given by

$$f(\lambda_i, \boldsymbol{\tau}_i) = \frac{2}{\epsilon_i}\left(1 - \frac{1}{\lambda_i}\right) e^{\nu_i(\lambda_i-1)} + \frac{1}{\lambda_i^2}\left[1 - \left(\frac{We_i}{\tilde{\beta}_i(1-\beta)}\right)^2 \frac{\alpha_i}{3} I_{\boldsymbol{\tau}_i\cdot\boldsymbol{\tau}_i}\right], \tag{2.104}$$

and

$$\lambda_i = \sqrt{1 + \frac{We_i}{\tilde{\beta}_i(1-\beta)}\frac{1}{3} I_{\boldsymbol{\tau}_i}}. \tag{2.105}$$

2.4.4 Generic model

A generic model is now presented, on the basis of the XPP model. Both versions of the XPP model are represented by just one constitutive equation, since they are fully equivalent as shown in Appendix C. The only difference is that the stretch λ is calculated differently in both models. The equations in the generic model read

$$\nabla \cdot \mathbf{u} = 0, \tag{2.106}$$

$$Re\left(\frac{\partial \mathbf{u}}{\partial t} + \mathbf{u} \cdot \nabla \mathbf{u}\right) = -\nabla p + \nabla \cdot \boldsymbol{\tau} + \beta \nabla^2 \mathbf{u}, \tag{2.107}$$

$$f(\lambda, \boldsymbol{\tau})\boldsymbol{\tau} + We \overset{\nabla}{\boldsymbol{\tau}} + (f(\lambda, \boldsymbol{\tau}) - 1)\frac{1-\beta}{We}\mathbf{I} + \frac{\alpha We}{1-\beta}\boldsymbol{\tau} \cdot \boldsymbol{\tau} = 2(1-\beta)\mathbf{d}, \tag{2.108}$$

where

$$f(\lambda, \boldsymbol{\tau}) = \frac{2}{\epsilon}\left(1 - \frac{1}{\lambda}\right)e^{\nu(\lambda-1)} + \frac{1}{\lambda^2}(1 - \frac{\alpha}{3}\left(\frac{We}{1-\beta}\right)^2 I_{\boldsymbol{\tau}\cdot\boldsymbol{\tau}}). \tag{2.109}$$

In Table 2.1 it is shown how λ needs to be calculated, and what value the different parameters need to be set to, to retrieve from this generic model, the double equation version of the XPP model, the single equation version the XPP model, the Oldroyd B, the UCM, the Navier-Stokes and the Stokes models respectively.

In Appendix B the equations in the generic model, and the expressions for the stretch λ in the double and single equation versions of the XPP model are given in two dimensional Cartesian coordinates.

2.5 Theoretical Issues

In the previous sections a few references have been made to some theoretical issues concerned with the constitutive models. Some of these issues will be presented in more detail here. First some comments will be made on the stability of the equations that have been presented. A study on the type of the equations will also be shown, and the

Table 2.1: Calculation of the stretch λ, and the parameter settings for the different models.

Model	Calculation of backbone stretch λ and other parameters				
double eq. XPP	$\frac{\partial \lambda}{\partial t} + \mathbf{u} \cdot \nabla \lambda = \frac{We}{3(1-\beta)} \frac{1}{\lambda} (\mathbf{d} : \boldsymbol{\tau}) - \frac{\lambda - 1}{\epsilon We} e^{\nu(\lambda - 1)}$				$\nu = \frac{2}{q}$
single eq. XPP	$\lambda = \sqrt{1 + \frac{We}{(1-\beta)} \frac{1}{3} I_{\boldsymbol{\tau}}}$				
Oldroyd B	$\lambda = 1$	$\alpha = 0$			
UCM	$\lambda = 1$	$\alpha = 0$	$\beta = 0$		
Navier-Stokes	$\lambda = 1$	$\alpha = 0$	$\beta = 0$	$We = 0$	
Stokes	$\lambda = 1$	$\alpha = 0$	$\beta = 0$	$We = 0$	$Re = 0$

boundary condition settings that arise from these problems are given. The viscoelastic effect of non-zero first and second normal stress differences that are predicted by the models is presented. Finally, the prediction of shear and extensional viscosity by the pom-pom models is given.

2.5.1 Well-posedness, existence, uniqueness and stability

According to Hadamard a deterministic solution to a set of equations is only possible under three conditions. These conditions are that a solution exists, the solution is unique, and that the solution is stable. The problem is called well-posed if it satisfies all three criteria. For Newtonian fluids well-posedness has been proven for some problems, and so numerical solutions can be sought for in the faith that they exist. For the equations that govern the flow of viscoelastic fluids existence and uniqueness of solutions have only been proven for some simple problems (see [47], for example) due to their complicated non-linear form. Although this makes the search for numerical solutions controversial from a mathematical viewpoint, a more pragmatic approach needs to be adopted and the field of computational rheology proceeds in the faith that existence and uniqueness exist, but have not been proven yet. To be able to make some comments on stability of the equations and on how boundary conditions can be imposed to constitute a well-posed problem, the type of the equations that are used in this thesis is analyzed in the next section.

2.5.2 Type of the equations

It is known that the type of the system of partial differential equations for the UCM model is mixed elliptic/hyperbolic and that the corresponding system for the Oldroyd B model is of mixed parabolic/elliptic/hyperbolic type (see [26]). The type of the set of equations provides information on how to impose boundary conditions. To determine the type of the system of governing equations for the XPP model, the double equation version is written in the form

$$A_0\frac{\partial\phi}{\partial t} + A_1\frac{\partial\phi}{\partial x} + A_2\frac{\partial\phi}{\partial y} + A_3\left(\frac{\partial^2\phi}{\partial x^2} + \frac{\partial^2\phi}{\partial y^2}\right) + S\phi = 0, \tag{2.110}$$

with $\phi = (p, u, v, \tau_{xx}, \tau_{yy}, \tau_{zz}, \tau_{xy}, \lambda)^T \equiv (p, u, v, \sigma, \gamma, \mu, \tau, \lambda)^T$ and R and W are the Reynolds and Weissenberg numbers, respectively, the matrices are given by

$$A_0 = \begin{pmatrix} 0 & 0 & 0 & 0 & 0 & 0 & 0 & 0 \\ 0 & R & 0 & 0 & 0 & 0 & 0 & 0 \\ 0 & 0 & R & 0 & 0 & 0 & 0 & 0 \\ 0 & 0 & 0 & W & 0 & 0 & 0 & 0 \\ 0 & 0 & 0 & 0 & W & 0 & 0 & 0 \\ 0 & 0 & 0 & 0 & 0 & W & 0 & 0 \\ 0 & 0 & 0 & 0 & 0 & 0 & W & 0 \\ 0 & 0 & 0 & 0 & 0 & 0 & 0 & 1 \end{pmatrix}, \tag{2.111}$$

$$A_1 = \begin{pmatrix} 0 & 1 & 0 & 0 & 0 & 0 & 0 & 0 \\ 1 & Ru & 0 & -1 & 0 & 0 & 0 & 0 \\ 0 & 0 & Ru & 0 & 0 & 0 & -1 & 0 \\ 0 & -2m_1 & 0 & Wu & 0 & 0 & 0 & 0 \\ 0 & 0 & -2m_3 & 0 & Wu & 0 & 0 & 0 \\ 0 & 0 & 0 & 0 & 0 & Wu & 0 & 0 \\ 0 & 0 & -m_1 & 0 & 0 & 0 & Wu & 0 \\ 0 & \dfrac{-\sigma}{3k\lambda} & \dfrac{-\tau}{3k\lambda} & 0 & 0 & 0 & 0 & u \end{pmatrix}, \tag{2.112}$$

$$A_2 = \begin{pmatrix} 0 & 0 & 1 & 0 & 0 & 0 & 0 & 0 \\ 0 & Rv & 0 & -1 & 0 & 0 & 0 & 0 \\ 1 & 0 & Rv & 0 & 0 & 0 & -1 & 0 \\ 0 & -2m_3 & 0 & Wv & 0 & 0 & 0 & 0 \\ 0 & 0 & -2m_2 & 0 & Wv & 0 & 0 & 0 \\ 0 & 0 & 0 & 0 & 0 & Wv & 0 & 0 \\ 0 & -m_2 & 0 & 0 & 0 & 0 & Wv & 0 \\ 0 & \dfrac{-\tau}{3k\lambda} & \dfrac{-\gamma}{3k\lambda} & 0 & 0 & 0 & 0 & v \end{pmatrix}, \tag{2.113}$$

$$A_3 = \begin{pmatrix} 0 & 0 & 0 & 0 & 0 & 0 & 0 & 0 \\ 0 & -\beta & 0 & 0 & 0 & 0 & 0 & 0 \\ 0 & 0 & -\beta & 0 & 0 & 0 & 0 & 0 \\ 0 & 0 & 0 & 0 & 0 & 0 & 0 & 0 \\ 0 & 0 & 0 & 0 & 0 & 0 & 0 & 0 \\ 0 & 0 & 0 & 0 & 0 & 0 & 0 & 0 \\ 0 & 0 & 0 & 0 & 0 & 0 & 0 & 0 \\ 0 & 0 & 0 & 0 & 0 & 0 & 0 & 0 \end{pmatrix}, \tag{2.114}$$

$$S = \begin{pmatrix} 0 & 0 & 0 & 0 & 0 & 0 & 0 & 0 \\ 0 & 0 & 0 & 0 & 0 & 0 & 0 & 0 \\ 0 & 0 & 0 & 0 & 0 & 0 & 0 & 0 \\ 0 & 0 & 0 & S_\sigma & 0 & 0 & 0 & 0 \\ 0 & 0 & 0 & 0 & S_\gamma & 0 & 0 & 0 \\ 0 & 0 & 0 & 0 & 0 & S_\mu & 0 & 0 \\ 0 & 0 & 0 & 0 & 0 & 0 & S_\tau & 0 \\ 0 & 0 & 0 & 0 & 0 & 0 & 0 & S_\lambda \end{pmatrix}, \tag{2.115}$$

where

$$\begin{aligned}
&l = 1 - \beta, \qquad k = \frac{l}{W}, \\
&m_1 = W\sigma + l, \qquad m_2 = W\gamma + l, \qquad m_3 = W\tau, \\
&S_\sigma = f + \frac{f-\epsilon}{\sigma} + \frac{\alpha\epsilon}{k}(\tau^2 + \sigma), \\
&S_\gamma = f + \frac{f-\epsilon}{\gamma} + \frac{\alpha\epsilon}{k}(\tau^2 + \gamma), \\
&S_\mu = f + \frac{f-\epsilon}{\mu} + \frac{\alpha\epsilon}{k}(\mu), \\
&S_\tau = f + \frac{\alpha\epsilon}{k}(\sigma + \gamma), \\
&f = 2(1 - \frac{1}{\lambda})e^{\frac{2}{q}(\lambda-1)} + \frac{\epsilon}{\lambda^2}\left(1 - \frac{\alpha}{3k^2}(\sigma^2 + \gamma^2 + \mu^2 + 2\tau^2)\right).
\end{aligned}$$

When a plane wave solution $\phi(\mathbf{x}, t) = \phi_0 e^{-i\omega t + i(\xi_1 x + \xi_2 y)}$ is inserted into (2.110), a non-trivial solution ϕ can be found if

$$det\left[-\omega A_0 + \xi_1 A_1 + \xi_2 A_2 + i(\xi_1^2 + \xi_2^2)A_3 - iS\right] = 0. \tag{2.116}$$

When we define $\nu = -\omega + \xi_1 u + \xi_2 v$, this leads to

$$\begin{vmatrix} 0 & \xi_1 & \xi_2 & 0 & 0 & 0 & 0 & 0 \\ \xi_1 & R\nu - i\beta|\boldsymbol{\xi}|^2 & 0 & -\xi_1 & 0 & 0 & -\xi_2 & 0 \\ \xi_2 & 0 & R\nu - i\beta|\boldsymbol{\xi}|^2 & 0 & -\xi_2 & 0 & -\xi_1 & 0 \\ 0 & r_1 & 0 & W\nu - iS_\sigma & 0 & 0 & 0 & 0 \\ 0 & 0 & r_2 & 0 & W\nu - iS_\gamma & 0 & 0 & 0 \\ 0 & 0 & 0 & 0 & 0 & W\nu - iS_\mu & 0 & 0 \\ 0 & r_3 & r_4 & 0 & 0 & 0 & W\nu - iS_\tau & 0 \\ 0 & -\dfrac{\xi_1\sigma + \xi_2\tau}{3k\lambda} & -\dfrac{\xi_1\tau + \xi_2\gamma}{3k\lambda} & 0 & 0 & 0 & 0 & \nu - iS_\lambda \end{vmatrix} = 0, \tag{2.117}$$

where

$$r_1 = -2\xi_1 m_1 - 2\xi_2 m_3,$$

$$r_2 = -2\xi_1 m_3 - 2\xi_2 m_2,$$

$$r_3 = -\xi_2 m_2,$$

$$r_4 = -\xi_1 m_1.$$

The determinant can be rearranged to give

$$-|\boldsymbol{\xi}|^2 (W\nu - iS_\sigma)(W\nu - iS_\gamma)(W\nu - iS_\mu)(W\nu - iS_\lambda) \\ [(R\nu - i\beta|\boldsymbol{\xi}|^2)(W\nu - iS_\tau) - (c_1\xi_1^2 m_1 + c_2\xi_2^2 m_1 + 2c_3\xi_1\xi_2 m_3)] = 0, \tag{2.118}$$

with

$$c_1 = (\xi_1^2 + \xi_2^2(2\frac{(W\nu - iS_\tau)}{(W\nu - iS_\sigma)} - 1))/|\boldsymbol{\xi}|^2,$$

$$c_2 = (\xi_2^2 + \xi_1^2(2\frac{(W\nu - iS_\tau)}{(W\nu - iS_\gamma)} - 1))/|\boldsymbol{\xi}|^2,$$

$$c_3 = (\xi_1^2\frac{(W\nu - iS_\tau)}{(W\nu - iS_\gamma)} + \xi_2^2\frac{(W\nu - iS_\tau)}{(W\nu - iS_\sigma)})/|\boldsymbol{\xi}|^2.$$

For the Oldroyd B model, the source entries S_σ, S_γ and S_τ are unity. There is also no need for the incorporation of the equations for μ and λ. This reduces the determinant to

$$-|\boldsymbol{\xi}|^2(W\nu - i)^2[(R\nu - i\beta|\boldsymbol{\xi}|^2)(W\nu - i) - (\xi_1^2 m_1 + \xi_2^2 m_1 + 2\xi_1\xi_2 m_3)] = 0, \quad (2.119)$$

which can also be expressed as

$$-|\boldsymbol{\xi}|^2(W\nu - i)^2[(R\nu - i\beta|\boldsymbol{\xi}|^2)(W\nu - i) - W\boldsymbol{\xi}\boldsymbol{\tau}_A\boldsymbol{\xi}^T] = 0, \quad (2.120)$$

where the tensor $\boldsymbol{\tau}_A$ is defined as $\boldsymbol{\tau}_A = \boldsymbol{\tau} + \frac{1-\beta}{W}$. For the UCM model the matrix $A_3 = 0$, which simplifies the determinant even more. It now reads

$$-|\boldsymbol{\xi}|^2(W\nu - i)^2[R\nu(W\nu - i) - W\boldsymbol{\xi}\boldsymbol{\tau}_A\boldsymbol{\xi}^T] = 0. \quad (2.121)$$

The tensor $\boldsymbol{\tau}_A$ can also be distilled from the determinant resulting from the XPP model. If we define the tensor $\boldsymbol{\tau}_B$ by

$$\boldsymbol{\tau}_B = \boldsymbol{\tau}_A + \frac{1}{|\boldsymbol{\xi}|^2}\begin{pmatrix} 2\xi_2^2 A\tau_{xx} & (\xi_1^2 B + \xi_2^2 A)\tau_{xy} \\ (\xi_1^2 B + \xi_2^2 A)\tau_{xy} & 2\xi_1^2 B\tau_{yy} \end{pmatrix}, \quad (2.122)$$

where

$$A = \frac{W\nu - iS_\tau}{W\nu - iS_\sigma} - 1 \qquad \text{and} \qquad B = \frac{W\nu - iS_\tau}{W\nu - iS_\gamma} - 1,$$

then the determinantal equation for the XPP model (2.118) can be written as

$$\begin{aligned} -|\boldsymbol{\xi}|^2(W\nu - iS_\sigma)(W\nu - iS_\gamma)(W\nu - iS_\mu)(W\nu - iS_\lambda) \\ [(R\nu - i\beta|\boldsymbol{\xi}|^2)(W\nu - iS_\tau) - W\boldsymbol{\xi}\boldsymbol{\tau}_B\boldsymbol{\xi}^T] = 0, \end{aligned} \quad (2.123)$$

The determinantal equation for the Oldroyd B model has a double root $\nu = i/W$ and two more roots satisfying the quadratic equation

$$\nu^2 - i\left(\frac{\beta|\boldsymbol{\xi}|^2}{R} + \frac{1}{W}\right)\nu - \frac{\boldsymbol{\xi}\boldsymbol{\tau}_A\boldsymbol{\xi}^T}{R} - \frac{\beta|\boldsymbol{\xi}|^2}{RW}. \quad (2.124)$$

The roots of the determinant of the UCM model are

$$\nu = \frac{i}{W}, \frac{i}{W}, \frac{i}{2W} \pm \sqrt{\frac{\boldsymbol{\xi}\boldsymbol{\tau}_A\boldsymbol{\xi}^T}{R} - \frac{1}{4W^2}}. \quad (2.125)$$

Since the tensor $\boldsymbol{\tau}_A$ is positive definite, the imaginary part of these roots is always positive. This means that the imaginary part of $\omega \leq 0$ and so the waves damp exponentially in time and the models cannot be Hadamard unstable. Although this indicates that the continuous problem is well-posed, this is not neccesarily true for the corresponding discrete problem in which $\boldsymbol{\tau}_A$ may lose its positive definiteness beyond some Weissenberg number.

As is shown in [26] and [38] the type of the equations can be determined by analyzing the factors of the principal part of the determinants above. For the Oldroyd B model the principal part of the left-hand side of (2.120) is

$$i\beta(\xi_1^2 + \xi_2^2)^2 W^3 \nu^3. \tag{2.126}$$

The three real characteristics associated with ν^3 represent the hyperbolic part of the Oldroyd B equations. These characteristics correspond to the three stress equations in the Oldroyd B model, indicating that the stress components are convected along the streamlines. The factor $(\xi_1^2 + \xi_2^2)^2$ represents the parabolic and elliptic parts of the equations.

The principal part of the determinant for the UCM model is

$$(\xi_1^2 + \xi_2^2) W^3 \nu^2 [\boldsymbol{\xi} \boldsymbol{\tau}_A \boldsymbol{\xi}^T - R\nu^2]. \tag{2.127}$$

The parabolic part of the principal part is missing in the UCM model. It is therefore of mixed elliptic and hyperbolic type. The principal part of the determinant for the XPP model (2.123) is similar to the principal part of the Oldroyd B model. It reads

$$i\beta(\xi_1^2 + \xi_2^2)^2 W^5 \nu^5. \tag{2.128}$$

There are now five quantities convected along the streamlines. They are the four stress components and the stretch, whose equations correspond to the five real characteristics associated to ν^5. The parabolic and elliptic parts associated with the factor

$(\xi_1^2 + \xi_2^2)^2$ are present in the XPP model as well.

The hyperbolic part of the equations is responsible for some of the numerical problems since discretization errors may propagate along real characteristics. Newtonian problems are purely elliptic and do not have real characteristics. A common observation in viscoelastic problems is that with increasing Weissenberg number, solutions can only be obtained on ever coarser meshes.

Gerritsma and Phillips [19] have analyzed the determinant of the UCM model, identified two characteristic variables that are transported along the streamlines and concluded that it would suffice to prescribe two stress boundary conditions at the inflow of a domain for the UCM model. These conditions may consist of combinations of the three stress components. The Oldroyd B model contains three real characteristics and therefore all three stress components may be prescribed as boundary conditions on an inflow boundary. The XPP model contains five real characteristics. This means that the four stress components and the stretch may be prescribed as boundary conditions at inflow.

2.5.3 The second normal stress difference

As is described in section 1.2.4, the first and second normal stress differences are responsible for many phenomena that can be observed in viscoelastic fluids. The normal stress differences in a simple shear flow, as predicted by the models described before will be presented here. The velocity field for a simple shear flow is given in Cartesian coordinates by

$$(u, v, w) = (\dot{\gamma} y, 0, 0). \tag{2.129}$$

For Newtonian fluids both the first normal stress difference $N_1 = T_{xx} - T_{yy}$ and the second normal stress difference $N_2 = T_{yy} - T_{zz}$ are zero. The normal stress differences predicted by the Maxwell and Oldroyd B models are given in Table 2.2. It is known that for viscoelastic fluids, the first normal stress difference is an order of magnitude larger than the second normal stress difference, and of opposite sign. For this reason, the corotational and the lower-convected derivatives are rejected, and only the upper-convected derivative will be used in this thesis.

Table 2.2: The first and second normal stress differences predicted by the Maxwell and Oldroyd B models.

Model	N_1	N_2
Upper Convected Maxwell	$2\lambda_1\eta\dot{\gamma}^2$	0
Corotational Maxwell	$\dfrac{2\lambda\eta\dot{\gamma}^2}{1+\lambda^2\dot{\gamma}^2}$	$-\dfrac{\lambda\eta\dot{\gamma}^2}{1+\lambda^2\dot{\gamma}^2}$
Lower Convected Maxwell	$2\lambda_1\eta\dot{\gamma}^2$	$-2\lambda_1\eta\dot{\gamma}^2$
Oldroyd B	$2(\lambda_1-\lambda_2)\eta\dot{\gamma}^2$	0

2.5.4 Shear and extensional viscosity

The shear and extensional viscosities that are predicted by a certain constitutive model can be found by substituting the appropriate velocity field into the model, and calculating the stress solution. With a shear rate $\dot{\gamma}$, the velocity field in shear is given in Cartesian coordinates by

$$(u, v, w) = (\dot{\gamma} y, 0, 0), \tag{2.130}$$

and the uniaxial extensional velocity field under a strain rate of $\dot{\epsilon}$ is given by

$$(u, v, w) = (\dot{\epsilon} x, -\frac{\dot{\epsilon}}{2} y, -\frac{\dot{\epsilon}}{2} z). \tag{2.131}$$

Newtonian fluids

For Newtonian fluids, the shear stress in the velocity field (2.130) is found to be $\tau_{xy} = \dot{\gamma}\eta$, giving rise to a constant shear viscosity of $\eta_S = \eta$. The first normal stress difference in extensional flow is $\tau_{xx} - \tau_{yy} = 3\dot{\epsilon}\eta$, so the extensional viscosity is $\eta_E = 3\eta$. The Trouton ratio is defined as the extensional over the shear viscosity, and it is $\eta_E/\eta_S = 3$ for Newtonian fluids.

The Maxwell and Oldroyd models

Both the Maxwell and the Oldroyd B model have a constant shear viscosity. They also both predict infinite extensional viscosity at a finite extensional rate. This can be easily shown by solving the constitutive equation for τ_{xx},

$$\frac{\partial}{\partial t}\tau_{xx} = 2\dot{\epsilon}\tau_{xx} - \frac{1}{\lambda}(\tau_{xx} - 2\eta\dot{\epsilon}). \tag{2.132}$$

This has the solution

$$\tau_{xx} = \frac{2\eta\dot{\epsilon}}{1 - 2\lambda\dot{\epsilon}}\left(1 - e^{\frac{2\lambda\dot{\epsilon}-1}{\lambda}t}\right), \tag{2.133}$$

which goes to infinity for the steady state when $\dot{\epsilon} > \frac{1}{2\lambda}$.

Analytic solutions to the pom-pom model

Analytic solutions for the shear and extensional viscosity are presented for the original pom-pom model, without the Blackwell modification to the stretch equation.

Shear viscosity

For the velocity field for a fluid in shear and in absence of convection, the equations (2.68) reduce to

$$\begin{aligned}
\frac{\partial}{\partial t}A_{xx}(t) - 2\dot{\gamma}A_{xy}(t) &= -\frac{A_{xx}(t) - 1/3}{\tau_b}, && (2.134)\\
\frac{\partial}{\partial t}A_{yy}(t) &= -\frac{A_{yy}(t) - 1/3}{\tau_b}, && (2.135)\\
\frac{\partial}{\partial t}A_{zz}(t) &= -\frac{A_{zz}(t) - 1/3}{\tau_b}, && (2.136)\\
\frac{\partial}{\partial t}A_{xy}(t) - \dot{\gamma}A_{yy}(t) &= -\frac{A_{xy}(t)}{\tau_b}. && (2.137)
\end{aligned}$$

The solutions to these equations are found to be

$$A_{xx}(t) = \frac{1}{3} + \frac{2}{3}\dot{\gamma}^2\tau_b^2\left(1 - e^{-t/\tau_b}(1 + t/\tau_b)\right), \tag{2.138}$$

$$A_{yy}(t) = A_{zz}(t) = \frac{1}{3}, \tag{2.139}$$

$$A_{xy}(t) = \frac{1}{3}\dot{\gamma}\tau_b\left(1 - e^{-t/\tau_b}\right). \tag{2.140}$$

The solutions to the equations for the other off-diagonal terms are all zero. When $t \to \infty$, the limits of these solutions for A_{xx} and A_{xy} are found to be

$$\lim_{t\to\infty} A_{xx}(t) = \frac{1}{3} + \frac{2}{3}\dot{\gamma}^2\tau_b^2, \qquad \lim_{t\to\infty} A_{xy}(t) = \frac{1}{3}\dot{\gamma}\tau_b.$$

The nonzero entries of the orientation tensor $\mathbf{S} = \mathbf{A}/I_{\mathbf{A}}$ can now be expressed as

$$\lim_{t\to\infty} S_{xx}(t) = \frac{2\dot{\gamma}^2\tau_b^2 + 1}{2\dot{\gamma}^2\tau_b^2 + 3}, \qquad \lim_{t\to\infty} S_{xy}(t) = \frac{\dot{\gamma}\tau_b}{2\dot{\gamma}^2\tau_b^2 + 3},$$

$$\lim_{t\to\infty} S_{yy}(t) = \lim_{t\to\infty} S_{zz}(t) = \frac{1}{2\dot{\gamma}^2\tau_b^2 + 3}.$$

The stretch equation (2.69) can now be written as

$$\frac{\partial\lambda(t)}{\partial t} = \lambda(t)\frac{2\dot{\gamma}^2\tau_b}{2\dot{\gamma}^2\tau_b^2 + 3} - \frac{\lambda(t) - 1}{\tau_s}. \tag{2.141}$$

Note that this is not a true time dependent solution, but just a method for deriving the limiting behaviour of λ. The solution to this equation is

$$\lambda(t) = \frac{1}{-\dot{\gamma}^2\tau_b\tau_s + (2\dot{\gamma}^2\tau_b^2 + 3)}\left((2\dot{\gamma}^2\tau_b^2 + 3) - \dot{\gamma}^2\tau_b\tau_s e^{-t\frac{-\dot{\gamma}^2\tau_b\tau_s + (2\dot{\gamma}^2\tau_b^2 + 3)}{(2\dot{\gamma}^2\tau_b^2 + 3)\tau_s}}\right), \tag{2.142}$$

and since $\tau_b > \tau_s$, this reduces in the limit of $t \to \infty$ to

$$\lim_{t\to\infty} \lambda(t) = \frac{2\dot{\gamma}^2\tau_b^2 + 3}{-\dot{\gamma}^2\tau_b\tau_s + (2\dot{\gamma}^2\tau_b^2 + 3)}. \tag{2.143}$$

The shear stress is given by

$$\sigma_{xy}(t) = 3G_0\lambda^2(t)S_{xy}(t), \tag{2.144}$$

and the shear viscosity is related to the shear stress through

$$\eta_S = \frac{1}{\dot{\gamma}}\lim_{t\to\infty} \sigma_{xy}(t), \tag{2.145}$$

and is found to be

$$\eta_S = 3G_0 \frac{\tau_b(2\dot{\gamma}^2\tau_b^2 + 3)}{(-\dot{\gamma}^2\tau_b\tau_s + (2\dot{\gamma}^2\tau_b^2 + 3))^2}. \tag{2.146}$$

The shear viscosity is plotted against $\dot{\gamma}$ in Fig. 2.7 for values of $\tau_b = 3.24$, $\tau_s = 1$, $G_0 = 1$. This ratio of relaxation times is similar to those used by Bishko [3].

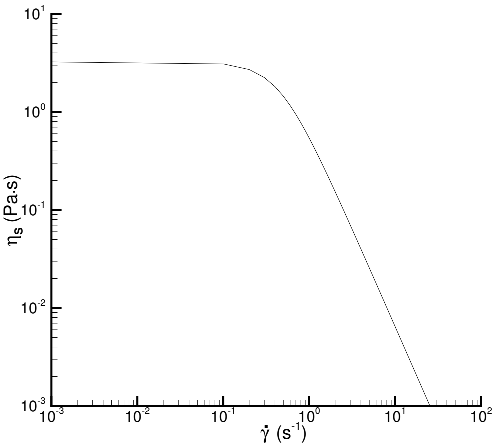

Figure 2.7: Shear viscosity predicted by the original pom-pom model without Blackwell's modification to the stretch equation.

Extensional viscosity

For the uniaxial extensional velocity field, the equations for the normal orientations in the original pom-pom model (2.68), in absence of convection, reduce to

$$\frac{\partial}{\partial t}A_{xx}(t) - 2\dot{\epsilon}A_{xx}(t) = -\frac{A_{xx}(t) - 1/3}{\tau_b}, \tag{2.147}$$

$$\frac{\partial}{\partial t}A_{yy}(t) + \dot{\epsilon}A_{yy}(t) = -\frac{A_{yy}(t) - 1/3}{\tau_b}, \tag{2.148}$$

$$\frac{\partial}{\partial t}A_{zz}(t) + \dot{\epsilon}A_{zz}(t) = -\frac{A_{zz}(t) - 1/3}{\tau_b}, \tag{2.149}$$

The solution to these problems are

$$A_{xx}(t) = -\frac{1/3}{2\dot{\epsilon}\tau_b - 1}\left(2\dot{\epsilon}\tau_b e^{\frac{(2\dot{\epsilon}\tau_b - 1)t}{\tau_b}} - 1\right), \tag{2.150}$$

$$A_{yy}(t) = A_{zz}(t) = \frac{1/3}{\dot{\epsilon}\tau_b + 1}\left(\dot{\epsilon}\tau_b e^{-\frac{(\dot{\epsilon}\tau_b + 1)t}{\tau_b}} + 1\right). \tag{2.151}$$

All the solutions to the equations for the off-diagonal terms are zero. It is clear that a discontinuity is present in the solution at $\dot{\epsilon}\tau_b = 1/2$. The limits for $t \to \infty$ are given by

$$\begin{aligned} \underset{t\to\infty}{lim} A_{xx}(t) &= \frac{-1/3}{2\dot{\epsilon}\tau_b - 1}, & \underset{t\to\infty}{lim} A_{yy}(t) = \underset{t\to\infty}{lim} A_{zz}(t) &= \frac{1/3}{\dot{\epsilon}\tau_b + 1}, & \text{when } \dot{\epsilon}\tau_b < 1/2, \\ \underset{t\to\infty}{lim} A_{xx}(t) &= \infty, & \underset{t\to\infty}{lim} A_{yy}(t) = \underset{t\to\infty}{lim} A_{zz}(t) &= \frac{1/3}{\dot{\epsilon}\tau_b + 1}, & \text{when } \dot{\epsilon}\tau_b > 1/2. \end{aligned}$$

And the corresponding limits for $\mathbf{S} = \mathbf{A}/I_{\mathbf{A}}$ are

$$\begin{aligned} \underset{t\to\infty}{lim} S_{xx}(t) &= -\frac{\dot{\epsilon}\tau_b + 1}{3(\dot{\epsilon}\tau_b - 1)}, & \underset{t\to\infty}{lim} S_{yy}(t) = \underset{t\to\infty}{lim} S_{zz}(t) &= \frac{2\dot{\epsilon}\tau_b - 1}{3(\dot{\epsilon}\tau_b - 1)}, & \text{when } \dot{\epsilon}\tau_b < 1/2, \\ \underset{t\to\infty}{lim} S_{xx}(t) &= 1, & \underset{t\to\infty}{lim} S_{yy}(t) = \underset{t\to\infty}{lim} S_{zz}(t) &= 0, & \text{when } \dot{\epsilon}\tau_b > 1/2. \end{aligned}$$

Without Blackwell's modification, the stretch equation (2.69) for extensional flow is

$$\frac{\partial \lambda(t)}{\partial t} = \lambda(t)\left(\dot{\epsilon} S_{xx}(t) - \frac{\dot{\epsilon}}{2} S_{yy}(t) - \frac{\dot{\epsilon}}{2} S_{zz}(t)\right) - \frac{\lambda(t) - 1}{\tau_s}. \tag{2.152}$$

Again this is not a true time dependent solution, but just a method for deriving the limiting behaviour of λ. The solution is

$$\lambda(t) = \frac{(\dot{\epsilon}\tau_b - 1) + \dot{\epsilon}^2\tau_b\tau_s e^{-\frac{\dot{\epsilon}^2\tau_b\tau_s + (\dot{\epsilon}\tau_b - 1)}{(\dot{\epsilon}\tau_b - 1)\tau_s} t}}{\dot{\epsilon}^2\tau_b\tau_s + (\dot{\epsilon}\tau_b - 1)}, \quad \text{when } \dot{\epsilon}\tau_b < 1/2, \tag{2.153}$$

$$\lambda(t) = \frac{1}{1 - \dot{\epsilon}\tau_s}\left(1 - \dot{\epsilon}\tau_s e^{\frac{\dot{\epsilon}\tau_s - 1}{\tau_s} t}\right), \quad \text{when } \dot{\epsilon}\tau_b > 1/2. \tag{2.154}$$

The denominator in the expression (2.153) when $\dot{\epsilon}\tau_b < 1/2$ is never equal to zero since $\tau_s < \tau_b$. There is a discontinuity in the expression for $\dot{\epsilon}\tau_b > 1/2$, and this is at $\dot{\epsilon}\tau_s = 1$. Three separate cases can now be identified, $\dot{\epsilon}\tau_b < 1/2$ and $\dot{\epsilon}\tau_b > 1/2$ with both $\dot{\epsilon}\tau_s < 1$ and $\dot{\epsilon}\tau_s > 1$. Since $\tau_b > \tau_s$, these can be expressed respectively as $\dot{\epsilon} < 1/2\tau_b$, $1/2\tau_b < \dot{\epsilon} < 1/\tau_s$ and $\dot{\epsilon} > 1/\tau_s$. The limits of the stretch for $t \to \infty$ are given by

$$\begin{aligned} \underset{t\to\infty}{lim} \lambda(t) &= \frac{\dot{\epsilon}\tau_b - 1}{\dot{\epsilon}^2\tau_b\tau_s + (\dot{\epsilon}\tau_b - 1)}, & \text{when } \dot{\epsilon} < \frac{1}{2\tau_b}, \\ \underset{t\to\infty}{lim} \lambda(t) &= \frac{1}{1 - \dot{\epsilon}\tau_s}, & \text{when } \frac{1}{2\tau_b} < \dot{\epsilon} < \frac{1}{\tau_s}, \\ \underset{t\to\infty}{lim} \lambda(t) &= \infty, & \text{when } \dot{\epsilon} > \frac{1}{\tau_s}. \end{aligned}$$

As mentioned before, there is an upper limit to the value of λ because of arm withdrawal when $\lambda = q$. This means that $\dot{\epsilon}\tau_s$ can never reach the value of one. Instead, the limiting value of $\dot{\epsilon}\tau_s$ is given by

$$\frac{1}{1-\dot{\epsilon}\tau_s} = q \qquad \rightarrow \qquad \dot{\epsilon}\tau_s = 1 - \frac{1}{q} \tag{2.155}$$

In the case of $\dot{\epsilon} > (1-1/q)/\tau_s$ the expression (2.154) is replaced by

$$\lambda(t) = q, \tag{2.156}$$

such that the $\underset{t\rightarrow\infty}{lim}\lambda(t)$ is not infinity, but simply q. The first normal stress difference N_1 is given by

$$N_1(t) = \sigma_{xx}(t) - \sigma_{yy}(t) = 3G_0\lambda^2(t)(S_{xx}(t) - S_{yy}(t)), \tag{2.157}$$

and the extensional viscosity is related to the first normal stress difference through

$$\eta_E = \frac{1}{\dot{\epsilon}}\underset{t\rightarrow\infty}{lim}N_1(t), \tag{2.158}$$

so for the different regimes, the extensional viscosity is found to be

$$\eta_E = \begin{cases} 3G_0\dfrac{\dot{\epsilon}\tau_b(1-\dot{\epsilon}\tau_b)}{\dot{\epsilon}(\dot{\epsilon}^2\tau_b\tau_s + \dot{\epsilon}\tau_b - 1)^2}, & \text{when } \dot{\epsilon} < \dfrac{1}{2\tau_b}, \\ 3G_0\dfrac{1}{\dot{\epsilon}(1-\dot{\epsilon}\tau_s)^2}, & \text{when } \dfrac{1}{2\tau_b} < \dot{\epsilon} < \dfrac{1}{\tau_s}(1-\dfrac{1}{q}), \\ 3G_0\dfrac{q^2}{\dot{\epsilon}}, & \text{when } \dot{\epsilon} > \dfrac{1}{\tau_s}(1-\dfrac{1}{q}). \end{cases}$$

Note that η_E is also continuous at $\dot{\epsilon}\tau_b = 1/2$. For values of $q = 5$, $\tau_b = 3.24$, $\tau_s = 1$, and $G_0 = 1$, the extensional viscosity is plotted as a function of $\dot{\epsilon}$ in Fig. 2.8. Clearly, the derivative of the extensional viscosity is discontinuous in two places. Following numerical results will show that the second discontinuity can be removed by introducing Blackwell's modification to the stretch equation.

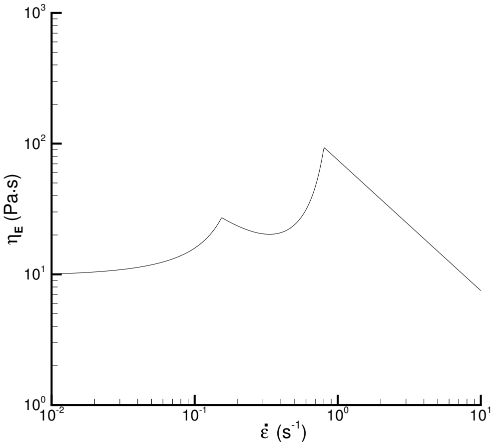

Figure 2.8: Extensional viscosity predicted by the original pom-pom model without Blackwell's modification to the stretch equation.

Numerical solutions to the pom-pom model

For the original pom-pom model with Blackwell's modification (2.68), (2.71), and for the extended pom-pom model (2.72), (2.73), numerical solutions to the predicted shear and extensional viscosities are sought for using Maple. Again, the convective terms in the equations for orientation and stretch are neglected.

For the original pom-pom model, three different values for the parameter ν in Blackwell's modification have been tested. Fig. 2.9 shows that, although there is no visible difference in the predicted shear viscosity, the parameter ν does affect the extensional viscosity. When $\nu = 0$ the solution is as in Fig. 2.8, and has a very distinct discontinuity in the derivative of the extensional viscosity. When ν increases the discontinuity gradually becomes weaker.

The same values of ν have been tested for the XPP model, combined with values of $\alpha = 0$ and $\alpha = 0.15$. It is clear from Fig. 2.10 that the plateau of shear viscosity decreases at a slower rate than in the original pom-pom model. When ν is set to zero, the shear viscosity even reaches a plateau value at high shear rates. With $\alpha = 0.15$,

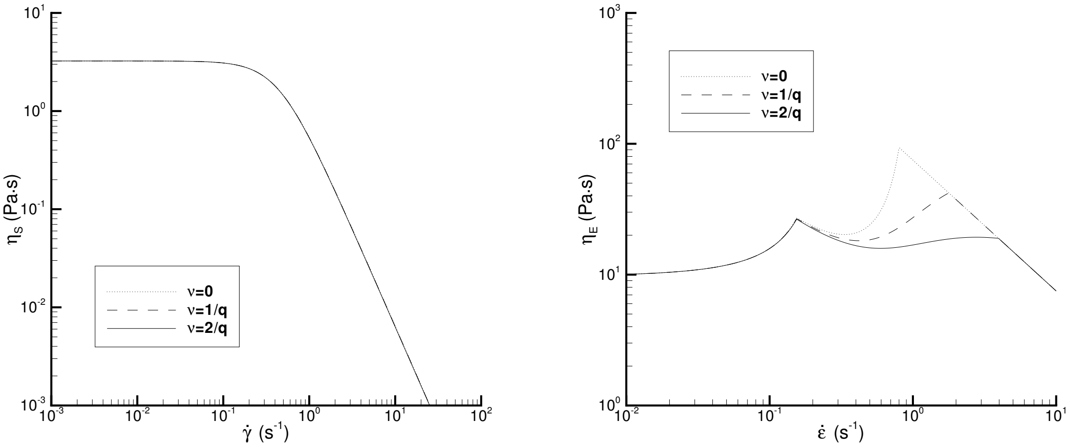

Figure 2.9: Shear and extensional viscosity predicted by the original pom-pom model with varying values for ν.

the solution could not be evaluated at large shear rates. The plateau at low shear rates is of the same value as for the original pom-pom model. Unlike in the original pom-pom model, the effect of different values of ν is visible in the shear viscosity. The higher the value of ν, the steeper the decrease in shear viscosity at high shear rates.

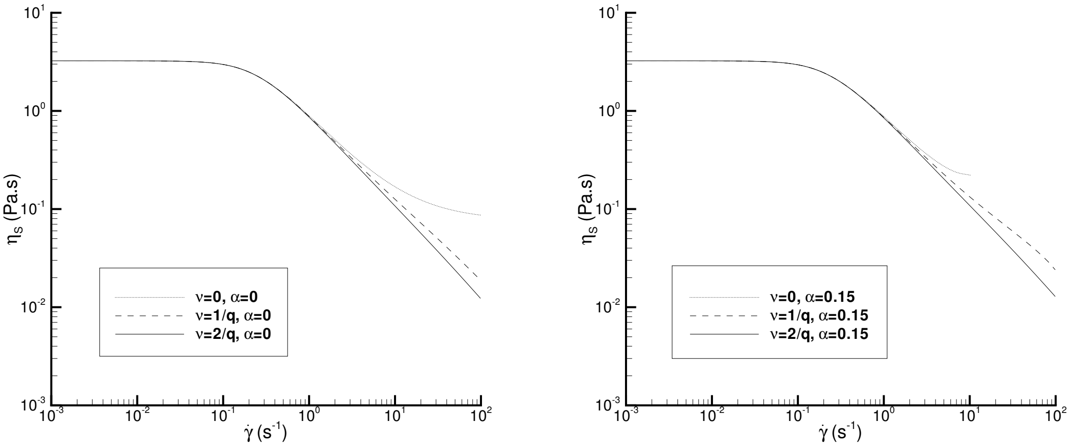

Figure 2.10: Shear viscosity predicted by the XPP model with varying values for ν, for both $\alpha = 0$ and $\alpha = 0.15$.

Fig. 2.11 shows the extensional viscosity predicted by the XPP model for different values of ν and α. The first thing that can be concluded is that there are no discontinuities in the derivative of the extensional viscosity predicted by the XPP model. When ν is set to zero, the extensional viscosity shoots to infinity. This is due to the effect that when $\nu = 0$, the stretch in the XPP model is unbounded since the condition $\lambda < q$ is removed from the equations. The value of the viscosity at low strain rates is again equivalent to the value predicted by the original pom-pom model. Increasing the value of ν has a decreasing effect on the extensional viscosity at high strain rates, similar to the original pom-pom model.

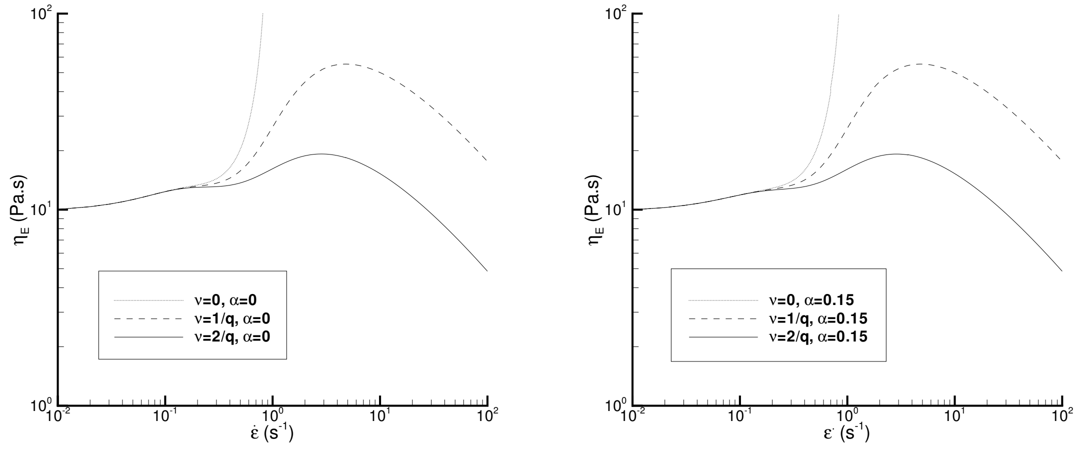

Figure 2.11: Extensional viscosity predicted by the XPP model with varying values for ν, for both $\alpha = 0$ and $\alpha = 0.15$.

A comparison of the predicted shear and extensional viscosities for the original pom-pom model, and the XPP model with $\alpha = 0$ and $\alpha = 0.15$ is shown in Fig. 2.12. The value of ν is fixed at $\nu = 2/q$, the value that will be used throughout the rest of this thesis. It is very clear that the original pom-pom model predicts a sharper fall in shear viscosity at high shear rates, although the plateau values of both shear and extensional viscosity are the same for the original pom-pom model and the XPP model. Note that the lines of the extensional viscosity for the XPP model intersects the second discontinuity of the original pom-pom model. The first discontinuity is not present in the XPP model either, although a slight 'bump' can be observed in

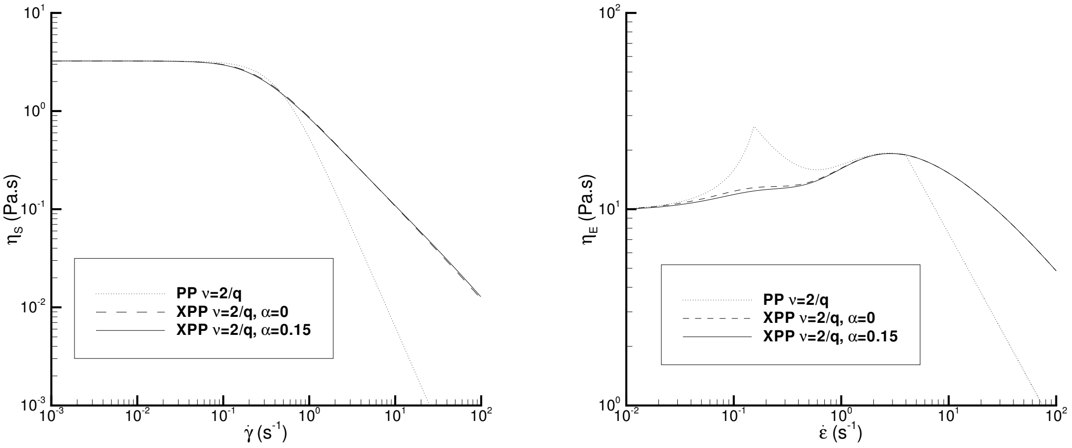

Figure 2.12: Comparison of shear and extensional viscosity predicted by the original pom-pom (PP) and the XPP models.

the solution. Increasing the value of α does not have a great effect on the shear and extensional viscosities.

Chapter 3

Temporal and Spatial Discretization

3.1 Introduction

The equations that govern the flow of any real fluid are, in many cases, impossible to solve analytically. The Stokes model or the Oldroyd B model for example, can be solved analytically for Poiseuille or Couette flow. The same excerise is not possible however for the pom-pom model, nor is it possible to solve analytically any of the presented models for the flow through a contraction, or past a confined cylinder. In all of these cases numerical techniques have to be reverted to.

There are many ways of finding a numerical approximation to flow problems, and the most popular ones are described in section 3.2. This chapter goes on to describe how the continuous equations from the previous chapter are discretized both in time (see section 3.3) and in space using the spectral element method (see sections 3.4-3.5). A modification to the test functions used in the spectral element method is proposed in section 3.6. The modified test function allows for easy implementation of zero

Neumann boundary conditions and circumvents problems arising due to a zero radial coordinate in axisymmetric problems. Section 3.7 presents the discretized equations.

3.2 Numerical Approximation Methods

The most popular methods that are used in numerical approximation are the finite difference (FD) method, the finite element (FE) method, the finite volume (FV) method and the spectral element (SE) method. In these numerical methods derivatives in the continuous equations are approximated on a grid by some approximation function. The methods have originally been developed for generating numerical solutions to elliptic problems, and for elliptic problems refinement of the grid results in approximations that converge to the exact solution, provided the solution is sufficiently regular. However, when convection is present or when elasticity is introduced it is not known a priori whether or not this property is satisfied. Therefore mesh convergence studies need to be carried out before anything can be said about numerical solutions to problems that are not purely elliptic.

In the FD, FE and FV methods the approximation functions are of a local nature, whereas in SE methods there is a longer range coupling to approximate the derivatives. This is achieved by choosing high-order polynomials as approximation functions. The major advantage of this is that for smooth problems SE methods exhibit superior convergence of the solution to the exact solution with refinement of the grid.

Comparison of the SE method with FE methods is obvious, since both methods discretize the so-called weak formulation of the equations. In the FE method, the grid covering the geometry of the problem under consideration consists of many small elements on which the derivatives are approximated. The accuracy of the approximation can be increased by decreasing the size h of these elements. For the same problem, a SE grid consists of only a few large elements in which the long range coupling takes place. In SE methods the accuracy of the approximation can be increased by decreasing the size of the elements h, or by increasing the order of the polynomial approximation p. Therefore spectral element methods are often referred to as h/p methods. It is this p-type refinement that results in superior convergence properties.

In viscoelastic flow calculations very narrow regions of high gradients of stress can be encountered in the solution. The advantage of the SE method in these cases is obvious. By placing smaller elements in these regions, the high-order approximation can reproduce these high gradients.

3.3 Discretization in Time

In the governing equations (2.106)-(2.108), the time t is an independent variable. It will not however be discretized using a spectral approximation. Instead, first and second-order temporal schemes are used, and time-stepping is required to find solutions to the equations. The discrete time levels are denoted as t^k, where $k = n + 1$ refers to the time level that is to be calculated next, $k = n$ refers to the time level at which the solution has just been calculated, and $k = n-1$ is the time level before that.

At this point, a distinction must be made between algorithms that solve all equations simultaneously, and algorithms that solve the field equations first, and then use the resulting velocity vector to solve the constitutive equation. The first is called a coupled solver, the latter an uncoupled solver.

Another distinction is whether the non-linear terms in the equations (2.106)-(2.108) are treated explicitly or implicitly. Most calculations presented in this thesis are performed using a coupled solver with explicit treatment of the non-linear terms, i.e.

the non-linear terms that are present in the constitutive equations are approximated by combinations of the terms at previous time levels t^n and t^{n-1}. The temporal scheme for this solver is presented first, followed by schemes that have been implemented for coupled and uncoupled solvers with implicit treatment of the non-linear terms.

3.3.1 Explicit coupled solver

In a coupled solver, the field equations are solved simultaneously with the constitutive equation such that the solutions to all variables at time t^{n+1} are found simultaneously. The equations (2.106)-(2.108) may be written as

$$\nabla \cdot \mathbf{u}^{n+1} = 0, \tag{3.1}$$

$$M_l \mathbf{u}^{n+1} + \nabla p^{n+1} - \nabla \cdot \boldsymbol{\tau}^{n+1} - \beta \nabla^2 \mathbf{u}^{n+1} = \mathbf{g}(\mathbf{u}), \tag{3.2}$$

$$C_l(\lambda, \boldsymbol{\tau}) \boldsymbol{\tau}^{n+1} - \mathbf{h}(\lambda, \boldsymbol{\tau}, \mathbf{u}) = 2(1-\beta)\mathbf{d}^{n+1}, \tag{3.3}$$

where M_l, $\mathbf{g}(\mathbf{u})$, $C_l(\lambda, \boldsymbol{\tau})$ and $\mathbf{h}(\lambda, \boldsymbol{\tau}, \mathbf{u})$ depend on the chosen temporal scheme to approximate the time derivatives and non-linear terms. Four distinct temporal schemes have been implemented, of which two are first-order, and two are second-order.

Euler/Euler

This temporal discretization is a first-order scheme, using an Euler scheme to approximate the material derivatives in the momentum, constitutive and stretch equations, and also an Euler approximation for the explicitly treated terms in the constitutive equation.

- The material derivative

  The Euler approximation of the material derivative of a function $\mathbf{G}$ is

$$\frac{D\mathbf{G}}{Dt} = \frac{\partial \mathbf{G}}{\partial t} + \mathbf{u} \cdot \nabla \mathbf{G} \approx \frac{\mathbf{G}^{n+1} - \mathbf{G}^n}{\Delta t} + \mathbf{u}^n \cdot \nabla \mathbf{G}^n. \tag{3.4}$$

- The non-linear terms

  An Euler approximation is used for the deformation terms and the other non-linear terms in the constitutive equation (2.108), calculated explicitly at the old time level, is

$$\mathbf{E}^{n+1}(\lambda, \boldsymbol{\tau}, \mathbf{u}) \approx \mathbf{E}^{n}(\lambda, \boldsymbol{\tau}, \mathbf{u}), \tag{3.5}$$

  where $\mathbf{E}^k(\lambda, \boldsymbol{\tau}, \mathbf{u}) = \mathbf{E}(\lambda^k, \boldsymbol{\tau}^k, \mathbf{u}^k)$, and

$$\mathbf{E}(\lambda, \boldsymbol{\tau}, \mathbf{u}) = (f(\lambda, \boldsymbol{\tau}) - 1)\frac{1-\beta}{We}\mathbf{I} + \frac{\alpha We}{1-\beta}\boldsymbol{\tau}\cdot\boldsymbol{\tau} - We(\nabla\mathbf{u})\boldsymbol{\tau} - We\boldsymbol{\tau}(\nabla\mathbf{u})^T. \tag{3.6}$$

BDF2/EX2

The BDF2/EX2 scheme is the second-order equivalent to the Euler/Euler temporal discretization. It comprises a second-order Backward Differentiation Formula (BDF) for the material derivatives of the velocity, stress and stretch, and a second-order Extrapolation Scheme (EX) for the other non-linear terms.

- The material derivative

  The second-order Backward Differentiation Formula, as used by Fiétier and Deville [15], approximates the material derivative of a function $\mathbf{G}$ as

$$\begin{aligned} \frac{D\mathbf{G}}{Dt} &= \frac{\partial \mathbf{G}}{\partial t} + \mathbf{u}\cdot\nabla\mathbf{G} \\ &\approx \frac{3\mathbf{G}^{n+1} - 4\mathbf{G}^{n} + \mathbf{G}^{n-1}}{2\Delta t} + 2\mathbf{u}^n\cdot\nabla\mathbf{G}^n - \mathbf{u}^{n-1}\cdot\nabla\mathbf{G}^{n-1}. \end{aligned} \tag{3.7}$$

- The non-linear terms

  The second-order Extrapolation Scheme, as used by Fiétier and Deville [15], approximates the non-linear terms in the constitutive equation as

$$\mathbf{E}^{n+1}(\lambda, \boldsymbol{\tau}, \mathbf{u}) \approx 2\mathbf{E}^{n}(\lambda, \boldsymbol{\tau}, \mathbf{u}) - \mathbf{E}^{n-1}(\lambda, \boldsymbol{\tau}, \mathbf{u}), \tag{3.8}$$

OIFS1/Euler

This scheme uses two first-order temporal discretizations. A first-order Operator Integration Factor Splitting (OIFS) technique for the material derivatives, and an Euler approximation for the other non-linear terms.

- The material derivative

  The discretization of the material derivatives of both the velocity in the momentum equations, and the stress in the constitutive equation, will be obtained using a first-order OIFS scheme (see Maday et al. [33]). The material derivative of a function $\mathbf{G}$ is approximated as

  $$\frac{D\mathbf{G}}{Dt} = \frac{\partial \mathbf{G}}{\partial t} + \mathbf{u} \cdot \nabla \mathbf{G} \approx \frac{1}{\Delta t}(\mathbf{G}^{n+1} - \tilde{\mathbf{G}}(t^{n+1})). \tag{3.9}$$

  The approximation $\tilde{\mathbf{G}}(t^{n+1})$ is the solution at time $t = t^{n+1}$ of the pure convection problem

  $$\frac{\partial \tilde{\mathbf{G}}}{\partial t} = -\mathbf{u}^n \cdot \nabla \tilde{\mathbf{G}}, \qquad t \in [t^n, t^{n+1}], \qquad \text{with } \tilde{\mathbf{G}}(\mathbf{x}, t^n) = \mathbf{G}^n(\mathbf{x}), \tag{3.10}$$

  A fourth-order explicit Runge-Kutta (RK4) method is used to solve the initial value problem. In the RK4 method, an additional time step is required. This time step h is defined as $h = \frac{\Delta t}{M}$, with M the number of RK4 iterations per outer time step, and $\Delta t = t^{n+1} - t^n$.

- The non-linear terms

  An Euler approximation for the non-linear terms, calculated explicitly at the old time level, is

  $$\mathbf{E}^{n+1}(\lambda, \boldsymbol{\tau}, \mathbf{u}) \approx \mathbf{E}^n(\lambda, \boldsymbol{\tau}, \mathbf{u}). \tag{3.11}$$

OIFS2/AB2

This is the second-order equivalent to the OIFS1/Euler scheme, and uses two second-order temporal discretizations. A second-order Operator Integration Factor Splitting

(OIFS) technique for the material derivatives of the velocity, stress and stretch, and a second-order Adams-Bashforth (AB) approximation for the other non-linear terms in the constitutive equation.

- The material derivative

  The material derivative of a function $\mathbf{G}$ is approximated as

$$\frac{D\mathbf{G}}{Dt} = \frac{\partial \mathbf{G}}{\partial t} + \mathbf{u} \cdot \nabla \mathbf{G} \approx \frac{1}{2\Delta t}(3\mathbf{G}^{n+1} - 4\tilde{\mathbf{G}}(t^{n+1}) + \tilde{\tilde{\mathbf{G}}}(t^{n+1})). \tag{3.12}$$

  The approximations $\tilde{\mathbf{G}}(t^{n+1})$ and $\tilde{\tilde{\mathbf{G}}}(t^{n+1})$ are the solutions at time $t = t^{n+1}$ of the pure convection problems

$$\frac{\partial \tilde{\mathbf{G}}}{\partial t} = -\mathbf{u}^* \cdot \nabla \tilde{\mathbf{G}}, \qquad t \in [t^n, t^{n+1}], \qquad \text{with } \tilde{\mathbf{G}}(\mathbf{x}, t^n) = \mathbf{G}^n(\mathbf{x}), \tag{3.13}$$

  and

$$\frac{\partial \tilde{\tilde{\mathbf{G}}}}{\partial t} = -\mathbf{u}^* \cdot \nabla \tilde{\tilde{\mathbf{G}}}, \qquad t \in [t^{n-1}, t^{n+1}], \qquad \text{with } \tilde{\tilde{\mathbf{G}}}(\mathbf{x}, t^{n-1}) = \mathbf{G}^{n-1}(\mathbf{x}), \tag{3.14}$$

  where $\mathbf{u}^*$ is a second-order approximation for the velocity at intermediate time levels given by

$$\mathbf{u}^* = \frac{(t - t^{n-1})}{\Delta t}\mathbf{u}^n + \left(1 - \frac{(t - t^{n-1})}{\Delta t}\right)\mathbf{u}^{n-1}. \tag{3.15}$$

  Again, the initial value problems are solved using a fourth-order explicit Runge-Kutta (RK4) method, which requires the additional time step $h = \frac{\Delta t}{M}$, with M the number of RK4 iterations per outer time step, and $\Delta t = t^{n+1} - t^n$.

- The non-linear terms

  An explicit second-order Adams-Bashforth (AB) scheme is used to approximate the deformation terms at the new time level $t = t^{n+1}$. The scheme is given by (see Karniadakis and Sherwin [27], for example)

$$\mathbf{F}^{n+1} \approx \sum_{q=0}^{J-1} \beta_q \mathbf{F}^{n+1-q}. \tag{3.16}$$

The factor J is the order of the AB scheme. For the second-order approximation ($J = 2$), the coefficients β_q are given by

$$\beta_0 = 0, \qquad \beta_1 = 3/2, \qquad \beta_2 = -1/2, \tag{3.17}$$

which yields the following approximation to the non-linear terms

$$\mathbf{E}^{n+1}(\lambda, \boldsymbol{\tau}, \mathbf{u}) \approx \frac{3}{2}\mathbf{E}^{n}(\lambda, \boldsymbol{\tau}, \mathbf{u}) - \frac{1}{2}\mathbf{E}^{n-1}(\lambda, \boldsymbol{\tau}, \mathbf{u}). \tag{3.18}$$

The semi-discrete equations

As an example, the OIFS2/AB2 scheme is applied to the set of governing equations (2.106)-(2.108). This yields the semi-discrete equations for the independent variables at the new time level t^{n+1},

$$\nabla \cdot \mathbf{u}^{n+1} = 0, \tag{3.19}$$

$$\frac{Re}{2\Delta t}(3\mathbf{u}^{n+1} - 4\tilde{\mathbf{u}}(t^{n+1}) + \tilde{\tilde{\mathbf{u}}}(t^{n+1})) = -\nabla p^{n+1} + \nabla \cdot \boldsymbol{\tau}^{n+1} + \beta \nabla^2 \mathbf{u}^{n+1}, \tag{3.20}$$

$$\begin{aligned} &(\frac{3}{2}f^{n}(\lambda,\boldsymbol{\tau}) - \frac{1}{2}f^{n-1}(\lambda,\boldsymbol{\tau}))\boldsymbol{\tau}^{n+1} + \\ &\qquad \frac{We}{2\Delta t}(3\boldsymbol{\tau}^{n+1} - 4\tilde{\boldsymbol{\tau}}(t^{n+1}) + \tilde{\tilde{\boldsymbol{\tau}}}(t^{n+1})) = \\ &\qquad\qquad 2(1-\beta)\mathbf{d}^{n+1} - (\frac{3}{2}\mathbf{E}^{n}(\lambda, \boldsymbol{\tau}, \mathbf{u}) - \frac{1}{2}\mathbf{E}^{n-1}(\lambda, \boldsymbol{\tau}, \mathbf{u})). \end{aligned} \tag{3.21}$$

The functions M_l, $\mathbf{g}(\mathbf{u})$, $C_l(\lambda, \boldsymbol{\tau})$ and $\mathbf{h}(\lambda, \mathbf{u}, \boldsymbol{\tau})$ in the semi-discrete equations (3.1)-(3.3) are determined from these equations. For the four different temporal schemes, the parameter M_l and the vector $\mathbf{g}(\mathbf{u})$ are defined in Table 3.1, the parameter $C_l(\lambda, \boldsymbol{\tau})$ in Table 3.2 and the tensor $\mathbf{h}(\lambda, \mathbf{u}, \boldsymbol{\tau})$ in Table 3.3.

When the double equation version of the XPP model is used, there is an extra equation for the stretch (2.97). After p^{n+1}, $\mathbf{u}^{n+1}$ and $\boldsymbol{\tau}^{n+1}$ have been calculated, the stretch λ^{n+1} can be found from the temporally discretized stretch equation,

$$\frac{3\lambda^{n+1} - 4\tilde{\lambda}(t^{n+1}) + \tilde{\tilde{\lambda}}(t^{n+1})}{2\Delta t} = \frac{We}{3(1-\beta)}\frac{(\mathbf{d}^{n+1} : \boldsymbol{\tau}^{n+1})}{\lambda^{n+1}} - \frac{\lambda^{n+1} - 1}{\epsilon We}e^{\nu(\lambda^{n+1}-1)}. \tag{3.22}$$

This equation can be solved iteratively at each time step by employing the iterative scheme

$$\frac{3\mu^{(m+1)} - 4\tilde{\lambda}(t^{n+1}) + \tilde{\tilde{\lambda}}(t^{n+1})}{2\Delta t} = \frac{We}{3(1-\beta)} \frac{(\mathbf{d}^{n+1} : \boldsymbol{\tau}^{n+1})}{\mu^{(m+1)}} - \frac{\mu^{(m+1)} - 1}{\epsilon We} e^{\nu(\mu^{(m)}-1)}, \tag{3.23}$$

with $\mu^{(0)} = \lambda^n$. When the convergence criterion $|\mu^{(m+1)} - \mu^{(m)}| < 10^{-8}$ is satisfied, we set $\lambda^{n+1} = \mu^{(m+1)}$.

In this thesis the stretch will be calculated using the direct coupling to the stress from the single equation version of the XPP model,

$$\lambda = \sqrt{1 + \frac{We}{(1-\beta)} \frac{1}{3} I_{\boldsymbol{\tau}}}. \tag{3.24}$$

Although Verbeeten et al. [62] noted that in their computations, the argument of this expression may become negative, we have never encountered this unphysical behaviour. Therefore we will only use expression 3.24 to calculate stretches in this thesis.

Table 3.1: The parameter M_l and the vector $\mathbf{g}(\mathbf{u})$ for the three temporal schemes.

Scheme	M_l	$\mathbf{g}(\mathbf{u})$
Euler/Euler	$\frac{Re}{\Delta t}$	$Re(\frac{\mathbf{u}^n}{\Delta t} - \mathbf{u}^n \cdot \nabla \mathbf{u}^n)$
BDF2/EX2	$\frac{3Re}{2\Delta t}$	$\frac{Re}{2\Delta t}(4\mathbf{u}^n - \mathbf{u}^{n-1}) - Re(2\mathbf{u}^n \cdot \nabla \mathbf{u}^n - \mathbf{u}^{n-1} \cdot \nabla \mathbf{u}^{n-1})$
OIFS1/Euler	$\frac{Re}{\Delta t}$	$\frac{Re}{\Delta t}\tilde{\mathbf{u}}(t^{n+1})$
OIFS2/AB2	$\frac{3Re}{2\Delta t}$	$\frac{Re}{2\Delta t}(4\tilde{\mathbf{u}}(t^{n+1}) - \tilde{\tilde{\mathbf{u}}}(t^{n+1}))$

3.3.2 Implicit coupled solver

As will be shown in chapter 6 instabilities in the numerical solutions may cause the solution to diverge eventually, even in smooth problems at relatively low Weissenberg numbers. The explicit treatment of the non-linear terms may be the cause of such

Table 3.2: The factor $C_l(\lambda, \boldsymbol{\tau})$ for the four temporal schemes.

Scheme	$C_l(\lambda, \boldsymbol{\tau})$
Euler/Euler	$f^n(\lambda, \boldsymbol{\tau}) + \frac{We}{\Delta t}$
BDF2/EX2	$(2f^n(\lambda, \boldsymbol{\tau}) - f^{n-1}(\lambda, \boldsymbol{\tau})) + \frac{3We}{2\Delta t}$
OIFS1/Euler	$f^n(\lambda, \boldsymbol{\tau}) + \frac{We}{\Delta t}$
OIFS2/AB2	$(\frac{3}{2}f^n(\lambda, \boldsymbol{\tau}) - \frac{1}{2}f^{n-1}(\lambda, \boldsymbol{\tau})) + \frac{3We}{2\Delta t}$

Table 3.3: The tensor $\mathbf{h}(\lambda, \mathbf{u}, \boldsymbol{\tau})$ for the three temporal schemes. The function $\mathbf{E}(\lambda, \boldsymbol{\tau}, \mathbf{u})$ represents $(f(\lambda, \boldsymbol{\tau}) - 1)\frac{1-\beta}{We}\mathbf{I} + \frac{\alpha We}{1-\beta}\boldsymbol{\tau} \cdot \boldsymbol{\tau} - We(\nabla \mathbf{u})\boldsymbol{\tau} - We\boldsymbol{\tau}(\nabla \mathbf{u})^T$.

Scheme	$\mathbf{h}(\lambda, \mathbf{u}, \boldsymbol{\tau})$
Euler/Euler	$We(\frac{\boldsymbol{\tau}^n}{\Delta t} - \mathbf{u}^n \cdot \nabla \boldsymbol{\tau}^n) - \mathbf{E}^n(\lambda, \boldsymbol{\tau}, \mathbf{u})$
BDF2/EX2	$\frac{We}{2\Delta t}(4\boldsymbol{\tau}^n - \boldsymbol{\tau}^{n-1}) - (2\mathbf{E}^n(\lambda, \boldsymbol{\tau}, \mathbf{u}) - \mathbf{E}^{n-1}(\lambda, \boldsymbol{\tau}, \mathbf{u}))$
OIFS1/Euler	$\frac{We}{\Delta t}\tilde{\boldsymbol{\tau}}(t^{n+1}) - \mathbf{E}^n(\lambda, \boldsymbol{\tau}, \mathbf{u})$
OIFS2/AB2	$\frac{We}{2\Delta t}(4\tilde{\boldsymbol{\tau}}(t^{n+1}) - \tilde{\tilde{\boldsymbol{\tau}}}(t^{n+1})) - (\frac{3}{2}\mathbf{E}^n(\lambda, \boldsymbol{\tau}, \mathbf{u}) - \frac{1}{2}\mathbf{E}^{n-1}(\lambda, \boldsymbol{\tau}, \mathbf{u}))$

instability. Therefore, an implicit coupled scheme has also been implemented. In this scheme the solution at the time-level $n+1$ is found using an iterative process in which the non-linear terms are calculated over and over again until the solution at t^{n+1} has converged to a certain criterion. A first-order implicit scheme, with $\frac{\partial G}{\partial t} \approx \frac{\mathbf{G}^{n+1} - \mathbf{G}^n}{\Delta t}$ for the use with the Oldroyd B model, is defined by

$$\begin{aligned}
\nabla \cdot \mathbf{u}^{n+1}_{(m+1)} &= 0 \\
\frac{Re}{\Delta t}\mathbf{u}^{n+1}_{(m+1)} + \nabla p^{n+1}_{(m+1)} - \nabla \cdot \boldsymbol{\tau}^{n+1}_{(m+1)} - \beta \nabla^2 \mathbf{u}^{n+1}_{(m+1)} &= Re(\frac{\mathbf{u}^n}{\Delta t} - \mathbf{u}^{n+1}_{(m)} \cdot \nabla \mathbf{u}^{n+1}_{(m)}), \\
(1 + \frac{We}{\Delta t})\boldsymbol{\tau}^{n+1}_{(m+1)} - 2(1-\beta)\mathbf{d}^{n+1}_{(m+1)} &= \\
&\frac{We}{\Delta t}\boldsymbol{\tau}^n - We\left(\mathbf{u} \cdot \nabla \boldsymbol{\tau} - (\nabla \mathbf{u})\boldsymbol{\tau} - \boldsymbol{\tau}(\nabla \mathbf{u})^T\right)^{n+1}_{(m)},
\end{aligned} \tag{3.25}$$

where m is the iteration parameter. The convergence criteria are $||\mathbf{u}^{n+1}_{(m+1)} - \mathbf{u}^{n+1}_{(m)}|| \leq \epsilon$ and $||\boldsymbol{\tau}^{n+1}_{(m+1)} - \boldsymbol{\tau}^{n+1}_{(m)}|| \leq \epsilon$. The starting conditions $\mathbf{u}^{n+1}_{(0)}$ and $\boldsymbol{\tau}^{n+1}_{(0)}$ are set to be

$$\mathbf{u}^{n+1}_{(0)} = \mathbf{u}^n \qquad \text{and} \qquad \boldsymbol{\tau}^{n+1}_{(0)} = \boldsymbol{\tau}^n. \tag{3.26}$$

It is obvious that this implicit coupled scheme it is quite expensive, since in every iteration a problem needs to be solved that is the same in size as a full explicit problem.

3.3.3 Implicit uncoupled solver

In the uncoupled solver, the constitutive equation is solved separate from the field equations. This approach allows for a more implicit treatment of the constitutive equation. Firstly, the field equations are solved as before, but with the divergence of the stresses now being reviewed at the previous time level. Using equivalent functions as in (3.1)-(3.3), the field equations now read

$$\nabla \cdot \mathbf{u}^{n+1} = 0, \tag{3.27}$$

$$M_l \mathbf{u}^{n+1} + \nabla p^{n+1} - \beta \nabla^2 \mathbf{u}^{n+1} = \mathbf{g}(\mathbf{u}) + \nabla \cdot \boldsymbol{\tau}^n, \tag{3.28}$$

In the uncoupled solver, only the first-order OIFS1/Euler temporal approximation will be used in the momentum equation. The values for M_l and of $\mathbf{g}(\mathbf{u})$ are the same as those given in Table 3.1 for the OIFS1/Euler scheme.

With the new values of pressure and velocity, the stress is updated using the following implicit formulation of the semi-discrete constitutive equation

$$\begin{aligned} C_l(\lambda^n, \boldsymbol{\tau}^n)\boldsymbol{\tau}^{n+1} + We\left(\mathbf{u}\nabla \cdot \boldsymbol{\tau} - (\nabla \mathbf{u})\boldsymbol{\tau} - \boldsymbol{\tau}(\nabla \mathbf{u})^T\right)^{n+1} \\ + \frac{\alpha We}{1-\beta}\boldsymbol{\tau}^n \cdot \boldsymbol{\tau}^{n+1} = 2(1-\beta)\mathbf{d}^{n+1} + \mathbf{h}(\lambda, \mathbf{u}, \boldsymbol{\tau}). \end{aligned} \tag{3.29}$$

Since many terms in the constitutive equation are treated implicitly, the factors $C_l(\lambda, \boldsymbol{\tau})$ and $\mathbf{h}(\lambda, \boldsymbol{\tau}, \mathbf{u})$ are different from the ones given in Tables 3.2 and 3.3. Instead they are given by

$$C_l(\lambda, \boldsymbol{\tau}) = f(\lambda, \boldsymbol{\tau}) + \frac{We}{\Delta t}, \tag{3.30}$$

$$\mathbf{h}(\lambda, \boldsymbol{\tau}, \mathbf{u}) = \frac{We}{\Delta t}\boldsymbol{\tau}^n - (f^n(\lambda, \boldsymbol{\tau}) - 1)\frac{1-\beta}{We}\mathbf{I}. \tag{3.31}$$

The values for the stretch λ are updated afer the stress is calculated.

Although an uncoupled solver is usually less stable than a coupled solver, it is less expensive to use in conjunction with implicit treatment of the non-linear terms. Due to a more critical CFL condition however, it is expected that smaller time steps should be taken when the uncoupled solver is used.

3.4 Weak Formulation

The equations as presented in chapter 2 are in their 'strong' formulation. In spectral element methods however, the equations are not solved in the strong form, but in their equivalent weak formulation. The weak formulation of a differential equation is found by multiplying the strong formulation by a test function in an appropriate space and then integrating the whole equation over the entire physical space in which the equation needs to be solved. The advantage of doing this is that the equations can now be reduced by one order through intergration by parts. For some problems it is possible to find a symmetric resulting matrix formulation of the approximated equation.

The spectral element method is applied to the weak formulation of the semi-discrete equations (3.1)-(3.3). Suitable function spaces are chosen for the dependent variables. The velocity is chosen to be in a subspace, $\mathcal{V}$, of $[H^1(\Omega)]^2$ whose elements satisfy the prescribed velocity boundary conditions. The appropriate spaces for pressure and stress for this generalized Stokes problem are

$$\begin{aligned}\mathcal{P} &= [L^2(\Omega)],\\ \mathcal{T} &= [L^2(\Omega)]^4_s,\end{aligned}$$

where the subscript s denotes the space of symmetric tensors. For this choice of function spaces, Gerritsma and Phillips [18] have shown that the integrals in the weak formulation are well-defined for the corresponding Stokes problem. The resulting weak formulation of the coupled equations (3.1)-(3.3) is then: Find $(\mathbf{u}^{n+1}, p^{n+1}, \boldsymbol{\tau}^{n+1}) \in \mathcal{V} \times \mathcal{P} \times \mathcal{T}$, such that

$$\begin{gathered} d(\mathbf{u}^{n+1}, q) = 0, \qquad \forall\, q \in \mathcal{P},\\ M_l c(\mathbf{u}^{n+1}, \mathbf{v}) + \beta e(\mathbf{u}^{n+1}, \mathbf{v}) - d^*(p^{n+1}, \mathbf{v}) + b(\boldsymbol{\tau}^{n+1}, \mathbf{v}) = (\mathbf{g}, \mathbf{v}), \;\; \forall\, \mathbf{v} \in \mathcal{V}, \quad (3.32)\\ C_l a(\boldsymbol{\tau}^{n+1}, \boldsymbol{\sigma}) - (1-\beta) b^*(\mathbf{u}^{n+1}, \boldsymbol{\sigma}) = (\mathbf{h}, \boldsymbol{\sigma}), \qquad \forall\, \boldsymbol{\sigma} \in \mathcal{T}.\end{gathered}$$

After this problem is solved, equation (3.24) is solved for λ^{n+1}. The bilinear forms $a(\cdot,\cdot)$ etc., are defined by

$$\begin{aligned} a(\boldsymbol{\tau}, \boldsymbol{\sigma}) &= \int_\Omega \boldsymbol{\tau} : \boldsymbol{\sigma} d\Omega, & b(\boldsymbol{\tau}, \mathbf{v}) &= \int_\Omega \boldsymbol{\tau} : \nabla \mathbf{v} d\Omega,\\ b^*(\mathbf{u}, \boldsymbol{\sigma}) &= \int_\Omega \nabla \mathbf{u} : \boldsymbol{\sigma} d\Omega, & c(\mathbf{u}, \mathbf{v}) &= \int_\Omega \mathbf{u} \cdot \mathbf{v} d\Omega,\\ d(\mathbf{u}, q) &= \int_\Omega \nabla \cdot \mathbf{u} q d\Omega, & d^*(p, \mathbf{v}) &= \int_\Omega p \nabla \cdot \mathbf{v} d\Omega,\\ e(\mathbf{u}, \mathbf{v}) &= \int_\Omega \nabla \mathbf{u} : \nabla \mathbf{v} d\Omega. \end{aligned}$$

The bilinear forms $a(\cdot,\cdot)$, $b(\cdot,\cdot)$, $c(\cdot,\cdot)$, $d(\cdot,\cdot)$ and $e(\cdot,\cdot)$ induce continuous linear operators $A : \mathcal{T} \to \mathcal{T}'$, $B : \mathcal{T} \to \mathcal{V}'$, $C : \mathcal{V} \to \mathcal{V}'$, $D : \mathcal{T} \to \mathcal{P}'$, and $E : \mathcal{V} \to \mathcal{V}'$, defined by

$$\begin{aligned}
[A\boldsymbol{\tau},\boldsymbol{\sigma}] &= a(\boldsymbol{\tau},\boldsymbol{\sigma}), && \forall\,\boldsymbol{\tau},\boldsymbol{\sigma}\in\mathcal{T}, \\
[B\boldsymbol{\tau},\mathbf{v}] &= b(\boldsymbol{\tau},\mathbf{v}), && \forall\,\boldsymbol{\tau}\in\mathcal{T}, \qquad \forall\,\mathbf{v}\in\mathcal{V}, \\
[B^*\mathbf{u},\boldsymbol{\sigma}] &= b^*(\mathbf{u},\boldsymbol{\sigma}), && \forall\,\mathbf{u}\in\mathcal{V}, \qquad \forall\,\boldsymbol{\sigma}\in\mathcal{T}, \\
[C\mathbf{u},\mathbf{v}] &= c(\mathbf{u},\mathbf{v}), && \forall\,\mathbf{u},\mathbf{v}\in\mathcal{V}, \\
[D\mathbf{u},q] &= d(\mathbf{u},q), && \forall\,\mathbf{u}\in\mathcal{V}, \qquad \forall\,q\in\mathcal{P}, \\
[D^*p,\mathbf{v}] &= d^*(p,\mathbf{v}), && \forall\,p\in\mathcal{P}, \qquad \forall\,\mathbf{v}\in\mathcal{V}, \\
[E\mathbf{u},\mathbf{v}] &= e(\mathbf{u},\mathbf{v}), && \forall\,\mathbf{u},\mathbf{v}\in\mathcal{V}.
\end{aligned}$$

In this notation, the dual problem to (3.32) is

$$\begin{aligned}
D\mathbf{u}^{n+1} &= 0, && \text{in } \mathcal{P}', \\
(M_lC+\beta E)\mathbf{u}^{n+1} - D^*p^{n+1} + B\boldsymbol{\tau}^{n+1} &= \mathbf{g}, && \text{in } \mathcal{V}', \\
C_lA\boldsymbol{\tau}^{n+1} - (1-\beta)B^*\mathbf{u}^{n+1} &= \mathbf{h}, && \text{in } \mathcal{T}'.
\end{aligned} \tag{3.33}$$

3.5 Spatial Discretization

In the spectral element method, finite dimensional approximations to the operators in (3.33) are constructed. The spatial discretization of the physical domain Ω of a certain geometry, involves dividing Ω into K non-overlapping spectral elements Ω_k, $1\leq k\leq K$, such that $\cup_{k=1}^{K}\Omega_k = \Omega$. This provides greater freedom in creating meshes in complicated geometries, and also allows for higher mesh resolution in flow regions where high gradients may occur. We denote by $\mathbb{P}_N(\Omega_k)$ the space of all polynomials on Ω_k of degree less than or equal to N, and further define $P_N(\Omega)=\{\phi : \phi|_{\Omega_k}\in\mathbb{P}_N(\Omega_k)\}$. Each of the spectral elements is mapped onto a parent element $D=[-1,1]\times[-1,1]$, where each point $\boldsymbol{\xi}=(\xi,\eta)\in D$ is associated with a point $\mathbf{x}=(x(\xi,\eta),y(\xi,\eta))\in\Omega_k$, through a mapping operator $\mathbf{F}$, such that $\mathbf{x}=\mathbf{F}(\boldsymbol{\xi})$ (see Fig. 3.1). More information about the mapping is given in section 3.5.1. The independent variables are then discretized using spectral approximations, as described in section 3.5.2. The resulting integral is approximated with a Gauss-Lobatto-Legendre integration rule (see section 3.5.3). The full discretized equations are given in section 3.7.

3.5.1 Transfinite mapping

The mapping from the grid in the parent element D onto the physical element Ω is shown in Fig. 3.1.

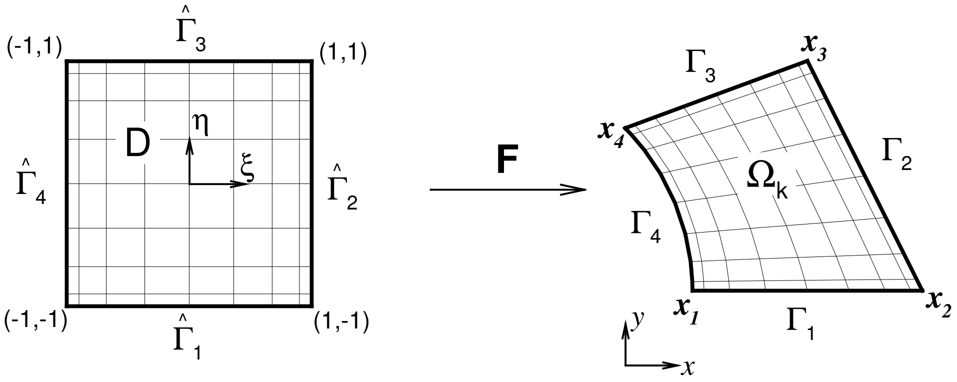

Figure 3.1: The parent element D in computational space and an element Ω_k in the physical space.

The transformation of the weak form of the conservation of mass equation in (3.32) from the physical space to the computational space is

$$\int_{\Omega_k} \left(\frac{\partial u(x,y)}{\partial x} + \frac{\partial v(x,y)}{\partial y} \right) q(x,y) dx dy = \int_D \left(\frac{\partial u(\xi,\eta)}{\partial x} + \frac{\partial v(\xi,\eta)}{\partial y} \right) q(\xi,\eta) \left| det(\mathbf{J}) \right| d\xi d\eta, \tag{3.34}$$

where $\mathbf{J}$ is the Jacobian of the transformation

$$\mathbf{J} = \begin{pmatrix} \dfrac{\partial x}{\partial \xi} & \dfrac{\partial x}{\partial \eta} \\ \dfrac{\partial y}{\partial \xi} & \dfrac{\partial y}{\partial \eta} \end{pmatrix} \tag{3.35}$$

From the Jacobian it can also be found that

$$\frac{\partial}{\partial x} = \frac{1}{det(\mathbf{J})}\left(\frac{\partial y}{\partial \eta}\frac{\partial}{\partial \xi} - \frac{\partial y}{\partial \xi}\frac{\partial}{\partial \eta}\right) \qquad \text{and} \qquad \frac{\partial}{\partial y} = \frac{1}{det(\mathbf{J})}\left(\frac{\partial x}{\partial \xi}\frac{\partial}{\partial \eta} - \frac{\partial x}{\partial \eta}\frac{\partial}{\partial \xi}\right). \tag{3.36}$$

The integral over the parent element D from (3.34) can now be expressed as

$$\int_D \left[\left(\frac{\partial y}{\partial \eta}\frac{\partial}{\partial \xi} - \frac{\partial y}{\partial \xi}\frac{\partial}{\partial \eta}\right) u(\xi,\eta) + \left(\frac{\partial x}{\partial \xi}\frac{\partial}{\partial \eta} - \frac{\partial x}{\partial \eta}\frac{\partial}{\partial \xi}\right) v(\xi,\eta)\right] q(\xi,\eta)\frac{|det(\mathbf{J})|}{det(\mathbf{J})} d\xi d\eta, \tag{3.37}$$

The mapping factors $\partial x/\partial\xi$, $\partial x/\partial\eta$, $\partial y/\partial\xi$ and $\partial y/\partial\eta$ depend on the mapping operator $\mathbf{F}$. For the transfinite mapping, Schneidesch and Deville [53] have introduced a general transfinite operator $\mathbf{F}_{a,b}$, where a and b denote the order of the polynomial spaces used in the mapping. So $\mathbf{F}_{1,1}$ is the operator that yields the bi-linear transfinite mapping that is used in this thesis. It is given by

$$\begin{aligned}\boldsymbol{F}_{1,1}(\xi,\eta) = \mathbf{x} =& \boldsymbol{\gamma}_1(\xi)\phi_1(\eta) + \boldsymbol{\gamma}_2(\eta)\phi_2(\xi) + \boldsymbol{\gamma}_3(\xi)\phi_2(\eta) + \boldsymbol{\gamma}_4(\eta)\phi_1(\xi)\\ &- \mathbf{x}_1\phi_1(\eta)\phi_2(\xi) - \mathbf{x}_2\phi_2(\xi)\phi_2(\eta) - \mathbf{x}_3\phi_2(\eta)\phi_1(\xi) - \mathbf{x}_4\phi_1(\xi)\phi_1(\eta),\end{aligned} \tag{3.38}$$

where the parametrizations $\boldsymbol{\gamma}_i$ map the parent element boundaries $\hat{\Gamma}_i$ onto the corresponding physical element boundaries Γ_i, $\boldsymbol{\gamma}_i : \hat{\Gamma}_i \rightarrow \Gamma_i$,

$$\begin{aligned}\boldsymbol{\gamma}_1(\xi) &= \mathbf{x}(\xi,-1), \qquad & \boldsymbol{\gamma}_3(\xi) &= \mathbf{x}(\xi,+1),\\ \boldsymbol{\gamma}_2(\eta) &= \mathbf{x}(+1,\eta), \qquad & \boldsymbol{\gamma}_4(\eta) &= \mathbf{x}(-1,\eta),\end{aligned}$$

in which the coordinates of the corners are $\mathbf{x}_1 = \boldsymbol{\gamma}_1(-1) = \boldsymbol{\gamma}_4(-1)$ etc. The basis functions are defined by

$$\phi_1(\xi) = \frac{1-\xi}{2}, \qquad \phi_2(\xi) = \frac{1+\xi}{2}. \tag{3.39}$$

A reason for choosing higher order mapping could be that with a Hermite mapping $\mathbf{F}_{3,3}$, the derivatives of the grid lines in physical space can be prescribed. This means that the grid lines can be made to be continuous over elemental boundaries or perpendicular to element boundaries, as shown for example in Fig. 3.2.

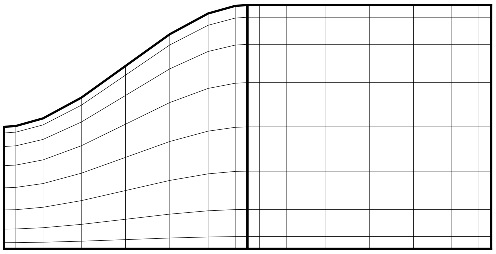

Figure 3.2: Continuous derivatives of grid lines over element boundaries due to the Hermite mapping.

The Hermite mapping operator is given by

$$\begin{aligned}\boldsymbol{F}_{3,3}(\xi,\eta) =& \boldsymbol{F}_{1,1}(\xi,\eta) + \frac{\partial\boldsymbol{\gamma}_1}{\partial\eta}(\xi)\bar{\phi}_1(\eta) + \frac{\partial\boldsymbol{\gamma}_2}{\partial\xi}(\eta)\bar{\phi}_2(\xi) + \frac{\partial\boldsymbol{\gamma}_3}{\partial\eta}(\xi)\bar{\phi}_2(\eta) + \frac{\partial\boldsymbol{\gamma}_4}{\partial\xi}(\eta)\bar{\phi}_1(\xi)\\
&- \frac{\partial\boldsymbol{\gamma}_1}{\partial\eta}(-1)\bar{\phi}_1(\eta)\phi_1(\xi) - \frac{\partial\boldsymbol{\gamma}_1}{\partial\eta}(+1)\bar{\phi}_1(\eta)\phi_2(\xi)\\
&- \frac{\partial\boldsymbol{\gamma}_2}{\partial\xi}(-1)\bar{\phi}_2(\xi)\phi_1(\eta) - \frac{\partial\boldsymbol{\gamma}_2}{\partial\xi}(+1)\bar{\phi}_2(\xi)\phi_2(\eta)\\
&- \frac{\partial\boldsymbol{\gamma}_3}{\partial\eta}(-1)\bar{\phi}_2(\eta)\phi_1(\xi) - \frac{\partial\boldsymbol{\gamma}_3}{\partial\eta}(+1)\bar{\phi}_2(\eta)\phi_2(\xi)\\
&- \frac{\partial\boldsymbol{\gamma}_4}{\partial\xi}(-1)\bar{\phi}_1(\xi)\phi_1(\eta) - \frac{\partial\boldsymbol{\gamma}_4}{\partial\xi}(+1)\bar{\phi}_1(\xi)\phi_2(\eta)\\
&- \frac{\partial\boldsymbol{\gamma}_1}{\partial\xi\partial\eta}(+1)\bar{\phi}_1(\eta)\bar{\phi}_2(\xi) - \frac{\partial\boldsymbol{\gamma}_2}{\partial\xi\partial\eta}(+1)\bar{\phi}_2(\xi)\bar{\phi}_2(\eta)\\
&- \frac{\partial\boldsymbol{\gamma}_3}{\partial\xi\partial\eta}(-1)\bar{\phi}_2(\eta)\bar{\phi}_1(\xi) - \frac{\partial\boldsymbol{\gamma}_4}{\partial\xi\partial\eta}(-1)\bar{\phi}_1(\xi)\bar{\phi}_1(\eta).\end{aligned}$$

The basis functions ϕ_1, ϕ_2 and $\bar{\phi}_1$, $\bar{\phi}_2$ for this cubic case are

$$\begin{aligned}\phi_1(\omega) &= \frac{\omega^3 - 3\omega + 2}{4}, & \phi_2(\omega) &= \phi_1(-\omega),\\
\bar{\phi}_1(\omega) &= \frac{\omega^3 - \omega^2 - \omega + 1}{4}, & \bar{\phi}_2(\omega) &= -\bar{\phi}_1(-\omega).\end{aligned}$$

Using this Hermite mapping might be a good idea in geometries like the undulated channel, but for the problems in this thesis it introduces unneccesary complications such as grid lines intersecting the outer boundaries as is shown in Fig. 3.3.

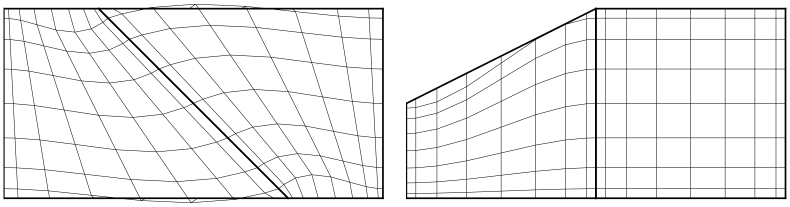

Figure 3.3: Continuous derivatives of grid lines over element boundaries and grid lines perpendicular to element boundaries resulting in invalid meshes.

3.5.2 Spectral approximations

The dependent variables are approximated on the parent element D using Lagrangian interpolants, based on Legendre polynomials of degree N in both spatial directions. The variables will be calculated explicitly on the points where the derivatives of the Legendre polynomials in both directions vanish. The grid connecting all these nodes within an element is called the Gauss-Lobatto-Legendre grid as can be seen in Figs. 3.1 to 3.3. The spectral element mesh shown in Fig. 3.4 is for a cylinder in a channel with $K = 5$ elements and approximating polynomials of degree $N = 11$ within each element.

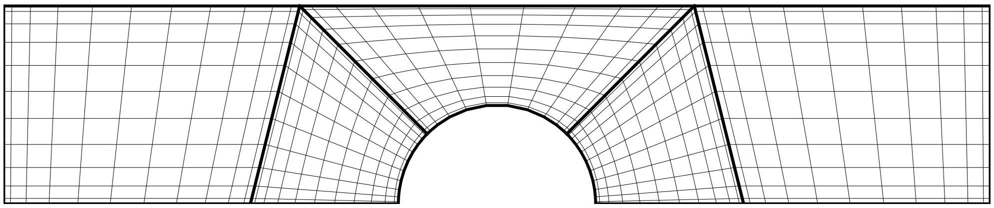

Figure 3.4: Spectral element mesh for a cylinder in a channel with $K = 5$ and $N = 11$.

The discrete approximation spaces must satisfy a compatibility condition to ensure that the problem is well-posed. For spectral elements Maday and Patera [33] have shown that this LBB condition is satisfied when the velocity approximation space is the polynomial space $P_N(\Omega)$, and the pressure approximation space is $P_{N-2}(\Omega)$. This is ensured by letting the pressures grid comprise only the internal nodes of the GLL grid. The pressure at the element boundaries can then be calculated by extrapolation. The velocity is continuous over element boundaries. The stress will be approximated by polynomials in the space $P_N(\Omega)$ as well. Although Gerritsma and Phillips [17] have shown that allowing the stresses to be discontinuous over element boundaries is a sufficient condition for stability of the three-field Stokes problem, this remains an open issue for the viscoelastic models. In this thesis discontinuous stresses are used to solve Newtonian problems, but continuous stresses are used for solving the viscoelastic models in complex flows.

The spectral approximations in an element Ω_k of the velocity and stress are given by

$$\mathbf{u}_N^k(\xi,\eta) = \sum_{i=0}^{N}\sum_{j=0}^{N} \mathbf{u}_{i,j}^k h_i(\xi)h_j(\eta), \tag{3.40}$$

$$\boldsymbol{\tau}_N^k(\xi,\eta) = \sum_{i=0}^{N}\sum_{j=0}^{N} \boldsymbol{\tau}_{i,j}^k h_i(\xi)h_j(\eta), \tag{3.41}$$

where the Lagrangian interpolants $h_i(\xi)$ are defined by

$$h_i(\xi) = -\frac{(1-\xi^2)L_N'(\xi)}{N(N+1)L_N(\xi_i)(\xi-\xi_i)}. \tag{3.42}$$

The interpolants satisfy the Kronecker delta property $h_i(\xi_m) = \delta_{im}$. The collocation points in the Gauss-Lobatto-Legendre grid can now be identified as $\xi_0 = -1$, $\xi_N = 1$, and ξ_i $(i = 1, .., N-1)$ the zeroes of $L_N'(\xi)$. The pressure representation is

$$p_N^k(\xi,\eta) = \sum_{i=1}^{N-1}\sum_{j=1}^{N-1} p_{i,j}^k \tilde{h}_i(\xi)\tilde{h}_j(\eta), \tag{3.43}$$

in which the Lagrangian interpolants $\tilde{h}_i(\xi)$ are defined by

$$\tilde{h}_i(\xi) = -\frac{(1-\xi_i^2)L_N'(\xi)}{N(N+1)L_N(\xi_i)(\xi-\xi_i)}, \qquad 1 \le i \le N-1. \tag{3.44}$$

This choice of the Lagrangian interpolant $\tilde{h}_i(\xi)$ ensures that the discrete pressure nodes are the internal collocation points in the Gauss-Lobatto-Legendre grid.

Substituting these spectral approximations in the weak formulation of the divergence of velocity on the parent element (3.37), yields for the first term

$$\int_D \left[\left(\frac{\partial y}{\partial \eta} \frac{\partial}{\partial \xi} - \frac{\partial y}{\partial \xi} \frac{\partial}{\partial \eta} \right) \sum_{i=0}^{N} \sum_{j=0}^{N} u_{ij}^k h_i(\xi) h_j(\eta) \right] q(\xi, \eta) \frac{|det(\mathbf{J})|}{det(\mathbf{J})} d\xi d\eta, \tag{3.45}$$

which can be written as

$$\int_D \left[\frac{\partial y}{\partial \eta} \sum_{i=0}^{N} \sum_{j=0}^{N} u_{ij}^k h_i'(\xi) h_j(\eta) - \frac{\partial y}{\partial \xi} \sum_{i=0}^{N} \sum_{j=0}^{N} u_{ij}^k h_i(\xi) h_j'(\eta) \right] q(\xi, \eta) \frac{|det(\mathbf{J})|}{det(\mathbf{J})} d\xi d\eta, \tag{3.46}$$

where the pressure test functions $q(\xi, \eta)$ are also based on the Lagrangian interpolants, according to

$$q(\xi, \eta) = \tilde{h}(\xi) \tilde{h}(\eta). \tag{3.47}$$

The derivatives of $h_i(\xi)$ with respect to its argument ξ are denoted as $h_i'(\xi)$. The derivatives $d_{ij} = h_j'(\xi_i)$ can be found to be

$$d_{ij} = \begin{cases} \dfrac{L_N(\xi_i)}{L_N(\xi_j)} \dfrac{1}{\xi_i - \xi_j} & i \neq j, \\[2ex] -\dfrac{N(N+1)}{4} & i = j = 0, \\[2ex] \dfrac{N(N+1)}{4} & i = j = N, \\[2ex] 0 \quad i = j, & 1 \leq i, j \leq N-1. \end{cases} \tag{3.48}$$

3.5.3 Gauss-Lobatto integration

A Gauss-Lobatto quadrature rule will be used to integrate the integrals in the weak formulation. In general, the Gauss-Lobatto integration is defined by

$$\int_{-1}^{1} \int_{-1}^{1} f(\xi, \eta) d\xi d\eta \approx \sum_{m=0}^{N} \sum_{n=0}^{N} f(\xi_m, \eta_n) w_m w_n, \tag{3.49}$$

which is exact when $f \in P_{2N-1}$. The numerical weights can be calculated as the integral of the Lagrange polynomials, $w_m = \int_{-1}^{1} h_m(\xi)d\xi$. This yields for the Gauss-Lobatto integration rule:

$$w_m = \frac{2}{N(N+1)[L_N(\xi_m)]^2}. \tag{3.50}$$

When the Gaus-Lobatto integration rule in applied to the first term in the expression (3.46), the following discrete sum is retrieved,

$$\sum_{m=0}^{N}\sum_{n=0}^{N}\frac{\partial y}{\partial \eta}_{mn}\sum_{i=0}^{N}\sum_{j=0}^{N}u_{ij}^{k}h_i'(\xi_m)h_j(\eta_n)q(\xi_m,\eta_n)\frac{|det(\mathbf{J})_{mn}|}{det(\mathbf{J})_{mn}}w_m w_n. \tag{3.51}$$

3.6 A Modified Lagrange Interpolant

A Lagrange interpolant is introduced that circumvents problems associated with the zero radial coordinate in axisymmetric problems. By imposing the derivative to disappear on the element boundaries corresponding to the axis of symmetry, the local zero Neumann boundary condition is automatically satisfied. The test functions associated with the axis of symmetry may then be excluded from the formulation for variables that satisfy this Neumann condition. The values of the variable at the axis can be calculated at the end of the computation, using the Lagrange interpolant to extrapolate the values from inside the computational domain.

3.6.1 The original Lagrange interpolant

The Lagrange interpolant that is commonly used in spectral element methods has already been introduced in equation (3.42). It is based on Legendre polynomials. For a computational domain with discrete points at the zeros $j = 0, 1, ..., N$ of the N-th Legendre polynomial, it is defined by

$$h_j(\eta) = \frac{L_N'(\eta)(\eta^2-1)}{N(N+1)L_N(\eta_j)(\eta-\eta_j)}, \qquad 0 \le j \le N \tag{3.52}$$

in which $L_N(\eta)$ are the Legendre polynomials. This Lagrange interpolant satisfies the following properties:

$$\begin{aligned} h_j(\eta_i) &= 0 \qquad && i \neq j, \\ h_j(\eta_i) &= 1 \qquad && i = j. \end{aligned}$$

The derivative matrix $d_{ij} = h_j'(\eta_i)$ is given in (3.48), and the numerical weights for the Gauss-Lobatto integration rule are given in (3.50).

3.6.2 The modified Lagrange interpolant

Let $u(\xi,\eta)$ be a variable that is approximated on a spectral element $[-1,1]\times[-1,1]$, and let $u(\xi,\eta)$ be subject to a zero Neumann boundary condition $\partial u/\partial\eta = 0$ at the element boundary $\eta = -1$. Using the modified Lagrange interpolant $\hat{h}_j(\eta)$, the spectral approximation to $u(\xi,\eta)$ is

$$u_N(\xi,\eta) = \sum_{i=0}^{N}\sum_{j=1}^{N} u_{i,j} h_i(\xi)\hat{h}_j(\eta). \tag{3.53}$$

Note that the nodes at the element boundary corresponding to $j = 0$ are excluded from the respresentation. If this boundary is an axis of symmetry, the problem with the zero radial coordinate is removed since it simply is not present in the discrete equations. The modified Lagrange interpolant $\hat{h}_j(\eta)$ has to satisfy $\dfrac{\partial u_N(\xi,\eta_0)}{\partial\eta} = u_N'(\xi,-1) = 0$ automatically. The general form of the modified Lagrangian interpolant is

$$\hat{h}_j(\eta) = \frac{L_N'(\eta)(1-\eta)}{(\eta-\eta_j)}(a\eta+b), \qquad 1 \le j \le N-1, \tag{3.54}$$

which satisfies

$$\begin{aligned} \hat{h}_j(\eta_i) \qquad &= 0, \qquad i \neq j, \qquad 1 \le i,j \le N-1, \\ \hat{h}_j(\eta_N) = \hat{h}_j(+1) \quad &= 0, \qquad 1 \le j \le N-1. \end{aligned}$$

The factors a and b are calculated using the following properties of $\hat{h}_j(\eta)$:

$$\hat{h}_j(\eta_i) = 1, \qquad i = j, \qquad 1 \leq j \leq N-1, \tag{3.55}$$

$$\frac{\partial}{\partial \eta}\hat{h}_j(\eta)|_{(\eta=\eta_0)} = 0, \qquad 1 \leq j \leq N-1, \tag{3.56}$$

the last of which ensures the derivative to be zero at $\eta = \eta_0$, the nodal point corresponding to the axis of symmetry.

Since the expression for $\hat{h}_j(\eta)$ is not valid for $j = N$, a separate interpolant $\hat{h}_N(\eta)$ has to be found. Similar as before, this one is of the form

$$\hat{h}_N(\eta) = L'_N(\eta)(c\eta + d), \tag{3.57}$$

which is set up such that it satisfies

$$\hat{h}_N(\eta_i) = 0, \qquad 1 \leq i \leq N-1. \tag{3.58}$$

Again, it also has to satisfy the following conditions:

$$\hat{h}_N(\eta_N) = 1, \tag{3.59}$$

$$\frac{\partial}{\partial \eta}\hat{h}_N(\eta)|_{(\eta=\eta_0)} = 0. \tag{3.60}$$

This will provide the factors c and d. The calculation of the modified Lagrangian interpolant $\hat{h}_j(\eta)$ and its derivative $\hat{d}_{ij}$ is presented in Appendix D, and it is shown that they can be expressed in terms of the original interpolants h:

$$\hat{h}_j(\eta) = h_j(\eta) - \frac{4(-1)^N}{N(N+1)L_N(\eta_j)(1+\eta_j)}h_0(\eta), \qquad 1 \leq j \leq N,$$

and

$$\hat{d}_{ij} = d_{ij} - \frac{4(-1)^N}{N(N+1)L_N(\eta_j)(1+\eta_j)}d_{i0}, \qquad 1 \leq j \leq N.$$

This makes evaluating the weights for the modified interpolant easy:

$$\hat{w}_j = w_j - \frac{4(-1)^N}{N(N+1)L_N(\eta_j)(1+\eta_j)}w_0, \qquad 1 \leq j \leq N,$$

When the Neumann boundary condition is at the other end of the domain, $j = N$, the modified polynomial, derivative and weights are found to be

$$\hat{h}_j(\eta) = h_j(\eta) + \frac{4}{N(N+1)L_N(\eta_j)(-1+\eta_j)} h_0(\eta), \qquad 0 \le j \le N-1,$$

and

$$\hat{d}_{ij} = d_{ij} + \frac{4}{N(N+1)L_N(\eta_j)(-1+\eta_j)} d_{i0}, \qquad 0 \le j \le N-1,$$

and

$$\hat{w}_j = w_j + \frac{4}{N(N+1)L_N(\eta_j)(-1+\eta_j)} w_0, \qquad 0 \le j \le N-1.$$

3.7 The Discrete Equations

The discrete equation for a single collocation point (k, l) can be found by inserting the appropriate test function into summation expressions similar to (3.51). This particular discretized term yields

$$\sum_{m=0}^{N}\sum_{n=0}^{N} \frac{\partial y}{\partial \eta}_{mn} \sum_{i=0}^{N}\sum_{j=0}^{N} u^k_{ij} h'_i(\xi_m) h_j(\eta_n) \tilde{h}_k(\xi_m) \tilde{h}_l(\eta_n) \frac{|det(\mathbf{J})_{mn}|}{det(\mathbf{J})_{mn}} w_m w_n, \qquad k, l = 1, .., N-1. \tag{3.61}$$

This can be expressed as a matrix vector product

$$M^k_N \mathbf{u}^k_N = \begin{pmatrix} m_{11,00} & \cdot & \cdot & m_{11,ij} & \cdot & \cdot & m_{11,NN} \\ \cdot & \cdot & \cdot & \cdot & \cdot & \cdot & \cdot \\ \cdot & \cdot & \cdot & \cdot & \cdot & \cdot & \cdot \\ m_{kl,00} & \cdot & \cdot & m_{kl,ij} & \cdot & \cdot & \cdot \\ \cdot & \cdot & \cdot & \cdot & \cdot & \cdot & \cdot \\ \cdot & \cdot & \cdot & \cdot & \cdot & \cdot & \cdot \\ m_{(N-1)(N-1),00} & \cdot & \cdot & \cdot & \cdot & \cdot & \cdot \end{pmatrix} \begin{pmatrix} u^k_{00} \\ \cdot \\ \cdot \\ u^k_{ij} \\ \cdot \\ \cdot \\ u^k_{NN} \end{pmatrix}, \tag{3.62}$$

where $m_{kl,ij}$ is

$$m_{kl,ij} = \sum_{m=0}^{N}\sum_{n=0}^{N} h'_i(\xi_m) h_j(\eta_n) \tilde{h}_k(\xi_m) \tilde{h}_l(\eta_n) \frac{\partial y}{\partial \eta}_{mn} \frac{|det(\mathbf{J})_{mn}|}{det(\mathbf{J})_{mn}} w_m w_n. \tag{3.63}$$

By making use of the identity of the Lagrangian interpolant that $h_j(\eta_n) = \delta_{jn}$, this may be simplified to

$$m_{kl,ij} = \sum_{m=0}^{N} h_i'(\xi_m)\tilde{h}_k(\xi_m)\tilde{h}_l(\eta_j)\frac{\partial y}{\partial \eta}_{mj}\frac{|det(\mathbf{J})_{mj}|}{det(\mathbf{J})_{mj}} w_m w_j. \tag{3.64}$$

When this spectral element discretization is applied to all the terms in the weak formulation of the continuity equation using test functions in the pressure space (3.37) the resulting equation is

$$D_N^k \mathbf{u}_N^k = 0. \tag{3.65}$$

These discrete elemental matrices need to be assembled over all elements. This provides the choice of continuous or discontinuous operators. The velocities are always chosen to be continuous, which means that discrete equations at coinciding collocation points of adjacent elements are added together and averaged over the multiplicity of the collocation point. After the element assembly, the matrix vector product is written as

$$D_N \mathbf{u}_N. \tag{3.66}$$

3.7.1 Extra terms using the modified interpolant

Although the integration rule that will be used in conjuntion with the modified interpolant is the same as in the original spectral element formulation, it contributes an extra term to the spectral operators in the discrete equations. The same term is evaluated as in (3.63), with an axis of symmetry located at the element boundary at $\eta = -1$, corresponding to $j = 0$. The velocity component u in the ξ-direction is subject to a zero Neumann boundary condition. The discrete sum after application of the Gauss-Lobatto integration is now

$$\sum_{m=0}^{N}\sum_{n=0}^{N}\frac{\partial y}{\partial \eta}_{mn}\sum_{i=0}^{N}\sum_{j=1}^{N} u_{ij}^k h_i'(\xi_m)\hat{h}_j(\eta_n) q(\xi_m, \eta_n)\frac{|det(\mathbf{J})_{mn}|}{det(\mathbf{J})_{mn}} w_m w_n, \tag{3.67}$$

which can be compared to the discrete sum (3.51) when the original interpolant. Note that the size of the problem is slightly decreased now, since there are no contributions on the axis of symmetry, where $j = 0$. The term $m_{kl,ij}$ is now

$$m_{kl,ij} = \sum_{m=0}^{N} \sum_{n=0}^{N} h_i'(\xi_m)\hat{h}_j(\eta_n)\tilde{h}_k(\xi_m)\tilde{h}_l(\eta_n) \frac{\partial y}{\partial \eta}_{mn} \frac{|det(\mathbf{J})_{mn}|}{det(\mathbf{J})_{mn}} w_m w_n, \tag{3.68}$$

but since $\hat{h}_l(\eta_0) \neq 1$, the equivalent of (3.64) becomes

$$\begin{aligned} m_{kl,ij} = & \sum_{m=0}^{N} h_i'(\xi_m)\tilde{h}_k(\xi_m)\tilde{h}_l(\eta_j) \frac{\partial y}{\partial \eta}_{mj} \frac{|det(\mathbf{J})_{mj}|}{det(\mathbf{J})_{mj}} w_m w_j + \\ & \sum_{m=0}^{N} h_i'(\xi_m)\hat{h}_j(\eta_0)\tilde{h}_k(\xi_m)\tilde{h}_l(\eta_0) \frac{\partial y}{\partial \eta}_{m0} \frac{|det(\mathbf{J})_{m0}|}{det(\mathbf{J})_{m0}} w_m w_0. \end{aligned} \tag{3.69}$$

The second summation is not present after discretization with the original Lagrange interpolant, which resulted in the expression (3.64). In section 5.4 the efficiency of the modified interpolant will be tested against calculations using the original interpolant.

3.7.2 The coupled equations

When the spectral element discretization is applied to all the equations in the weak formulation of the coupled set of equations (3.33), the following discrete equations are retrieved

$$\begin{aligned} D_N \mathbf{u}_N^{n+1} &= 0, \\ (M_l C_N + \beta E_N)\mathbf{u}_N^{n+1} - D_N^T \mathbf{p}_N^{n+1} + B_N \boldsymbol{\tau}_N^{n+1} &= \mathbf{g}_N, \\ C_l A_N \boldsymbol{\tau}_N^{n+1} - (1-\beta) B_N^T \mathbf{u}_N^{n+1} &= \mathbf{h}_N, \end{aligned} \tag{3.70}$$

where D_N and B_N are the discrete divergence operators acting on velocity and stress, respectively, D_N^T and B_N^T are gradient operators acting on pressure and velocity, E_N is the discrete Laplace operator, C_N and A_N are the discrete velocity and stress mass matrices, and $\mathbf{g}_N$ and $\mathbf{h}_N$ denote the discrete forms of the right-hand sides of (3.33).

3.7.3 The uncoupled equations

Following the same procedure and using the same discrete operators as for the coupled equations, the discrete form of the uncoupled set of field equations (3.27)-(3.28) is

$$\begin{aligned} D_N \mathbf{u}_N^{n+1} &= 0, \\ (M_l C_N + \beta E_N)\mathbf{u}_N^{n+1} - D_N^T \mathbf{p}_N^{n+1} &= \mathbf{g}_N - B_N \boldsymbol{\tau}_N^n. \end{aligned} \tag{3.71}$$

The discretized form of the constitutive equation (3.29) reads

$$S_N \boldsymbol{\tau}_N^{n+1} - (1-\beta) B_N^T \mathbf{u}_N^{n+1} = \mathbf{h}_N, \tag{3.72}$$

in which S_N is the non-symmetric discrete operator that contains all the terms in the left-hand side of the constitutive equation (3.29). The right-hand side $\mathbf{h}_N$ is the discrete form of (3.31).

Chapter 4

Numerical Algorithm

4.1 Introduction

In this chapter the algorithm that is used to solve the discretized equations is described. The nodes in the spectral element mesh need to be numbered conveniently (see section 4.2) such that the discrete operators can be set up and solved efficiently by using iterative inversion methods (see section 4.3). The preconditioners that are used in these iterative methods are described in section 4.4. To speed up the calculations the Schur complement method has been implemented that reduces the size of the operators that need to be inverted. This method is presented in section 4.5. The zero volume of pressure condition that is used to obtain a better conditioning of the Uzawa operator, is proposed in section 4.6. When using the uncoupled equations, upwinding techniques for the stresses can be adopted. The most recent of these methods, the Locally Upwinded Spectral Technique (LUST) due to Owens et al. [39], is presented in the last section 4.7.

4.2 Node Numbering

A subroutine has been developed that can read mesh files that were created using Gambit, a widely available meshing software package provided with the commercial Fluent code. In Gambit meshes are easy to create using a graphical user interface. Only the spectral elements need to be created and element edges can be assigned with a certain boundary type, which makes it possible to incorporate boundary conditions. The mesh and boundary types are written as output to a so-called neutral file. A neutral file starts by providing a list of the vertices of the elements, with their physical coordinates. It then defines the elements using four vertices, always ordered anti-clockwise. The end of the neutral file contains a list of the boundary types. Given with each boundary type is a list of edges of elements associated to that type.

The nodes in the Gauss-Lobatto-Legendre (GLL) grid are not defined in the neutral file. They are only created on the parent element, but their physical coordinates can be found through the transfinite mapping described in section 3.5.1. The GLL nodes need to be numbered both locally on the spectral element level, and globally on the whole of the geometry. A convenient local numbering is nessecary since most operations can be performed on the elemental level. Nodes on the element boundaries that are shared by other elements, are characterized by more than one local number. The number of elements that share one node is called the multiplicity M of this node, and so there are M different equations associated to this particular node. When solutions need to be continuous over element boundaries, these equations are added together, and a global node numbering is needed to provide this coupling between the elements.

The Schur complement method that is described in section 4.5 is based on a certain global numbering of the nodes. It is essential for this method to function well that the boundary nodes are easily separated from the internal GLL nodes, and the global nodal numbering can provide just that. To find a global node number from a local number and vice-versa, a mapping function provides the one-to-many mapping from the global to the local numbering and a many-to-one mapping in the reverse direction.

Both the local and the global numbering depend on the neutral file. In the local numbering, the origin of the element, i.e. where $i = 0$ and $j = 0$, is placed at the first vertex of the element under consideration. Even in geometries consisting of only rectangular elements, the first vertex is randomly chosen, and so the origins of the local element numbering is not necessarily the same in every element. In Fig. 4.1 for example, element 1 has its origin in the bottom left corner, whereas the origin of element 2 is top left. For the local numbering, a quick and convenient mapping from the discrete coordinates $0 \leq i, j \leq N$ is given by the following relation

$$m = i + j(N + 1). \tag{4.1}$$

The numbering m contains $(N + 1)^2$ entries, ranging from $0 \leq m \leq (N + 1)^2 - 1$. In Fig. 4.1 the local numbering m is presented for two adjacent elements, using an approximation order $N = 4$. The figure also represents the fact that the origin of the numbering is random, and that as a result of this an edge of a certain spectral element, can share any other edge of the adjacent element. In this figure edge number 2 of element 1 is shared by edge number 1 of element 2.

The global numbering depends on the neutral file since the first few nodes in the global numbering are the vertices of the elements as numbered in the file. Fig. 4.2 shows that these six vertices are numbered first, followed by the nodes on the element boundaries and last the inner nodes are numbered. Node numbers 2, 5, 10, 11 and 12 have a multiplicity $M = 2$ but are characterized by only one global number.

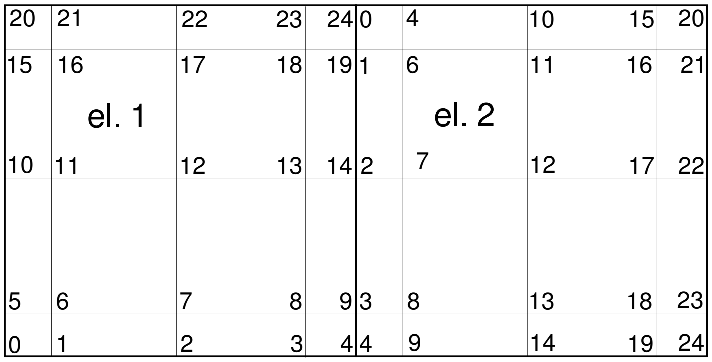

Figure 4.1: Local numbering m in neighbouring elements.

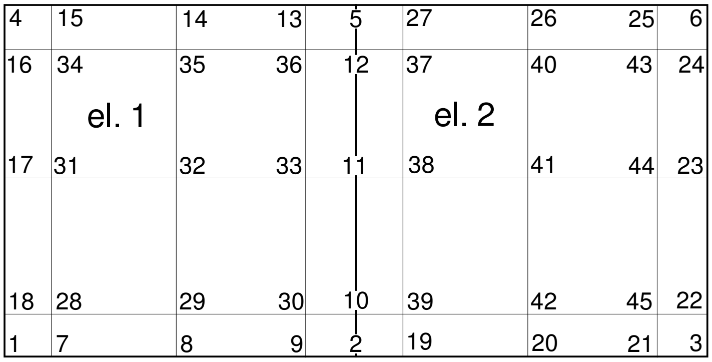

Figure 4.2: Global numbering m in neighbouring elements.

4.3 Solving the Discretized Equations

The algorithms are set up in such a way that there is no need to explicitly construct the discrete matrices. This results in a low memory usage and therefore relatively large problems may be calculated. In this light, the choice of iterative methods to invert the discrete operators is made. In the process of inversion, only matrix-vector multiplications have to be performed. As opposed to direct methods, there is no need to store the matrix. Section 4.3.1 shows the operators that need to be inverted, and section 4.3.2 describes how iterative methods can be applied to invert these operators.

4.3.1 Discrete operators

The form of the discrete operators that need to be inverted in order to solve the system of discrete equations, depends on the temporal discretization.

The coupled equations

Combining the discrete momentum and constitutive equations from the set of coupled equations (3.70) yields

$$-D_N^T \mathbf{p}_N^{n+1} + H_N \mathbf{u}_N^{n+1} = \mathbf{g}_N - \frac{1}{C_l} B_N A_N^{-1} \mathbf{h}_N, \tag{4.2}$$

in which H_N is the discrete Helmholtz-like operator, given by

$$H_N = \frac{(1-\beta)}{C_l} B_N A_N^{-1} B_N^T + M_l C_N + \beta E_N. \tag{4.3}$$

Eliminating the velocity using the discrete continuity equation yields the equation that the pressure has to satisfy, i.e.

$$D_N H_N^{-1} D_N^T \mathbf{p}_N^{n+1} = -D_N H_N^{-1} \left(\mathbf{g}_N - \frac{1}{C_l} B_N A_N^{-1} \mathbf{h}_N \right). \tag{4.4}$$

The operator $U_N = D_N H_N^{-1} D_N^T$ is known as the Uzawa operator. Simplified, the pressure equation may be written as

$$U_N \mathbf{p}_N^{n+1} = \mathbf{b}_N, \tag{4.5}$$

where $\mathbf{b}_N$ is the right-hand side of (4.4). When the pressure equation (4.4) is solved, the velocity is found from (4.2), after which the stress can be calculated from the discretized constitutive equation in (3.70). In this process both the Helmholtz operator and the Uzawa operator need to be inverted. After the stresses have been found, the values of the stretch λ are calculated separately using using (3.24).

The uncoupled equations

The Helmholtz operator following from the uncoupled discrete equations (3.71) differs from (4.3) since the stresses are not implicit in the momentum equation. The discrete pseudo Laplacian is not included in the Helmholtz operator which now reads

$$H_N = M_l C_N + \beta E_N. \tag{4.6}$$

Although it is now based on a different Helmholtz operator, the expression for the Uzawa operator remains the same, i.e.

$$U_N = D_N H_N^{-1} D_N^T. \tag{4.7}$$

Again these Helmholtz and Uzawa operators need to be inverted to compute the velocity and pressure from the field equations. After this calculation a separate inversion needs to be performed to find the stress tensor. This inversion involves the operator S_N from the discretized constitutive equation (3.72), which contains the stress source term, the convection of the stresses, the deformation terms and the Giesekus term. Finally the the values of the stretch λ are again computed using (3.24).

4.3.2 Iterative methods

For the inversion of symmetric operators the Preconditioned Conjugate Gradient (PCG) method is used. In the uncoupled equations, the operator S_N is non-symmetric and in this case the Bi-Conjugate Gradient Stabilized (Bi-CGStab) method [58] is used. It is chosen over the also frequently used GMRES method [52], since it requires less storage. To overcome the problem of storage associated with the GMRES method, the iterations can be restarted after every m iterations. Choosing this parameter however is rather arbitrary, and by choosing it to be either too small or too large, the GMRES(m) method might not converge at all or may be very slow.

The PCG method

To solve the pressure equation (4.7), both the Uzawa operator $U = DH^{-1}D^T$ and the Helmholtz operator H need to be inverted. Since both operators are symmetric, the preconditioned conjugate gradient (PCG) method can be used, albeit in a nested structure (see Deville et al. [10], for example). The inversion of the Helmholtz operator is nested within the inversion of the Uzawa operator.

The standard PCG method for inversion of the problem $U\mathbf{p} = \mathbf{b}$, where U is the Uzawa operator, is given by the following steps

- Use an initial guess p_0 for the pressure to calculate the initial residual r_0,

  $$\mathbf{r}_0 = \mathbf{b} - U\mathbf{p}_0.$$

- Initialize the other PCGM variables,

  $$\begin{aligned} \mathbf{z}_0 &= P_U^{-1}\mathbf{r}_0, \\ \mathbf{q}_0 &= \mathbf{z}_0, \end{aligned}$$

  where P_U is the preconditioner for the Uzawa operator.

- The iteration to search for the correct solution vector $\mathbf{x}$ is,

  $$\begin{aligned} \alpha_n &= \frac{\mathbf{r}_{n-1}^T\mathbf{z}_{n-1}}{\mathbf{q}_{n-1}U\mathbf{q}_{n-1}}, \\ \mathbf{r}_n &= \mathbf{r}_{n-1} - \alpha_n U\mathbf{q}_{n-1}, \\ \mathbf{z}_n &= P^{-1}\mathbf{r}_n, \\ \beta_n &= \frac{\mathbf{r}_n^T\mathbf{z}_n}{\mathbf{r}_{n-1}^T\mathbf{z}_{n-1}}, \\ \mathbf{x}_n &= \mathbf{x}_{n-1} + \alpha_n\mathbf{q}_{n-1}, \\ \mathbf{q}_n &= \mathbf{z}_n + \beta_n\mathbf{q}_{n-1}, \end{aligned}$$

  which is repeated until a converged residual $\epsilon_U = \mathbf{r}_n^T\mathbf{z}_n$ is reached.

To calculate $U\mathbf{q}_{n-1}$ in every iteration, an inner PCGM iteration has to be performed to find H^{-1}, since $H^{-1}D^T\mathbf{q}_{n-1}$ is needed. The inner problem reads

$$U\mathbf{q}_{n-1} \rightarrow H^{-1}D^T\mathbf{q}_{n-1} = H^{-1}\tilde{\mathbf{b}} = \tilde{\mathbf{x}}. \tag{4.8}$$

To find the vector $\tilde{\mathbf{x}}$ a nested loop, identical to the one above, has to be called on. A second preconditioner P_H can be used in this process. Obviously, the Uzawa inversion can only converge if the convergence criterion for the Helmholtz inversion, ϵ_H, is smaller than the convergence criterion for the Uzawa operator, ϵ_U. We also found that this difference should increase with decreasing time step. As an empirical result, we suggest a Uzawa convergence criterion of ϵ_U requires a Helmholtz convergence criterion of $\epsilon_H < 10^{-3}\epsilon_U \cdot \Delta t$.

The Bi-CGStab method

The Bi-CGStab method is a stabilized version of the earlier Bi-Conjugate Gradient (Bi-CG) method and avoids the irregular convergence patterns associated with the Bi-CG method. The Bi-CGStab method is used in this thesis to invert the non-symmetric operator S_N that appears in the discretized form of the constitutive equations The steps in this method are given by

- Use an initial guess $\mathbf{x}_0$ for the stresses to calculate the initial residual r_0,

$$\mathbf{r}_0 = \mathbf{b} - A\mathbf{x}_0.$$

- Set $\tilde{\mathbf{r}} = \mathbf{r}_0$

- The iteration $n = 1, 2, ...$ to search for the correct solution vector $\mathbf{x}$ is,

```
$\rho_{n-1} = \tilde{\mathbf{r}}^T\mathbf{r}_{n-1}$        (method fails if $\rho_{n-1} = 0$)
if $n = 1$ then
    $\mathbf{q}_n = \mathbf{r}_{n-1}$
```

```
else
    $\beta_{n-1} = \frac{\rho_{n-1}}{\rho_{n-2}} \frac{\alpha_{n-1}}{\omega_{n-1}}$
    $\mathbf{q}_n = \mathbf{r}_{n-1} + \beta_{n-1}(\mathbf{q}_{n-1} - \omega_{n-1} A \hat{\mathbf{q}}_{n-1})$
endif
$\hat{\mathbf{q}}_n = P^{-1}\mathbf{q}_n$
$\alpha_n = \frac{\rho_{n-1}}{\tilde{\mathbf{r}}^T A \hat{\mathbf{q}}_n}$
$\mathbf{s} = \mathbf{r}_{n-1} - \alpha_n A \hat{\mathbf{q}}_n$
if norm of $\mathbf{s}$ is small enough set $\mathbf{x}_n = \mathbf{x}_{n-1} + \alpha_n \hat{\mathbf{q}}_n$ and stop
$\hat{\mathbf{s}} = P^{-1}\mathbf{s}$
$\omega_n = \frac{(A\hat{\mathbf{s}})^T \mathbf{s}}{(A\hat{\mathbf{s}})^T (A\hat{\mathbf{s}})}$
$\mathbf{x}_n = \mathbf{x}_{n-1} + \alpha_n \hat{\mathbf{q}}_n + \omega \hat{\mathbf{s}}$
$\mathbf{r}_n = \mathbf{s} - \omega_n A \hat{\mathbf{s}}$
```

which is repeated until a converged residual $\epsilon_S = \mathbf{r}_n^T \mathbf{z}_n$ is reached. P is a preconditioner.

4.4 Preconditioners

As shown in the previous section, preconditioners can be used to speed up the calculation. The idea is that a preconditioner is an operator very similar to the operator that needs to be inverted, but has a known inverse, or properties that make it relatively easy to invert. The preconditioners that have been used to invert each of the operators is given below. When the identity matrix is used as a preconditioner the PCG method simplifies to the normal Conjugate Gradient method. In later chapters the identity matrix will be used as a benchmark to determine the efficiency of the other preconditioners.

4.4.1 Preconditioners for the Helmholtz operator

Two preconditioners have been used to invert the Helmholtz operator. The first one is a so-called overlapping Schwarz preconditioner, the second one is a preconditioner based on the diagonals of the spectral element operators. Both will be described below.

The overlapping Schwarz preconditioner

The overlapping Schwarz preconditioner is based on the classical additive Schwarz method developed by Dryja and Widlund [12]. The preconditioner is based on solutions of similar local problems using finite element approximations on subdomains that overlap the spectral elements. In a problem with K spectral elements Ω_k, $k = 1, \ldots, K$, these subdomains $\tilde{\Omega}_k$ are the existing spectral elements extended by a constant number of Gauss-Lobatto Legendre nodes in each direction into adjacent elements as is shown in Fig. 4.3.

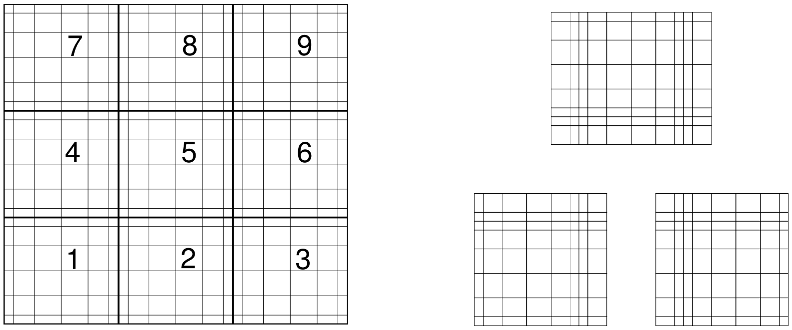

Figure 4.3: Spectral element mesh, with numbering of the elements, and the subdomains $\tilde{\Omega}_1$, $\tilde{\Omega}_3$ and $\tilde{\Omega}_8$ with an overlap consisting of two nodes on adjacent elements

The square mini-elements are then triangulated to constitute the local finite element mesh. The local finite element mesh on $\tilde{\Omega}_8$ for example, is given in Fig. 4.4.

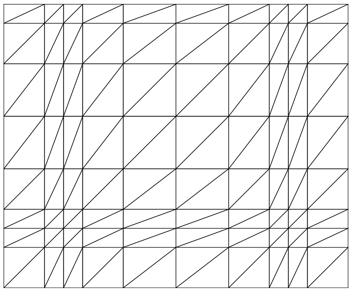

Figure 4.4: The local finite element mesh on $\tilde{\Omega}_8$.

Homogeneous Dirichlet conditions are assumed on the boundaries of these extended subdomains. To provide the global coupling in the preconditioner, the solution on one extra domain, known as the coarse grid, is needed. The coarse grid, also known as the skeleton spectral element grid, consists of the vertices of the spectral element mesh. The coarse grid is also triangulated and this means that every spectral element is divided into two finite elements. By adding up all contributions, the overlapping Schwarz preconditioner can be written as

$$P_H^{-1} = S_P^{-1} = R_0^T A_0^{-1} R_0 + \sum_{k=1}^{K} R_k^T A_k^{-1} R_k. \tag{4.9}$$

The different operators in the preconditioners will be discussed separately:

- The restriction operators R_k restricts a vector which has as many entries as there are global grid points to a vector with entries for every node on the element k including overlaps, i.e. the subdomain $\tilde{\Omega}_k$.

- The operators A_k are the finite element approximations of the Helmholtz operator, on each of the subdomains $\tilde{\Omega}_k$. Every finite element in this subdomain is a triangle defined by three GLL nodes. The mapping from the physical coordinates $\mathbf{x} = (x, y)$ to the computational coordinates $\boldsymbol{\xi} = (\xi, \eta)$ is given by

$$\mathbf{x}(\xi, \eta) = (1 - \xi - \eta)\mathbf{x}_1 + \xi \mathbf{x}_2 + \eta \mathbf{x}_3, \tag{4.10}$$

where the corners of the triangle are $\mathbf{x}_1$ to $\mathbf{x}_3$ and the triangle in computational space is defined by the corners $(\xi, \eta) = (0,0), (0,1), (1,0)$. The mapping also defines the test functions of the finite element discretization

$$\phi_1 = 1 - \xi - \eta, \qquad \phi_2 = \xi, \qquad \phi_3 = \eta. \tag{4.11}$$

The finite element mass matrix is a result of the discretization of the weak formulation of a source term of a variable $u(\mathbf{x})$, for example. The weak formulation of the source term in a finite element Ω_e is

$$\int_{\Omega_e} u(\mathbf{x})\phi_i(\mathbf{x})dxdy = \int_{D_e} u(\boldsymbol{\xi})\phi_i(\boldsymbol{\xi})|det(J)|d\xi d\eta, \tag{4.12}$$

where ϕ_i, $i = 1, 2, 3$, are the test functions defined in (4.11). The determinant of the Jacobian of the transformation $det(J)$ is constant for triangular elements. This means that the integrals leading to the finite element mass and stiffness operators can be evaluated exactly. This is the advantage of using triangles over quadrilaterals, for which either the Jacobian or the integrals for stiffness operator have to be approximated.

The finite element mass matrix M_k for the whole subdomain $\tilde{\Omega}_k$ is found by assembling all the contributions from the finite elements in the subdomain. The resulting matrix is found to be a banded tridiagonal matrix. In the same way, the stiffness matrix E_k is the finite element discretization of the weak formulation of the Laplacian acting on a variable.

The operator A_k can now be written as

$$A_k = \frac{Re}{\Delta t} M_k + \left(\beta + \frac{(1-\beta)}{C_l^n}\right) E_k. \tag{4.13}$$

- The prolongation operators R_k^T map the resulting vector with values on the subdomain back to the global vector, only taking account for the values on the element k, and disregarding the values on the overlap.

- When the above operations are performed for each of the subdomains $\tilde{\Omega}_k$, the coupling between the subdomains has to be provided by the coarse grid. The coarse grid operators are R_0, A_0 and R_0^T. The operator A_0 is the finite element operator (4.13) resulting from the finite element discretization of the coarse grid problem. The prolongation operator R_0^T interpolates the linear functions on the coarse mesh to values on every node in the spectral element mesh. The restriction matrix R_0 is its transpose.

Results obtained using this preconditioner will be presented in section 6.7 and 7.6.

Diagonals of spectral element matrices

Since the Helmholtz operator contains a mass matrix, a Laplace operator and a pseudo Laplacian, it makes sense to build a preconditioner based on these operators. Local to each element, the diagonals of the discrete mass matrix and the discrete Laplace operator are used to construct the following preconditioner

$$P_H = M_l C_N + \left(\beta + \frac{(1-\beta)}{C_l^n} \right) diag(E'_N), \tag{4.14}$$

where E'_N is the discrete local Laplacian. Results obtained using this preconditioner will be presented in section 7.6.

4.4.2 Preconditioners for the Uzawa operator

Five different types of preconditioner have been tested for the Uzawa operator. These are the pressure mass matrix, a preconditioner based on work by Cahouet and Chabard [6], a preconditioner based on the diagonal of spectral element operators, a preconditioner based on the full spectral element operators and a preconditioner based on finite element matrices. Details of these five preconditioners are given below

The pressure mass matrix

This is a very simple preconditioner. It is diagonal since it involves the spectral element mass matrix in pressure space, acting on the pressures. The preconditioner is given by $P_U = M_p$. Results obtained using this preconditioner will be presented in sections 6.7 and 7.6.

Cahouet and Chabard based preconditioner

This preconditioner is given by

$$P_U^{-1} = C_P^{-1} = (\frac{(1-\beta)}{C_l} + \beta)M_p^{-1} + M_l(DC^{-1}D^T)^{-1}. \tag{4.15}$$

The preconditioner that was developed by Cahouet and Chabard [6] is based on the operator identity

$$-\nabla \cdot (a\mathbf{I} - b\nabla^2)^{-1}\nabla = (b\mathbf{I} - a(\nabla^2)^{-1})^{-1}, \tag{4.16}$$

where $\nabla \cdot (\frac{Re}{\Delta t}\mathbf{I} - \nabla^2)^{-1}\nabla$ arises from the continuous Navier-Stokes equations. The preconditioner was constructed so that it matches the asymptotic behaviour of the Uzawa operator in the steady Stokes and high Reynolds number limits. The appropriate preconditioner is

$$P_U^{-1} = M_p^{-1} + \frac{Re}{\Delta t}(DC^{-1}D^T)^{-1} \tag{4.17}$$

Escriva et al. [13] adopted this strategy for viscoelastic problems. Since the factors a and b in (4.16) were found to be

$$a = \frac{Re}{\Delta t}, \quad \text{and} \qquad b = \beta + \frac{1-\beta}{\frac{We}{\Delta t}+1}, \tag{4.18}$$

the following preconditioner was proposed

$$P_U^{-1} = \left(\beta + \frac{1-\beta}{\frac{We}{\Delta t}+1}\right) M_p^{-1} + \frac{Re}{\Delta t}(DC^{-1}D^T)^{-1} \tag{4.19}$$

This preconditioner may be effective in terms of reduction of numbers of iterations. However, to calculate the preconditioner itself, a further PCG iteration has to be used to invert the pseudo Laplacian $DC^{-1}D^T$, which in itself is very time consuming. Some results obtained using this preconditioner are given in section 6.7.

Diagonals of spectral element matrices

The preconditioner for the Uzawa operator that is used in combination with the XPP model, is similar to those based on the Cahouet and Chabard preconditioner. It is constructed to be a linear combination of the pressure mass matrix and the Laplacian in pressure space. These operators need to be multiplied by appropriate factors for the preconditioner to be efficient. The preconditioner is given by

$$P_U^{-1} = (\frac{(1-\beta)}{C_l} + \beta)M_p^{-1} + M_l diag(E_N^p)^{-1}, \tag{4.20}$$

where M_p is the pressure mass matrix and E_N^p is the discrete local Laplacian in pressure space. The efficiency of this preconditioner in comparison to others will be presented in section 7.6.

Full spectral element matrices

Instead of using only the diagonal of the Laplacian in pressure space, the full Laplacian can be used as well. It is stored in an LU-decomposition, and inverted when needed in the iterative methods. This preconditioner has been found to work very well when the uncoupled method is used. It reads

$$P_U = \frac{M_p}{\beta} + M_l E_N^p. \tag{4.21}$$

Some results obtained using this preconditioner will be presented in section 7.6.

Finite element matrices

The nodes in the finite element mesh used for this preconditioner are the inner GLL nodes of an element Ω_k used for the spectral pressure approximation. Again the mesh is triangulated, but no overlap to other elements is included. The preconditioner is based on the finite element mass and stiffness matrices on these local finite element problems, M_k^{FE} and E_k^{FE}, respectively. It reads

$$P_U^{-1} = \sum_{k=1}^{K} R_k^T \left(\frac{M_k^{FE}}{\beta} + M_l E_k^{FE} \right)^{-1} R_k. \tag{4.22}$$

The restriction operators R_k now maps a global vector to a vector with the size of the number the inner GLL nodes of an element Ω_k. The preconditioner is stored in an LU-decomposition, and inverted when needed in the iterative methods. Some results obtained using this preconditioner will be presented in section 7.6.

4.4.3 Preconditioners for the non-symmetric operator

The non-symmetric operator S_N appears in the discretized constitutive equation (3.72) when the equations are solved uncoupled. In the Bi-CGStab inversion, the stress mass matrix A_N is used as a very simple, yet very efficient preconditioner for this operator, as will be shown in section 7.6.

4.5 The Schur Complement Method

The Schur complement method can be used to decrease the size of the Helmholtz problem that needs to be solved iteratively. The problem is split up into two parts. The first part involves finding the solution vector corresponding to only the nodes on the element boundaries. In the second part the solution vector on all internal element nodes are easily calculated from the solution on the boundaries. To achieve this the Helmholtz operator is arranged using a convenient node numbering as described in section 4.2.

A visual matrix representation of the rearranged Helmholtz operator is shown in Fig. 4.5. The Helmholtz matrix consists of four blocks. The block H_{BB} is a banded matrix in which only the contributions of the influence of the nodes on the boundary of the elements on other boundary nodes are accounted for. The block H_{II} is the part of the Helmholtz operator containing the influence of inner element nodes on one another. Since this influence is restricted to only the element itself, the block H_{II} has a block structure, and these sub-blocks themselved are banded, allowing for quick solution using simple Gaussian elimination. All these sub-blocks are stored in an LU decomposition to speed up this process. Since the Helmholtz operator is symmetric, the blocks H_{BI} and H_{IB} obey $H_{BI} = H_{IB}^T$. These two blocks also consist of sub-blocks in which the influence of inner nodes on boundary nodes and vice versa is represented.

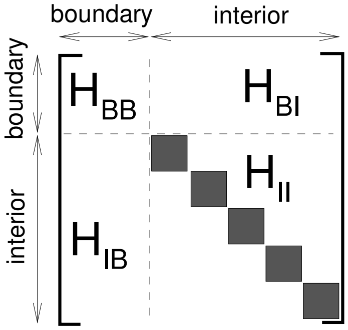

Figure 4.5: A visual matrix representation of the rearranged Helmholtz operator.

The Helmholtz problem $H\mathbf{x} = \mathbf{b}$ can be written as

$$\begin{pmatrix} H_{BB} & H_{BI} \\ H_{IB} & H_{II} \end{pmatrix} \begin{pmatrix} \mathbf{x}_B \\ \mathbf{x}_I \end{pmatrix} = \begin{pmatrix} \mathbf{b}_B \\ \mathbf{b}_I \end{pmatrix}, \tag{4.23}$$

where the subscript B refers to degrees of freedom on the element boundaries, and the subscript I refers to degrees of freedom internal to the spectral elements. The problem can also be written as

$$\begin{pmatrix} H_{BB} - H_{BI} H_{II}^{-1} H_{BI}^T & 0 \\ H_{IB} & H_{II} \end{pmatrix} \begin{pmatrix} \mathbf{x}_B \\ \mathbf{x}_I \end{pmatrix} = \begin{pmatrix} \mathbf{b}_B - H_{BI} H_{II}^{-1} \mathbf{b}_I \\ \mathbf{b}_I \end{pmatrix}. \tag{4.24}$$

The matrix $H_{BB} - H_{BI}H_{II}^{-1}H_{BI}^{T}$ is known as the Schur complement of the Helmholtz operator and will be denoted as S_H. The result of the rearrangement is that instead of having to solve the full Helmholtz problem, the problem is reduced to one whose the size is equal to the number of degrees of freedom on the boundaries of the elements, i.e.

$$S_H \mathbf{x}_B = \mathbf{b}_B - H_{BI}H_{II}^{-1}\mathbf{b}_I. \tag{4.25}$$

After calculation of the solution on the boundaries, the solution inside the elements is found by solving once

$$\mathbf{x}_I = H_{II}^{-1}\left(\mathbf{b}_I - H_{BI}^{T}\mathbf{x}_B\right). \tag{4.26}$$

The Schur method is implemented so that is can be used within the PCG method. If the Schur complement matrix is statically condensed however, it constitutes a relatively small problem. For this reason the Schur complement may also be stored as an LU decomposition which can be inverted when needed. This LU decomposition is used as a preconditioner in the PCG method. Obviously the PCG method then takes only one iteration to converge. Although this compromises the use of storage it constitutes the most efficient algorithm in this thesis, as will be shown in section 7.6.

4.6 The Zero Volume of Pressure Condition

Since the Uzawa operator is only positive *semi*-definite, problems arise when trying to reach convergence in the PCG method when a tolerance of less than 10^{-14} is prescribed. The tolerance becomes harder to attain with increasing Weissenberg number. The indefiniteness of the Uzawa operator can be removed by adding the domain integral of the pressure to the right-hand side of the continuity equation. The Uzawa operator for the modified problem is then positive definite. This modification of the continuity equation ensures that the pressure approximation has a zero mean value.

The zero volume of pressure condition enforces the continuity constraint to be satisfied at all iterations within the PCG iteration. This is done by replacing the continuity equation by

$$\nabla \cdot \mathbf{u} = -\alpha \int_{\Omega} p d\Omega, \tag{4.27}$$

where α is a positive constant. Integrating this equation over Ω and using Green's theorem, one can show that

$$\int_{\Omega} p d\Omega = 0. \tag{4.28}$$

So this formulation will automatically ensure that $p \in L_0^2(\Omega)$, as well as leading to a better conditioned problem in the sense that the condition number of the discrete Uzawa operator is lower than that for the original formulation for a range of values of α. In evaluating the right-hand side of (4.27) the pressure is integrated over all elements Ω in the computational domain. After discretization of the integral, the modified discrete continuity equation is

$$D_N \mathbf{u}_N = -\alpha Q_N \mathbf{p}_N, \tag{4.29}$$

where Q_N is a matrix of rank one. This equation replaces the discretized continuity equation. The pressure equation (4.7) will now be of the form

$$(U_N + \alpha Q_N)\mathbf{p}_N = \mathbf{b}_N. \tag{4.30}$$

The efficiency of the algorithm has been tested for different values of α, for the channel flow problem described in Section 6.7. The only difference is that the convergence criterion for the outer PCG iteration to invert the Uzawa operator is set to 10^{-20} and the convergence criterion for the inner PCG iteration to invert the Helmholtz operator is set to 10^{-24}.

Table 4.1 and Fig. 4.6 show that there is an optimum value of α, for the efficiency of the Uzawa inversion, although the algorithm behaves well for a wide range of values

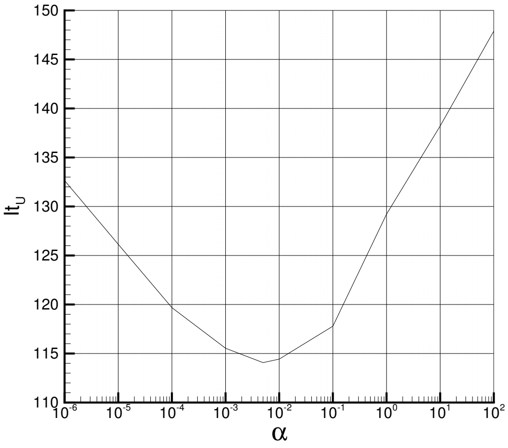

Figure 4.6: Average number of iterations in the Uzawa inversion within one time-step as a function of α.

Table 4.1: Average number of iterations in the Uzawa inversion within one time-step for different values of α.

α	10^{-6}	10^{-4}	10^{-3}	$5 \cdot 10^{-3}$	10^{-2}	10^{-1}	10^{0}	10^{2}
It_U	132.64	119.68	115.54	114.07	114.43	117.79	129.21	147.89

of α. The optimum value of α may vary when either the problem or the convergence criteria are changed.

4.7 The Locally Upwinded Spectral Technique

In the coupled equations the spaces in which the velocity and the stress are approximated have to obey a compatibility condition. This condition ensures that the divergence operator acting on the stresses in velocity space, is the transpose of the gradient operator acting on the velocities in stress space. Without this compatibility substitution of the constitutive into the momentum equation on a discrete level would not be possible. In the uncoupled equations however, this substitution is not performed, and the choice of stress space is free. This allows for application of upwinding methods such as SUPG.

Both SUPG and the Locally Upwinded Spectral Technique (LUST) developed by Owens et al. [39] will be used. Both are based on the addition of an upwinding term to the test function for the stress.

In the original weak formulation (3.32) the test function in the constitutive equation is $\boldsymbol{\sigma}$. The modified test function including the upwinding factor reads $\boldsymbol{\sigma} - h\mathbf{u} \cdot \nabla\boldsymbol{\sigma}$. The difference between SUPG and LUST lies in different calculation of the shift factors h. In SUPG this is a global quantity and for spectral element methods it is common to use $h = 1/N^2$, where N is the order of the approximating polynomials.

The shift factors in LUST are calculated by considering mini-elements formed by four GLL nodes inside a spectral element. Let $\mathbf{x}_{ij}$ be one of the four corners in a mini-element. For $We \neq 0$ a coordinate $\mathbf{z}_{ij} = \mathbf{x}_{ij} - h_{ij}\mathbf{u}(\mathbf{x}_{ij})$ lies inside the mini-element at the place where the function

$$P_{N+1}(\mathbf{x}) = (1-\xi^2)L'_N(\xi)(1-\eta^2)L'_N(\eta), \tag{4.31}$$

has a streamline derivative that satisfies

$$P_{N+1}(\mathbf{z}_{ij}) + We(\mathbf{u} \cdot \nabla)P_{N+1}(\mathbf{z}_{ij}) = 0. \tag{4.32}$$

By expanding this as a Taylor series about $\mathbf{x}_{ij}$ an expression is found from which the shift factors can be calculated. The expression reads

$$\begin{aligned}P_{N+1}(\mathbf{x}) - h_{ij}(\mathbf{u}\cdot\nabla)P_{N+1}(\mathbf{x}) + \frac{h_{ij}^2}{2}(\mathbf{u}\cdot\nabla)^2P_{N+1}(\mathbf{x}) - \frac{h_{ij}^3}{3!}(\mathbf{u}\cdot\nabla)^3P_{N+1}(\mathbf{x}) + ...\\ +We\Bigg((\mathbf{u}\cdot\nabla)P_{N+1}(\mathbf{x}) - h_{ij}(\mathbf{u}\cdot\nabla)^2P_{N+1}(\mathbf{x}) + \frac{h_{ij}^2}{2}(\mathbf{u}\cdot\nabla)^3P_{N+1}(\mathbf{x}) -\\ \frac{h_{ij}^3}{3!}(\mathbf{u}\cdot\nabla)^4P_{N+1}(\mathbf{x}) + ...\Bigg) = 0.\end{aligned} \tag{4.33}$$

In appendix E the derivation of the shift factors from this expression is presented. It is found that for internal nodes the shift factor is the positive root of the quadratic equation

$$\frac{2WeN(N+1)}{3}\left(\frac{u_{ij}^2}{1-\xi^2} + \frac{v_{ij}^2}{1-\eta^2}\right)h_{ij}^2 + h_{ij} - 2We = 0. \tag{4.34}$$

The calculation of the shift factors on the edges of the elements can also be found in appendix E.

Since the upwinding schemes only change the space that the stresses are approximated in, the discrete equations in operator notation as presented in 3.71 do not change. The operators themselves are, of course, different for the standard Galerkin formulation and for the upwinding methods. In appendix F part of the discretization of the convective term $\mathbf{u}\cdot\nabla\boldsymbol{\tau}$ is written out to show this difference.

Chapter 5

Newtonian Computations

5.1 Introduction

As a precursor to the solution of non-Newtonian fluid models, the Stokes and Navier-Stokes equations are solved to show the validity of the code. For some problems analytical results can be found that satisfy the Stokes equations, and therefore the Stokes equations are often used to show mesh convergence of numerical approximations to a known exact solution, as is shown in section 5.2. Moreover, the Stokes equations can be solved very cheaply, since no time stepping is required in the solution process. This means that it is possible to find either very accurate results, i.e. on very fine meshes, or results for problems that would simply be too large to solve with other models. Some accurate solutions and solutions to large problems are presented in section 5.3. When new ideas are implemented into numerical schemes, it is often best to test them on the Stokes equations first. When proven to work in the Stokes case, they can be extended to non-Newtonian fluid models. The modified Lagrange polynomial presented in section 3.6 is such an idea that is applied first to Stokes flow. The results are presented in section 5.4. The results of a study into the dependence of drag on cylinders and spheres in confined flow, for the Navier-Stokes equations, are presented in section 5.5.

5.2 Mesh Convergence

Convergence of the spectral element method with increasing number of elements and increasing approximating polynomial order will be shown. The problem is the same as the one considered by Gerritsma and Phillips [17]. On the domain $\Omega = (-1,1)\times(-1,1)$, we solve the three-field Stokes problem

$$\nabla\cdot\mathbf{u} = 0, \tag{5.1}$$

$$\nabla p = \nabla\cdot\mathbf{T}+\mathbf{f}, \tag{5.2}$$

$$\mathbf{T} = 2\mathbf{d}, \tag{5.3}$$

subject to prescribed velocity boundary conditions on $\partial\Omega$, for which the exact solution is given by

$$p = \sin\pi x\sin\pi y, \tag{5.4}$$

$$\mathbf{u}^T = (-\sin 2\pi x\cos 2\pi y, \cos 2\pi x\sin 2\pi y). \tag{5.5}$$

The extra-stress solution follows by inserting (5.5) into (5.3). This exact solution satisfies the Stokes problem in the presence of a body force $\mathbf{f}$ which is given by

$$\mathbf{f} = \begin{pmatrix}\pi\cos\pi x\sin\pi y - 8\pi^2\sin 2\pi x\cos 2\pi y\\ \pi\sin\pi x\cos\pi y + 8\pi^2\cos 2\pi x\sin 2\pi y\end{pmatrix}. \tag{5.6}$$

The problem is tested for both $K = 1$ and $K = 4$ equally sized elements, allowing the polynomial order N to vary. We denote by $E(\phi)$ the L^2-norm of the error in the spectral element approximation of ϕ, i.e. $\|\phi-\phi_N\|_2$. The errors are given in Tables 5.1 and 5.2 for $K = 1$ and $K = 4$, respectively. As displayed in Fig. 5.1, exponential convergence for all variables is found for this smooth problem. The errors reach machine precision for modest values of N. Note that the performance is comparable to that obtained in [17].

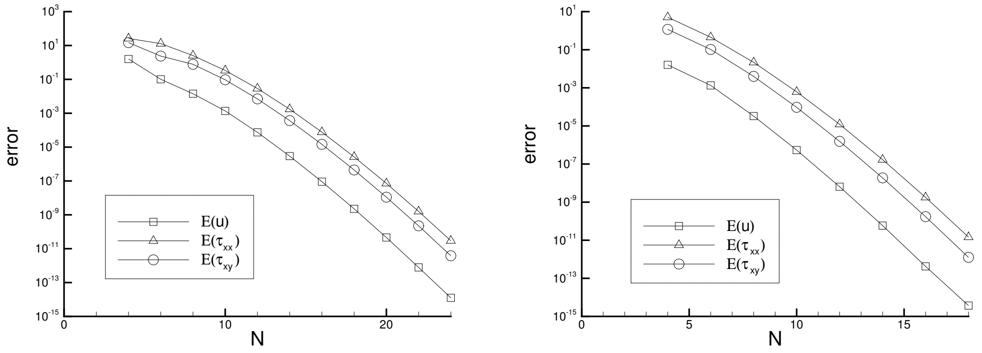

Figure 5.1: Convergence of the L^2 norms of the error in u, τ_{xx} and τ_{xy} with spectral refinement for $K = 1$ (left) and $K = 4$ (right).

Table 5.1: Convergence of the errors in u, τ_{xx} and τ_{xy}, with increasing approximation order N, for $K = 1$.

N	$E(u)$	$E(\tau_{xx})$	$E(\tau_{xy})$
4	$1.593E+00$	$2.608E+01$	$1.483E+01$
6	$1.012E-01$	$1.296E+01$	$2.377E+00$
8	$1.423E-02$	$2.547E+00$	$7.788E-01$
10	$1.368E-03$	$3.356E-01$	$9.466E-02$
12	$7.421E-05$	$2.886E-02$	$7.006E-03$
14	$2.941E-06$	$1.732E-03$	$3.680E-04$
16	$9.086E-08$	$7.687E-05$	$1.451E-05$
18	$2.253E-09$	$2.633E-06$	$4.461E-07$
20	$4.590E-11$	$7.177E-08$	$1.102E-08$
22	$7.829E-13$	$1.596E-09$	$2.240E-10$
24	$1.256E-14$	$2.948E-11$	$3.808E-12$

5.3 Stokes Flow

In this thesis the flow of different types of fluid will be considered in three different geometries. The first is flow through a planar channel, giving rise to what is known as Poiseuille flow. The second is the flow past a cylinder. Finally, we consider flow through a contraction-expansion geometry. The last two are examples of

Table 5.2: Convergence of the errors in u, τ_{xx} and τ_{xy}, with increasing approximation order N, for $K = 4$.

N	$E(u)$	$E(\tau_{xx})$	$E(\tau_{xy})$
4	$1.616E-02$	$5.093E+00$	$1.173E+00$
6	$1.342E-03$	$4.532E-01$	$1.036E-01$
8	$3.290E-05$	$2.173E-02$	$3.984E-03$
10	$5.390E-07$	$6.192E-04$	$9.475E-05$
12	$6.428E-09$	$1.218E-05$	$1.553E-06$
14	$5.866E-11$	$1.695E-07$	$1.868E-08$
16	$4.242E-13$	$1.778E-09$	$1.723E-10$
18	$3.706E-15$	$1.455E-11$	$1.256E-12$

complex flows. All three problems are symmetric, and therefore only the half domain needs to be solved. In Cartesian coordinates (x, y), the plane of symmetry will be assumed on $y = 0$. In the cylindrical polar coordinate system (r, θ, z), the line $r = 0$ represents the axis of symmetry, the coordinate z is in axial direction, and θ is the azimuthal coordinate. The three geometries together with characteristic length scales are shown in Fig. 5.2. Note that in the cylinder problem there is a discontinuity in the boundary conditions at the intersection of the symmetry plane with the cylinder. This discontinuity is not present in the contraction expansion problem.

In these geometries the steady three-field Stokes problem is solved in the Cartesian coordinate system. The equations read

$$\begin{aligned} \nabla \cdot \mathbf{u} &= 0, && (5.7) \\ \nabla p &= \nabla \cdot \mathbf{T} + \mathbf{f}, && (5.8) \\ \mathbf{T} &= 2\mathbf{d}, && (5.9) \end{aligned}$$

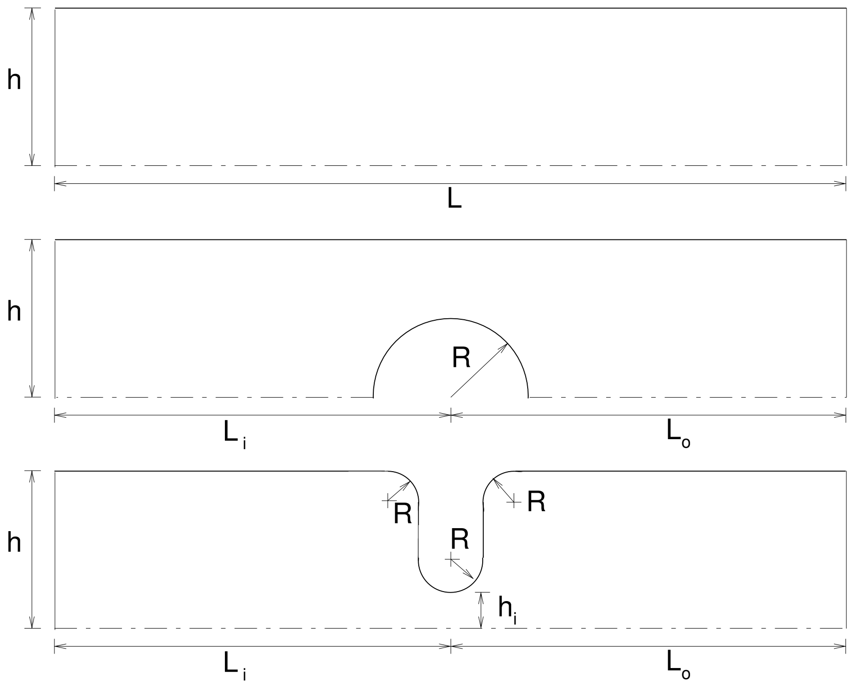

Figure 5.2: The geometry of the channel flow, flow past a cylinder or sphere and flow through a contraction-expansion.

and are subject to the Cartesian boundary conditions

$$u = 0, \quad v = 0 \qquad \text{on all solid walls,} \tag{5.10}$$

$$u = u_c\left(1 - (y/h)^2\right), \quad v = 0 \qquad \text{at inflow and outflow,} \tag{5.11}$$

$$\frac{\partial u}{\partial y} = 0, \quad v = 0 \qquad \text{on the plane of symmetry,} \tag{5.12}$$

where u_c is the velocity on the plane of symmetry. The solution of the channel flow problem can be calculated exactly and it is given in Cartesian coordinates by

$$p = C - \frac{2u_c}{h^2}x, \qquad \mathbf{u} = \begin{pmatrix} u_c\left(1 - (y/h)^2\right) \\ 0 \end{pmatrix}, \qquad \boldsymbol{\tau} = \begin{pmatrix} 0 & -\frac{2u_c}{h^2}y \\ -\frac{2u_c}{h^2}y & 0 \end{pmatrix}, \tag{5.13}$$

where C is an arbitrary constant.

The cylinder problem is characterized by a channel half-width of $h = 2$, and the ratio of the radius of the cylinder to the half width of the channel is $R/h = 0.5$. The inflow and outflow lengths are both taken as $L_i = L_o = 25$. The solution is computed using the mesh shown in Fig. 5.3. There are $K = 20$ elements and the degree of the spectral approximation is $N = 7$.

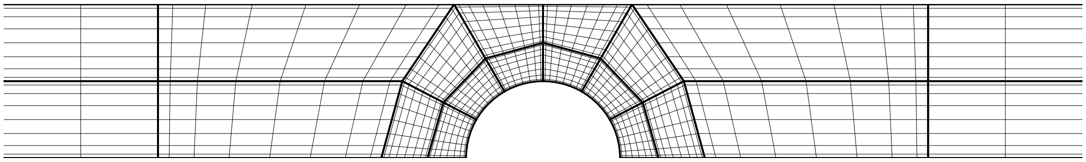

Figure 5.3: Spectral element mesh for the cylinder problem, with the spectral elements printed bold.

The non-dimensional drag on the cylinder is computed using the expression

$$F = 2\int_0^{\pi} \left\{ (-p + 2\beta\frac{\partial u}{\partial x} + \tau_{xx})\cos\theta + (\beta(\frac{\partial v}{\partial x} + \frac{\partial u}{\partial y}) + \tau_{xy})\sin\theta \right\} d\theta, \qquad (5.14)$$

where F has been made dimensionless with $\mu_t U$. Fig. 5.4 shows the convergence of the drag with increasing mesh resolution. The error E in computing the drag is calculated relative to an approximation obtained on a fine mesh ($N = 15$), i.e. $E = |F_{N=15} - F_N|$. The total number of GLL nodes on the spectral element mesh is with $N = 15$ is 4737. The value of the drag in the Navier-Stokes problem is compared to a result generated by Hulsen et al. [24] on a finite element mesh with 16737 nodal points. For a Reynolds number of $Re = 0.01$, they found the drag to be $F = 132.3584$, which compares favourably against our value of $F = 132.3507$.

The contraction expansion geometry is characterized by a contraction ratio $h/h_i = 4$, and the radius of the rounded corners at the contraction expansion is $R = h/8$. The inflow and outflow lengths are $L_i = L_o = 20$. The mesh given in Fig. 5.5 has $K = 30$ elements and an approximation order $N = 8$.

Figs. 5.6 show contour plots of pressure, velocities, stresses and streamfunction

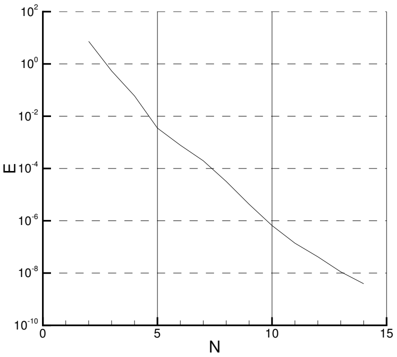

Figure 5.4: Convergence of the error in the drag, relative to the drag at $N = 15$, with increasing order of approximation N.

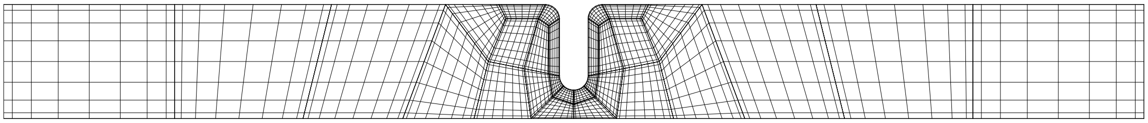

Figure 5.5: Spectral element mesh for the contraction expansion problem, with the spectral elements printed bold.

around the contraction-expansion. A polynomial order of $N = 8$ is used to find these results, but they are interpolated to a finer mesh with $N_f = 20$.

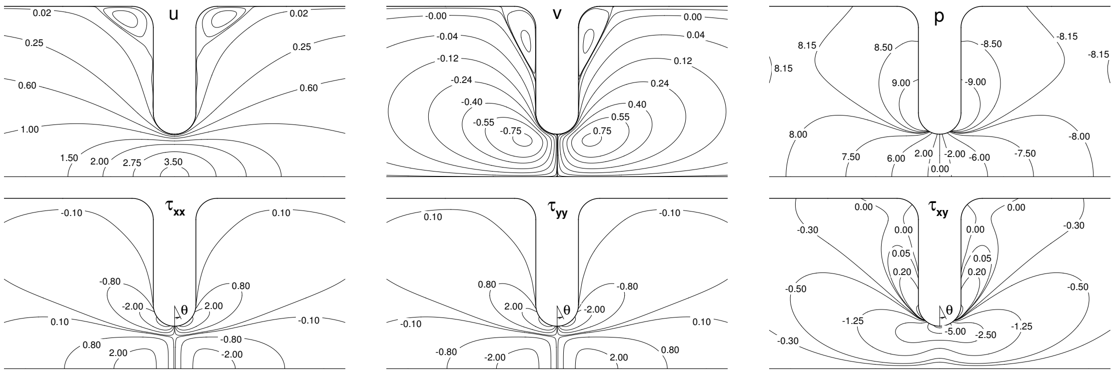

Figure 5.6: Contour plots of the velocities, pressure and stresses for the contraction expansion problem. The angle θ is defined in the plots of the stresses.

Maxima and minima of the stresses occur at the rounded contraction. The semi-circle that describes the geometry of this contraction is characterized using the angle θ that is defined in the contour plots of the stresses in Fig. 5.6. Using this coordinate, the stresses are plotted along the semi-circle, see Fig. 5.7

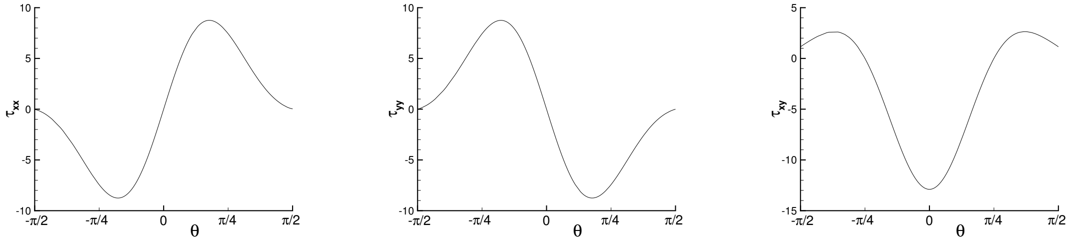

Figure 5.7: The components of the stress as a function of θ plotted around the semi-circular contraction.

The flow rate for this contraction expansion problem is 8/3. So if we let the streamfunction be zero on the upper wall, then the streamfunction will be $\Psi = 8/3$ at the axis of symmetry. The only negative values of the streamfunction occur in the recirculation areas in the salient corners of the geometries. A contour plot of the stream function Ψ is shown in Fig. 5.8.

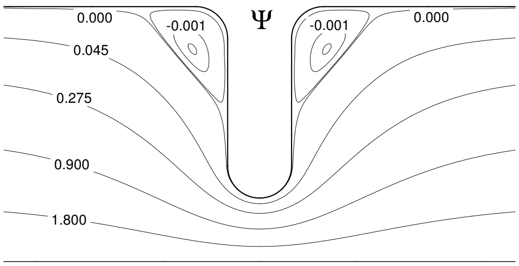

Figure 5.8: Contour plots of the stream function Ψ around the contraction expansion

Mesh convergence is demonstrated by monitoring the minimum value of the streamfunction. On the finest mesh with $N = 12$, the minimum value is $\Psi_m = -1.947 \cdot 10^{-3}$. Relative to this the error on coarser meshes is computed as $E = |\Psi_m^{N=12} - \Psi_m^N|$. The convergence plot is shown in Fig. 5.9.

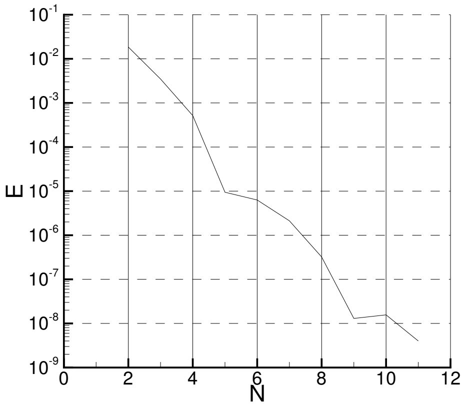

Figure 5.9: Mesh convergence of the error $E = |\Psi_m^{N=12} - \Psi_m^N|$ in the stream function.

5.4 The Modified Lagrange Interpolant

To answer the question if the smaller discrete problem outweighs the disadvantage of having to calculate the extra terms in the discrete operators, we test the efficiency of the modified interpolant compared to the original interpolant by solving flow past a cylinder in a channel, and the equivalent axisymmetric problem, the flow past a sphere in a tube. The mesh is presented in Fig. 5.10. The ratio of the channel height to the radius of the cylinder or sphere is $h/R = 2$, inflow and outflow lengths are $5R$.

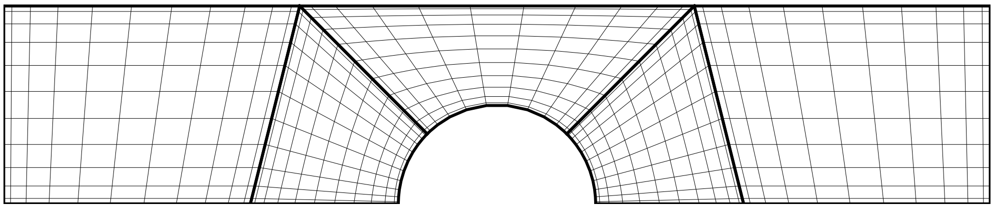

Figure 5.10: Spectral element mesh for flow past a cylinder in a channel with $K = 5$ and $N = 11$.

By monitoring the drag on the cylinder and sphere, we are able to demonstrate mesh convergence and to comment on the accuracy of both methods.

In Tables 5.3 and 5.4 the number of iterations needed to invert the Uzawa operator arising in the discrete problem, is given for an increasing order of approximation. The Helmholtz operator needs to be inverted in every single iteration of the Uzawa inversion. The average number of iterations of the Helmholtz operator is also given. Obviously, the number of Uzawa inversions times the average number of Helmholtz is a measure of the efficiency of the methods. The total time for the inversion of the Uzawa operator is also given. The calculations are performed on a Linux PC, Pentium 4 (2.4GHz, 512kB) with 256 MB internal memory.

Table 5.3: Number of iterations and time needed to invert operators for the cylinder problem, using the original and modified interpolants.

N	Uzawa iterations		Helmholtz iterations		Time(s) for one Uzawa inversion	
	Original	Modified	Original	Modified	Original	Modified
6	50	50	106.46	95.22	0.043	0.046
7	67	67	129.54	116.78	0.074	0.081
8	81	80	156.10	143.81	0.135	0.154
9	96	95	182.16	168.18	0.217	0.252
10	111	107	214.01	200.79	0.341	0.402
11	132	130	240.28	225.19	0.510	0.597
12	147	144	277.23	259.89	0.764	0.906

From these tables it can be concluded that the modified interpolant is a more efficient way of solving problems that include an axis of symmetry. The number of Uzawa iterations remains the same since the problem is still the same size on the pressure grid, which only comprises the internal nodes of the spectral elements. The Helmholtz operator however is smaller, and this is reflected in a lower number of iterations needed for the inversion. Although the total number of iterations is always

Table 5.4: Number of iterations and time needed to invert operators for the sphere problem, using the original and modified interpolants.

N	Uzawa iterations		Helmholtz iterations		Time(s) for one Uzawa inversion	
	Original	Modified	Original	Modified	Original	Modified
6	101	103	288.75	163.77	0.100	0.068
7	164	163	382.47	215.60	0.183	0.127
8	239	239	474.25	270.55	0.332	0.239
9	320	318	572.11	329.92	0.548	0.401
10	405	405	682.64	397.87	0.844	0.632
11	542	541	775.53	458.48	1.258	0.956
12	678	679	884.52	533.37	1.858	1.470

lower for the modified interpolant, the calculation time shows that the method is not efficient for Cartesian problems with a plane of symmetry rather than an axis of symmetry. This may be explained by the fact that for Cartesian problems, there are no zero-rows and columns in the discrete operators, as is the case in axisymmetric problems. This reflects the fact that the modified interpolant increases the well-posedness of the discrete system of equations for axisymmetric problems, but not neccesarily for Cartesian problems. With increasing polynomial order, the difference in efficiency appears to decrease. This is, of course, because a smaller percentage of the total number of nodes is located on the axis of symmetry.

Table 5.5 shows the drag on the cylinder and sphere with mesh refinement. The value of the drag for the cylinder on the finest mesh ($N = 12$) is 132.3575 calculated with the original interpolant or 132.3576 using the modified interpolant. These values compare to the value of 132.3584 found by Hulsen et al. [24] and a value of 132.3507, found by Van Os and Phillips [59] on a different mesh. Apart from mesh convergence

Table 5.5: Calculated drag on cylinder with increasing mesh size, for the original and the modified interpolant.

N	Cylinder drag		Sphere drag	
	Original	Modified	Original	Modified
6	132.221547	132.222540	44.9665300	44.9667043
7	132.409436	132.410144	45.0168664	45.0170450
8	132.357527	132.358018	44.9743815	44.9745025
9	132.362405	132.362749	44.9665990	44.9666721
10	132.359743	132.360001	44.9614268	44.9614748
11	132.358194	132.358392	44.9591513	44.9591860
12	132.357463	132.357620	44.9582976	44.9583229

the table also shows that both interpolants appear to converge to the same value for drag. The mesh convergence of the drag on cylinder and sphere is also shown in Fig. 5.11, for both interpolants. From Table 5.5 is may also be concluded that the values of the drag, computed using the different interpolants, converge towards the same value with mesh refinement. This can also be seen in Fig. 5.12 in which the convergence of the difference between the computed values for drag using both interpolants is depicted for both the cylinder and sphere problems.

5.5 Navier-Stokes Equations

The solution of the Navier-Stokes equations will be presented for two problems: plane Poiseuille channel flow and flow past a cylinder that is asymmetrically positioned in a channel. Boundary conditions for these problems are either given by steady state solutions, or by transient start-up of the flow.

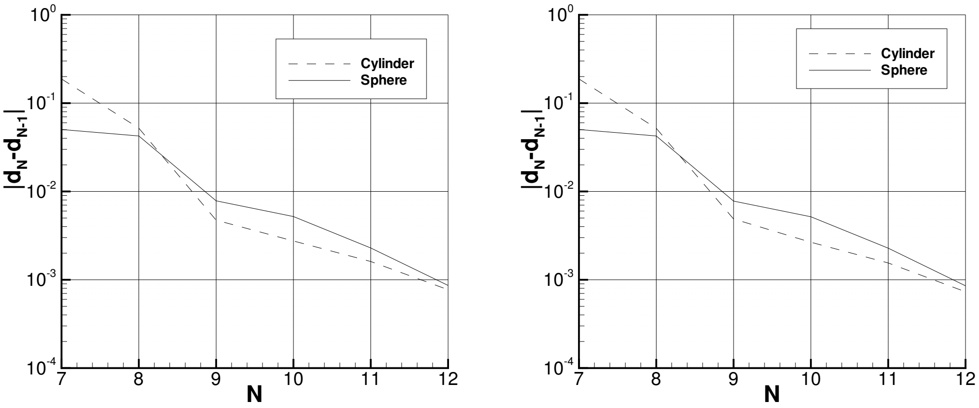

Figure 5.11: Convergence of the drag with mesh refinement for the original interpolant (left) and the modified interpolant(right).

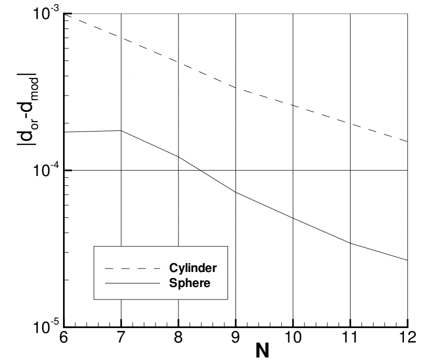

Figure 5.12: Convergence to the same value of drag, computed with the original and modified interpolants.

The steady conditions consist of no-slip conditions on all non-penetratable walls and a parabolic velocity profile on the inflow and outflow of the channel. Inside the domain, all initial conditions are set to zero.

Transient boundary conditions comprise zero initial conditions, with no-slip boundary conditions on all walls. The flow is driven by imposing a constant pressure gradient $\partial p/\partial x$. This induces developing velocity and stress profiles in time. This developing start-up of the channel flow is calculated by solving a 1D problem. The solutions to these 1D problems can be used as transient boundary conditions for the 2D domain.

When steady boundary conditions are used, there is no physical interpretation possible for the way the flow reaches steady state. By using transient start-up boundary conditions, however, the flow may be seen as transient flow behaviour after a pump induces a certain pressure difference that drives the flow.

5.5.1 1D calculations

The Navier-Stokes equations for the start-up of Poiseuille flow in the x-direction can be found by neglecting all derivatives of velocity and stress with respect to x, and by setting the cross-stream velocity, v, to zero. The equations then read

$$Re\frac{\partial u}{\partial t} = -\frac{\partial p}{\partial x} + \frac{\partial T_{xy}}{\partial y}, \tag{5.15}$$

$$T_{xy} = \frac{\partial u}{\partial y}. \tag{5.16}$$

When the pressure gradient $\partial p/\partial x$ is given, the start-up of the channel flow to the fully developed parabolic profile can be calculated.

The transient start-up has been calculated for a channel with walls at $y = 0$ and $y = 1$, and a given pressure gradient of $\partial p/\partial x = -8$, for a Reynolds number $Re = 1$. Two equally sized elements are used in the cross-stream direction, with an approximation order $N = 10$. The value of the time step is $\Delta t = 10^{-3}$.

The development of the velocity and the shear stress profiles is shown in Figs. 5.13 and 5.14, respectively. Note that at intermediate times, the velocity profile is not parabolic, and the shear stress is not a straight line. This confirms the need for a high-order approximation for the transient problem.

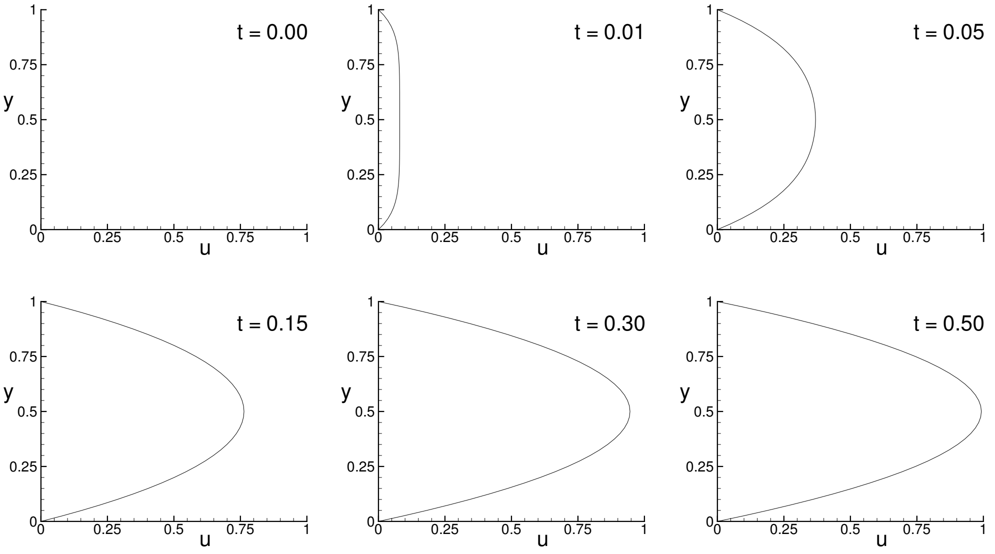

Figure 5.13: Velocity profile at intermediate time levels for the start-up of channel flow, $Re = 1$.

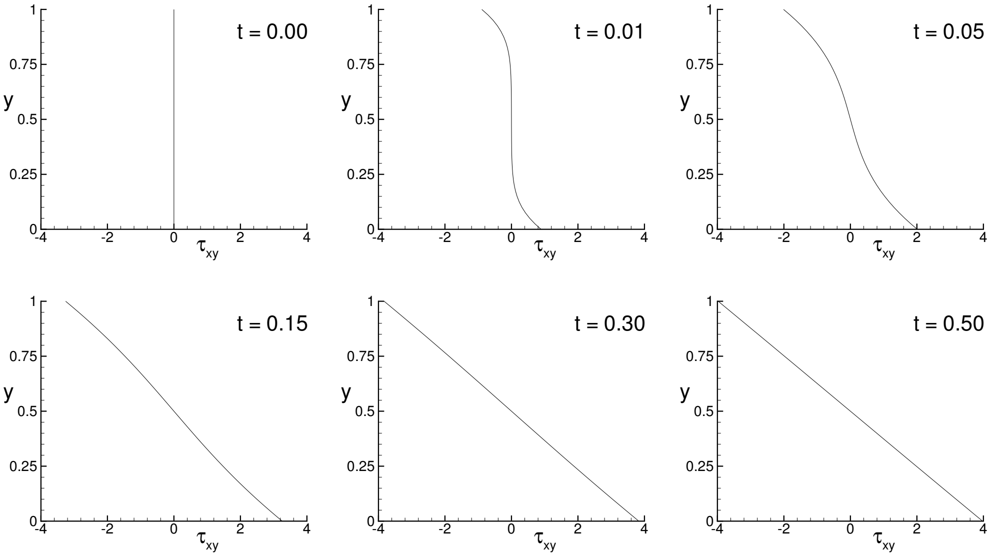

Figure 5.14: Shear stress profile at intermediate time levels in start up of channel flow, $Re = 1$.

5.5.2 2D-calculations

For 2D calculations the 1D solutions obtained in the previous subsection can be used as boundary conditions on the inflow and the outflow of the domain. This will be done for the Poiseuille flow through a planar channel. For flow past a cylinder, steady boundary conditions have been used as well.

Poiseuille flow

The transient start-up profiles are used as boundary conditions to the 2D channel flow problem. The 2D mesh contains four equally sized elements, with $K_y = 2$ and $K_x = 2$ elements in the vertical and horizontal directions, respectively. The approximation order is $N = 10$. The global timestep is $\Delta t = 10^{-2}$. The OIFS2/AB2 temporal scheme is used to approximate the convection of the velocities, and is characterized by $M = 8$, the number of RK4 iterations within one time step.

The boundary conditions calculated from the 1D problem are compared to the solution inside the domain at the penultimate vertical grid line in the Gauss-Lobatto-Legendre grid, i.e. one before the outflow. The comparison is made on the basis of the value of the velocity at the centre line of the channel and the value of the shear stress on the lower wall. Fig. 5.15 shows the nodes A and B where the velocity is monitored, and the nodes C and D where the shear stress is monitored.

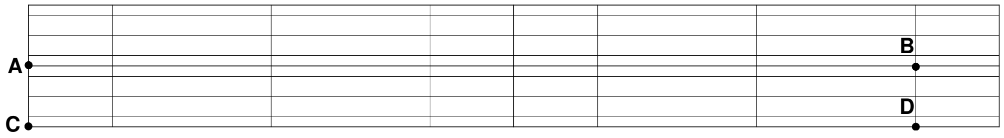

Figure 5.15: The nodes where the velocity component u and the shear stress τ_{xy} are monitored, on a mesh with $K_x = 2$, $K_y = 2$ and $N = 4$.

In Fig. 5.16 the values of velocity and shear stress are plotted against the time for $Re = 1$, and in Fig. 5.17 for $Re = 10$. Note that the only visible change when increasing the Reynolds number is that the time to steady state increases by the same order of magnitude.

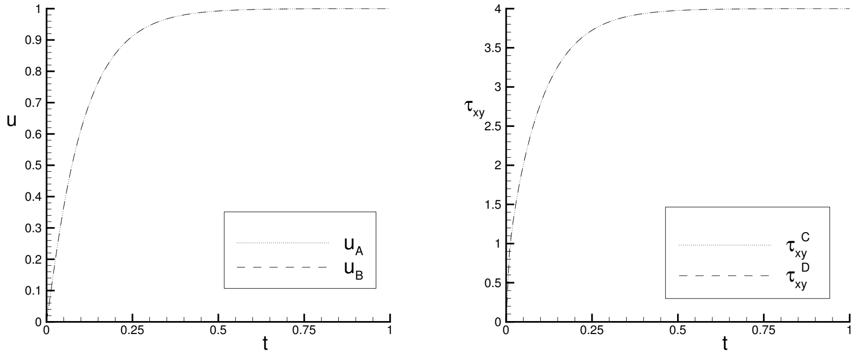

Figure 5.16: Velocity at $y = 1/2$ and shear stress at $y = 0$, in start up of channel flow, for $Re = 1$.

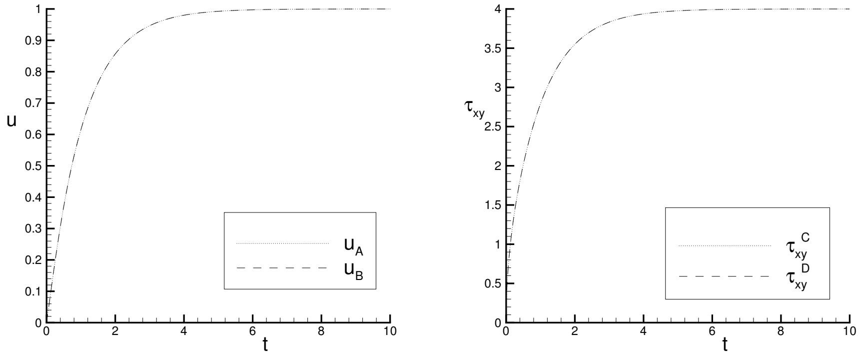

Figure 5.17: Velocity at $y = 1/2$ and shear stress at $y = 0$, in start up of channel flow, for $Re = 10$.

Flow past a confined cylinder

The flow of a Newtonian fluid around a cylinder placed in a channel will now be studied. The full problem is solved now instead of the half problem with a plane of symmetry. The same notations is used as in Fig. 5.2, and the ratio of the channel half height h to the radius of the cylinder is $h/R = 2$. The inflow length is $L_i = 20$, and the outflow length $L_o = 40$. The coordinates of the centre of the cylinder are given by (x_c, y_c), where $y_c = 0$ corresponds to the middle of the channel. The cylinder can be moved in the vertical direction. Geometric restrictions mean that y_c is in the range of $-R \leq y_c \leq R$.

The full mesh contains 10 elements, distributed as shown in Fig. 5.18. The shape of the mesh depends on the positioning of the cylinder. The higher the cylinder is placed in the channel, the skewer the two elements above the cylinder become. Fig. 5.19 shows how the shape of the elements around the cylinder is changed to reduce the skewness.

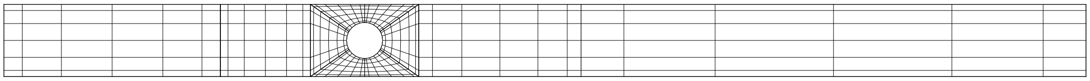

Figure 5.18: Mesh for the flow around a cylinder.

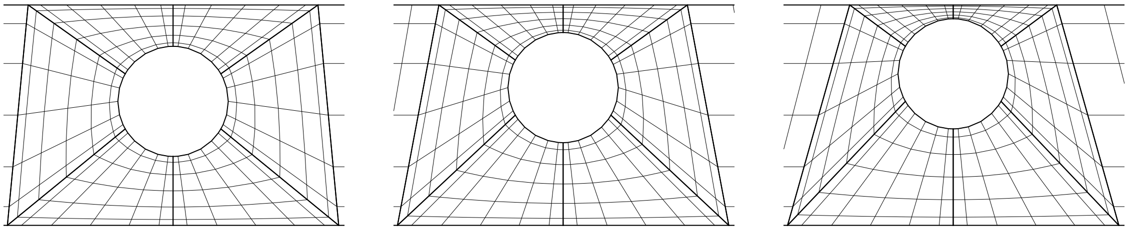

Figure 5.19: Zoom in at the mesh around the cylinder, for $y_c = R/4$, $y_c = R/2$ and $y_c = 3R/4$.

For the Stokes problem mesh convergence is studied again. The dependence of the drag on p-refinement for differently positioned cylinders is shown in Table 5.6. An important observation is that the drag converges to a similar value as presented in Table 5.5 for the half problem with a plane of symmetry. Since the Stokes problem does not contain a time derivative, steady boundary conditions are used.

For the Navier-Stokes problem, a mesh refinement test is performed as well. At a Reynolds number of $Re = 10$, the influence of p-refinement is shown in Table 5.7 for

Table 5.6: Calculated drag on cylinder at different positions y_c for the Stokes problem. Convergence with p-type mesh refinement.

N	Drag, $y_c = 0$	Drag, $y_c = R/4$	Drag, $y_c = R/2$	Drag, $y_c = 3R/4$
6	132.7529	121.1758	96.0518	71.3862
7	132.5407	120.9789	95.8872	71.2481
8	132.4331	120.8840	95.8126	71.1900
9	132.3849	120.8448	95.7830	71.1675
10	132.3667	120.8308	95.7725	71.1590
11	132.3603	120.8261	95.7689	71.1560
12	132.3583	120.8247	95.7678	71.1552

Table 5.7: Convergence of the calculated drag on cylinder at $Re = 10$, with p-type mesh refinement.

N	Drag at $y_c = 0$
5	137.0150
6	137.3025
7	137.4669
8	137.4580
9	137.3735
10	137.3083
11	137.2709
12	137.2519

the centrally placed cylinder. The time step used in these calculations is $\Delta t = 10^{-2}$, and the boundary conditions are steady. The OIFS2/AB2 temporal scheme, with $M = 8$ RK4 iterations per time step, is used to approximate the convection term. The simulation is terminated when the L_2 norms of the velocities and the stresses is smaller than 10^{-8}, where the L_2 norms are defined by

$$||\Delta\mathbf{u}||_{L^2} = \left[\int_\Omega |u^{n+1} - u^n|^2 + |v^{n+1} - v^n|^2 d\Omega\right]^{1/2}, \tag{5.17}$$

$$||\Delta\boldsymbol{\tau}||_{L^2} = \left[\int_\Omega |\tau_{xx}^{n+1} - \tau_{xx}^n|^2 + |\tau_{yy}^{n+1} - \tau_{yy}^n|^2 + 2|\tau_{xy}^{n+1} - \tau_{xy}^n|^2 d\Omega\right]^{1/2}. \tag{5.18}$$

The result for the approximating order $N = 10$, is repeated with the use of transient boundary conditions. This is to verify that the two different methods do indeed result is the same computed drag. In Fig. 5.20 the build up of the drag on the cylinder is shown as the flow starts up. The transient calculation was stopped at $t = 200$, at which point the drag was 137.30820 which is indeed in agreement with the value of 137.30825 calculated using the steady boundary conditions.

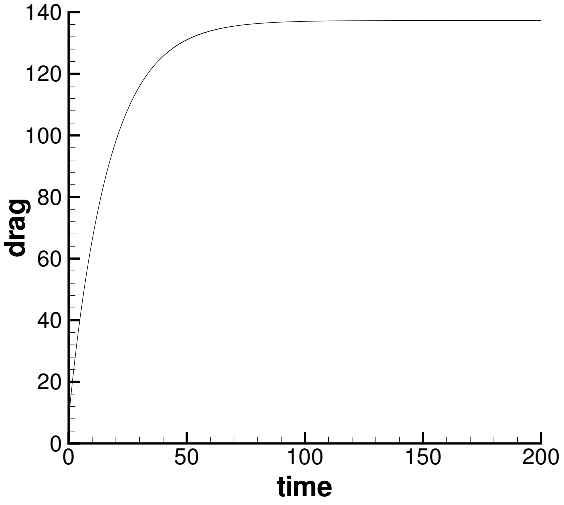

Figure 5.20: The evolution of drag on a centrally positioned cylinder in a channel.

Next the influence of the choice of time step on the solution is shown by computing the drag with time steps of 10^{-1}, 10^{-3} and 10^{-4}. Steady boundary conditions are again applied. Table 5.8 shows that the drag differ less than 0.001% for these choices of the time step. The computation with a time step of $\Delta t = 10^{-1}$ failed to converge.

For the cylinder placed at $y_c = 0$, i.e. in the middle of the channel, the influence of

Table 5.8: Calculated drag on cylinder for different values of the time step at $Re = 10$.

Δt	Drag at $y_c = 0$
10^{-1}	-
10^{-2}	137.30825
10^{-3}	137.30782
10^{-4}	137.30815

the Reynolds number on the solution is computed. For Reynolds numbers of 0, 5, 10, 20 and 40, the predicted values of the drag are given in Table 5.9. For the Reynolds number of $Re = 40$, contour plots are presented in Figs. 5.21-5.23.

Table 5.9: Calculated drag on cylinder for different values of the Reynolds number.

Re	Drag at $y_c = 0$
0	132.3667
1	132.4224
5	133.7008
10	137.3083
20	149.7149
40	185.6382

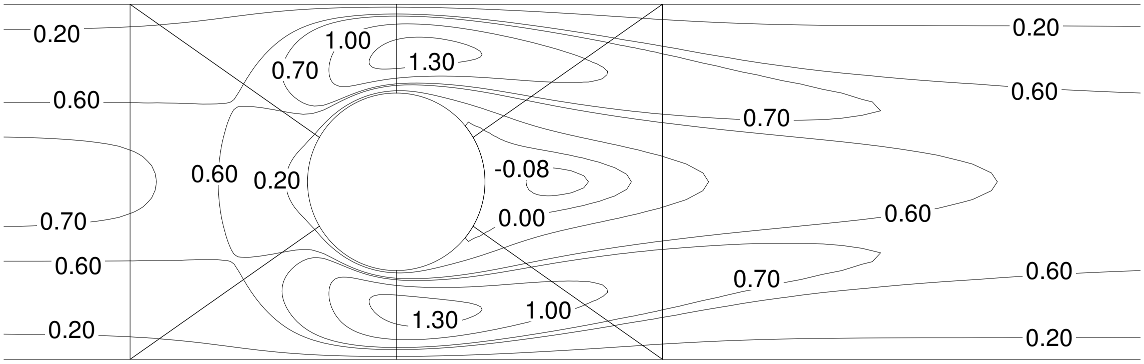

Figure 5.21: Contours of the horizontal velocity component u for $Re = 40$.

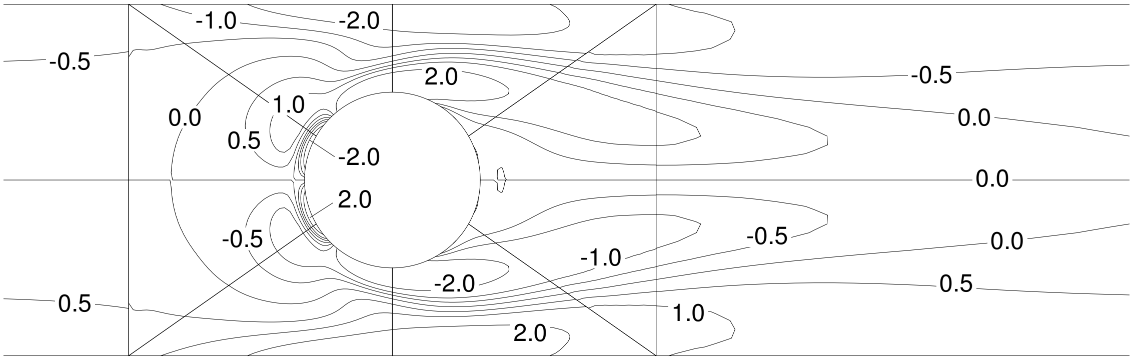

Figure 5.22: Contours of the shear stress τ_{xy} for $Re = 40$.

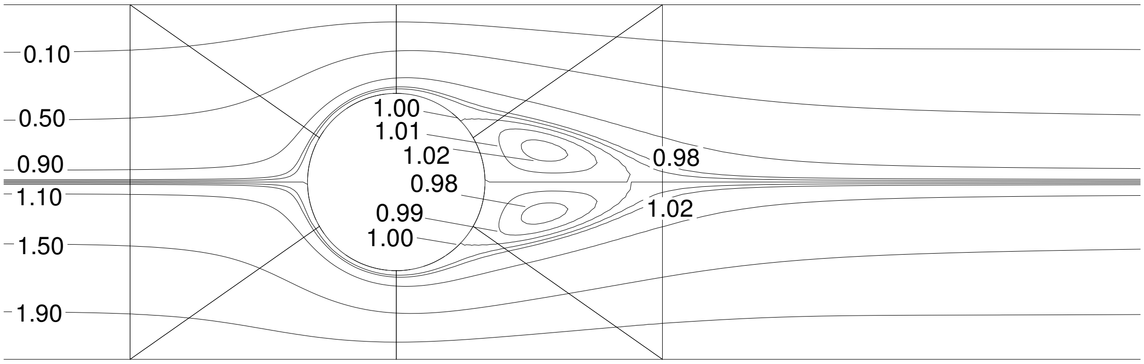

Figure 5.23: Contours of the stream function Ψ for $Re = 40$.

Table 5.10: Calculated drag on cylinder for different vertical positions of the cylinder at $Re = 10$.

y_c	Drag
0	149.7149
0.25	148.8482
0.50	137.4772
0.75	111.3690

With $Re = 20$ the position of the cylinder is varied, and the influence on the drag is shown in Table 5.10. Contours of the stream line value Ψ are shown in Fig. 5.24 as the vertical position of the cylinder is varied. As the cylinder is moved more away from the centre, the flow around the cylinder is slower and this results in a decrease in drag. Although the drag decreases less than one percent when the cylinder placement changes from $y_c = 0$ to $y_c = 0.25$, the recirculation area behind the cylinder has already disappeared. When the cylinder is placed closer to the wall though, large recirculation areas form detached from the cylinder on the wall of the channel.

The more commonly observed drag reduction with increasing Reynolds number is obtained using a non-dimensionalization suitable for situations in which convection dominates diffusion. In this case the dimensionless momentum equation is

$$\frac{\partial \mathbf{u}}{\partial t} + \mathbf{u} \cdot \nabla \mathbf{u} = -\nabla p + \frac{1}{Re} \nabla \cdot \boldsymbol{\tau}. \tag{5.19}$$

instead of the dimensionless momentum equation used in the calculations above,

$$Re \left(\frac{\partial \mathbf{u}}{\partial t} + \mathbf{u} \cdot \nabla \mathbf{u} \right) = -\nabla p + \nabla \cdot \boldsymbol{\tau}. \tag{5.20}$$

Table 5.11 provides the drag on the cylinder generated using both formulations of the momentum equation, for a range of Reynolds numbers. These calculations were performed on a mesh with $N = 4$ and 20 elements as shown in Fig. 5.3.

Table 5.11: Drag force F with varying Reynolds numbers for different non-dimensionalizations of the momentum equation.

Re	drag F for Eq.(5.20)	drag F for Eq.(5.19)
10^{-2}	132.3487	9239.6207
10^{-1}	132.3487	960.2873
10^{0}	132.4079	132.4079
10^{1}	137.5319	50.8827

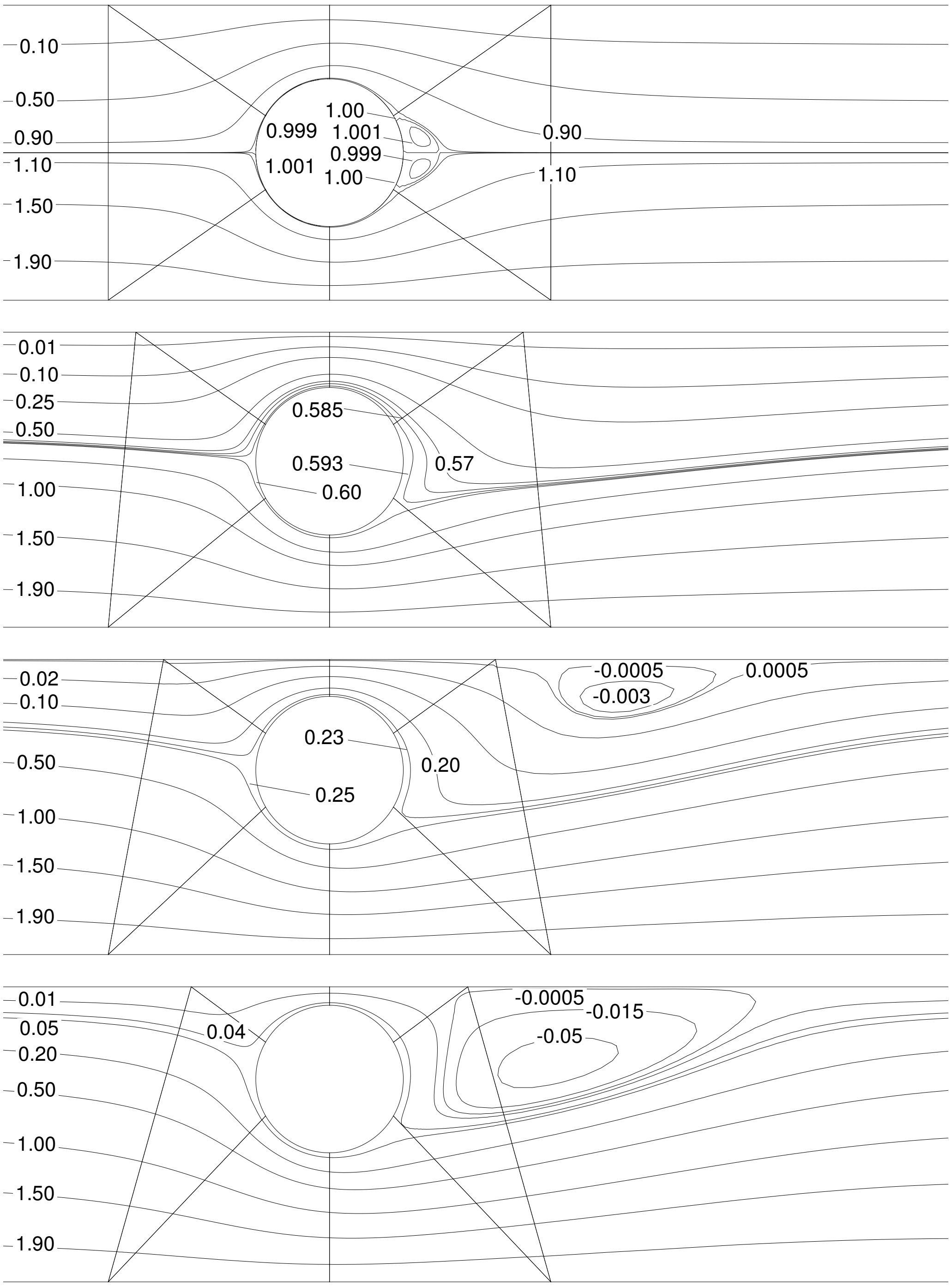

Figure 5.24: Contours of the stream function Ψ for $Re = 20$ for different vertical positions of the cylinder. From top to bottom the vertical position is $y_c = 0$, $y_c = 1/4$, $y_c = 1/2$ and $y_c = 3/4$.

Chapter 6

Prediction of Flow of Polymer Solutions

6.1 Introduction

The major part of this chapter deals with the Poiseuille flow of Oldroyd B and UCM fluids through a planar channel. In section 6.2 the analytic solutions that are available for both the steady and transient start-up of Poiseuille flow are presented. This transient start-up is then compared to the 1D numerical solutions generated in section 6.3. In sections 6.4 and 6.5, 2D solutions to the Poiseuille flow are calculated. Section 6.4 deals with steady flows and section 6.5 deals with the transient start-up problem. For the steady calculations both the coupled and the uncoupled solver have been used. It is shown that even in this simple flow, instabilities lead to divergence of the numerical solution and that very modest maximum attainable Weissenberg numbers are found. The uncoupled solver in combination with the LUST method however, increases the stability, and using this scheme results for the flow of an Oldroyd B fluid past a confined cylinder is presented in section 6.6. In section 6.7 the efficiency of some of the preconditioners described in section 4.4 is demonstrated.

6.2 Poiseuille Flow in a Planar Channel

The benchmark problem of plane Poiseuille flow in a channel bounded by two parallel fixed plates has been chosen since an analytical solution exists for both the steady and transient problems. This enables the accuracy as well as the stability of numerical schemes to be investigated.

The analytical solution for the flow of an Oldroyd B fluid in a planar channel (see Fig. 6.1) can easily be found at steady state. With all derivatives in the channel direction (x) set to zero, and the cross channel velocity $v = 0$, a parabolic velocity profile for the velocity component, u, is obtained in the form

$$u(y) = A(y) = 4(1-y)y. \tag{6.1}$$

This is valid in a channel of height $h = 1$ and $0 \leq y \leq h$, with a maximum centreline velocity of $U = 1$. The elastic stresses can now be found by solving the constitutive equation using the above assumptions. This yields

$$\tau_{xx} = 2We(1-\beta)(\frac{\partial u}{\partial y})^2 = 2We(1-\beta)(A'(y))^2, \tag{6.2}$$

$$\tau_{xy} = (1-\beta)(\frac{\partial u}{\partial y}) = (1-\beta)(A'(y)), \tag{6.3}$$

$$\tau_{yy} = 0. \tag{6.4}$$

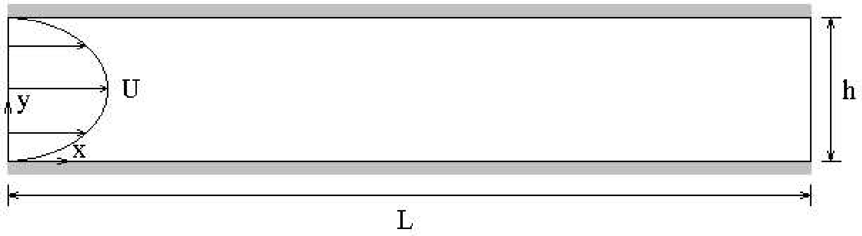

Figure 6.1: Poiseuille flow in a planar channel.

With a constant pressure gradient applied, the analytical solution to the transient start-up of a channel flow of an Oldroyd B fluid has been derived by Waters and King

[64] for $Re \neq 0$. The velocity components of this solution are given by

$$\begin{aligned} u(y,t) &= U\left[A(y) - 32\sum_{n=1}^{\infty}\frac{\sin(Ny)}{N^3}\exp\left(-\frac{\alpha_N t}{2We}\right)G_N(t)\right], && (6.5)\\ v(y,t) &= 0, && (6.6)\end{aligned}$$

where $G_N(t)$ is defined as

$$G_N(t) = \cosh\left(\frac{\beta_N t}{2We}\right) + \left[\frac{1+(\beta-2)EN^2}{\beta_N}\right]\sinh\left(\frac{\beta_N t}{2We}\right),$$

and the other factors are

$$\begin{aligned} N &= (2n-1)\pi,\\ E &= \frac{We}{Re},\\ \alpha_N &= 1+\beta EN^2,\\ \beta_N &= ((1+\beta EN^2)^2 - 4EN^2)^{1/2}.\end{aligned}$$

The stress components are given by

$$\begin{aligned} \tau_{xx} &= 2ReC_{xy}(y)\left[A'(y)\exp\left(-t/We\right) - 32\sum_{n=1}^{\infty}\frac{\cos(Ny)}{N^2}I_N(t)\right] && (6.7)\\ &\quad +2ReA'(y)(1-\beta)\left[EA'(y) - 32\sum_{n=1}^{\infty}\frac{\cos(Ny)}{N^2}H_N(t)\right]\\ &\quad -\frac{64ReA'(y)(1-\beta)}{E}\sum_{m=1}^{\infty}\frac{\cos(My)}{M^2}J_M(t)\\ &\quad +\frac{2048Re(1-\beta)}{E}\sum_{n,m=1}^{\infty}\frac{\cos(Ny)}{N^2}\frac{\cos(My)}{M^2}K_{NM}(t) + C_{xx}(y)\exp\left(-t/We\right),\\ \tau_{xy} &= \frac{(1-\beta)}{E}\left[EA'(y) - 32\sum_{n=1}^{\infty}\frac{\cos(Ny)}{N^2}H_N(t)\right] + C_{xy}(y)\exp\left(-t/We\right), && (6.8)\\ \tau_{yy} &= 0, && (6.9)\end{aligned}$$

where $M = (2m-1)\pi$, and C_{xy} and C_{xx} are time-independent functions defined by the requirement that τ_{xy} and τ_{xx} are zero at $t = 0$. Details of the other coefficients are given Carew et al. [7].

The transient development of the stress can exhibit both overshoots and undershoots as it evolves toward the steady-state solution. The problem has a smooth solution, being a pure transient shear flow, with a shear boundary layer at the channel walls and no shear along the centreline. There are no geometric singularities in the flow. Here, interest lies solely in determining the quality of the numerical solutions, evolved over time, and in detecting sensitivity to numerical instability for the algorithms under consideration.

For $\beta = 1/9$, the analytical solution displays overshoots and undershoots in the streamwise velocity component and the stress components, as We is increased from a value of zero to unity. As We is increased beyond unity, the velocity overshoot increases, whilst the velocity undershoot and stress overshoot/undershoot are damped. Once We reaches 100 there is no velocity undershoot or stress overshoot/undershoot. Also of interest is the relative settling times taken for velocity and stress components to settle down to their steady-state values. For $We < 1$, velocity and stress components take approximately the same time to achieve such states. However, for $We \geq 1$, the normal stress components take longer to attain their steady-state values as compared with the velocity components and the shear stress. Reproducing these features is a severe test of the time accuracy of any transient algorithm, given the different time-scales involved.

6.3 Comparison of 1D Numerical Solutions with Analytic Solutions

The analytic Waters and King solution is compared to a 1D numerical solution for the start-up of Poiseuille flow. The height of the channel is $h = 1$. The mesh consists of two spectral elements of equal size, with $N = 10$. The start-up of both an Oldroyd B fluid with $\beta = 1/9$ and a UCM model is computed. The Reynolds number and Weissenberg number are both set to unity, and the flow is driven by a pressure gradient of $\partial p/\partial x = -8$. The timestep in the 1D calculation is $\Delta t = 10^{-3}$. In Fig. 6.2 the numerical solution is compared to the Waters and King solution for the Oldroyd B model. Both the velocity and the shear stress and first normal stress exhibit large overshoots and undershoots before settling to the steady state Poiseuille flow. Only for the first normal stress τ_{xx} does the numerical solution shows slightly larger values in the overshoot.

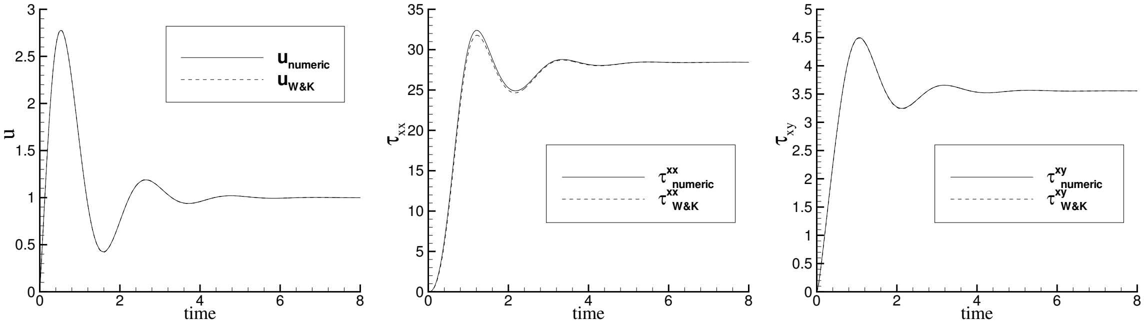

Figure 6.2: Comparison of the velocity approximation at the centre of the channel and the stress approximation at the channel wall, with the Waters and King solutions, for an Oldroyd B fluid with $\beta = 1/9$, $We = 1$ and $Re = 1$.

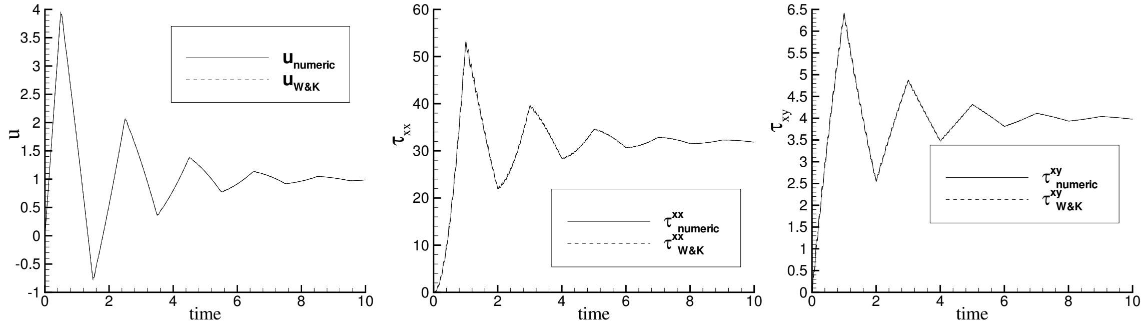

Figure 6.3: Comparison of the velocity approximation at the centre of the channel and the stress approximation at the channel wall, with the Waters and King solutions, for a UCM fluid with $We = 1$ and $Re = 1$.

The same comparison for the UCM model is shown in Fig. 6.3. The overshoots and undershoots are much larger for the UCM model, and they also exhibit more discontinuous behaviour then the overshoots and undershoots in the Oldroyd B model. Still the numerical solution represents the exact solution well in the eyeball norm. Note that the velocity in the start-up of the Poiseuille flow of a UCM fluid even becomes negative before settling.

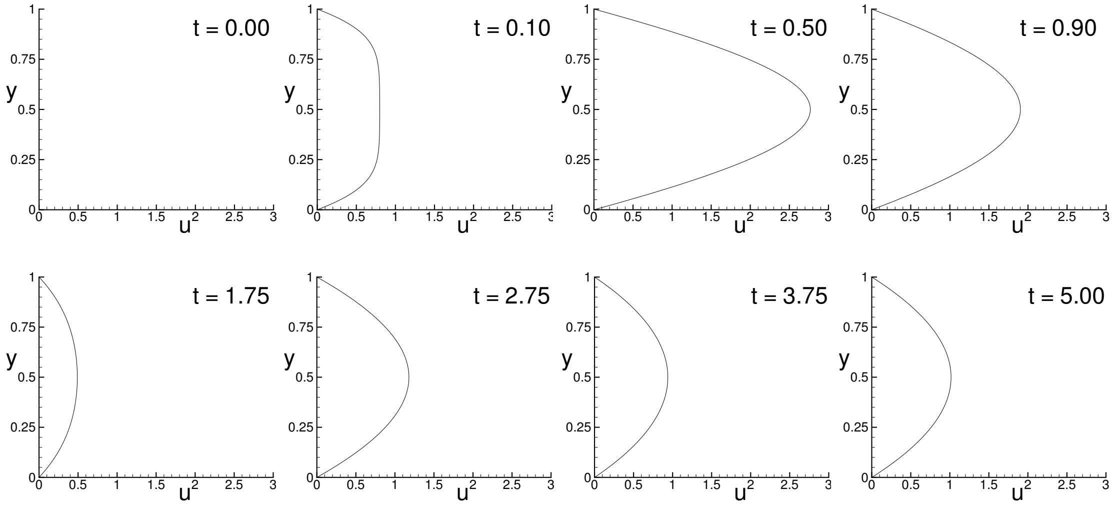

Figure 6.4: Velocity profile at intermediate time levels in the start-up of channel flow for an Oldroyd B fluid with $\beta = 1/9$, $We = 1$ and $Re = 1$.

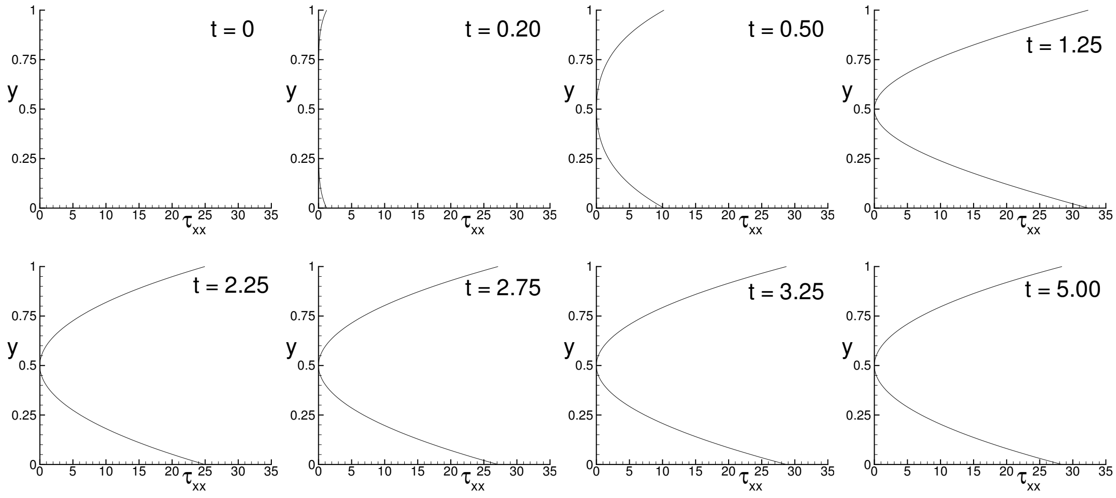

Figure 6.5: First normal stress profile at intermediate time levels in the start-up of channel flow for an Oldroyd B fluid with $\beta = 1/9$, $We = 1$ and $Re = 1$.

The development of the profiles of velocity and first normal stress are also shown for both the Oldroyd B model and the UCM model. Figs. 6.4 to 6.7 show the profiles at a few time levels. Again this shows that to capture the correct transient behaviour, a higher order approximating polynomial is necessary. Especially, the intermediate velocity profiles in Fig. 6.6 call for high order approximation. When the only interest is in the solution to the steady problem, a second-order approximation will do, since all the profiles in steady flow are parabolic.

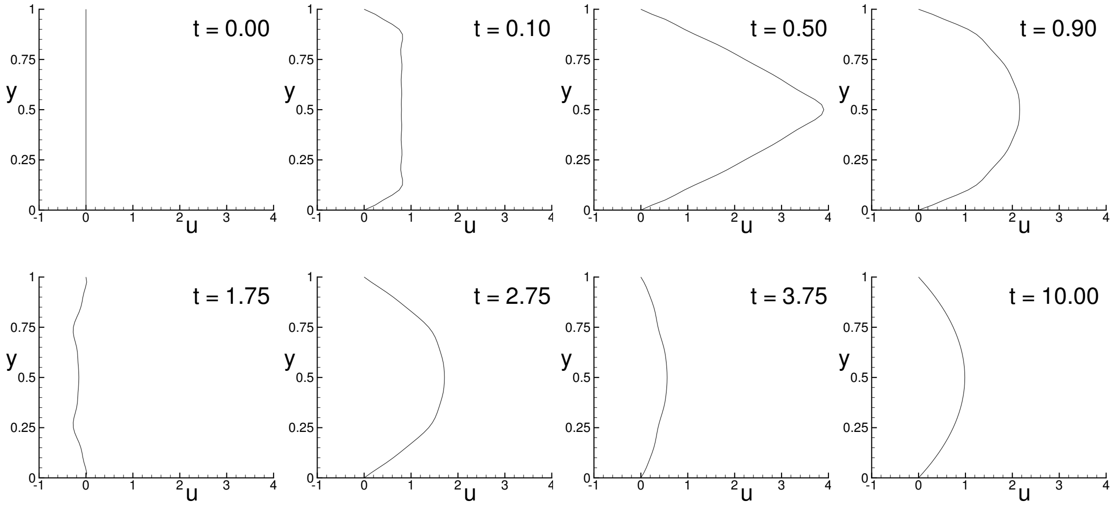

Figure 6.6: Velocity profile at intermediate time levels in start up of channel flow for a UCM fluid with $We = 1$ and $Re = 1$.

6.4 Steady Channel Flow

To find steady solutions to the Poiseuille flow in a channel, two approaches can be used. In this section, the fully developed flow is prescribed as a steady boundary condition. Starting with zero initial conditions, the solution will converge to the fully developed flow in the whole channel, using a transient algorithm. The transient development from the initial conditions is in this case only a means of finding the steady-state solution, and the time dependent start-up of the flow itself has no physical interpretation. In Section 6.5, the Waters and King solution will be used

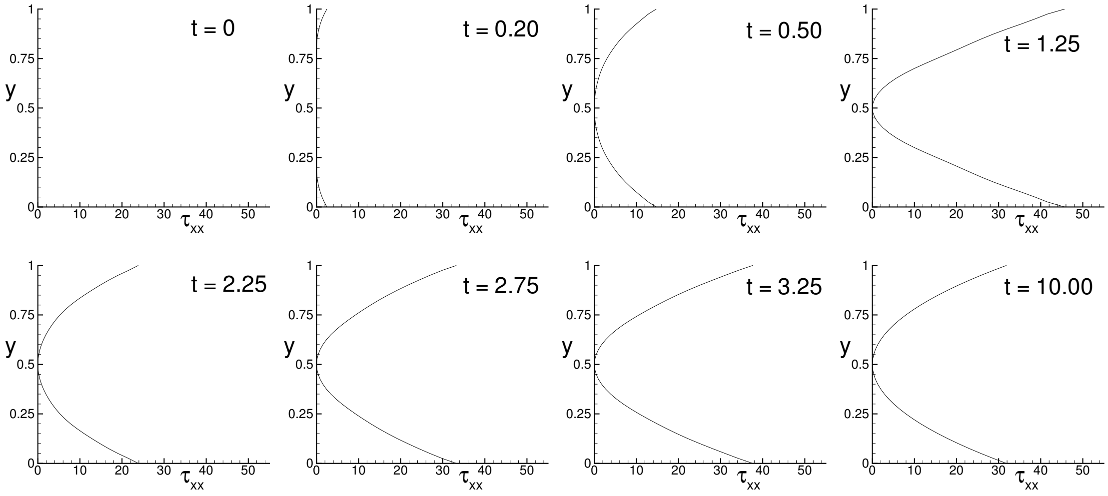

Figure 6.7: First normal stress profile at intermediate time levels in start up of channel flow for a UCM fluid with $We = 1$ and $Re = 1$.

as a transient boundary condition. This time dependent solution may be physically interpreted as the start-up of Poiseuille flow of an Oldroyd B fluid.

For the steady channel flow, a parabolic profile is used to prescribe the steady velocity boundary condition at both inflow and ouflow. The corresponding extra-stress profiles are prescribed as boundary conditions only at the inflow of the channel. A no-slip condition is applied at the walls of the channel $y = 0$, and $y = h$. Zero initial conditions for both velocity and stress are assumed inside the domain.

Both the coupled and uncoupled solvers have been used to solve this problem. An extensive study of the influence of the different parameters is performed using the coupled solver. After this, the uncoupled solver is used and the results using different test functions are compared to the results of the coupled solver.

6.4.1 Coupled solver

The influence on the maximum attainable Weissenberg numbers of the different time integration methods, different values of β, N, L, and the number of elements, has been tested using the coupled solver.

Time integration method of material derivative/deformation terms

For the Oldroyd B and UCM models different time integration methods have been tested. The following parameters are used: $N = 4$, $K = 1$, $Re = 0$ and $Re = 0.1$, with a timestep $\Delta t = 0.1$. The channel length is $L = 64$, and height $h = 1$. The boundary conditions are based on the velocity profile $u = -4y(y-1)$, $y \in [0,1]$.

The convergence criteria on the residuals of the preconditioned conjugate gradient loops for the inversion of the Uzawa and Helmholtz operators are set to 10^{-9} and 10^{-14} respectively. The convergence criteria $||\Delta\mathbf{u}||_{L^2}$ and $||\Delta\boldsymbol{\tau}||_{L^2}$ norms are set to 10^{-8}. When these criterion are met, the Weissenberg number is increased, according to

$$We = We + 0.05 \qquad \text{if } We \leq 1 \tag{6.10}$$

$$We = We * 1.1 \qquad \text{if } We > 1 \tag{6.11}$$

In Table 6.1 the maximum attainable Weissenberg numbers for the Euler/Euler method and for BDF2/EX2 and OIFS2/AB2 are presented for the UCM model and for an Oldroyd B model with $\beta = 1/9$. The results in this table show that a nonzero Reynolds number clearly has a stabilizing effect on the calculations for the UCM model and the Oldroyd B model.

The calculations performed for the UCM model show that a larger maximum Weissenberg number can be achieved when a first-order temporal scheme is used rather

Table 6.1: Maximum attainable Weissenberg numbers for different temporal discretizations and models, for a one element mesh with $N = 4$ and $L = 64$.

		$We_{\max}$, $Re = 0$	$We_{\max}$, $Re = 0.1$
UCM	Euler/Euler	8.95	17.45
	OIFS2/AB2	6.73	8.95
	BDF2/EX2	5.05	8.95
Oldroyd B	Euler/Euler	28.10	34.00
	OIFS2/AB2	28.10	34.00
	BDF2/EX2	28.10	34.00

than a second-order scheme. We do not have an explanation for this for the steady problem at the moment. However, we speculate that it is related to the relative regularity of the solutions to the UCM and Oldroyd B problems as indeed it is for the corresponding inertial transient problems.

Time discontinuity in UCM solution

The enormous difference in maximum attainable Weissenberg number for the UCM and the Oldroyd B models in Table 6.1, using second-order temporal discretization, may be explained by looking at the convergence of the series (6.5). The rate of convergence is determined by the asymptotic behaviour of the coefficients as $N \to \infty$

$$Q_N(t) = \frac{1}{N^3} \exp\left(-\frac{\alpha_N t}{2E}\right) G_N(t). \tag{6.12}$$

In the case of the Oldroyd B model, $\beta E > 0$ which means that $\beta_N = \mathcal{O}(N^2)$ as $N \to \infty$ and $Q_N(t) = \mathcal{O}(N^{-3})$ as $N \to \infty$. For the UCM model, $\beta E = 0$ and there are two cases to consider: $E > 1/4\pi^2$ and $E < 1/4\pi^2$. When $E > 1/4\pi^2$ then $\beta_N = \mathcal{O}(N)$ as $N \to \infty$ and is purely imaginary. In this case

$$Q_N(t) \sim N^{-3} \left[\frac{2N^2E - 1}{\sqrt{4N^2E - 1}}\right], \tag{6.13}$$

which is effectively $\mathcal{O}(N^{-2})$ as $N \to \infty$. When $E < 1/4\pi^2$, β_N is real for $N \leq N^*$, and imaginary for $N > N^*$, for some N^*. So $G_N(t)$ is exponential for small N before oscillations set in and result (6.13) again holds in the limit $N \to \infty$.

The local truncation error of a first-order approximation to $\frac{\partial u}{\partial t}$ is proportional to $\Delta t \sup \left|\frac{\partial^2 u}{\partial t^2}\right|$, while that for a second-order approximation is $(\Delta t)^2 \sup \left|\frac{\partial^3 u}{\partial t^3}\right|$. The asymptotic decay rate of $Q_N(t)$ for the UCM model suggests that $\frac{\partial u}{\partial t}$ is continuous, while $\frac{\partial^2 u}{\partial t^2}$, is discontinuous. Therefore a first-order approximation may be able to simulate the UCM fluid, while a second-order approximation may fail. The decay rate for the Oldroyd B model suggests that both approximations may perform well.

Parameter β

Using the Euler/Euler scheme to approximate the material derivative and deformation terms, the Oldroyd B model has been tested for $\beta = 0$ (UCM), $\beta = 1/9$ and $\beta = 0.9$. The convergence criteria for $||\Delta \mathbf{u}||_{L^2}$ and $||\Delta \boldsymbol{\tau}||_{L^2}$ are set to 10^{-8}, and for the inversion of the Helmholtz operator, a preconditioner based on an overlapping Schwarz method has been used, with an overlap of two nodes. The mesh is defined by $N = 4$ and $K = 8$, with two elements in vertical and four in horizontal direction. The timestep is $\Delta t = 0.1$, the channel length is $L = 64$, and the height $h = 1$, with a parabolic inflow profile: $u = -4y(y-1)$, $y \in [0, 1]$. The convergence criteria are 10^{-9} for the Uzawa loop, and 10^{-14} for the Helmholtz loop.

In Table 6.2 the maximum attainable Weissenberg numbers for Reynolds numbers of $Re = 0$ and $Re = 1$ are given, with $\beta = 0$ (UCM) and $\beta = 1/9$ and $\beta = 0.9$. The influence of changes in the Reynolds number and the parameter β is less obvious than in the results for the one element case which are presented in Table 6.1. A high value of β however, clearly provides a more stable problem.

Table 6.2: Maximum attainable Weissenberg numbers for different values of β and Re, on a mesh whith $K = 8$, $N = 4$ and $L = 64$.

		$We_{\max}$
Re=0	$\beta = 0$	1.77
	$\beta = 1/9$	1.77
Re=1	$\beta = 0$	1.77
	$\beta = 1/9$	1.77
	$\beta = 0.9$	3.14

Timestep

For the Oldroyd B model with $\beta = 1/9$, $Re = 1$, and $We = 0.5$, different values for the timestep are tested. The other parameters are the same as in Section 6.4.1. Convergence for the norms of the stresses are shown in Fig. 6.8, for $\Delta t = 10^{-1}$ and $\Delta t = 10^{-3}$. Whereas the convergence of the stress approximation using the larger time step is predominantly monotonic until machine precision is reached, the convergence history for the smaller time step is more irregular and is undulatory in behaviour.

Number of elements and order of polynomial approximation

For the UCM ($\beta = 0$) model under the creeping flow assumption ($Re = 0$), different values for the number of elements K and the polynomial order N are tested. All other values are the same as in Section 6.4.1. For one element no Schwarz overlap based preconditioner is possible, so for the Helmholtz operator for one element, the identity is used (no preconditioner) in the PCG iteration.

Maximum attainable Weissenberg numbers are given in Table 6.3, for $K = 1$ with both $N = 4$ and $N = 8$, and $K = 8$ equally sized element, four in horizontal and

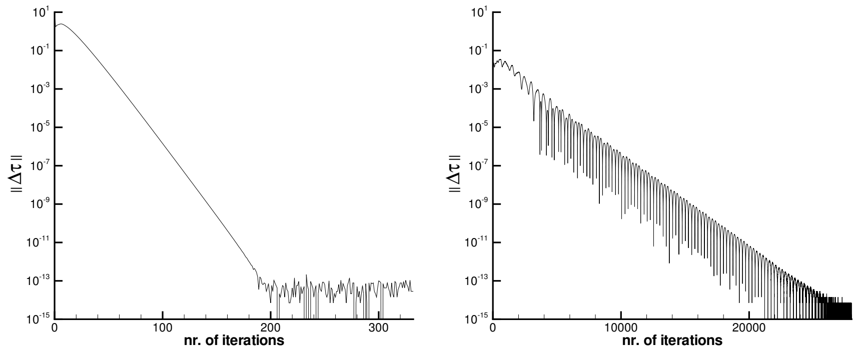

(a) (b)

Figure 6.8: Convergence of norms of stresses for (a) $\Delta t = 10^{-1}$ and (b) $\Delta t = 10^{-3}$, for an Oldroyd B model with $\beta = 1/9$, $Re = 1$, and $We = 0.5$, on a mesh whith $K = 8$, $N = 4$ and $L = 64$.

two in vertical direction, also with both $N = 4$ and $N = 8$. The ability of the model to produce valid results at high Weissenberg numbers decreases with increasing the mesh resolution.

Table 6.3: Maximum attainable Weissenberg numbers for different polynomial orders and number of elements, for a UCM model with $Re = 0$.

		$We_{\max}$
$N = 4$	$K = 1$	7.59
	$K = 8$	1.77
$N = 8$	$K = 1$	3.80
	$K = 8$	0.50

Fig. 6.9 shows a plot of $||\Delta\boldsymbol{\tau}||_{L^2}$, against the non-dimensional time, for the mesh with $N = 8$ and $K = 8$. Only the last three Weissenberg numbers are plotted. The maximum attainable Weissenberg number is $We = 0.50$, and any higher value causes the solution to diverge.

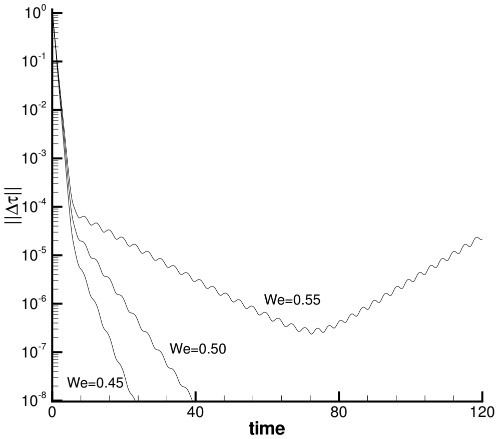

Figure 6.9: Convergence plot of $||\Delta\boldsymbol{\tau}||_{L^2}$, for a UCM model with $Re = 0$, on a mesh with $K = 8$, $N = 8$ and $L = 64$. Only the plots for the highest three Weissenberg number are shown.

Channel length

For an Oldroyd B model with $\beta = 1/9$, with a Reynolds number of $Re = 1$, different values for the the length of the channel are tested. All other values are the same as before in the list in Section 6.4.1.

Table 6.4: Maximum attainable Weissenberg for different channel lengths on a mesh with $K = 8$, $N = 4$, and $L = 64$, for an Oldroyd B model with $\beta = 1/9$, $Re = 1$.

Channel length	$We_{\max}$
8	0.25
16	0.45
32	0.90
64	1.77

Maximum attainable Weissenberg numbers are given in Table 6.4. When the length of the channel is shortened, this maximum Weissenberg number decreases, notably in an almost linear fashion. This may represent the same behaviour of decreasing We_{max} with increasing mesh resolution, since a shorter channel is effectively a refinement of the mesh in the lengthwise direction.

6.4.2 Uncoupled solver

Using the same parameters as before, the Oldroyd B model is now solved using the uncoupled solver. The only change is the time step. Since in an uncoupled solver, the CFL condition is lower, the time step needs to be chosen carefully. Here a time step of 10^{-2} is used. At the shortest tested channel length $L = 8$, the mesh is defined by $K = 8$ and $N = 4$. The Oldroyd model is used with $\beta = 1/9$, $Re = 1$.

The LUST method has been tested against the SUPG and the standard Galerkin method. Table 6.5 shows that using the uncoupled solver instead of the coupled solver leads to a dramatic improvement on the maximum attainable Weissenberg number. Both upwinding methods raise $We_{\max}$ even more, with the LUST method reaching slightly higher numbers than when SUPG is used.

Table 6.5: Maximum attainable Weissenberg for different numerical methods, for a channel with $L = 8$, on a mesh with $K = 8$, $N = 4$, for an Oldroyd B model with $\beta = 1/9$, $Re = 1$.

Solver	$We_{\max}$
Coupled (Galerkin)	0.25
Uncoupled (Galerkin)	1.05
Uncoupled (SUPG)	1.69
Uncoupled (LUST)	1.86

6.5 Transient Channel Flow

Solutions to the planar start-up of channel flow of the Oldroyd B model, are calculated using the Waters and King solution for the start-up of Poiseuille flow as transient boundary conditions. The velocity solution is used at inflow and outflow, the stress solution only at inflow. All other initial conditions are zero. All these results for transient flow have been calculated using the coupled solver.

The performance of the algorithm is shown by solving the transient start-up problem for an Oldroyd B model with $\beta = 1/9$. The Weissenberg and Reynolds numbers are fixed at $We = 1$ and $Re = 1$, the timestep is 10^{-2}, and $h = 1$. Convergence of the solution to the exact Waters and King solution is shown in Tables 6.6 to 6.9, for different values of N, L, K_x and K_y. Here K_x and K_y denote the number of spectral elements in the lengthwise and cross channel directions, respectively.

From Table 6.6 it can be concluded that at a fixed channel length, increasing K_x results in poorer convergence behaviour. This is also the case if K_x is kept fixed, and the channel length is decreased. At a lower approximation order N, Table 6.7 shows that convergence is reached easier at the same values for K_x and L. This reflects the findings for the steady channel flow where either a decrease in channel length or an increase in the value of K_x or N resulted in lower maximum attainable Weissenberg numbers.

The influence of the number of elements in the cross channel direction, K_y, on the convergence behaviour is considerably weaker, as can be seen in Tables 6.8 and 6.9. Although divergence sets in slightly later when $K_y = 1$ only, no examples have been found where the choice of K_y influenced whether or not the solution eventually diverged. The results in Table 6.9, at a lower approximation order N, again show better

Table 6.6: Convergence behaviour for varying values of K_x and L, at a fixed value of $N = 6$. A converged solution is denoted with a C. If the solution does not converge, the approximate time at which the solution diverges is given.

$K_x \times K_y$	N	$L = 8$	$L = 16$	$L = 32$	$L = 64$
1×2	6	C	C	C	C
2×2	6	4.10	10.80	C	C
3×2	6	2.10	5.30	22.00	C
4×2	6	1.00	3.50	11.20	C

Table 6.7: Convergence behaviour for varying values of K_x and L, at a fixed value of $N = 4$. A converged solution is denoted with a C. If the solution does not converge, the approximate time at which the solution diverges is given.

$K_x \times K_y$	N	$L = 8$	$L = 16$	$L = 32$	$L = 64$
2×2	4	12.10	C	C	C
4×2	4	3.00	12.60	C	C
6×2	4	1.30	5.60	C	C
8×2	4	0.90	3.00	13.00	C

convergence behaviour than the results at higher N in Table 6.8.

The exact solution that is prescribed at inflow, according to the Waters and King solution, is compared to the solution that is calculated at the Gauss-Lobatto point on the penultimate vertical gridline, i.e. one before the outflow of the channel. Fig. 6.10 shows the nodes A and B where the velocity is monitored, and the nodes C and D where the stresses are monitored.

The time-dependent solutions at these two points are superimposed in Fig. 6.11,

Table 6.8: Convergence behaviour for varying values of K_y and L, at a fixed value of $N = 6$. A converged solution is denoted with a C. If the solution does not converge, the approximate time at which the solution diverges is given.

$K_x \times K_y$	N	$L = 8$	$L = 16$	$L = 32$
2 × 1	6	5.90	20.20	C
2 × 2	6	4.10	10.80	C
2 × 3	6	3.90	10.90	C
2 × 4	6	3.90	11.00	C

Table 6.9: Convergence behaviour for varying values of K_y and L, at a fixed value of $N = 4$. A converged solution is denoted with a C. If the solution does not converge, the approximate time at which the solution diverges is given.

$K_x \times K_y$	N	$L = 8$	$L = 16$
2 × 1	4	24.00	C
2 × 2	4	12.10	C
2 × 3	4	11.00	C
2 × 4	4	11.00	C

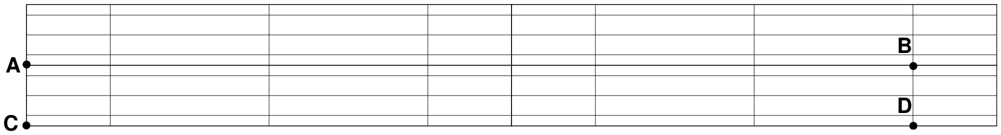

Figure 6.10: The nodes where the velocity component u and the stress components τ_{xx} and τ_{xy} are monitored, on a mesh with $K_x = 2$, $K_y = 2$ and $N = 4$.

where $K_y = 2$, $K_x = 4$, $L = 64$ and $N = 6$. Slight differences in the peak of the time-dependent solution can be observed. The spectral approximation of τ_{xx} overshoots the first peak in the exact solution by approximately 2%. The spectral approximation of u, undershoots the first peak in the exact solution by less than 1%. No such under- or overshoots are observed in the comparison of the numerical and exact values for τ_{xy}. Apart from these differences, the curves are hardly distinguishable.

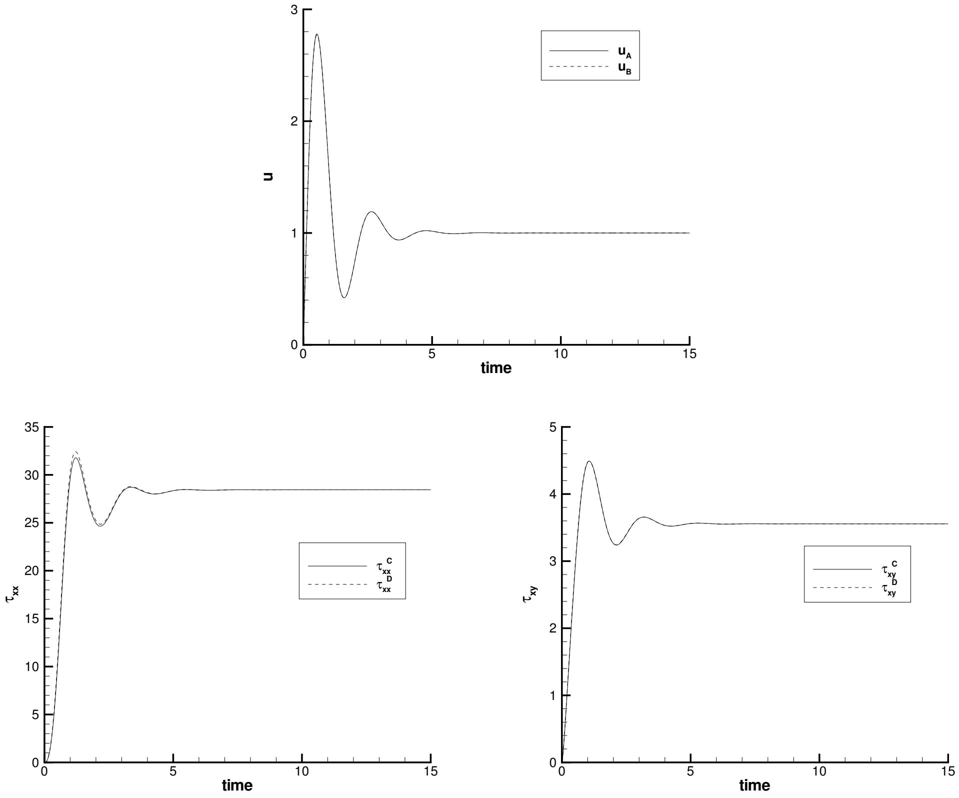

Figure 6.11: Transient solution for a channel with $K = 8$ elements, with a distribution $K_x = 4$, $K_y = 2$ and $N = 6$, for $We = 1$ and $Re = 1$.

The length of the channel is now halved to $L = 32$, keeping K_y, K_x and N fixed. As can be seen in Table 6.6, the solution to this problem diverges at around $t = 11.20$. Fig. 6.12 shows this typical divergence behaviour of the numerical solution away from the exact solution. Although the transient numerical solution seems to follow the exact solution and to settle down to the steady state solution, dramatic divergence sets in after a certain number of iterations. With all other parameters fixed this happens when either the channel is shortened or K_x is increased or N is increased. All of these actions represent refinement of the mesh in the lengthwise direction.

Decreasing the timestep might delay the divergence slightly, but does not change the overall result.

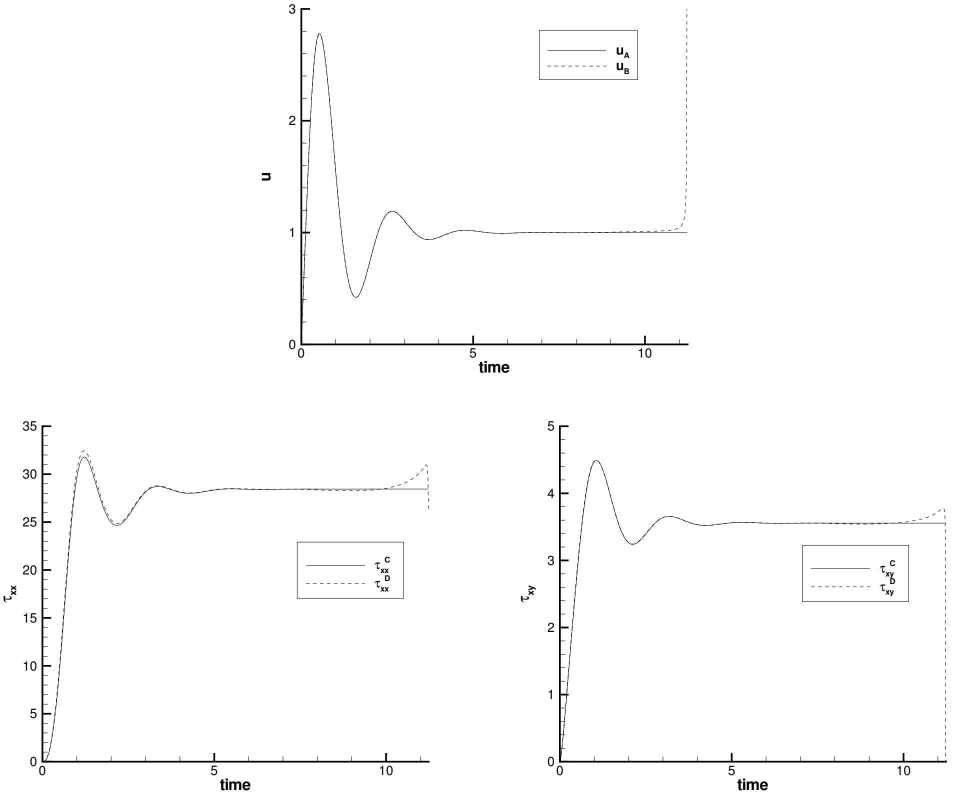

Figure 6.12: Typical divergence of the numerical solution from the exact solution of a transient start-up of a channel flow. Divergence at around $t = 11.20$.

On meshes with $K_x = 1$, converged solutions can be found for higher Weissenberg numbers. This seems to suggest that the spatial discretization and, in particular, the presence of spectral element interfaces in the streamwise direction is partially responsible for the onset of spurious instabilities. Fiétier [14] showed that mesh discretization has a strong impact on the location of the eigenvalues of the associated generalized eigenvalue problem and therefore on numerical stability. This seems to be in agreement with statements made by Beris and Sureshkumar [56] and Wilson et al. [65] about the generation of spurious oscillations caused by the inadequate resolution of the continuous spectrum. Lozinski and Owens observed no limit on the critical Weissenberg number when solving this problem using a single spectral element. However, unlike the numerical simulations of Fiétier and Deville [15] and those under consideration in the present article, periodic boundary conditions were applied across the channel. Therefore, it is impossible to make a direct comparison with this work. However, we should comment that, in the context of spectral methods, the imposition of periodic boundary conditions generally leads to the attainment of a higher critical value of the Weissenberg number compared with the imposition of Dirichlet conditions.

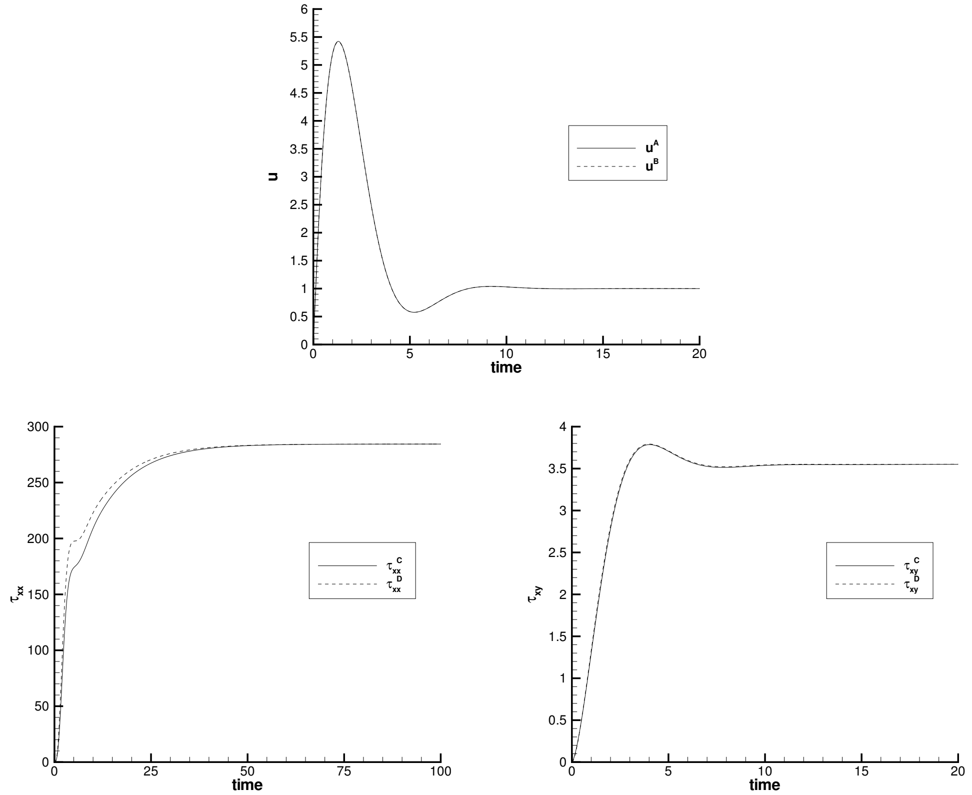

Figure 6.13: Transient solution for a channel with $K = 1$ elements, with $N = 4$, for $We = 10$ and $Re = 1$.

Converged solutions have been obtained for the Oldroyd B model ($\beta = 1/9$) for $We = 10$ and $We = 20$ with $Re = 1$ on a mesh with $K_x = 1$, $K_y = 1$, $L = 64$, $N = 4$ and $\Delta t = 10^{-2}$. Figs. 6.13 and 6.14 show the Waters and King solution at the points

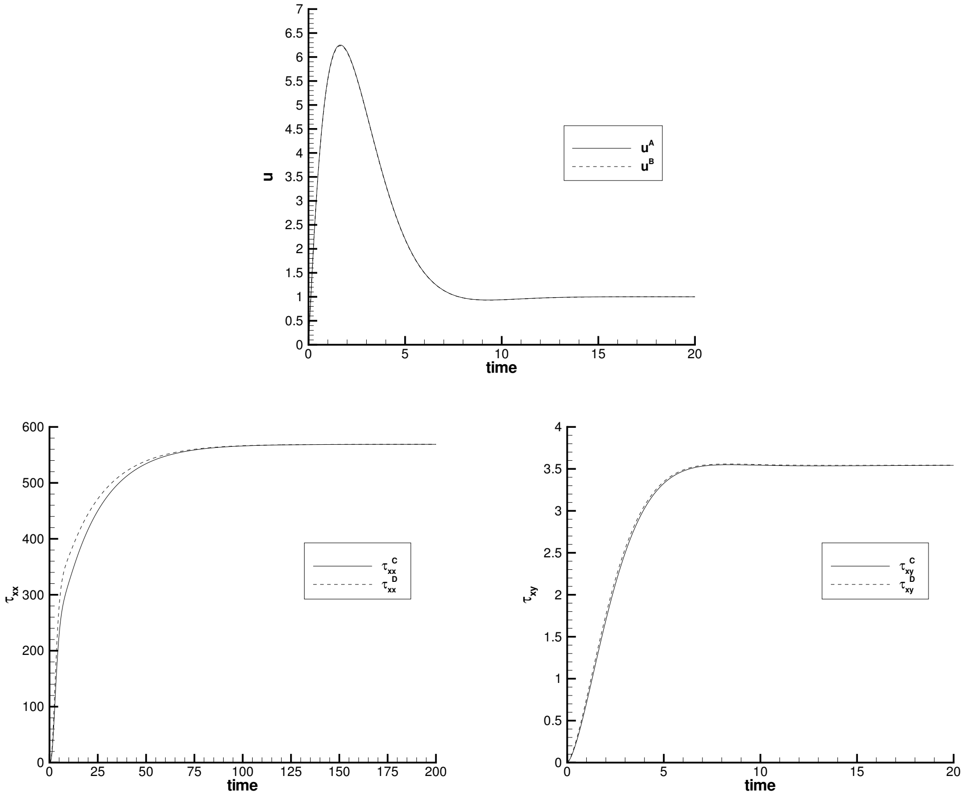

Figure 6.14: Transient solution for a channel with $K = 1$ element, with $N = 4$, for $We = 20$ and $Re = 1$.

A and B, compared to the numerical solution at points B and D for $We = 10$ and $We = 20$, respectively. A very clear overshoot can be observed for τ_{xx}, but the profiles for u and τ_{xy} are hardly distinguishable. The normal stress τ_{xx} takes considerably longer (around a factor of 10 for $We = 20$) to reach its steady state value compared with u and τ_{xy} and dominates the shear stressin absolute value. The same converged solutions have been found on meshes with $K_x = 1$, $K_y = 4$. Again, the value of K_y does not seem to play an important role, and negligible difference is observed between the transient numerical solutions shown in Figs. 6.13 and 6.14 for $K_y = 1$ and those obtained using $K_y = 4$. The same is true for the comparison of solutions obtained by the first-order Euler/Euler temporal scheme, and the second-order OIFS2/AB2 scheme.

Finally, we comment on the alternative implicit scheme presented in section 3.3.2 for solving this problem. No substantial change in the critical value of the Weissenberg number was observed for either the steady or the transient problem. Fiétier and Deville [15] observed similar behaviour when a fully implicit unsteady solver was used. The problem of spurious oscillations in the solution caused by the inadequate spatial resolution of the continuous spectrum seems to dominate the temporal stability of explicit and implicit schemes to such an extent that the enhanced stability properties one would expect of implicit schemes are imperceptible.

6.6 Flow Past a Cylinder

With uncoupled solver and using LUST, the flow past a confined cylinder has been computed for an Oldroyd B model with a Weissenberg number of $We = 0.5$. Other parameters are $Re = 1$, $\beta = 1/9$. The mesh is depicted in Fig. 5.3. It consists of 20 spectral elements, and the approximating polynomial order is $N = 7$. The time step that is used is $\Delta t = 10^{-2}$, and the calculations are stopped when the L_2-norms given in (5.17) and (5.18) have both reduced to 10^{-8}. The convergence criteria in the PCG methods are set to 10^{-9} for the Uzawa operator and 10^{-14} for the Helmholtz operator. The convergence criterion in the Bi-CGStab method for the non symmetric operator S_N is set to 10^{-12}.

The boundary conditions are from the transient Waters and King solution. The development of the drag is shown in Fig. 6.15. The computation has been run up till $t = 20$ seconds and no instabilities that can cause divergence of the numerical solution as presented in the previous section have been detected. The final value of the drag is 115.5426, which has reduced considerably compared to the Newtonian value of 132.4079.

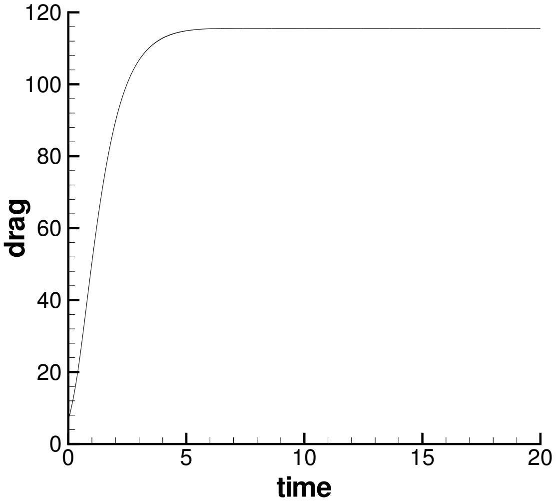

Figure 6.15: Drag on cylinder as a function of time in start-up of Poiseuille flow of an Oldroyd B fluid with $\beta = 1/9$, $We = 0.5$ and $Re = 1$.

Contour plots of the components of the polymeric stress are shown in Figs. 6.16 to 6.18. Some steep gradients are present in the solution near the upper wall, but all the maxima and minima of the stresses are found to be on the cylinder. Fig. 6.19 therefore presents the stress components along the plane of symmetry and the cylinder wall.

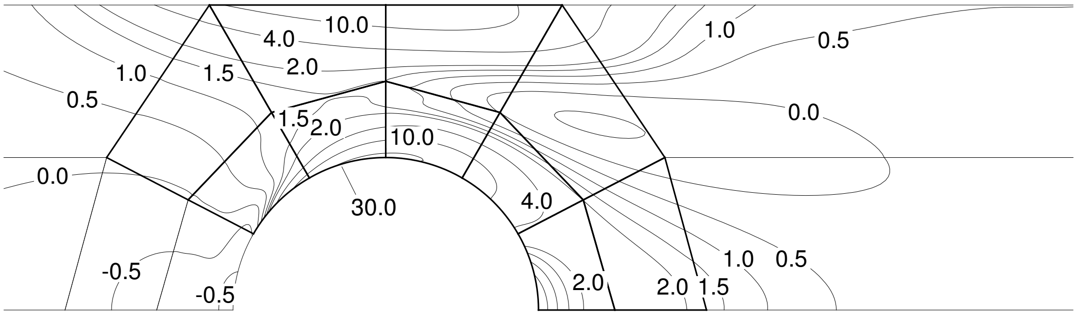

Figure 6.16: Contours of τ_{xx} for an Oldroyd B fluid with $\beta = 1/9$, $We = 0.5$ and $Re = 1$.

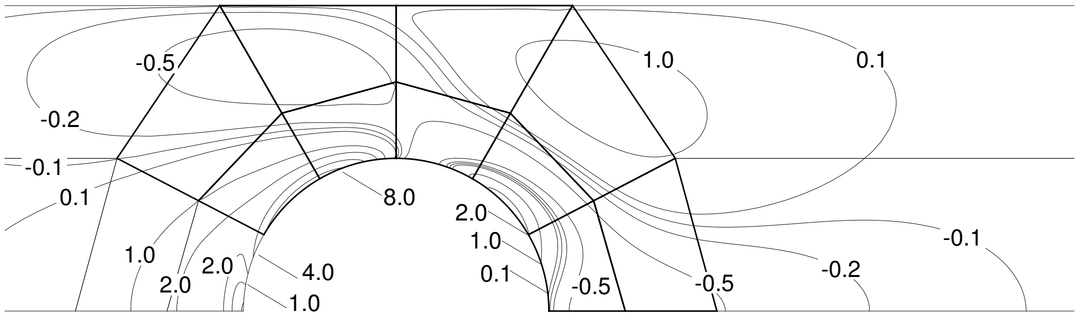

Figure 6.17: Contours of τ_{yy} for an Oldroyd B fluid with $\beta = 1/9$, $We = 0.5$ and $Re = 1$.

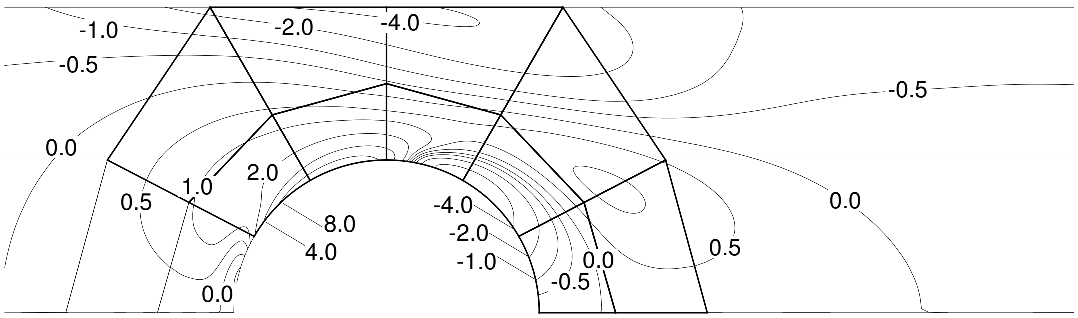

Figure 6.18: Contours of τ_{xy} for an Oldroyd B fluid with $\beta = 1/9$, $We = 0.5$ and $Re = 1$.

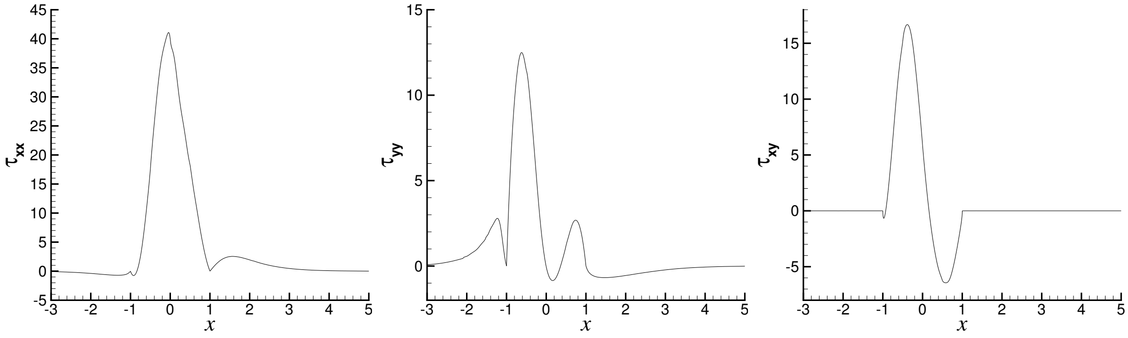

Figure 6.19: Contours of τ_{xx}, τ_{yy} and τ_{xy} for an Oldroyd B fluid with $\beta = 1/9$, $We = 0.5$ and $Re = 1$.

6.7 Results for Different Preconditioners

The performance of some of the different preconditioners described in sections 4.4 is tested in a coupled solver for steady flow, for different values of N, K, Re and We for a channel with $L = 32$ and $h = 1$. The boundary conditions are based on the parabolic velocity profile $u = -6y(y-1)$.

The Euler/Euler temporal scheme is used, with a timestep $\Delta t = 0.1$. The convergence criteria for the PCG algorithms for the Uzawa and the Helmholtz operators are set to be 10^{-12} and 10^{-16}, respectively. The solution is assumed to be converged when the L^2-norm of the difference between two successive velocity and stress approximations is less than 10^{-6}. These L^2-norms are defined by the expressions given in (5.17) and (5.18).

Summarizing, the parameters that have been used to test the performance of the preconditioners are (unless otherwise stated): $N = 8$, $K = 4$, $Re = 1$, $We = 0.1$, $\beta = 1/9$, $\Delta t = 0.1$, $L = 32$, $h = 1$. The distribution of the four equally sized elements is as is depicted in Fig. 6.10.

In Tables 6.10 to 6.13 the efficiency of the various preconditioners is indicated using three quantities. These are:

- The average number of iterations per time step, It_U, needed to invert the Uzawa operator.
- The average number of iterations, It_H, needed to invert the Helmholtz operator, averaged over the total number of Helmholtz inversions. Since the Helmholtz operator needs to be inverted in every Uzawa iteration, the total number of Helmholtz inversions equals the number of time steps times the average number

of Uzawa iterations per time step, It_U.

- The average time to invert the Uzawa operator is given by Δt_U, in seconds. The computations are run on a Compaq XP1000 workstation.

Table 6.10: Performance of the preconditioners with increasing polynomial order N. To achieve a converged solution, 28 time steps were needed.

N	It_U	It_H	Δt_U	P_U	P_H
4	23.29	21.50	0.411	C_P	S_P
4	31.39	21.18	0.211	M_p^*	S_P
4	37.32	22.01	0.258	I	S_P
4	31.39	31.00	0.111	M_p^*	I
4	37.43	32.40	0.139	I	I
8	49.96	36.13	≈ 80	C_P	S_P
8	76.89	35.25	2.646	M_p^*	S_P
8	138.50	36.30	4.874	I	S_P
8	75.57	141.26	4.016	M_p^*	I
8	137.71	145.16	7.384	I	I
12	70.61	47.52	≈ 1800	C_P	S_P
12	103.18	48.64	13.37	M_p^*	S_P
12	231.04	44.95	25.599	I	S_P
12	103.54	308.41	29.954	M_p^*	I
12	231.64	284.51	62.513	I	I

The efficiency of the Cahouet-Chabard based preconditioner C_P for the Uzawa operator, is clear in terms of reduction of the number of iterations in the Uzawa PCG iteration. However, the calculation of this preconditioner, involves the inversion of the pseudo-Laplacian $(DC^{-1}D^T)^{-1}$. The number of iterations needed for this PCG inversion increases dramatically with increasing polynomial order, N, and number of elements, K. This reduces the performance of this preconditioner considerably. Although the pressure mass matrix M_p^* does not decrease the number of iterations as the C_P preconditioner does, it is more efficient since it only involves inverting the diagonal mass matrix.

Table 6.11: Performance of the preconditioners with increasing number of elements K. The 4 elements are ordered as in Fig. 6.10, the 8 elements are of equal size, with $K_x = 4$ and $K_y = 2$. A converged solution was obtained in 28 time steps.

K	It_U	It_H	Δt_U	P_U	P_H
4	49.96	36.13	≈ 80	C_P	S_P
4	76.89	35.25	2.646	M_p^*	S_P
4	138.50	36.30	4.874	I	S_P
4	75.57	141.26	4.016	M_p^*	I
4	137.71	145.16	7.384	I	I
8	73.96	41.54	≈ 320	C_P	S_P
8	109.71	41.60	8.016	M_p^*	S_P
8	189.18	38.77	13.080	I	S_P
8	106.32	165.35	12.896	M_p^*	I
8	188.39	152.97	21.336	I	I

Table 6.12: Performance of the preconditioners with different Reynolds number Re. Converged solutions were obtained in 28 and 26 time steps for $Re = 1$ and $Re = 10$, respectively.

Re	It_U	It_H	Δt_U	P_U	P_H
1	49.96	36.13	≈ 80	C_P	S_P
1	76.89	35.25	2.646	M_p^*	S_P
1	138.50	36.30	4.874	I	S_P
1	75.57	141.26	4.016	M_p^*	I
1	137.71	145.16	7.384	I	I
10	69.00	26.55	≈ 110	C_P	S_P
10	155.31	26.07	4.271	M_p^*	S_P
10	230.54	26.30	6.295	I	S_P
10	153.04	80.37	5.016	M_p^*	I
10	229.92	80.55	7.533	I	I

Table 6.13: Performance of the preconditioners with different Weissenber number We. The parameter β is set to zero. 28 time steps were needed to achieve a converged solution for $We = 0.1$, 7 time steps when $We = 0$.

We	It_U	It_H	Δt_U	P_U	P_H
0	46.57	39.46	≈ 75	C_P	S_P
0	64.14	38.97	2.376	M_p^*	S_P
0	129.43	39.02	4.747	I	S_P
0	65.00	153.44	3.626	M_p^*	I
0	130.29	155.02	7.262	I	I
0.1	49.96	36.13	≈ 80	C_P	S_P
0.1	76.89	35.25	2.646	M_p^*	S_P
0.1	138.50	36.30	4.874	I	S_P
0.1	75.57	141.26	4.016	M_p^*	I
0.1	137.71	145.16	7.384	I	I

The advantage of the overlapping Schwarz preconditioner for the Helmholtz operator is obvious. In all cases it provides reductions in both the number of iterations in the Helmholtz PCG loop and the time to reach convergence.

Chapter 7

Prediction of Flow of Polymer Melts

7.1 Introduction

In this chapter results are presented for the flow of an XPP fluid. It starts by giving some results for the transient start-up of Poiseuille flow through a planar channel. For the XPP fluid however, no analytic solution to this problem is available, and it has to be computed numerically. These numerical results are shown in section 7.2. The 1D solutions can be used as boundary conditions to 2D problems. An alternative is to impose periodic boundary conditions. The way periodic boundary conditions are imposed is explained in section 7.3. Results for the 2D channel flow problem are then presented in section 7.4 using both methods of imposing boundary conditions. The flow past a cylinder has been computed and the results are given in section 7.5. Both the coupled solver and the uncoupled solver have been used to simulate this flow. Finally the efficiency of some of the preconditioners described in section 4.4 is given in section 7.6.

A standard set of non-dimensional parameters has been derived from dimensional parameters for the DSM Stamlyn LD 2008 XC43 LDPE melt, characterized in [62]. Only one of the four modes given in [62] is used. The parameters for this mode are $q = 2$, $\epsilon = 1/3$, $\alpha = 0.15$. The ratio of viscosity parameter has been chosen the same as is used in the Oldroyd B model, i.e. $\beta = 1/9$. The influence on the solutions for the XPP model when varying these parameters, is being studied in this chapter. The same parameter setting is also used as one of the modes in the multimode calculations. The other modes are variations to these parameters, and they do not reflect different modes in the DSM Stamlyn melt. The multimode calculations are included in this chapter to demonstrate the ability of the developed software to simulate multimode models. Future work can involve using the exact modal parameter settings necessary to simulate the DSM Stamlyn LDPE.

7.2 1D Start-up to Poiseuille Flow

For the XPP model, no exact solution exists for steady Poiseuille flow through a planar channel, let alone an exact solution to the start-up of such a flow. For Newtonian fluids and for the Oldroyd B and UCM models the pressure gradient $\partial p/\partial x$ is related to the steady parabolic velocity profile through

$$\frac{\partial p}{\partial x} = \frac{\partial^2 u}{\partial y^2}, \tag{7.1}$$

but for the XPP model such a relation is not available. This means that is not known what pressure gradient induces what flow rate. However, to be able to make a fair comparison for the drag on a cylinder of a Newtonian or an Oldroyd B fluid to the drag evoked by an XPP fluid, the flows need to have the same flow rate.

First the same pressure gradient $\partial p/\partial x = -8$, that has been used to start up the flow of the Oldroyd B fluid in section 6.3, is used to start the flow of the XPP fluid as well. The height of the channel is $h = 1$, and it is divided into two equally sized spectral elements, with an approximation order $N = 10$. The time step is $\Delta t = 10^{-3}$. The Weissenberg number is set to $We = 1$ and also the Reynolds number is $Re = 1$. The other parameters are $q = 2$, $\epsilon = 1/3$, $\alpha = 0.15$, and $\beta = 1/9$. In Figs. 7.1 and 7.2 the start-up of the velocity at the centreline of the channel, and of the stretch and polymeric stress components at the channel wall is shown. There is a large overshoot in the shear stress before it reaches steady state, but the other overshoots and undershoots are not as those predicted for the Oldroyd B model in figure 6.2. The flow rate that results from this pressure gradient is computed to be 4.299, compared to the flow rate of 2/3 for the Oldroyd B model at the same pressure gradient. Next, a pressure gradient of $\partial p/\partial x = -2.820$ is applied to the

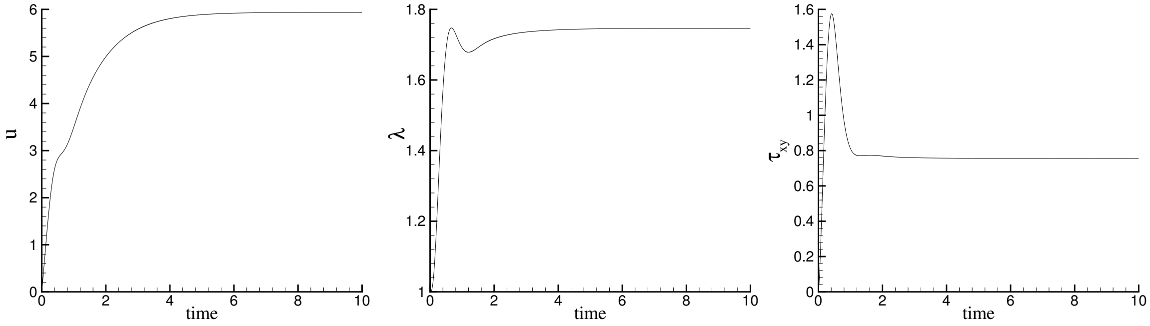

Figure 7.1: Evolution of the centreline velocity, and the stretch and polymeric shear stress at the wall of the channel, for an XPP fluid with $\partial p/\partial x = -8$.

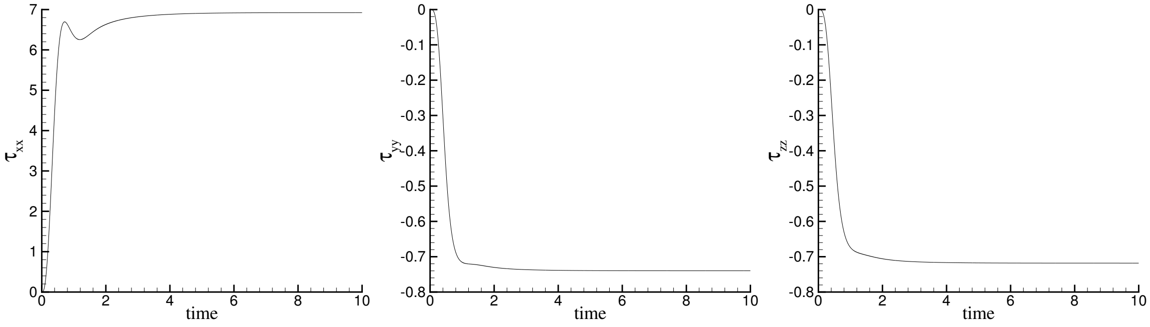

Figure 7.2: Evolution of the normal components of the polymeric stress at the wall of the channel, for an XPP fluid with $\partial p/\partial x = -8$.

same flow problem. Again the centreline velocity, the stretch and the components of the polymeric stress are monitored as they evolve in time. Figs. 7.3 and 7.4 show there is now an apparent overshoot in the transient velocity. The overshoots and undershoots in the transient stress components have decreased in size. The flow rate that accompanies this pressure gradient is 0.667, the same as the flow rate for the Oldroyd B model with a pressure gradient of $\partial p/\partial x = -8$. How this is achieved is explained in the next section.

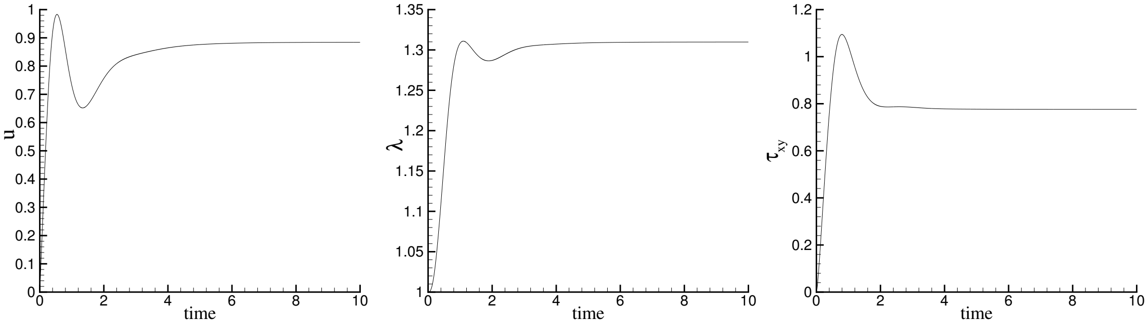

Figure 7.3: Evolution of the centreline velocity, and the stretch and polymeric shear stress at the wall of the channel, for an XPP fluid with $\partial p/\partial x = -2.820$.

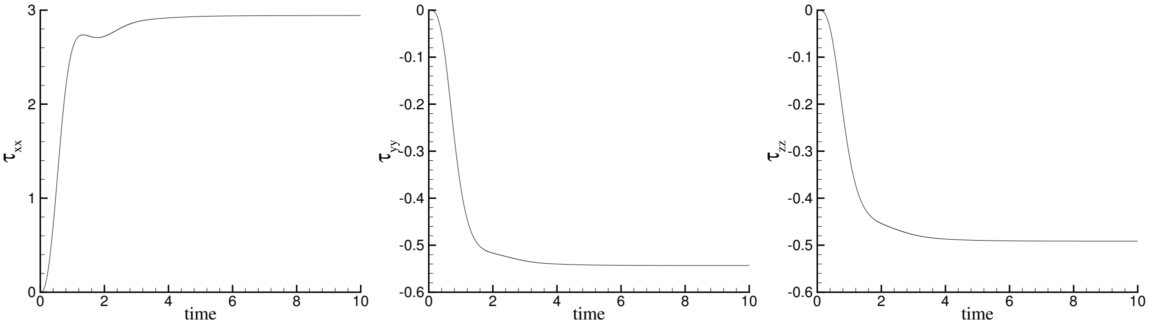

Figure 7.4: Evolution of the normal components of the polymeric stress at the wall of the channel, for an XPP fluid with $\partial p/\partial x = -2.820$.

The profile of the velocity at intermediate time levels for both values of the pressure gradient is shown in figure 7.5 and 7.6. It seems that the shear-thinning mechanism, which causes the velocity profile to blunt, only influences the solution after the

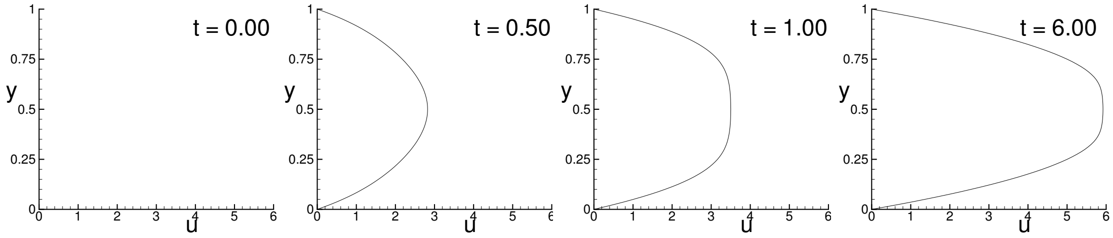

Figure 7.5: Velocity profile at intermediate time levels in start up of channel flow for an XPP fluid with $\partial p/\partial x = -8$.

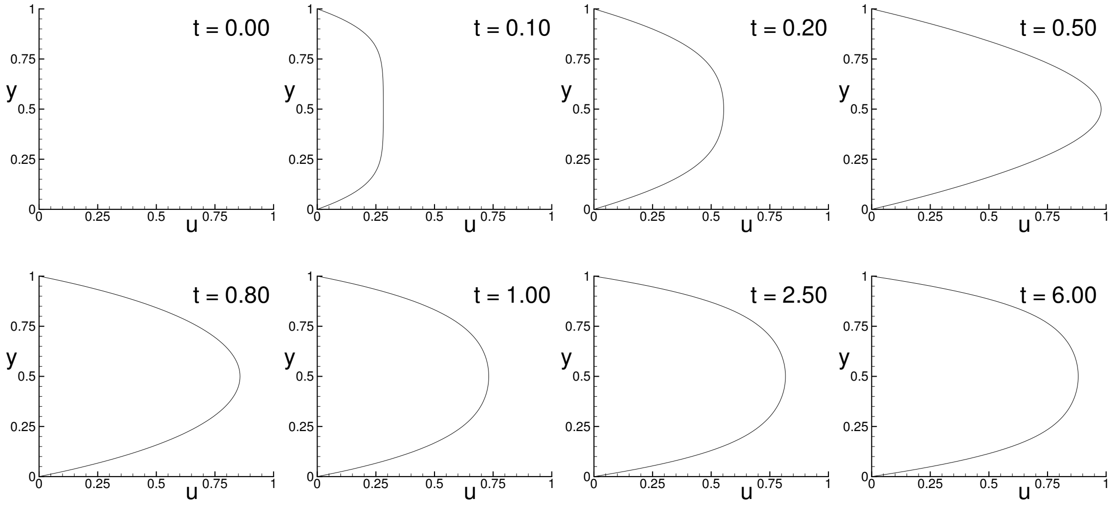

Figure 7.6: Velocity profile at intermediate time levels in start up of channel flow for an XPP fluid with $\partial p/\partial x = -2.820$.

overshoot has taken place.

7.3 Boundary Conditions

The governing equations for the XPP model do not possess an analytical solution for plane Poiseuille flow like the Oldroyd B model for example. The pressure gradient that was used in the previous section to bring about the correct flow rate for the transient calculation, is determined by imposing periodic boundary conditions. How these conditions are imposed is decribed below.

First of all a flow rate is prescribed and the solution of the Stokes problem is obtained. Together with zero extra-stresses everywhere in the domain, these make up the initial conditions for the viscoelastic problem. After every time step, the boundary conditions are modified as follows. The velocity, extra-stress, and stretch profiles at the penultimate line of points on the Gauss-Lobatto grid, i.e. one before the outflow, at each time step are used as inflow conditions for the next time step. In addition, the velocity profile is imposed as an outflow condition. At the wall no-slip conditions are assumed, and symmetry conditions are imposed along the line of symmetry.

7.4 Steady Channel Flow

In this section we describe how the steady state solutions for stretch, velocity profiles, pressure and stress components depend on the model parameters. The periodic boundary conditions as described above have been used. The build-up to the steady state now has no physical interpretation.

The non-dimensional length of the channel is $L = 128$, which is long enough to avoid the destabilizing effects of short channels reported in [15] and [60]. The height of the channel is taken to be $h = 2$. The mesh for the planar channel consists of four equally sized spectral elements: two elements in the cross channel direction, and two elements in the lengthwise direction. The iterations are stopped when the following convergence criterion is satisfied:

$$||\Delta\boldsymbol{\tau}||_{L_2} < 10^{-6} \qquad \text{and} \qquad ||\Delta\mathbf{u}||_{L_2} < 10^{-6}, \tag{7.2}$$

where the L_2 norms are defined in (5.17) and (5.18). The time step for these calculations is $\Delta t = 0.1$.

For the channel flow problem, the stretches for the channel flow have been calculated using both the direct relation (3.24) and the iterative scheme (3.23) and as should be expected they produce the same results. Since the cross channel derivatives of velocity for the pom-pom model are in general nonlinear, unlike the situation for the Stokes and Oldroyd B models, a mesh convergence study has been performed before obtaining further results. The channel flow problem is solved using spectral approximations ranging from $N = 3$ to $N = 10$. The Weissenberg number is $We = 1$, and also $Re = 1$. The parameters have been chosen as $\beta = 1/9$, $\alpha = 0.15$, $\epsilon = 1/3$, and the number of arms in the pom-pom molecule is $q = 2$. Fig. 7.7 shows convergence of the trace of the orientation tensor, $I_{\mathbf{s}}$, to the value 1 when using the iterative scheme (3.23). The error, $E(I_{\mathbf{s}})$, is the average error at the outflow of the channel,

$$E(I_{\mathbf{s}}) = \frac{1}{2(N+1)} \sum_{i=1}^{2(N+1)} |I_{\mathbf{s}(\mathbf{y_i})} - 1|, \tag{7.3}$$

where $2(N + 1)$ is the number of Gauss-Lobatto points located along the outflow of the channel. Based on this information, the remaining results shown in this section have been obtained with a polynomial order of $N = 7$.

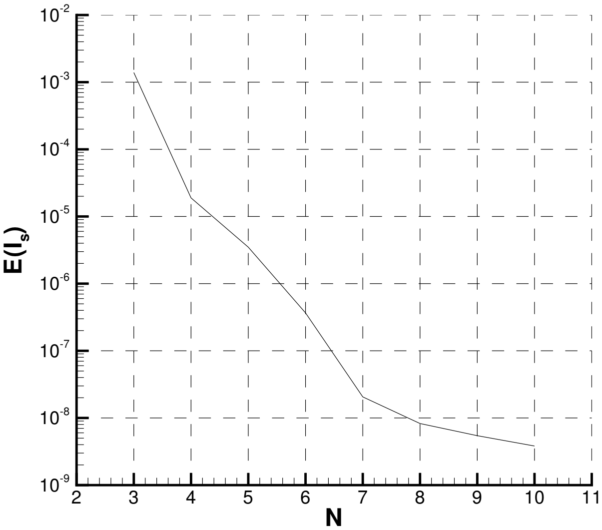

Figure 7.7: Convergence of $I_{\mathbf{s}}$.

In the remainder of this section, the parameters are fixed at $We = 3$, $Re = 1$, $\beta = 1/9$, $\alpha = 0.15$, $\epsilon = 1/3$, $q = 2$, unless otherwise mentioned.

The influence of varying Weissenberg number on the solution is plotted in Fig. 7.8. With increasing Weissenberg number the velocity profiles become more blunted, indicating stronger shear-thinning behaviour. Although the stretch keeps increasing with increasing We, the polymeric contribution to the extra-stress component τ_{xx} initially grows, but relaxes at higher values of We.

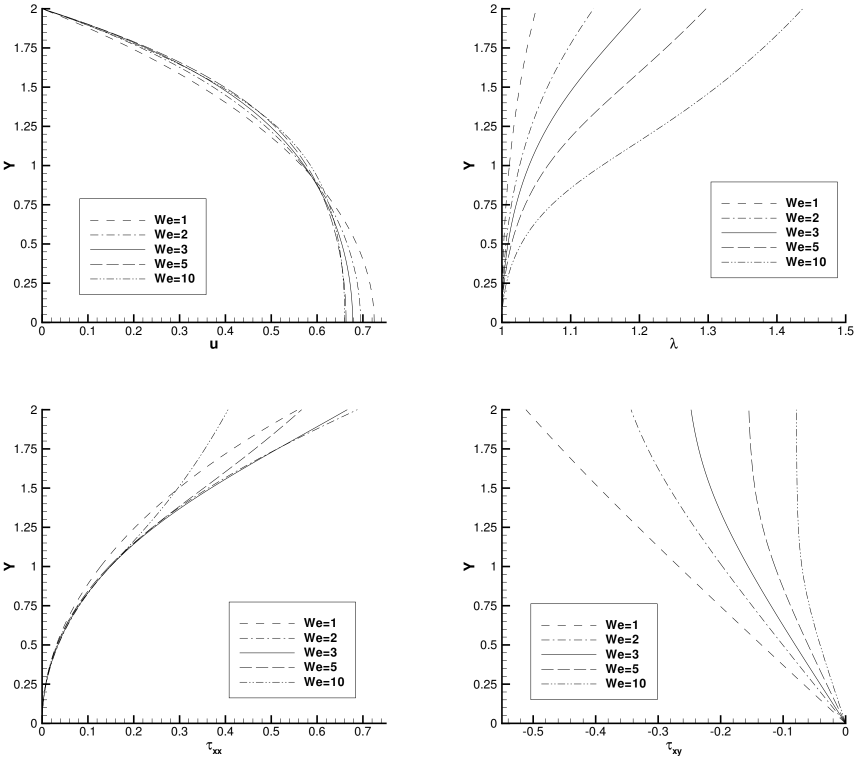

Figure 7.8: Dependence of the profiles of velocity, stretch, and polymeric contribution to the extra-stress components τ_{xx} and τ_{xy} at the outflow of the channel on Weissenberg number.

By varying the parameter ϵ, we effectively change the structure of the polymer melt. Higher values for ϵ correspond to less entangled backbones. In this case the molecules have relatively short backbones and the orientation and the stretch relax almost simultaneously. Lower values for ϵ on the other hand correspond to highly entangled melts. The orientation relaxation time is now much slower than the relaxation time of the stretch. Note that since the Weissenberg number is kept fixed, changing ϵ corresponds to changing λ_{0s}, the relaxation time of the stretch. Caution has to be taken in selecting the parameter ϵ, since the pom-pom model describes the behaviour of branched polymers. Values of ϵ for this class of polymers are well in between these two extrema. Fig. 7.9 shows that, although the flattening of the velocity profile is larger at low values of ϵ, the stretch and stresses near the wall are lower than for higher values of ϵ.

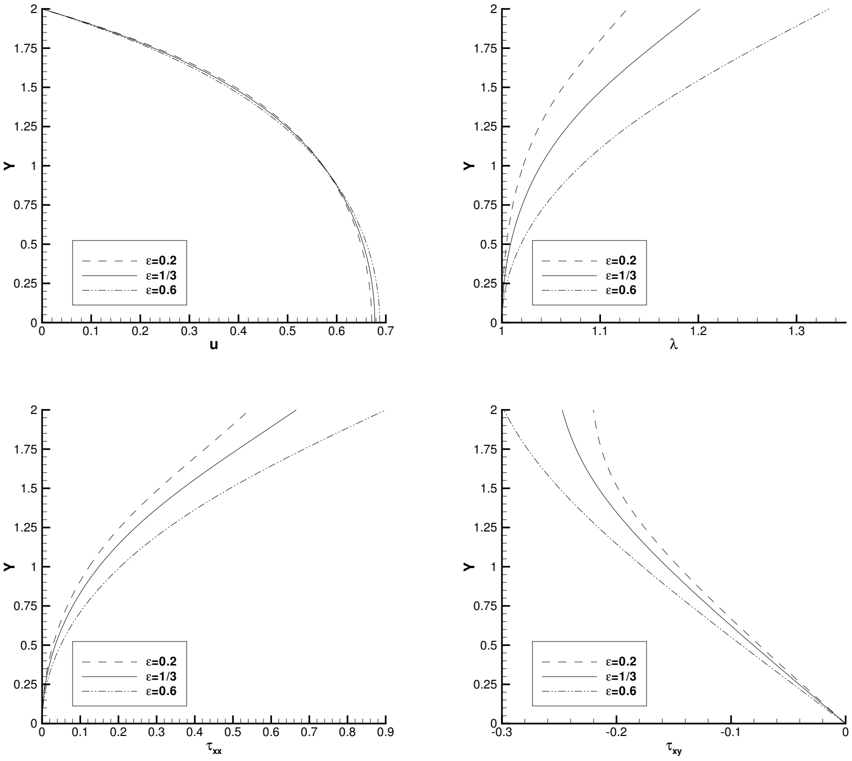

Figure 7.9: Dependence of the profiles of velocity, stretch, and polymeric contribution to the extra-stress components τ_{xx} and τ_{xy} at the outflow of the channel on ϵ.

With all other parameters fixed, the variation of the number of arms q hardly affects

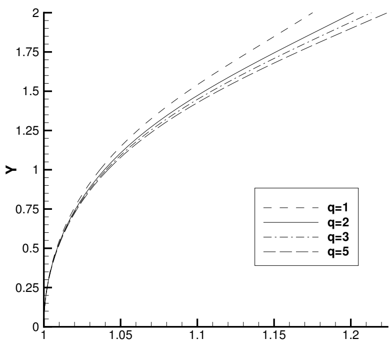

Figure 7.10: Dependence of the profile of the stretch λ in the cross channel direction y at the outflow of the channel, on the number of arms q.

the velocity profile, although when the number of arms is increased, a slight increase in stretch may be observed in Fig. 7.10. Note here that when $q = 1$, the molecule is actually linear and falls outside the range of the pom-pom molecules. The melt may now be seen as a linear polymer, the behaviour of which is known not to be predicted correctly using the pom-pom model.

The parameter α has no visual effect on the velocity, extra-stress and stretch profiles. Since α is the parameter that endows the model with a nonzero second normal stress differences, this result is hardly surprising. Since the second normal stress difference in a plane channel has no influence on the solution, te influence of α is similarly insignificant.

When a higher value for the parameter β is chosen, the melt is effectively diluted, and lower stretches are expected to be found, together with a less flattened velocity profile, and more Oldroyd-like extra-stress behaviour. Fig. 7.11 shows exactly this behaviour as β is increased from $\beta = 0$ to $\beta = 0.5$.

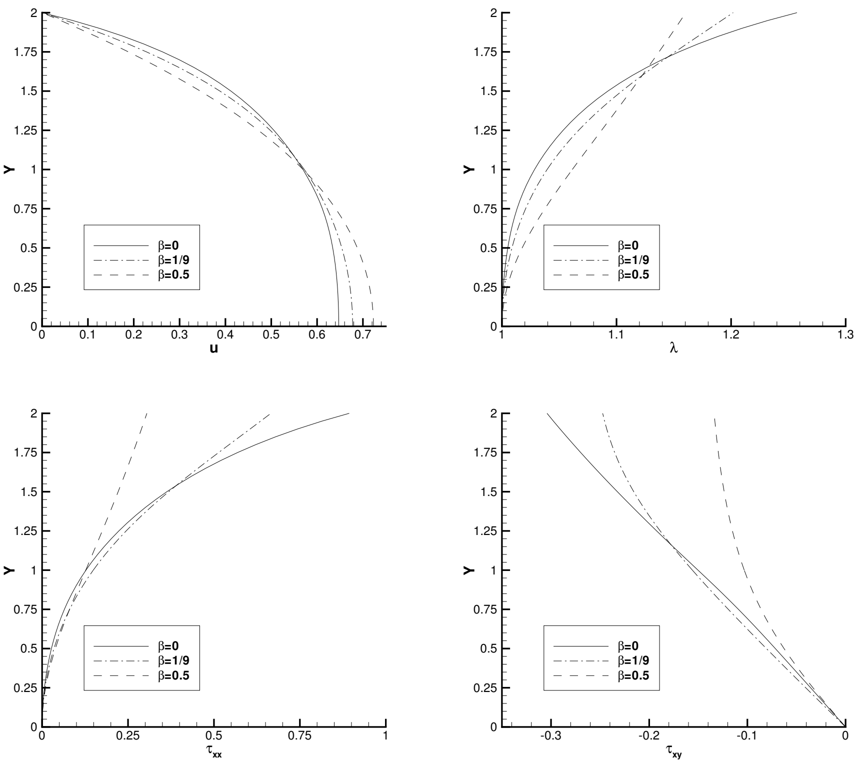

Figure 7.11: Dependence of the profiles of velocity, stretch, and polymeric contribution to the extra-stress components τ_{xx} and τ_{xy} at the outflow of the channel on β.

7.4.1 Multimode solutions

Three parameter settings from the single mode solutions are used as modes in a multimode solution for the same channel flow problem. The settings for the modes are

$$\text{mode 1:}\quad We = 3, \quad \tilde{\beta} = 1/3, \quad \alpha = 0.15, \quad \epsilon = 1/3, \quad q = 2,$$

$$\text{mode 2:}\quad We = 3, \quad \tilde{\beta} = 1/3, \quad \alpha = 0.15, \quad \epsilon = 0.6, \quad q = 2,$$

$$\text{mode 3:}\quad We = 3, \quad \tilde{\beta} = 1/3, \quad \alpha = 0.15, \quad \epsilon = 1/3, \quad q = 5,$$

and the values in the momentum equation are $Re = 1$ and $\beta = 1/9$. In Fig. 7.12 the velocity profile of the steady solution is shown, together with profiles of the stretch and stresses. Since each of the modes is characterized by a parameter setting that has also been used in the previous subsection to model single mode XPP fluids, comparisons can be made between the multimode solutions in Fig. 7.12 and the corresponding single modes solutions in Figs. 7.9 and 7.10. It can be seen that that each mode i is stretched approximately the same way as in the corresponding single mode solutions. The modal stresses however are lower than their single mode solution counterparts.

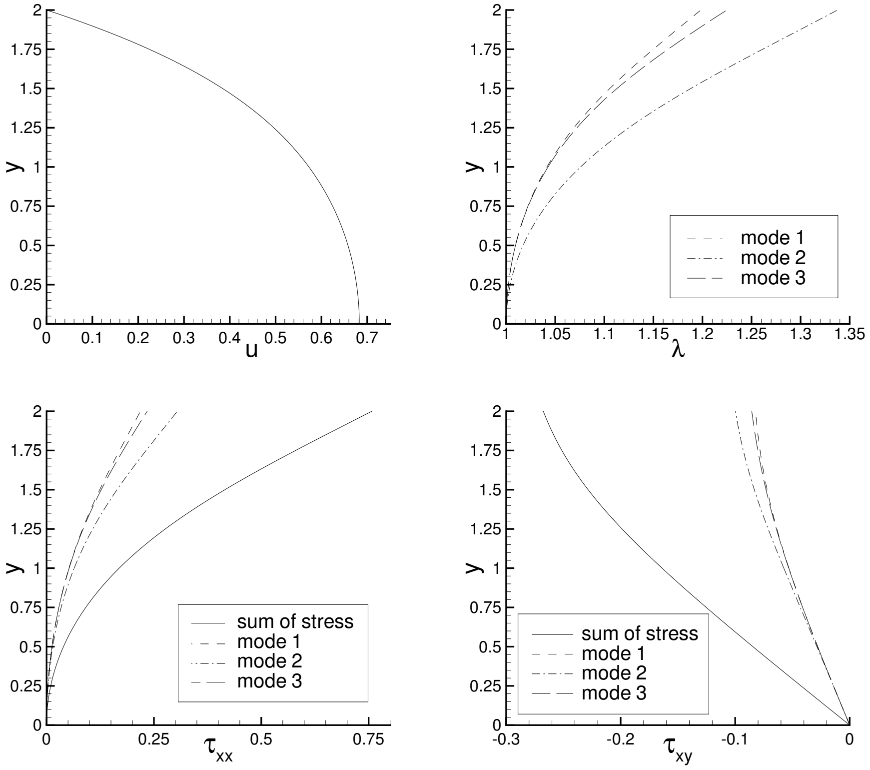

Figure 7.12: Profiles of velocity, stretch and stress components τ_{xx} and τ_{xy} for the channel flow of a multimode XPP model.

In Fig. 7.13 the normal stress components computed using the multimode model, are compared to the normal stress components predicted by the single mode calculations based on each of the constituent modes of the multimode calculation. Apparently, the multimode stresses are approximately an average solution of the stresses in the single mode solutions.

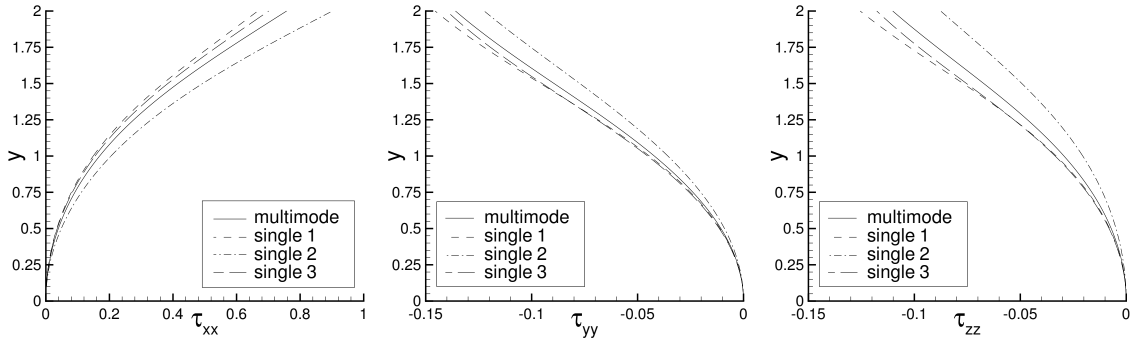

Figure 7.13: Profiles of all normal stress components of a multimode XPP model compared to the corresponding single mode solutions.

Another multimode simulation has been performed using only two modes. They are essentially the same as the first two modes from the previous multimode model, but the relative viscosity ratios $\tilde{\beta}_i$ are changed. The modes are now

$$\text{mode 1:}\quad We = 3,\quad \tilde{\beta} = 1/4,\quad \alpha = 0.15,\quad \epsilon = 1/3,\quad q = 2,$$

$$\text{mode 2:}\quad We = 3,\quad \tilde{\beta} = 3/4,\quad \alpha = 0.15,\quad \epsilon = 0.6,\quad q = 2.$$

The viscosity of the second mode is now three times the viscosity of the first mode.

Again, the solutions of the two-mode model shown in Fig. 7.14 can be compared to the solutions of the single mode calculations based on each of the constituent modes of the multimode calculation. These corresponding single mode solutions can be found in Fig. 7.9. The stretches that are predicted for the individual modes are similar to the stretches predicted by these equivalent single mode models. Since the viscosity of the second mode takes up a larger part of the total polymeric viscosity, the stress of the second mode has a greater influence on the total stress. This can also be seen in Fig. 7.15, in which the normal stress components of the multimode model are compared to the stress components predicted by the equivalent single mode simulations. As can be seen, the stress in the multimode model is still an average of the corresponding single mode stresses, but it is weighted by the viscosity ratios $\tilde{\beta}_i$.

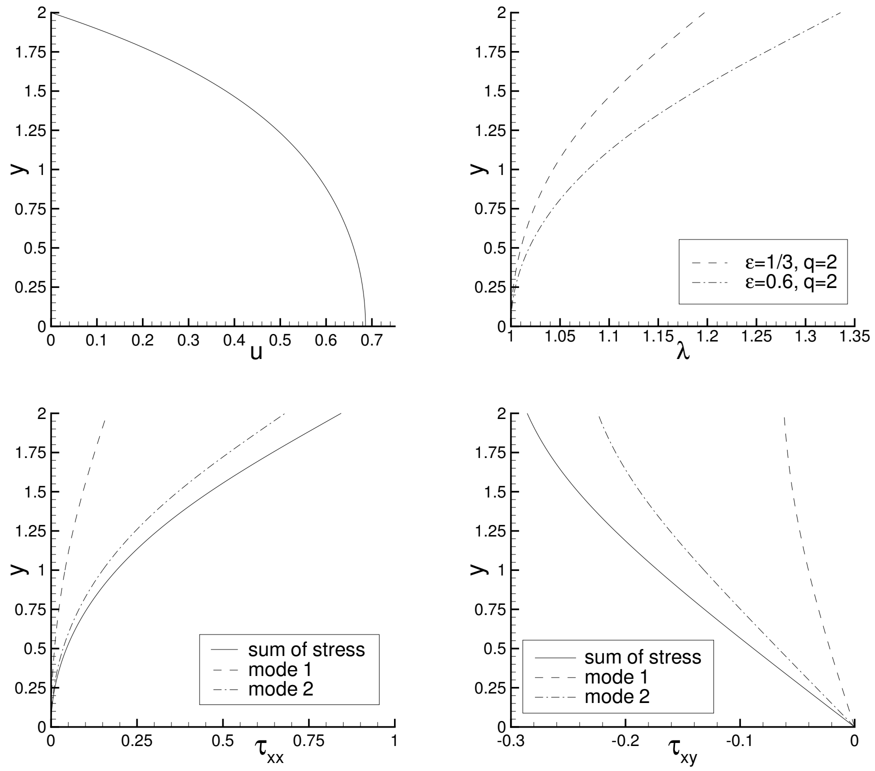

Figure 7.14: Profiles of velocity, stretch and stress components τ_{xx} and τ_{xy} for the channel flow of a multimode XPP model.

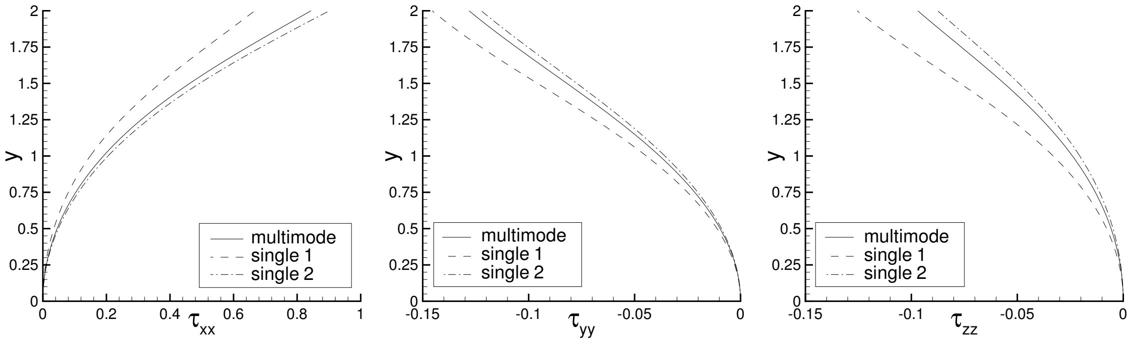

Figure 7.15: Profiles of all normal stress components of a multimode XPP model compared to the corresponding single mode solutions.

7.5 Flow Past a Cylinder

The flow of an XPP fluid past a cylinder is computed using both the coupled solver and the uncoupled solver. As the Weissenberg number is increased, solutions for the various variables are analyzed. The uncoupled solver allows for prediction of higher Weissenberg numbers and therefore a study of parameter variation is performed using this solver only.

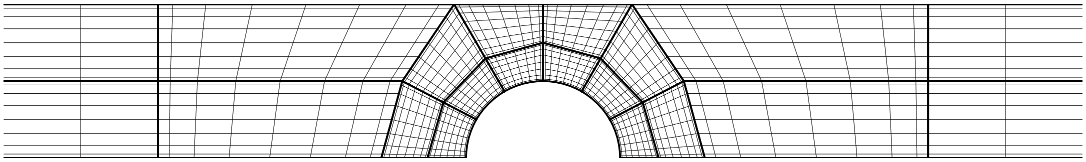

Figure 7.16: Spectral element mesh with the spectral elements printed bold.

The cylinder is placed symmetrically in a channel of 2 units half-width. The ratio of the radius of the cylinder to the half width of the channel is $R/h = 0.5$. The geometry of the problem is shown in Fig. 5.2. The benchmark problem is acknowledged to be more difficult than the related sphere problem because, for the same aspect ratio R/h, the planar flow past a cylinder undergoes a stronger contraction and expansion than the axisymmetric flow past a sphere.

The computational domain extends a distance $L_i = 25$ units upstream and $L_o = 25$ units downstream of the cylinder so that the assumption of fully developed flow conditions at entry and exit is valid. The spectral element mesh used to solve this problem consists of $K = 20$ elements and is shown in Fig. 7.16. These conditions are taken from the solution for the start-up of Poiseuille flow in a planar channel obtained earlier. With the uncoupled method, transient boundary conditions have also been used to find solutions to this flow.

7.5.1 Coupled solver

Solutions have been obtained using a degree of the spectral approximation of $N = 7$. The time step is chosen to be $\Delta t = 5 \times 10^{-3}$. The pure convection problems are solved with time steps that are an eighth of the size of the global time step ($M = 8$).

The convergence criteria in the PCG methods are set to 10^{-9} for the Uzawa operator and 10^{-14} for the Helmholtz operator. The iterations are stopped when the following convergence criterion is satisfied:

$$||\Delta\boldsymbol{\tau}||_{L_2} < 10^{-6} \qquad \text{and} \qquad ||\Delta\mathbf{u}||_{L_2} < 10^{-6}. \tag{7.4}$$

The non-dimensional drag on the cylinder is computed using the expression

$$F = 2\int_0^{\pi} \left\{ (-p + 2\beta\frac{\partial u}{\partial x} + \tau_{xx})\cos\theta + (\beta(\frac{\partial v}{\partial x} + \frac{\partial u}{\partial y}) + \tau_{xy})\sin\theta \right\} \, d\theta, \tag{7.5}$$

where F has been made dimensionless with $\mu_t U$.

Results have been obtained for the flow of an XPP fluid past the confined cylinder. The material parameters that have been used in the XPP model are: $\beta = 1/9$, $\epsilon = 1/3$, $\alpha = 0.15$. The velocity has been made dimensionless using the flow rate, and the characteristic length is the radius of the cylinder. For a Reynolds number of $Re = 1$ and Weissenberg numbers of $We = 0.25$ and $We = 0.35$, contour plots of the stretch, and the first normal stress difference, $N_1 = \tau_{xx} - \tau_{yy}$, are presented in Figs. 7.17 and 7.18, respectively. High values for the stretch are found at the wall above the cylinder, but the highest peak in stretch is on the cylinder wall itself, shifted slightly to the right as a result of inertia and the convective derivatives of stress and stretch.

The stretch, and the components of the polymeric contribution to the stress along the cylinder wall and the plane of symmetry located at $y = 0$, are plotted in Fig. 7.19 and Fig. 7.20, for $We = 0.25$ and in Fig. 7.21 and Fig. 7.22, for $We = 0.35$. Although the stretch along the cylinder wall has increased with increasing Weissenberg number, a relaxation of the stresses can be observed. This can be attributed to the fact that local Weissenberg numbers may be higher than the global Weissenberg number. Therefore the solution exhibits a similar behaviour to the stress relaxation at higher

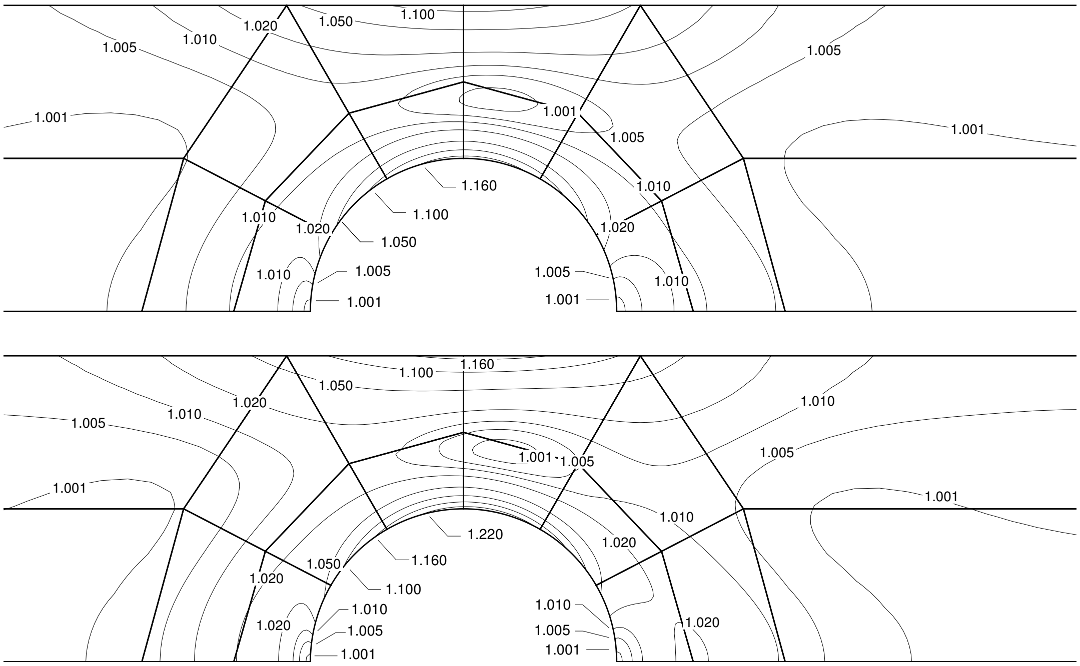

Figure 7.17: Contours of the stretch λ, for $We = 0.25$ (top) $We = 0.35$ (bottom).

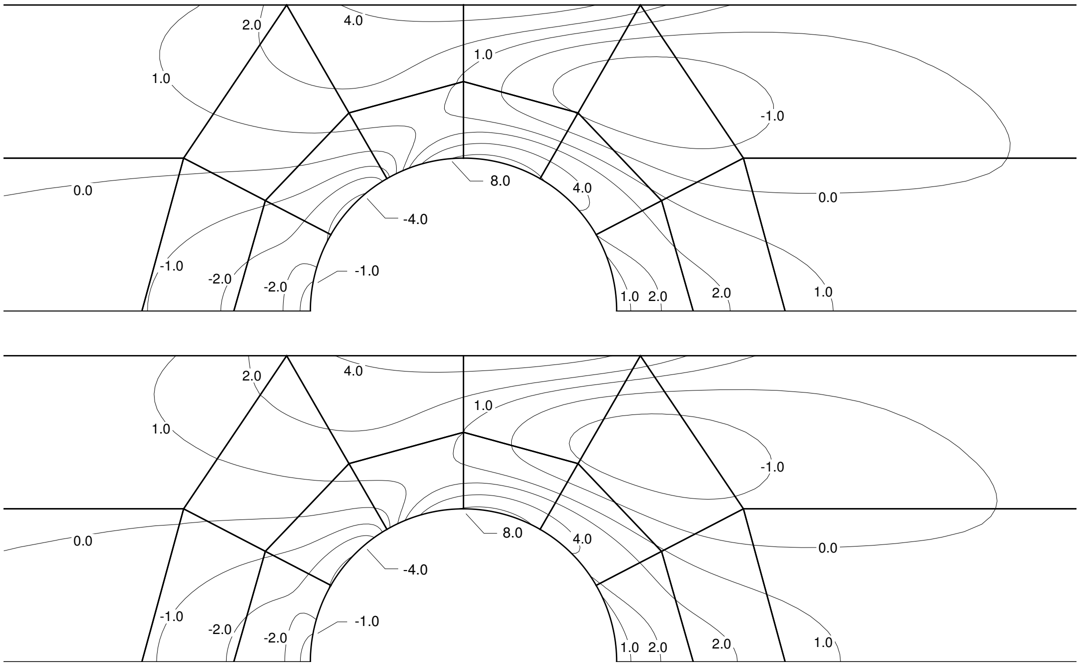

Figure 7.18: Contours of the first normal stress difference N_1, for $We = 0.25$ (top) $We = 0.35$ (bottom).

Weissenberg numbers that is observed in the channel flow, see Fig.7.8.

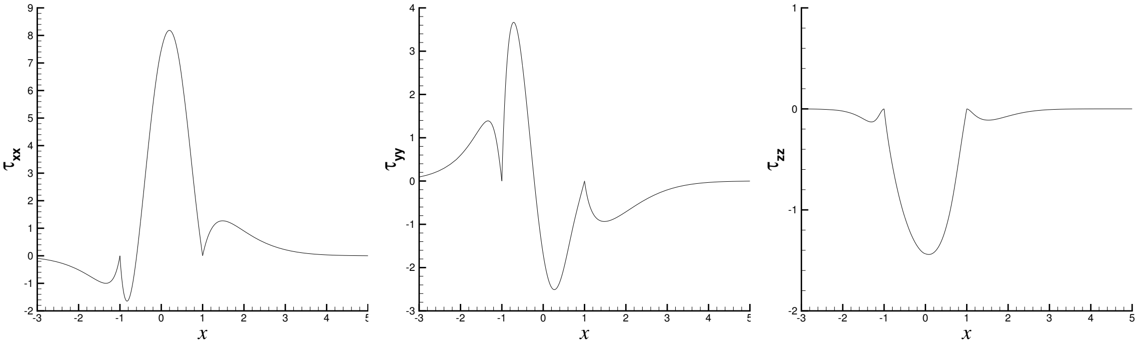

Figure 7.19: The components of the polymeric stress on the line $y = 0$ and the cylinder wall, for an XPP fluid with $We = 0.25$.

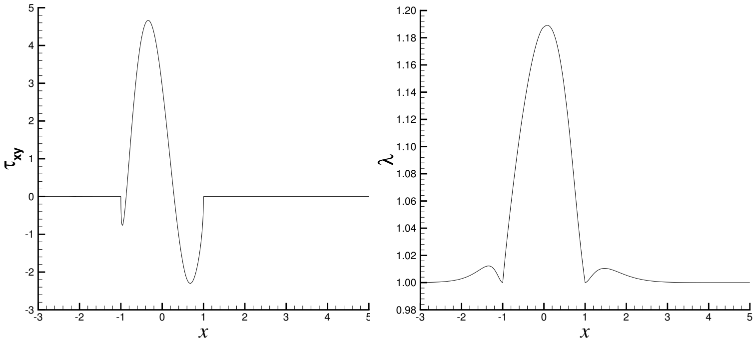

Figure 7.20: The shear stress component and the stretch on the line $y = 0$ and the cylinder wall, for an XPP fluid with $We = 0.25$.

Table 7.1 shows the drag reduction at increasing values for the Weissenberg number. Note that even for these small Weissenberg numbers, the drag has decreased considerably more than in the Oldroyd B model for $We = 0.5$, for which the predicted drag is 115.5426. This may be explained by the fact that the stresses predicted in the XPP model on the cylinder wall are much lower than the stresses predicted by the Oldroyd B model.

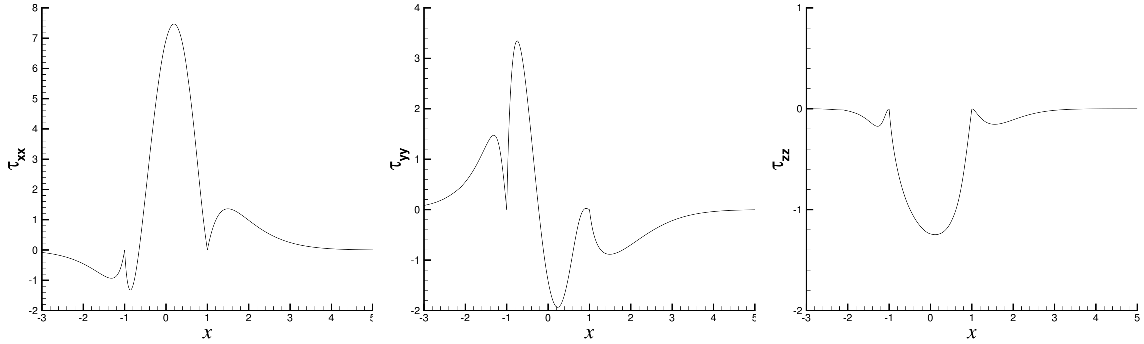

Figure 7.21: The components of the polymeric stress on the line $y = 0$ and the cylinder wall, for an XPP fluid with $We = 0.35$.

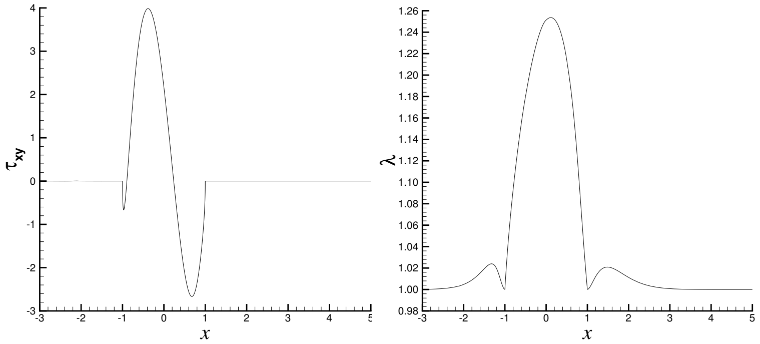

Figure 7.22: The shear stress component and the stretch on the line $y = 0$ and the cylinder wall, for an XPP fluid with $We = 0.35$.

Table 7.1: Drag force F with varying Weissenberg number.

We	0	0.25	0.35
F	132.4057	93.8314	82.0643

7.5.2 Uncoupled solver

The results shown in the previous subsection and in [59] are only for modest Weissenberg. Higher Weissenberg numbers can be reached using the uncoupled solver. The time step that is used in the uncoupled solver is $\Delta t = 10^{-2}$, and the calculations are stopped when the L_2-norms given in (5.17) and (5.18) have both reduced to 10^{-8}. The convergence criteria in the PCG methods are set to 10^{-9} for the Uzawa operator and 10^{-14} for the Helmholtz operator. The convergence criterion in the Bi-CGStab method for the non symmetric operator S_N is set to 10^{-12}. Unless otherwise mentioned, the LUST method is used.

First a mesh convergence study is performed. The computed drag on the cylinder for a XPP fluid with $We = 1$, $Re = 1$, $\beta = 1/9$, $\alpha = 0.15$, $q = 2$, $\epsilon = 1/3$ is given for different values of the approximation order N in Fig. 7.23. The stretch λ on the cylinder wall for increasing N is also shown in Fig. 7.23. The coordinate θ is defined on the cylinder wall as $\theta = \pi/2 - \arccos(x)$. Based on these results a value of $N = 7$ is used to obtain results for different parameter settings.

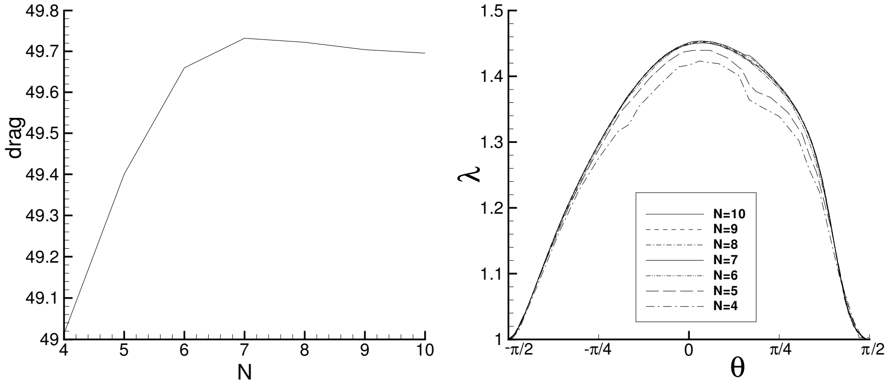

Figure 7.23: Mesh convergence of the drag and of the stretch on the cylinder wall with increasing N.

For the different parameters, the stretch on the cylinder wall is shown in Fig. 7.24. The results are similar to what was concluded for the flow through a planar channel. The influence of the parameter α is very limited. Increasing the number of arms from $q = 2$ to $q = 5$ though, causes the maximum stretch to increase from 47% to around 58%. An even greater effect on the maximum stretch is caused by increasing the value of ϵ. The maximum stretch is now around 70%. By setting the parameter β to zero, there is no Newtonian viscosity in the system. This not only increases the stretch to about 62%, but also changes the shape of the curve. The maximum is now tilted more towards the downstream end of the cylinder.

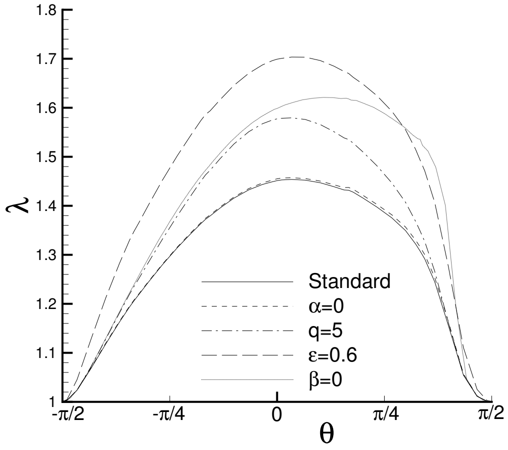

Figure 7.24: The stretch on the cylinder wall with varying parameter settings. Standard parameters are $Re = 1$, $We = 1$, $\beta = 1/9$, $\epsilon = 1/3$, $q = 2$ and $\alpha = 0.15$.

The change in the parameter β also constitutes the greatest change in the computed drag. It decreases from 49.7320 with $\beta = 1/9$ to 37.9850 with $\beta = 0$. All other changes lead to an increase of the drag. Changing ϵ from $\epsilon = 1/3$ to $\epsilon = 0.6$ increases the drag from 49.7320 to 55.2346. The change from $\alpha = 0$ to $\alpha = 0.15$ only increases the drag to 50.2972, and the change from two arms to five arms increases the drag to 50.8165.

The computations involving zero Newtonian viscosity have been performed on a mesh in which narrow elements have been placed around the cylinder, as depicted in Fig. 7.25. Moreover, the approximation order has also been increased from $N = 7$ to $N = 10$. This ensures that the stress boundary layer around the cylinder is captured with sufficient resolution. Since the smallest mesh size of the smallest elements has now decreased, the time step is also decreased from 10^{-2} to $2 \cdot 10^{-3}$. To show the decrease in size of the boundary layers, contour plots of the first normal polymeric stress component τ_{xx} are shown in Fig. 7.26. Contours of 25% and 50% stress levels are shown. Fig. 7.27 shows the contours of 50% stretch, and that the stretch also forms a boundary layer on the cylinder. At the higher Weissenberg number of $We = 2$, the 50% contour may be further away from the cylinder wall, but high stresses and stretches are also predicted in the regions in front of the cylinder and behind the cylinder.

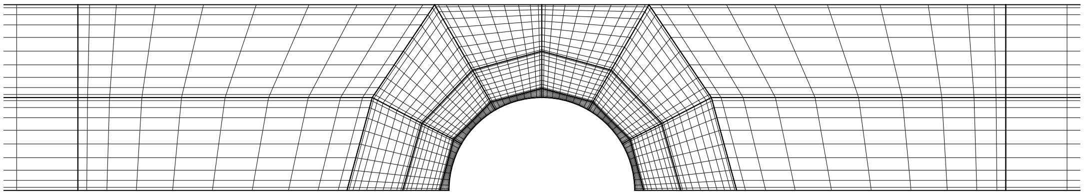

Figure 7.25: Mesh with 26 spectral elements and $N = 10$.

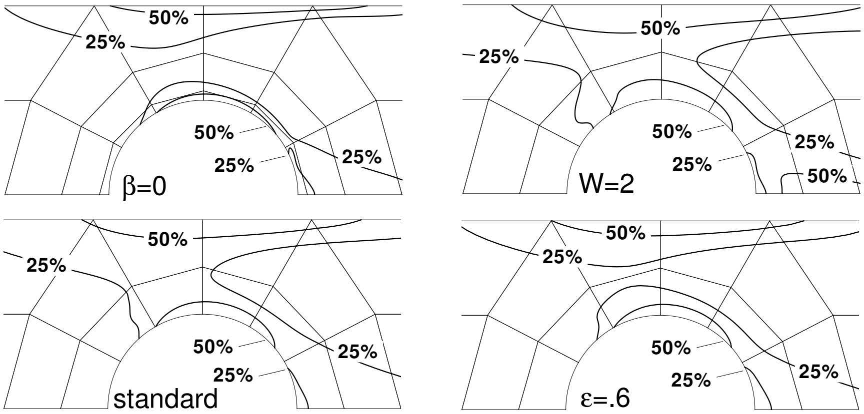

Figure 7.26: Contours of the first normal stress component τ_{xx} indicating the size of the stress boundary layer for the different parameter settings. The standard parameter setting is $We = 1$, $\beta = 1/9$, $\epsilon = 1/3$, $q = 2$ and $\alpha = 0.15$.

The influence of an increase of Weissenberg number on the stretch along the cylinder wall is also monitored. Fig. 7.28 shows the stretch profiles for a range of Weissenberg

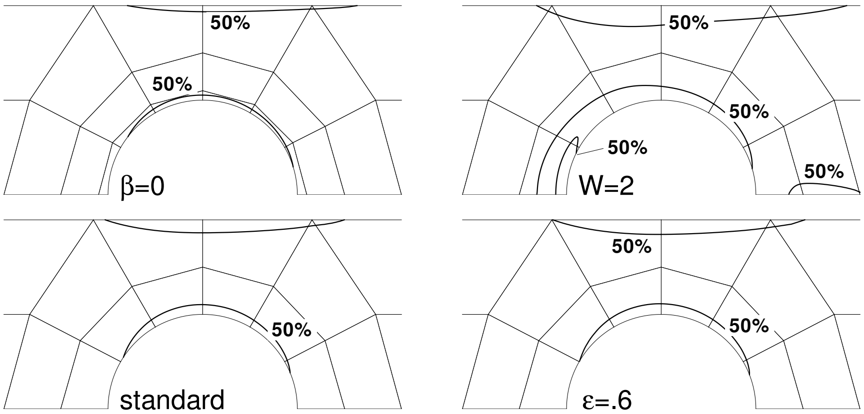

Figure 7.27: Contours of the stretch λ indicating the size of the stretch boundary layer for the different parameter settings. The standard parameter setting is $We = 1$, $\beta = 1/9$, $\epsilon = 1/3$, $q = 2$ and $\alpha = 0.15$.

numbers between $We = 0.25$ and $We = 5$. The stretch keeps increasing with increasing Weissenberg number. At the higher Weissenberg numbers $We \geq 2$, there is a need for a finer approximation to avoid divergence of the numerical solution, so the value of N has been increased. This behaviour is opposite to what is often observed in computations involving the Oldroyd B model, where increasing mesh resolution can result in a lower maximum attainable Weissenberg number. At the Weissenberg number of three, a result has been added for a value of $\epsilon = 0.6$ as well. This solution and the solution for $We = 5$ still show some irregularities, and an even higher value for N could be used to obtain better solutions to these problems. The values of the drag that have been computed for these Weissenberg numbers are given in Table 7.2. Especially at the low Weissenberg numbers, the drag reduction is large. At the Weissenberg number of five, the drag is only 18.4% of the Newtonian value.

Table 7.2: Drag force F with varying Weissenberg number.

We	0	0.25	0.5	1.0	2.0	3.0	5.0
F	132.4057	93.8730	69.9838	49.7320	35.1179	29.3267	24.3724

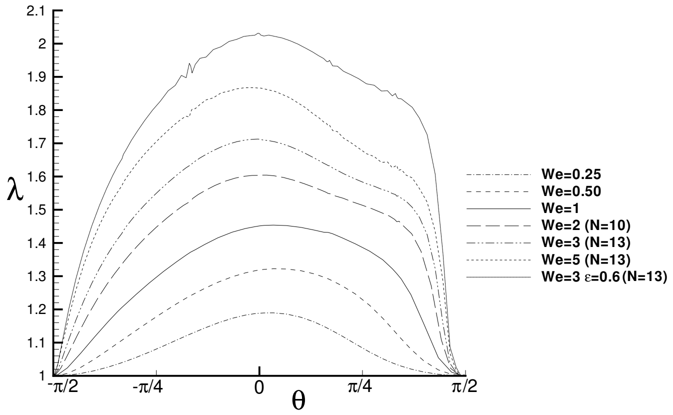

Figure 7.28: The stretch on the cylinder wall with increasing We. Other parameters are $Re = 1$, $\beta = 1/9$, $\epsilon = 1/3$, $q = 2$ and $\alpha = 0.15$. The result for $We = 3$ and $\epsilon = 0.6$ is also included.

For a Weissenberg number of $We = 1$ and with parameters $Re = 1$, $\beta = 1/9$, $\alpha = 0.15$, $q = 2$, $\epsilon = 1/3$, the flow past a cylinder is calculated. Contour plots of the first normal stress difference N_1 and the stretch λ are shown in Fig. 7.29.

The highest values for the stretch that have been computed in this problem are for a parameter set of $We = 3$ and $\epsilon = 0.6$, and also $Re = 1$, $\beta = 1/9$, $\alpha = 0.15$ and $q = 2$. For this set of parameters, the stretch along the cylinder wall is already shown in Fig. 7.28. The drag computed with these parameters is 32.5506. The stretch on the cylinder wall locally exceeds $\lambda = 2$, which is more than the number of arms. In the original pom-pom model this would not be possible, but in the XPP model the constraint that the stretch can not exceed the number of arms is removed. Contour plots of the first normal stress difference and the stretch are shown in Fig. 7.30.

In Figs. 7.31 - 7.34 the profiles along the plane of symmetry $y = 0$ and the cylinder are plotted both for the XPP fluid with $We = 1$, $\epsilon = 1/3$, $Re = 1$, $\beta = 1/9$, $\alpha = 0.15$, $q = 2$ and for the XPP fluid with $We = 3$, $\epsilon = 0.6$, $Re = 1$, $\beta = 1/9$, $\alpha = 0.15$,

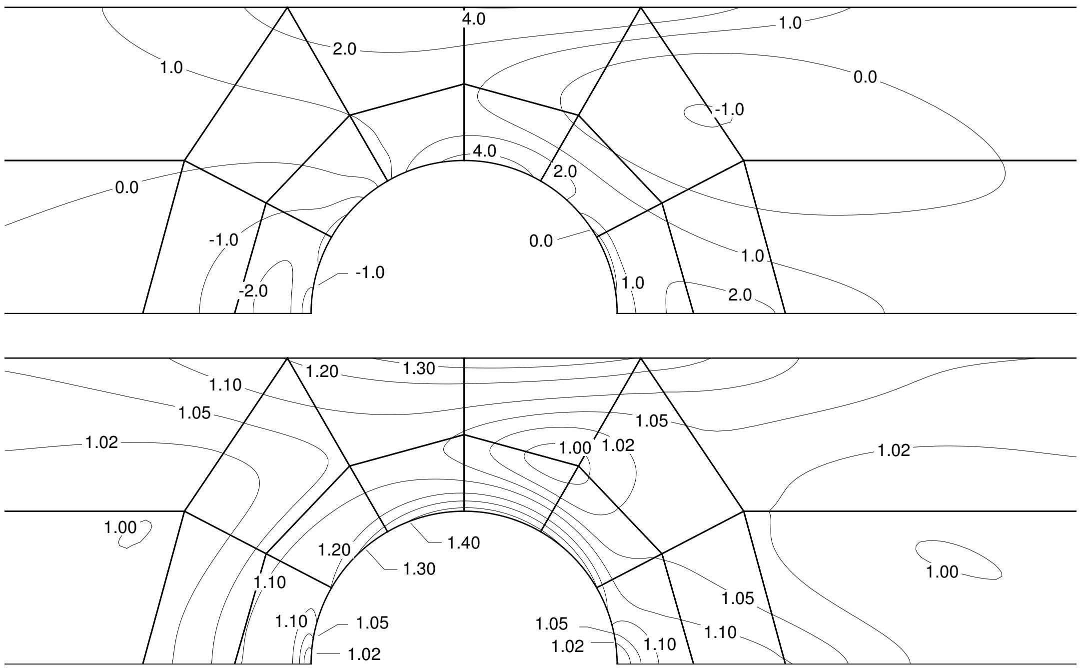

Figure 7.29: Contours of the first normal stress difference N_1 (top) and for the stretch λ (bottom), for $We = 1$.

$q = 2$. For the Weissenberg number of one, it can be seen that the levels of the polymeric stress components on the cylinder wall have decreased in comparison to Figs. 7.21 and 7.22, but that the stresses on the symmetry line have kept increasing. The maximum stretch has increased to 45%, but the stretch along the symmetry line has increased more notably to about 16% in both stagnation areas in front of and just behind the cylinder. The results for $We = 3$ and $\epsilon = 0.6$ show that these trends persist. The stress levels are of equal size on the cylinder and in the stagnation areas, and the stretch shows the same pattern. The maximum stretch is still on the cylinder wall and amounts to 103%, the levels of the stretch just in front of and just behind the cylinder have increased to 85% and 90% respectively.

For the XPP fluid with $We = 1$, $\epsilon = 1/3$, $Re = 1$, $\beta = 1/9$, $\alpha = 0.15$ and $q = 2$, the solution has been calculated using the LUST method as well as the SUPG method and the Galerkin method. In [39] it is found that compared to Galerkin and SUPG,

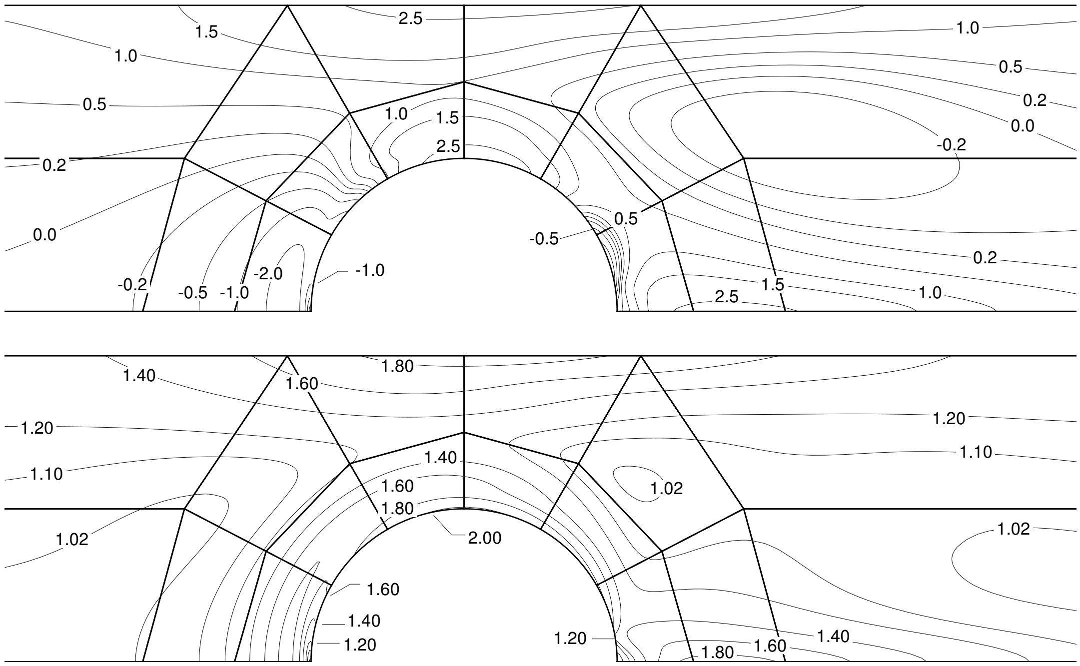

Figure 7.30: Contours of the first normal stress difference N_1 (top) and for the stretch λ (bottom), for $We = 3$ and $\epsilon = 0.6$.

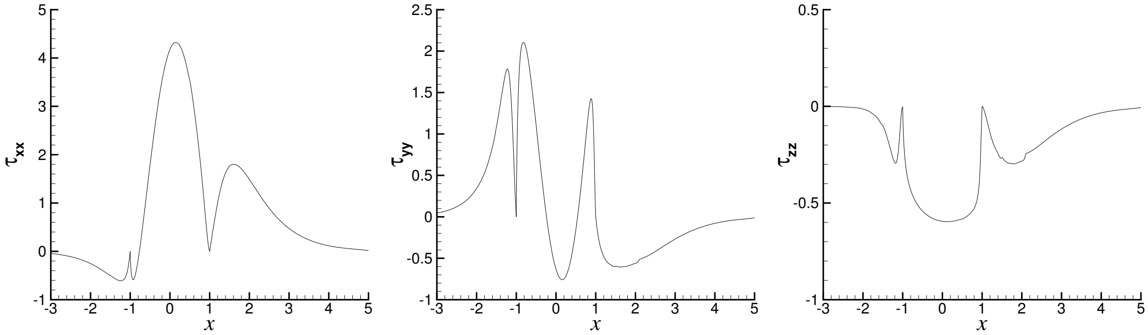

Figure 7.31: The normal components of the polymeric stress on the line $y = 0$ and the cylinder wall, for an XPP fluid with $We = 1$.

the use of LUST results in superior smoothness of the polymeric stress solutions of the Oldroyd B model in flow past a cylinder. This superior smoothness has not been found for this XPP fluid. There is however a slight decrease of about 0.1% in the computed drag on the cylinder as can be seen in Table 7.3

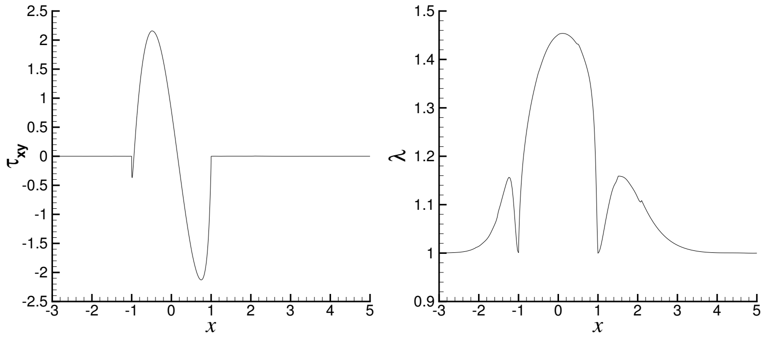

Figure 7.32: The shear stress component and the stretch on the line $y = 0$ and the cylinder wall, for an XPP fluid with $We = 1$.

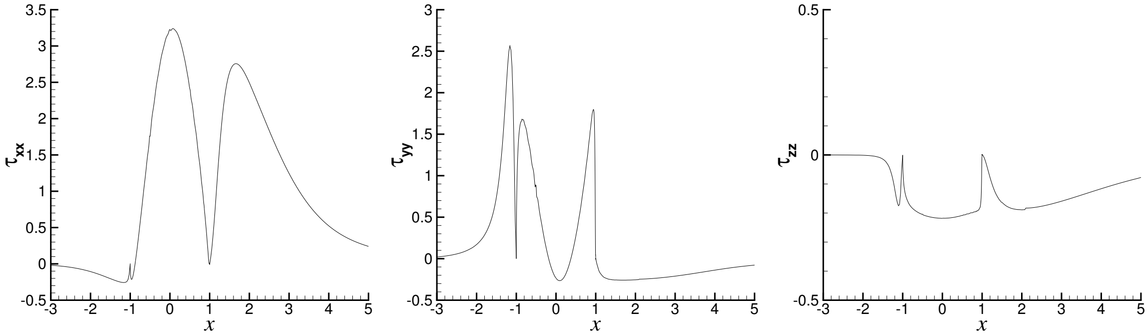

Figure 7.33: The normal components of the polymeric stress on the line $y = 0$ and the cylinder wall, for an XPP fluid with $We = 3$ and $\epsilon = 0.6$.

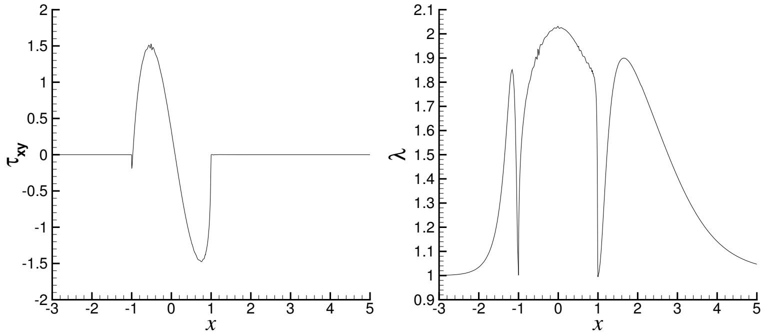

Figure 7.34: The shear stress component and the stretch on the line $y = 0$ and the cylinder wall, for an XPP fluid with $We = 3$ and $\epsilon = 0.6$.

Table 7.3: Computed drag using different test functions.

Galerkin	SUPG	LUST
49.7881	49.7689	49.7320

Transient boundary conditions

Two transient calculations have been performed for the start-up of the flow past the cylinder. In Fig. 7.35 the drag is shown as a function of time for an XPP fluid for the Weissenberg numbers $We = 0.5$ and $We = 1$. The other parameters are $Re = 1$, $\beta = 1/9$, $\alpha = 0.15$, $q = 2$, $\epsilon = 1/3$.

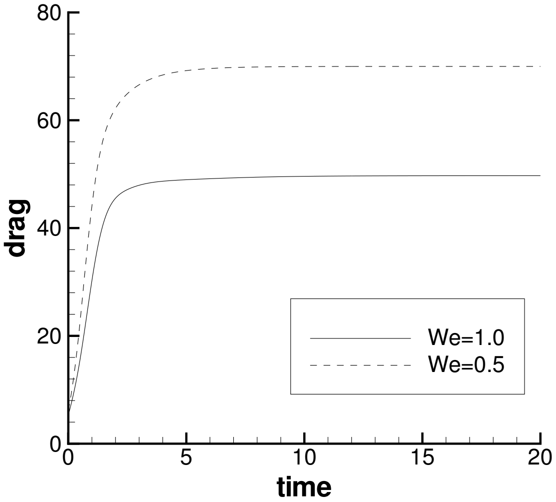

Figure 7.35: Drag on cylinder as a function of time in start-up of Poiseuille flow of an XPP fluid for two different Weissenberg numbers and with $Re = 1$, $\beta = 1/9$, $\alpha = 0.15$, $q = 2$, $\epsilon = 1/3$.

Multimode solutions

Multimode calculations have been performed on the flow past the cylinder using the same parameter settings presented in section 7.4.1, but now with $We = 1$. For the three-mode model, the components of the polymeric stress and the stretch are plotted along the line $y = 0$ and the cylinder wall and are shown in Figs. 7.36 and 7.37, respectively. The drag predicted for this three mode model is 51.8607, which is close to the average of the drags predicted for the equivalent single mode models.

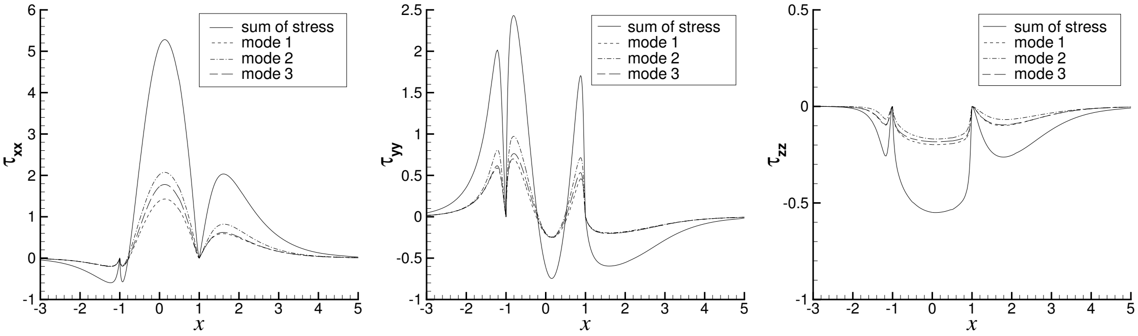

Figure 7.36: The normal components of the polymeric stress on the line $y = 0$ and the cylinder wall, for the three-mode XPP fluid.

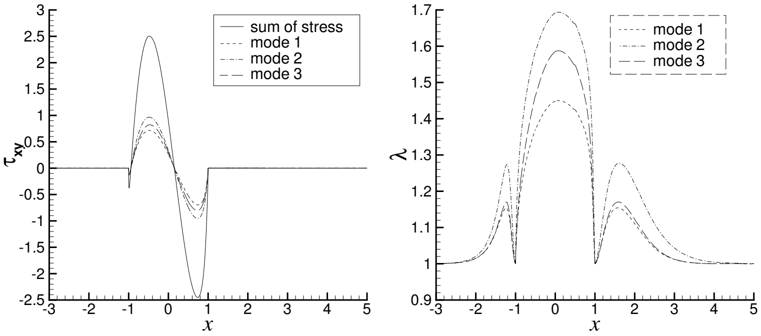

Figure 7.37: The shear stress component and the stretch on the line $y = 0$ and the cylinder wall, for the three-mode XPP fluid.

In Figs. 7.38 and 7.39 the components of the polymeric stress and the stretch are plotted along the line $y = 0$ and the cylinder wall, for the two-mode model presented in section 7.4.1. Again the different values for $\tilde{\beta}$ cause the second mode to be dominant in determining the values of the stress components. The drag predicted by the two-mode model is 53.7946, which is similar to the weighted average of 75% of the drag of the single mode with $\epsilon = 0.6$, and 25% of the drag of the single mode with all standard parameters ($We = 1$, $\epsilon = 1/3$, $q = 2$ and $\alpha = 0.15$).

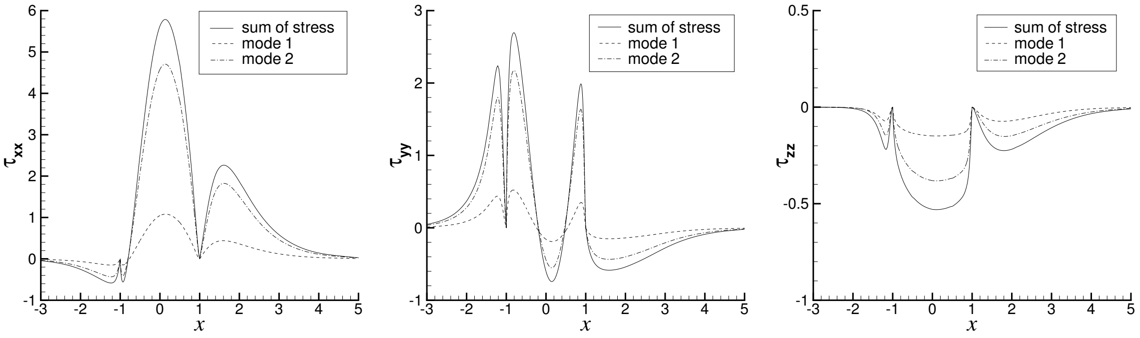

Figure 7.38: The normal components of the polymeric stress on the line $y = 0$ and the cylinder wall, for the two-mode XPP fluid.

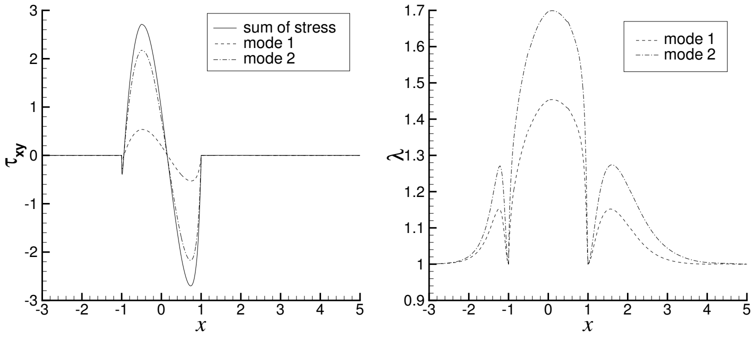

Figure 7.39: The shear stress component and the stretch on the line $y = 0$ and the cylinder wall, for the two-mode XPP fluid.

7.6 Preconditioners and the Schur Method

The preconditioners described in section 4.4 are applied here to the problem of the flow of an XPP fluid past a cylinder as described in section 7.5.2. The parameter set is $We = 1$, $Re = 1$, $\beta = 1/9$, $\alpha = 0.15$, $q = 2$, $\epsilon = 1/3$. For the mesh with 20 elements, the order of approximation is varied from $N = 7$ to $N = 10$ and $N = 13$.

Only the first time step of this problem is solved. Note that this is the most difficult time step to solve as the full spectrum of the pressure must be computed. In later time steps, only perturbations from the previous time step are needed. The convergence criteria in the PCG methods for the Uzawa and Helmholtz operators are set to 10^{-9} and 10^{-14} respectively, and the convergence criterion for the non-symmetric operator S_N is set to 10^{-12}.

To recap, the preconditioners that will be used in this section are given. The preconditioners that will be tested here for the Uzawa operator are the diagonal spectral operator based on the Cahouet and Chabard preconditioner, which in this case reduces to

$$P_U^{-1} = D_U^{-1} = \beta M_p^{-1} + M_l diag(E_N^p)^{-1}. \tag{7.6}$$

Furthermore the preconditioner based on the full Laplacian operator in pressure space is used

$$P_U = F_U = \frac{M_p}{\beta} + M_l E_N^p, \tag{7.7}$$

the finite element preconditioner is used

$$P_U^{-1} = FE_U^{-1} = \sum_{k=1}^{K} R_k^T \left(\frac{M_k^{FE}}{\beta} + M_l E_k^{FE} \right)^{-1} R_k, \tag{7.8}$$

and last the pressure mass matrix is also used

$$P_U = M_p. \tag{7.9}$$

For the Helmholtz operator we have the preconditioner based on the overlapping Schwarz method,

$$P_H^{-1} = O_H^{-1,i} = R_0^T A_0^{-1} R_0 + \sum_{k=1}^{K} R_k^T A_k^{-1} R_k, \tag{7.10}$$

where i denotes the number of GLL points that overlap onto adjacent elements. The other preconditioner is based on the diagonals of the spectral mass and stiffness operators,

$$P_H = D_H = M_l C_N + \left(\beta + \frac{(1-\beta)}{C_l^n}\right) diag(E_N'). \tag{7.11}$$

Instead of applying these preconditioners on the Helmholtz operator, the Schur method can be used. As mentioned in 4.5 the problem is then reduced to inverting the Schur complement of the Helmholtz operator, which reads

$$S_H = H_{BB} - H_{BI} H_{II}^{-1} H_{BI}^T. \tag{7.12}$$

Since the Schur operator is smaller in size, an LU decomposition of this matrix is stored and it is inverted when neccesary. This direct inversion is denoted in the following tables by S_S, and a unit entry will be placed in the corresponding columns for the Helmholtz iterations. The Schur matrix can also be solved iteratively however, and this process will be indicated by S_D. As a preconditioner the diagonal of the Schur matrix is used. When no preconditioner is used in the iterative inversion of the Schur complement, it will be denoted by S_I.

For the problem with $N = 7$, Table 7.4 shows the number of iterations needed to complete the Uzawa inversion, using the preconditioner F_U. The column It_H shows the average number of iterations needed to invert the Helmholtz operator within every Uzawa iteration. The CPU time taken to complete the Uzawa inversion is also shown. These calculations are performed on a Pentium 4, 2.6GHz processor.

For the Helmholtz operator, the Schur method leads to the quickest inversion of the problem. As far as the preconditioners is concerned, the preconditioner D_H results in slightly less iterations than the overlapping Schwarz preconditioner O_H. There is a large reduction in iterations compared to the number of iterations needed when no preconditioner is used. When comparing the two inversion methods of the Schur complement, it can be seen that iterative inversions S_D and S_I of the Helmholtz operator leads to a higher iteration count for the Uzawa operator than the direct inversion S_S.

Table 7.4: Efficiency of preconditioners for the Helmholtz operator, for $N = 7$.

Method	It_U	$\mathrm{av}(\mathrm{It}_\mathrm{H})$	CPU
S_S	260	1.00	17.04
S_D	323	14.21	35.12
S_I	326	77.08	110.96
D_H	317	26.59	72.28
O_H^2	325	35.20	150.12
O_H^3	329	32.89	178.77
O_H^4	330	32.83	241.83
I	308	201.36	407.49

Table 7.5 shows the efficiency of the preconditioners used for the Uzawa operator. For the Helmholtz operator the Schur method S_S with direct inversion is used here, so there is no iterative inversion of the Helmholtz operator. The advantage of the preconditioners F_U and FE_U is obvious over the other preconditioners which reduce the number of iterations only marginally.

Table 7.5: Efficiency of preconditioners for the Uzawa, for $N = 7$.

Method	It_U	CPU
F_U	260	17.04
FE_U	311	21.14
D_U	1234	80.14
M_p	1499	100.22
I	1706	110.36

In Table 7.6 the efficiency of the combination of preconditioners for the problem with $N = 10$ is shown. The method column now contains the method used to invert both the Uzawa and the Helmholtz operator. As the problem has inceased in size from $N = 7$ to $N = 10$, the number of iterations needed to invert the Helmholtz operator has decreased for the overlapping Schwarz preconditioner O_H. It is clearly more robust than the preconditioner based on the diagonals of the spectral operators, D_H. Note that the iteration count for the Uzawa operator has increased for both the D_H and the F_U preconditioner. Relative to one another, F_U decreased the iterations for $N = 7$ almost five-fold. For $N = 10$ the decrease in iterations is almost six-fold. The FE_U preconditioner decreases the number iterations even more. It is also more robust than the F_U preconditioner since the increase in iterations from $N = 7$ to $N = 10$ is not as large.

Table 7.6: Efficiency of preconditioners for the Uzawa and Helmholtz operators, for $N = 10$.

Method		$\mathrm{It_U}$	$\mathrm{av(It_H)}$	CPU
FE_U	S_S	369	1.00	125.31
F_U	S_S	396	1.00	134.06
F_U	S_D	499	18.18	268.81
F_U	S_I	508	84.17	684.90
F_U	O_H^2	508	34.31	883.01
F_U	O_H^3	519	29.59	861.86
F_U	O_H^4	519	29.10	998.75
F_U	D_H	502	39.30	725.42
D_U	S_S	2304	1.00	773.39

The approximation order is now increased to $N = 13$ and the results are given in Table 7.7. As the order of the approximation N increases, higher values for the overlap become more efficient. For $N = 10$ and $N = 13$, the overlap of three is the most efficient although an overlap of four nodes results in a lower iteration count. For this highest tested value of N the finite element preconditioner FE_U provides a considerable reduction in iterations compared with the F_U preconditioner.

Table 7.7: Efficiency of preconditioners for the Uzawa and Helmholtz operators, for $N = 13$.

Method		$\mathrm{It_U}$	$\mathrm{av(It_H)}$	CPU
FE_U	S_S	485	1.00	546.08
F_U	S_S	621	1.00	700.90
F_U	O_H^2	801	31.42	3305.08
F_U	O_H^3	792	28.74	3229.96
F_U	O_H^4	760	27.76	3530.76
F_U	D_H	784	52.44	3503.94
F_U	S_D	780	20.90	1364.83
F_U	S_I	769	86.81	2847.79

Of course the comparison between the direct inversion of the Schur complement of the Helmholtz operator and the iterative methods is not a completely fair one. The direct inversion involves computational time for setting up the LU decomposition, and uses more memory to store this LU decomposition. For the problems presented in this thesis however, memory usage has never been a problem on a machine with 256 Mb internal memory. The conclusion that can be draw from this section is that in order to achieve the most efficient algorithm compromises have to be made. On the one hand the size of the problem is almost limitless using iterative solvers, but this means the speed of the algorithm is compromised. On the other hand direct methods can be used to invert problems quicker, but the size of the problem is limited. The most efficient method in this thesis is an example of a combination of both methods.

An iterative method is used to solve the pressure system, although the preconditioners used in the inversion are based on operators that have been stored in memory. By using the Schur complement method, the size of the problem is reduced and this reduces the claim on storage space such that the Schur complement of the Helmholtz operator may be stored as well. As is shown above, a preconditioner can be used to produce a quick iterative inversion for the the Schur complement as well.

The algorithms used in this research have been developed to run on one processor. The real strength of the overlapping Schwarz preconditioner however, lies in the fact that the work can be divided over multiple processors easily, since it is based on the local finite element matrices.

The inversion of the non-symmetric operator S_N takes up only a fraction of the CPU time of the inversion of the Uzawa operator, typically around 1%. The number of iterations needed to invert this operator however are very high when no preconditioner is used. The use of the mass matrix on some occasions reduces the iteration count by an amount of the order 10^3.

Chapter 8

Conclusions

In this thesis a spectral element technique has been developed for efficiently solving the flow of polymer melts using the extended pom-pom (XPP) model and of polymer solutions using the Oldroyd B model. Both steady and transient solutions have been analyzed with respect to the stability of the spectral element method. The spectral element technique incorporates a three-field formulation of the problem in terms of velocity, pressure and extra-stress.

Some theoretical issues concerning the XPP model have been addressed. The type of the equations in the XPP model is investigated, and it is shown that the XPP model is of similar type as the Oldroyd B model. The predictions of the shear and extensional viscosity by the XPP model are compared to the original pom-pom model. The extensional viscosity of the original pom-pom model exhibits two discontinuities. It is shown that these are both overcome in the XPP model.

The use of a modified test function has been investigated that allows for easy implementation of zero Neumann boundary symmetry conditions. For the Stokes problem the efficiency has been compared to that of the original test function. By using the modified test function, the size of the discrete problem is reduced since the nodes on the symmetry axis or plane are not included. The modified test function however generates some extra terms in the discrete operators. Although the original interpolant is found to be more efficient for planar symmetric problems, for axisymmetric problems the modified test function leads to a faster solver. The reason for this is that the modified interpolant does not generate zero rows or columns in the discrete operators that are associated with a zero radial coordinate in axisymmetric problems.

A modified continuity equation is implemented that ensures that the zero mean condition on pressure is satisfied automatically. This leads to a better conditioned Uzawa operator, and the result of this is that the Uzawa operator may be iteratively inverted to any convergence criterion. Without the use of the zero mean condition, problems in the inversion arise when the convergence criteria are set too strict.

The performance of three different temporal discretization schemes has been compared. When the Oldroyd B model is reduced to the UCM model, by setting $\beta = 0$, the first-order method performs better than the two second-order methods. As expected, the numerical solution of the planar Poiseuille flow becomes more stable when the parameter β is increased and when a nonzero Reynolds number is chosen.

Increasing the order of the numerical approximation results in a decrease in the critical value of the Weissenberg number, both for steady and transient flows. The same behaviour is observed when the length of the channel is shortened, or the number of elements in the lengthwise direction is increased. Increasing the number of elements in the cross channel direction does not influence the stability of the scheme. Apparently, any type of refinement in the lengthwise direction decreases the maximum attainable Weissenber number, whereas this number is insensitive to refinement in the cross channel direction. This is in agreement with the findings of Fiétier and Deville [15].

The start-up of Poiseuille flow through a planar channel has been analyzed for Newtonian flow, for Oldroyd B fluids and for XPP fluids. For the Oldroyd B model an exact solution to this transient problem is available, and comparisons of the numerical to the analytic solutions have been made.

A number of different preconditioners have been tested on both the flow of an Oldroyd B fluid through a planar channel and on the flow of an XPP fluid past a cylinder. The efficiency of preconditioners based on both spectral element approximations and finite element approximations has been demonstrated. For the XPP model the use of the Schur complement method, which reduces the size of the Helmholtz operator, has also been tested. It is found that the use of preconditioners based on the storage of spectral element matrices in combination with the Schur complement method results in the most efficient solver.

The upwinding methods SUPG and LUST have been implemented. These can only be used in combination with an algorithm that solves the constitutive equations separately from the field equations. The use of the uncoupled method has lead to an increase of the maximum attainable Weissenberg number compared to a method that solved all the equations in a coupled fashion. This is the case even when no upwinding methods are used. The highest Weissenberg numbers can be reached using the LUST method together with the uncoupled solver. Using this algorithm the flow of an XPP fluid past a confined cylinder has been computed and an analysis of the flow has been performed.

The influence of different parameter settings in the XPP model has been analyzed with respect to predicted velocity, stresses and molecular stretch. This has been done for the planar channel flow and the flow past a confined cylinder. The application of a multimode model is also investigated for both these flows.

Appendix A

Derivation of Conservation Equations

The derivations of the conservation equations are given, followed by a derivation of the deformation tensor. The derivation of the field equations that satisfy the conservation of mass and momentum is given below. All derivations are made under the assumption that the continuum hypothesis is valid. This means that the length scale of an infinitesimal element, which is used to integrate over volumes and surfaces, is still considerably larger than the largest molecular length scale.

Conservation of mass equation

Consider a fixed volume V in space, with a surface area S, through which a medium passes. Under the assumption of the continuum hypothesis, the mass of medium that enters or leaves V through an infinitesimal part of its area dS, can be calculated as

$$\rho \mathbf{u} \cdot dS, \tag{A.1}$$

where ρ is the density of the medium, and $\mathbf{u}$ is the velocity vector. Note that $\rho \mathbf{u} \cdot dS$ is positive for an outward pointing velocity vector, i.e. for outflow. The net mass outflow through the surface S then becomes

$$\int\int_S \rho\mathbf{u} \cdot dS. \tag{A.2}$$

Since the mass of the medium that is inside a infinitesimal volume element dV is given by ρdV, the decrease in time of mass inside V can be expressed as

$$-\frac{\partial}{\partial t}\int\int\int_V \rho dV, \tag{A.3}$$

where the time derivative does not apply to the volume dV, since V is fixed in space. Of course the outflow through the area S must equal the decrease of mass inside V, so the equation governing the conservation of mass is

$$\int\int\int_V \frac{\partial \rho}{\partial t} dV + \int\int_S \rho\mathbf{u} \cdot dS = 0. \tag{A.4}$$

Applying the divergence theorem to the second term yields

$$\int\int\int_V \left(\frac{\partial \rho}{\partial t} + \nabla \cdot (\rho\mathbf{u})\right) dV = 0. \tag{A.5}$$

Since V is chosen arbitrarily in space, the integrand needs to be zero. This gives the conservation of mass in its differential form

$$\frac{\partial \rho}{\partial t} + \nabla \cdot (\rho\mathbf{u}) = 0. \tag{A.6}$$

In this thesis the medium is always a fluid. Since compressibility in fluids is negligible, the density ρ does not change with time or space. In this case the conservation of mass reduces to

$$\nabla \cdot \mathbf{u} = 0. \tag{A.7}$$

In a two dimensional Cartesian coordinate system, this is

$$\frac{\partial u}{\partial x} + \frac{\partial v}{\partial y} = 0. \tag{A.8}$$

Conservation of momentum equation

The equation governing the conservation of momentum is based on Newton's second law $\mathbf{F} = m\mathbf{a}$, or

$$\mathbf{F} = \frac{d}{dt}(m\mathbf{u}), \tag{A.9}$$

when change of mass is taken into account. The term $m\mathbf{u}$ is the momentum of a volume of fluid with mass m. The force $\mathbf{F}$ can be broken up into body forces ($\mathbf{f}_b$) and surface forces. The body force, gravity for example, which acts on a volume dV is given by $\mathbf{f}_b dV$. The surface force consists of a pressure force, and a force due to viscous and elastic stresses. The pressure force acting on the surface dS, is $-pdS$, where p is the pressure. The force due to stresses in the medium is $\mathbf{T}dS$, where $\mathbf{T}$ is the extra-stress tensor. Since moments acting on a volume dV are assumed to be zero, the tangential stresses must satisfy $T_{ij} = T_{ji}$, so the extra-stress tensor is symmetric. Using all this information, the force $\mathbf{F}$ can be written as

$$\mathbf{F} = \int\int\int_V \mathbf{f}_b dV - \int\int_S p dS + \int\int_S \mathbf{T} dS, \tag{A.10}$$

or, using the divergence theorem

$$\mathbf{F} = \int\int\int_V \mathbf{f}_b dV + \int\int\int_V \nabla \cdot \boldsymbol{\sigma} dV, \tag{A.11}$$

where $\boldsymbol{\sigma}$ is the total stress tensor, defined as $\boldsymbol{\sigma} = -p\mathbf{I} + \mathbf{T}$.

Analogous to the time rate of change in the mass conservation, the time rate of change of momentum is the sum of the net outflow of momentum through the surface S, and the change of momentum, with time, inside the volume V. Again, the mass flowing through dS is $\rho\mathbf{u} \cdot dS$, so the flow of momentum is $(\rho\mathbf{u} \cdot dS)\mathbf{u}$. The amount of momentum contained inside a volume dV is $(\rho dV)\mathbf{u}$. The term $\frac{\partial}{\partial t}(m\mathbf{u})$ may now be expressed as

$$\frac{d}{dt}(m\mathbf{u}) = \int\int\int_V \frac{\partial(\rho\mathbf{u})}{\partial t} dV + \int\int_S (\rho\mathbf{u} \cdot dS)\mathbf{u}, \tag{A.12}$$

or, using the divergence theorem on the second term in the right, and applying the conservation of mass to it,

$$\frac{d}{dt}(m\mathbf{u}) = \int\int\int_V \frac{\partial(\rho\mathbf{u})}{\partial t} dV + \int\int\int_V \rho\mathbf{u}\cdot(\nabla\mathbf{u})^T dV. \tag{A.13}$$

So the conservation of momentum equation in integral form is given by

$$\int\int\int_V \left(\frac{\partial(\rho\mathbf{u})}{\partial t} + \rho\mathbf{u}\cdot(\nabla\mathbf{u})^T - \nabla\cdot\boldsymbol{\sigma} - \mathbf{f}_b\right) dV = 0. \tag{A.14}$$

In its differential form, the conservation of momentum equation reads

$$\frac{\partial(\rho\mathbf{u})}{\partial t} + \rho\mathbf{u}\cdot(\nabla\mathbf{u})^T = \nabla\cdot\boldsymbol{\sigma} + \mathbf{f}_b. \tag{A.15}$$

For an incompressible fluid, and substituting $\boldsymbol{\sigma} = -p\mathbf{I} + \mathbf{T}$, the momentum equation reads

$$\rho\left(\frac{\partial\mathbf{u}}{\partial t} + \mathbf{u}\cdot(\nabla\mathbf{u})^T\right) = -\nabla p + \nabla\cdot\mathbf{T} + \mathbf{f}_b. \tag{A.16}$$

In a two dimensional Cartesian coordinate system, this is

$$\frac{\partial u}{\partial t} + u\frac{\partial u}{\partial x} + v\frac{\partial u}{\partial y} = -\frac{\partial p}{\partial x} + \frac{\partial\mathbf{T}_{xx}}{\partial x} + \frac{\partial\mathbf{T}_{xy}}{\partial y}, \tag{A.17}$$

$$\frac{\partial v}{\partial t} + u\frac{\partial v}{\partial x} + v\frac{\partial v}{\partial y} = -\frac{\partial p}{\partial y} + \frac{\partial\mathbf{T}_{xy}}{\partial x} + \frac{\partial\mathbf{T}_{yy}}{\partial y}. \tag{A.18}$$

Rate of deformation tensor

Depicted in Fig. A.1 is the deformation of an infinitesimal fluid element $[dx \times dy]$ over an infinitesimal time dt.

The rate of deformation, or strain rate, in the x-direction is the percentual increase in length of the horizontal line-elements, in that direction, or

$$d_{xx}dt = \frac{(dx + \frac{\partial u}{\partial x}dxdt) - dx}{dx} \qquad \rightarrow \qquad d_{xx} = \frac{\partial u}{\partial x}. \tag{A.19}$$

In the same way, the rate of deformation in y-direction is

$$d_{yy} = \frac{\partial v}{\partial y}. \tag{A.20}$$

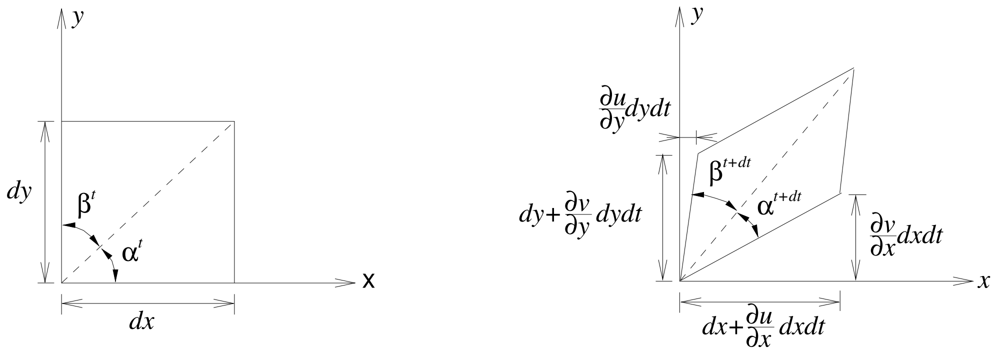

Figure A.1: Deformation of a infinitesimal fluid element.

The shear rate of deformation is defined as the average decrease of the angles α and β, and is given by

$$d_{xy}dt = \frac{1}{2}\left(\frac{(\frac{\partial v}{\partial x}dxdt)}{dx} + \frac{(\frac{\partial u}{\partial y}dydt)}{dy}\right) \qquad \rightarrow \qquad d_{xy} = \frac{1}{2}(\frac{\partial u}{\partial y} + \frac{\partial v}{\partial x}). \tag{A.21}$$

Like the stress tensor, the rate of deformation tensor $\mathbf{d}$ is also symmetric. In two dimensions, $\mathbf{d}$ can be expressed as

$$\mathbf{d} = \begin{pmatrix} d_{xx} & d_{xy} \\ d_{xy} & d_{yy} \end{pmatrix} = \begin{pmatrix} \frac{\partial u}{\partial x} & \frac{1}{2}(\frac{\partial u}{\partial y} + \frac{\partial v}{\partial x}) \\ \frac{1}{2}(\frac{\partial u}{\partial y} + \frac{\partial v}{\partial x}) & \frac{\partial v}{\partial y} \end{pmatrix} = \frac{1}{2}\left(\nabla \mathbf{u} + (\nabla \mathbf{u})^T\right). \tag{A.22}$$

Appendix B

Equations in Component Form

Given here are the equations for the generic model that is used in this thesis, in two dimensional Cartesian component form.

$$\frac{\partial u}{\partial x} + \frac{\partial v}{\partial y} = 0,$$

$$Re\left(\frac{\partial u}{\partial t} + u\frac{\partial u}{\partial x} + v\frac{\partial u}{\partial y}\right) = -\frac{\partial p}{\partial x} + \frac{\partial \tau_{xx}}{\partial x} + \frac{\partial \tau_{xy}}{\partial y} + \beta\frac{\partial^2 u}{\partial x^2} + \beta\frac{\partial^2 u}{\partial y^2},$$

$$Re\left(\frac{\partial v}{\partial t} + u\frac{\partial v}{\partial x} + v\frac{\partial v}{\partial y}\right) = -\frac{\partial p}{\partial y} + \frac{\partial \tau_{xy}}{\partial x} + \frac{\partial \tau_{yy}}{\partial y} + \beta\frac{\partial^2 v}{\partial x^2} + \beta\frac{\partial^2 v}{\partial y^2},$$

$$f\tau_{xx} + We\left(\frac{\partial \tau_{xx}}{\partial t} + u\frac{\partial \tau_{xx}}{\partial x} + v\frac{\partial \tau_{xx}}{\partial y} - 2\tau_{xx}\frac{\partial u}{\partial x} - 2\tau_{xy}\frac{\partial u}{\partial y}\right) + \frac{1-\beta}{We}(f-1) + \frac{\alpha We}{1-\beta}(\tau_{xx}^2 + \tau_{xy}^2) = 2(1-\beta)\frac{\partial u}{\partial x},$$

$$f\tau_{yy} + We\left(\frac{\partial \tau_{yy}}{\partial t} + u\frac{\partial \tau_{yy}}{\partial x} + v\frac{\partial \tau_{yy}}{\partial y} - 2\tau_{xy}\frac{\partial v}{\partial x} - 2\tau_{yy}\frac{\partial v}{\partial y}\right) + \frac{1-\beta}{We}(f-1) + \frac{\alpha We}{1-\beta}(\tau_{xy}^2 + \tau_{yy}^2) = 2(1-\beta)\frac{\partial v}{\partial y},$$

$$f\tau_{zz} + We\left(\frac{\partial \tau_{zz}}{\partial t} + u\frac{\partial \tau_{zz}}{\partial x} + v\frac{\partial \tau_{zz}}{\partial y}\right) + \frac{1-\beta}{We}(f-1) + \frac{\alpha We}{1-\beta}\tau_{zz}^2 = 0,$$

$$f\tau_{xy} + We\left(\frac{\partial \tau_{xy}}{\partial t} + u\frac{\partial \tau_{xy}}{\partial x} + v\frac{\partial \tau_{xy}}{\partial y} - \tau_{xx}\frac{\partial v}{\partial x} - \tau_{yy}\frac{\partial u}{\partial y}\right) + \frac{\alpha We}{1-\beta}\tau_{xy}\left(\tau_{xx} + \tau_{xy}\right) = (1-\beta)\left(\frac{\partial u}{\partial y} + \frac{\partial v}{\partial x}\right),$$

where

$$f = \frac{2}{\epsilon}\left(1 - \frac{1}{\lambda}\right) e^{\nu(\lambda-1)} + \frac{1}{\lambda^2}\left(1 - \frac{\alpha}{3}\left(\frac{We}{1-\beta}\right)^2 (\tau_{xx}^2 + \tau_{yy}^2 + \tau_{zz}^2 + 2\tau_{xy}^2)\right). \tag{B.1}$$

The expression for the backbone stretch λ in the double equation version of the XPP model in two dimensional Cartesian coordinates is

$$\frac{\partial\lambda}{\partial t} + u\frac{\partial\lambda}{\partial x} + v\frac{\partial\lambda}{\partial y} = \frac{We}{3(1-\beta)}\frac{1}{\lambda}\left(\tau_{xx}\frac{\partial u}{\partial x} + \tau_{yy}\frac{\partial v}{\partial y} + \tau_{xy}(\frac{\partial u}{\partial y} + \frac{\partial v}{\partial x})\right) - \frac{\lambda-1}{\epsilon We}e^{\nu(\lambda-1)}, \tag{B.2}$$

and for the single equation version the expression is

$$\lambda = \sqrt{1 + \frac{We}{(1-\beta)}\frac{1}{3}(\tau_{xx} + \tau_{yy} + \tau_{zz})}. \tag{B.3}$$

The three field Stokes problem is written out in Table B.1 in component form, for both a two dimensional Cartesian coordinate system and for a cylindrical polar coordinate system with components (z, r, θ). All θ dependence has been removed from these equations to give the axisymmetric equations.

Table B.1: The Stokes equations in component form, for planar and for axisymmetric problems.

Planar	Axisymmetric
$\frac{\partial u}{\partial x} + \frac{\partial u}{\partial y} = 0$	$\frac{\partial u_r}{\partial r} + \frac{\partial u_z}{\partial z} + \frac{u_r}{r} = 0$
$\frac{\partial p}{\partial x} = \frac{\partial T_{xx}}{\partial x} + \frac{\partial T_{xy}}{\partial y}$	$\frac{\partial p}{\partial z} = \frac{\partial T_{zz}}{\partial z} + \frac{\partial T_{zr}}{\partial r} + \frac{T_{zr}}{r}$
$\frac{\partial p}{\partial y} = \frac{\partial T_{xy}}{\partial x} + \frac{\partial T_{yy}}{\partial y}$	$\frac{\partial p}{\partial r} = \frac{\partial T_{zr}}{\partial z} + \frac{1}{r}\frac{\partial T_{rr}}{\partial r} + \frac{T_{rr} - T_{\theta\theta}}{r}$
$T_{xx} = 2\eta\frac{\partial u}{\partial x}$	$T_{zz} = 2\eta\frac{\partial u_z}{\partial z}$
$T_{xy} = \eta\left(\frac{\partial u}{\partial y} + \frac{\partial v}{\partial x}\right)$	$T_{zr} = \eta\left(\frac{\partial u_z}{\partial r} + \frac{\partial u_r}{\partial z}\right)$
$T_{xx} = 2\eta\frac{\partial v}{\partial y}$	$T_{rr} = 2\eta\frac{\partial u_r}{\partial r}$ $\quad T_{\theta\theta} = 2\eta\frac{u_r}{r}$

Appendix C

Derivation of the Single Equation Version of the XPP Model

This appendix gives the derivation of the single equation version of the extended pom-pom model from the double equation version. The equations in the double extended version are

$$\overset{\nabla}{\mathbf{s}} + \mathbf{f}(\mathbf{u}, \mathbf{s}, \lambda)\mathbf{s} + \frac{\alpha - 1}{3\lambda_{0b}\lambda^2}\mathbf{I} + \frac{3\alpha\lambda^2}{\lambda_{0b}}\mathbf{s}\cdot\mathbf{s} = 0, \tag{C.1}$$

where

$$\mathbf{f}(\mathbf{u}, \mathbf{s}, \lambda) = 2[\mathbf{d} : \mathbf{s}] + \frac{1}{\lambda_{0b}\lambda^2}(1 - \alpha - 3\alpha\lambda^4 I_{\mathbf{s}\cdot\mathbf{s}}), \tag{C.2}$$

$$\frac{D\lambda}{Dt} = \lambda[\mathbf{d} : \mathbf{s}] - \frac{\lambda - 1}{\lambda_{0s}}e^{\nu(\lambda-1)}. \tag{C.3}$$

Multiply constitutive equation (C.1) with λ^2 to find

$$\overset{\nabla}{(\lambda^2\mathbf{s})} - (\frac{D\lambda^2}{Dt})\mathbf{s} + \mathbf{f}(\mathbf{u}, \mathbf{s}, \lambda)(\lambda^2\mathbf{s}) + \frac{\alpha - 1}{3\lambda_{0b}}\mathbf{I} + \frac{3\alpha}{\lambda_{0b}}(\lambda^2\mathbf{s})\cdot(\lambda^2\mathbf{s}) = 0. \tag{C.4}$$

Substitute the equation for stretch (C.3) rewritten as

$$\frac{D\lambda^2}{Dt} = 2\lambda^2[\mathbf{d} : \mathbf{s}] - 2\lambda\frac{\lambda - 1}{\lambda_{0s}}e^{\nu(\lambda-1)}, \tag{C.5}$$

to find

$$\overset{\nabla}{(\lambda^2\mathbf{s})} + \left(\mathbf{f}(\mathbf{u}, \mathbf{s}, \lambda) - 2[\mathbf{d} : \mathbf{s}] + \frac{2(\lambda - 1)}{\lambda\lambda_{0s}}e^{\nu(\lambda-1)}\right)(\lambda^2\mathbf{s}) + \frac{\alpha - 1}{3\lambda_{0b}}\mathbf{I} + \frac{3\alpha}{\lambda_{0b}}(\lambda^2\mathbf{s})\cdot(\lambda^2\mathbf{s}) = 0, \tag{C.6}$$

or

$$\overset{\nabla}{(\lambda^2 \mathbf{s})} + \mathbf{g}(\mathbf{s},\lambda)(\lambda^2\mathbf{s}) + \frac{\alpha-1}{3\lambda_{0b}}\mathbf{I} + \frac{3\alpha}{\lambda_{0b}}(\lambda^2\mathbf{s})\cdot(\lambda^2\mathbf{s}) = 0, \tag{C.7}$$

with

$$\mathbf{g}(\mathbf{s},\lambda) = \frac{2(\lambda-1)}{\lambda\lambda_{0s}}e^{\nu(\lambda-1)} + \frac{1}{\lambda_{0b}\lambda^2}(1-\alpha-3\alpha\lambda^4 I_{\mathbf{s}\cdot\mathbf{s}}). \tag{C.8}$$

Now multiply (C.7) by 3, subtract the identity tensor $\mathbf{I}$ from each occurrence of $\lambda^2\mathbf{s}$, and call this $\mathbf{A} = 3\lambda^2\mathbf{s} - \mathbf{I}$. Also, use the identity $(\mathbf{B}-\mathbf{I})\cdot(\mathbf{B}-\mathbf{I}) = \mathbf{B}\cdot\mathbf{B} - 2\mathbf{B} + \mathbf{I}$. Then

$$\overset{\nabla}{\mathbf{A}} + \overset{\nabla}{\mathbf{I}} + \mathbf{g}(\mathbf{s},\lambda)\mathbf{A} + \mathbf{g}(\mathbf{s},\lambda)\mathbf{I} + \frac{\alpha-1}{\lambda_{0b}}\mathbf{I} + \frac{\alpha}{\lambda_{0b}}\mathbf{A}\cdot\mathbf{A} - \frac{\alpha}{\lambda_{0b}}(\mathbf{I} - 2(3\lambda^2\mathbf{s})) = 0, \tag{C.9}$$

or

$$\overset{\nabla}{\mathbf{A}} + (\mathbf{g}(\mathbf{s},\lambda) + \frac{2\alpha}{\lambda_{0b}})\mathbf{A} + (\mathbf{g}(\mathbf{s},\lambda) + \frac{2\alpha}{\lambda_{0b}} - \frac{1}{\lambda_{0b}})\mathbf{I} + \frac{\alpha}{\lambda_{0b}}\mathbf{A}\cdot\mathbf{A} = 2\mathbf{d}, \tag{C.10}$$

or

$$\overset{\nabla}{\mathbf{A}} + \mathbf{h}(\mathbf{s},\lambda)\mathbf{A} + (\mathbf{h}(\mathbf{s},\lambda) - \frac{1}{\lambda_{0b}})\mathbf{I} + \frac{\alpha}{\lambda_{0b}}\mathbf{A}\cdot\mathbf{A} = 2\mathbf{d}, \tag{C.11}$$

where

$$\mathbf{h}(\mathbf{s},\lambda) = \frac{2(\lambda-1)}{\lambda\lambda_{0s}}e^{\nu(\lambda-1)} + \frac{1}{\lambda_{0b}\lambda^2}(1-\alpha-3\alpha\lambda^4 I_{\mathbf{s}\cdot\mathbf{s}}) + \frac{2\alpha}{\lambda_{0b}}. \tag{C.12}$$

We now write $\mathbf{h}(\mathbf{s},\lambda)$. Noting that $I_{(\mathbf{B}-\mathbf{I})\cdot(\mathbf{B}-\mathbf{I})} = I_{\mathbf{B}\cdot\mathbf{B}} - 2I_{\mathbf{B}} + 3$, then

$$\mathbf{h}(\mathbf{A},\lambda) = \frac{2(\lambda-1)}{\lambda\lambda_{0s}}e^{\nu(\lambda-1)} + \frac{1}{\lambda_{0b}\lambda^2}(2\alpha\lambda^2 + 1 - \alpha - \frac{\alpha}{3}(I_{\mathbf{A}\cdot\mathbf{A}} - 3 + 2(I_{\mathbf{A}} + 3)), \tag{C.13}$$

or

$$\mathbf{h}(\mathbf{A},\lambda) = \frac{2(\lambda-1)}{\lambda\lambda_{0s}}e^{\nu(\lambda-1)} + \frac{1}{\lambda_{0b}\lambda^2}(1 - \frac{\alpha}{3}I_{\mathbf{A}\cdot\mathbf{A}} - 2\alpha(\frac{I_{\mathbf{A}}}{3} + 1 - \lambda^2)). \tag{C.14}$$

Of course, $\boldsymbol{\tau} = G_0\mathbf{A}$, so the constitutive equation for the double equation version is found to be the same as the constitutive equation for the single equation version:

$$\lambda_{0b}\overset{\nabla}{\boldsymbol{\tau}} + \mathbf{f}(\boldsymbol{\tau},\lambda)\boldsymbol{\tau} + G_0(\mathbf{f}(\boldsymbol{\tau},\lambda) - 1)\mathbf{I} + \frac{\alpha}{G_0}\boldsymbol{\tau}\cdot\boldsymbol{\tau} = 2G_0\lambda_{0b}\mathbf{d}, \tag{C.15}$$

where

$$\mathbf{f}(\boldsymbol{\tau},\lambda) = 2\frac{\lambda_{0b}}{\lambda_{0s}}(1-\frac{1}{\lambda})e^{\nu(\lambda-1)} + \frac{1}{\lambda^2}(1 - \frac{\alpha}{3G_0^2}I_{\boldsymbol{\tau}\cdot\boldsymbol{\tau}} - 2\alpha(\frac{I_{\boldsymbol{\tau}}}{3G_0} + 1 - \lambda^2)). \tag{C.16}$$

The trace of the orientation tensor equals one, and since $I_{\boldsymbol{\tau}} = G_0(3\lambda^2 I_{\mathbf{s}} - 3)$, we find that $\frac{I_\tau}{3G_0} + 1 - \lambda^2 = 0$. This simplifies $\mathbf{f}(\boldsymbol{\tau}, \lambda)$ and provides the expression for the stretch

$$\mathbf{f}(\boldsymbol{\tau}, \lambda) = 2\frac{\lambda_{0b}}{\lambda_{0s}}(1 - \frac{1}{\lambda})e^{\nu(\lambda-1)} + \frac{1}{\lambda^2}(1 - \frac{\alpha}{3G_0^2} I_{\boldsymbol{\tau}\cdot\boldsymbol{\tau}}), \tag{C.17}$$

$$\lambda = \sqrt{1 + \frac{I_{\boldsymbol{\tau}}}{3G_0}}. \tag{C.18}$$

When the parameter α equals zero then $\tau_{zz} = \tau_{yy}$, and the trace of the stress tensor is $I_{\boldsymbol{\tau}} = \tau_{xx} + 2\tau_{yy}$. When $\alpha \neq 0$ however, τ_{zz} needs to be calculated separately. It may not be calculated from $I_{\boldsymbol{\tau}} = G_0(3\lambda^2 I_{\mathbf{s}} - 3)$, otherwise this statement is used twice.

Appendix D

Calculation of the Modified Lagrangian Interpolant

Presented here is the calculation of the modified Lagrangian interpolant $\hat{h}_j(x)$ and its derivative $\hat{d}_{ij}$, for $1 \le j \le N-1$ and for $j = N$.

Calculation of $\hat{h}_j(x)$, $1 \le j \le N-1$

Using the first property in Eq. (3.55), we can deduce a relation between a and b.

$$\begin{aligned} \hat{h}_j(x_j) = 1 \Rightarrow \qquad & \lim_{x \to x_j} \frac{P'_N(x)(1-x)}{(x-x_j)}(ax+b) = \\ & \lim_{x \to x_j} \frac{P''_N(x)(1-x)(ax+b) - P'_N(x)(ax+b) + P'_N(x)(1-x)a}{1} = 1. \end{aligned}$$

Using the property that $P'_N(x_j) = 0$ for $1 \le j \le N-1$, we find

$$P''_N(x_j)(1-x_j)(ax_j+b) = 1. \tag{D.1}$$

Now use the second property in Eq. (3.56) to find a second relation

$$\begin{aligned} \hat{h}'_j(x) &= \frac{(P''_N(x)(1-x) - P'_N(x))(x-x_j) - P'_N(x)(1-x)}{(x-x_j)^2}(ax+b) + \frac{P'_N(x)(1-x)}{(x-x_j)}a, \\ \hat{h}'_j(-1) = 0 &\Rightarrow \frac{(2P''_N(-1) - P'_N(-1))(-1-x_j) - 2P'_N(-1)}{(1+x_j)^2}(b-a) + \frac{2P'_N(-1)}{(-1-x_j)}a = 0. \end{aligned}$$

This simplifies to give

$$\left[-(2P_N''(-1) - P_N'(-1)) - \frac{2P_N'(-1)}{(1+x_j)}\right](b-a) - 2P_N'(-1)a = 0. \tag{D.2}$$

At this point we make use of some well-known properties of Legendre polynomials:

$$\begin{aligned} P_N(\pm 1) &= (\pm 1)^N, \\ P_N'(\pm 1) &= \pm\frac{1}{2}N(N+1)(\pm 1)^N, \\ P_N''(\pm 1) &= \frac{1}{8}N(N+1)(N^2+N-2)(\pm 1)^N. \end{aligned} \tag{D.3}$$

So we find that

$$2P_N''(-1) - P_N'(-1) = (-1)^N\left(\frac{N(N+1)}{2}\right)^2.$$

And thus we find that Eq. (D.2) becomes

$$\left[-(-1)^N\left(\frac{N(N+1)}{2}\right)^2 + (-1)^N\frac{N(N+1)}{(1+x_j)}\right](b-a) + (-1)^N N(N+1)a = 0.$$

This simplifies to

$$\left[-\frac{N(N+1)}{4} + \frac{1}{(1+x_j)}\right](b-a) + a = 0,$$

or

$$\left[\frac{x_j}{1+x_j} + \frac{N(N+1)}{4}\right]a + \left[\frac{1}{(1+x_j)} - \frac{N(N+1)}{4}\right]b = 0.$$

The second relation between a and b is:

$$\frac{b}{a} = -\frac{\left[\frac{x_j}{1+x_j} + \frac{N(N+1)}{4}\right]}{\left[\frac{1}{(1+x_j)} - \frac{N(N+1)}{4}\right]} = \frac{N(N+1)(1+x_j)+4x_j}{N(N+1)(1+x_j)-4}. \tag{D.4}$$

When we use this relation in Eq. (D.1), we obtain

$$P_N''(x_j)(1-x_j)(ax_i+b) = P_N''(x_j)(1-x_j)\left(ax_j + \frac{N(N+1)(1+x_j)+4x_j}{N(N+1)(1+x_j)-4}a\right) = 1,$$

which yields the expression for a

$$a = \frac{1}{P_N''(x_j)(1-x_j)} \cdot \frac{N(N+1)(1+x_j)-4}{N(N+1)(1+x_j)^2},$$

and together with Eq. (D.4) the factor b is found:

$$b = \frac{1}{P_N''(x_j)(1-x_j)} \cdot \frac{N(N+1)(1+x_j)+4x_j}{N(N+1)(1+x_j)^2}.$$

The new Lagrange interpolant in Eq. (3.54) may now be written in the form

$$\hat{h}_j(x) = \frac{P_N'(x)(1-x)}{P_N''(x_j)(x-x_j)} \cdot \frac{N(N+1)(1+x_j)(1+x)-4(x-x_j)}{N(N+1)(1+x_j)(1-x_j^2)}, \qquad 1 \leq j \leq N-1. \tag{D.5}$$

Calculation of $\hat{h}_N(x)$

Again, the first property in Eq. (3.59) gives a relation between c and d:

$$\hat{h}_N(x_N) = 1 \Rightarrow P_N'(1)(c+d) = 1,$$

or, using the properties listed in Eqs. (D.3),

$$c + d = \frac{2}{N(N+1)}. \tag{D.6}$$

We use the second property Eq. (3.60) to find the second relation between c and d:

$$\hat{h}_N'(x) = P_N''(x)(cx+d) + P_N'(x)c,$$
$$\hat{h}_N'(-1) = 0 \Rightarrow P_N''(-1)(d-c) + P_N'(-1)c = 0.$$

With the properties in Eqs. (D.3) this yields

$$\frac{N^2+N+2}{4}c = \frac{N^2+N-2}{4}d \Rightarrow \frac{d}{c} = \frac{N^2+N+2}{N^2+N-2}. \tag{D.7}$$

Combining Eqs. (D.6) and (D.7) provides the factors c and d:

$$c = \frac{N^2+N-2}{N^2(N+1)^2},$$
$$d = \frac{N^2+N+2}{N^2(N+1)^2}.$$

The Lagrange interpolant $\hat{h}_N(x)$ is now, according to Eq. (3.57)

$$\hat{h}_N(x) = \frac{P_N'(x)}{N^2(N+1)^2} \cdot [N(N+1)(1+x)+2(1-x)]. \tag{D.8}$$

Calculation of $\hat{d}_{ij}$, $1 \leq j \leq N-1$

The derivative matrix

$$\hat{d}_{ij} = \hat{h}_j'(x_i), \tag{D.9}$$

will now be calculated, again considering the cases $1 \leq j \leq N-1$ and $j = N$ separately. To shorten the equations in this section, we introduce the following factors, that are independent of x:

$$\begin{aligned} A &= N(N+1)(1+x_j), \\ B &= N(N+1)P_N(x_j). \end{aligned} \tag{D.10}$$

Now $\hat{h}_j(x)$ can be written as

$$\hat{h}_j(x) = \frac{P_N'(x)(x^2-1)}{B} \cdot [\frac{1}{(x-x_j)} - \frac{4}{A(1+x)}]. \qquad 1 \leq j \leq N-1.$$

Making use of the property of the Legendre polynomials that

$$\frac{d}{dx}(P_N'(x)(1-x^2)) + N(N+1)P_N(x) = 0, \tag{D.11}$$

the derivative of $\hat{h}_j(x)$ with respect to x can be expressed as

$$\begin{aligned} B\hat{h}_j'(x) = &P_N'(x)(1-x^2)\left[\frac{1}{(x-x_j)^2} - \frac{4}{A(1+x)^2}\right] \quad + \\ &N(N+1)P_N(x)\left[\frac{1}{x-x_j} - \frac{4}{A(1+x)}\right]. \end{aligned}$$

Evaluating this derivative at $x = x_i$, where $i \neq j$ and $1 \leq i \leq N-1$ yields

$$\hat{h}_j'(x_i) = \frac{P_N(x_i)}{P_N(x_j)}\left[\frac{1}{x_i - x_j} - \frac{4}{N(N+1)(1+x_j)(1+x_i)}\right], \quad i \neq j, \quad 1 \leq i, j \leq N-1. \tag{D.12}$$

When $x = x_j$ the derivative can be calculated by applying l'Hôpitals rule:

$$\begin{aligned} \lim_{x \to x_j} B\hat{h}_j'(x) \quad &= \lim_{x \to x_j}\left[\frac{P_N'(x)(1-x^2) + N(N+1)P_N(x)(x-x_j)}{(x-x_j)^2}\right] + \\ &\qquad -P_N'(x_j)(1-x_j^2)\frac{4}{A(1+x_j)^2} - N(N+1)P_N(x_j)\frac{4}{A(1+x_j)} \\ &= \lim_{x \to x_j}\left[\frac{N(N+1)P_N'(x)(x-x_j)}{2(x-x_j)}\right] - P_N(x_j)\frac{4}{(1+x_j)^2}. \end{aligned}$$

So finally we find an expression for the derivative $\hat{h}'_j(x_i)$ at $i = j$:

$$\hat{h}'_j(x_i) = -\frac{4}{N(N+1)(1+x_j)^2}, \qquad 1 \leq i = j \leq N-1.$$

At $x = x_N = +1$ the derivative becomes

$$\hat{h}'_j(+1) = \frac{1}{P_N(x_j)}\left[\frac{1}{(1-x_j)} - \frac{4}{2N(N+1)(1+x_j)}\right], \qquad 1 \leq j \leq N-1,$$

which is in fact, Eq. (D.12) with $i = N$, so this is not a special case. Instead we may write:

$$\hat{h}'_j(x_i) = \frac{P_N(x_i)}{P_N(x_j)}\left[\frac{1}{(x_i - x_j)} - \frac{4}{N(N+1)(1+x_j)(1+x_i)}\right], \quad \begin{array}{l} i \neq j, \\ 1 \leq j \leq N-1, \\ 1 \leq i \leq N. \end{array} \tag{D.13}$$

At $x = x_0 = -1$ we check if this approach results in a zero derivative

$$\begin{aligned}
\lim_{x\to -1} B\hat{h}'_j(x) \quad &= \lim_{x\to -1}\left[\frac{-4P'_N(x)(1-x^2) - 4N(N+1)P_N(x)(1+x)}{A(1+x)^2}\right] + \\
&\qquad -N(N+1)P_N(-1)\frac{1}{(1+x_j)} \\
&= \lim_{x\to -1}\left[\frac{-4N(N+1)P'_N(x)(1+x)}{2A(1+x)}\right] - \frac{N(N+1)(-1)^N}{(1+x_j)} \\
&= \frac{-2P'_N(-1)}{(1+x_j)} - \frac{N(N+1)(-1)^N}{(1+x_j)} \\
&= -2\frac{-N(N+1)(-1)^N}{2(1+x_j)} - \frac{N(N+1)(-1)^N}{(1+x_j)} = 0.
\end{aligned} \tag{D.14}$$

Calculation of $\hat{d}_{iN}$

The derivative of $\hat{h}_N(x)$ is found to be

$$\hat{h}'_N(x) = \frac{P''_N(x)}{N(N+1)}\left[(x+1) + \frac{2(1-x)}{N(N+1)}\right] + \frac{P'_N(x)}{N(N+1)}\left[1 - \frac{2}{N(N+1)}\right]. \tag{D.15}$$

At $x = x_i$, $1 \leq i \leq N-1$, this expression becomes

$$\hat{h}'_N(x_i) = \frac{P''_N(x_i)}{N(N+1)}\left[(x_i+1) + \frac{2(1-x_i)}{N(N+1)}\right], \qquad 1 \leq i \leq N-1,$$

which may be rewritten as

$$\hat{h}'_N(x_i) = P_N(x_i)\left[\frac{1}{(x_i-1)} - \frac{2}{N(N+1)(1+x_i)}\right], \qquad 1 \le i \le N-1. \tag{D.16}$$

At $x = x_N = +1$ we find

$$\begin{aligned}\hat{h}'_N(+1) \quad &= \frac{2P''_N(1)}{N(N+1)} + \frac{P_N(1)}{N(N+1)}\left[1 - \frac{2}{N(N+1)}\right] \\ &= (N^2+N-2)\left[\frac{1}{4} + \frac{1}{2N(N+1)}\right] \\ &= \frac{(N^2+N-2)(N^2+N+2)}{4N(N+1)}.\end{aligned} \tag{D.17}$$

Again a check is performed on the derivative at $x = x_0 = -1$

$$\begin{aligned}\hat{h}'_N(-1) \quad &= \frac{4P''_N(-1)}{N^2(N+1)^2} + \frac{P_N(-1)}{N(N+1)}\left[1 - \frac{2}{N(N+1)}\right] \\ &= \frac{N^2+N-2}{2N(N+1)}(-1)^N - \frac{N^2+N-2}{2N(N+1)}(-1)^N = 0.\end{aligned} \tag{D.18}$$

Gathering the evidence and the numerical weights

To summarize, the total form of the Lagrange interpolant is given again as

$$\begin{aligned}\hat{h}_j(x) \quad &= \frac{P'_N(x)(1-x)}{P''_N(x_j)(x-x_j)} \cdot \frac{N(N+1)(1+x_j)(1+x) - 4(x-x_j)}{N(N+1)(1+x_j)(1-x_j^2)}, \qquad 1 \le j \le N-1, \\ \hat{h}_N(x) \quad &= \frac{P'_N(x)}{N^2(N+1)^2} \cdot [N(N+1)(1+x) + 2(1-x)].\end{aligned}$$

Together, these interpolants satisfy the properties

$$\begin{aligned}\hat{h}_j(x_i) \quad &= 0, \qquad i \ne j, \qquad 1 \le i,j \le N \\ \hat{h}_j(x_i) \quad &= 1, \qquad i = j, \qquad 1 \le i,j \le N, \\ \hat{h}_j(+1) \quad &= 0, \qquad j \ne N, \qquad 1 \le j \le N, \\ \hat{h}'_j(-1) \quad &= 0, \qquad 1 \le j \le N.\end{aligned}$$

The derivative matrix $\hat{d}_{ij}$ is given by

$$\hat{d}_{ij} = \begin{cases} 0 \qquad i=0, \quad 1 \le j \le N-1, \\[2ex] \dfrac{P_N(x_i)}{P_N(x_j)} \left[\dfrac{1}{x_i - x_j} - \dfrac{4}{N(N+1)(1+x_j)(1+x_i)} \right] \quad i \ne j, \quad 1 \le i,j \le N-1, \\[2ex] -\dfrac{4}{N(N+1)(1+x_j)^2} \qquad 1 \le i = j \le N-1, \\[2ex] \dfrac{1}{P_N(x_j)} \left[\dfrac{1}{1-x_j} - \dfrac{4}{2N(N+1)(1+x_j)} \right] \qquad i=N, \quad 1 \le j \le N-1, \\[2ex] 0 \qquad i=0, \quad j=N, \\[2ex] P_N(x_i) \left[\dfrac{1}{x_i - 1} - \dfrac{2}{N(N+1)(1+x_i)} \right] \qquad 1 \le i \le N-1, \quad j=N, \\[2ex] \dfrac{(N^2+N-2)(N^2+N+2)}{4N(N+1)} \qquad i=N, \quad j=N. \end{cases} \tag{D.19}$$

When we use the following relation for Legendre polynomials

$$P''_N(x_j)(1-x_j^2) + N(N+1)P_N(x_j) = 0, \qquad 1 \le j \le N-1, \tag{D.20}$$

the Lagrange interpolants $\hat{h}_j(x)$ and $\hat{h}_N(x)$ can be rewritten in the form

$$\begin{aligned} \hat{h}_j(x) &= \frac{P'_N(x)(x^2-1)}{N(N+1)P_N(x_j)} \cdot \left[\frac{1}{x-x_j} - \frac{4}{N(N+1)(1+x_j)(1+x)} \right], \qquad 1 \le j \le N-1, \\ \hat{h}_N(x) &= \frac{P'_N(x)(x^2-1)}{N(N+1)} \cdot \left[\frac{1}{x-1} - \frac{2}{N(N+1)(x+1)} \right] = \hat{h}_j(x)|_{j=N}, \end{aligned}$$

which enables us to make a comparison with the original Lagrange interpolant in Eq. (3.52) very straightforwardly. In fact, the new interpolant $\hat{h}$ and its derivative can be expressed in terms of the original h:

$$\hat{h}_j(x) = h_j(x) - \frac{4(-1)^N}{N(N+1)P_N(x_j)(1+x_j)} h_0(x), \qquad 1 \le j \le N,$$

and

$$\hat{d}_{ij} = d_{ij} - \frac{4(-1)^N}{N(N+1)P_N(x_j)(1+x_j)} d_{i0}, \qquad 1 \le j \le N.$$

This makes evaluating the weights for the modified interpolant easy:

$$\hat{w}_j = w_j - \frac{4(-1)^N}{N(N+1)P_N(x_j)(1+x_j)} w_0, \qquad 1 \le j \le N,$$

which may also be written as

$$\hat{w}_j = \frac{2}{N(N+1)[P_N(x_j)]^2} \left[1 - \frac{4(-1)^N P_N(x_j)}{N(N+1)(1+x_j)} \right], \qquad 1 \le j \le N.$$

Repeating the whole exercise for an axis of symmetry at the other end of the domain, $j = N$, the modified polynomial, derivative and weights are found to be

$$\hat{h}_j(x) = h_j(x) + \frac{4}{N(N+1)P_N(x_j)(-1+x_j)} h_0(x), \qquad 0 \le j \le N-1,$$

and

$$\hat{d}_{ij} = d_{ij} + \frac{4}{N(N+1)P_N(x_j)(-1+x_j)} d_{i0}, \qquad 0 \le j \le N-1,$$

and

$$\hat{w}_j = w_j + \frac{4}{N(N+1)P_N(x_j)(-1+x_j)} w_0, \qquad 0 \le j \le N-1.$$

Appendix E

Calculation of LUST Shift Factors

Presented here is the derivation of the factors h_{ij} in the Locally-Upwinded Spectral Technique (LUST). They can be found by solving the equation

$$
\begin{aligned}
P_{N+1}(\mathbf{x}) - h_{ij}(\mathbf{u}\cdot\nabla)P_{N+1}(\mathbf{x}) + \frac{h_{ij}^2}{2}(\mathbf{u}\cdot\nabla)^2 P_{N+1}(\mathbf{x}) - \frac{h_{ij}^3}{3!}(\mathbf{u}\cdot\nabla)^3 P_{N+1}(\mathbf{x}) + ...\\
+We\Big((\mathbf{u}\cdot\nabla)P_{N+1}(\mathbf{x}) - h_{ij}(\mathbf{u}\cdot\nabla)^2 P_{N+1}(\mathbf{x}) + \frac{h_{ij}^2}{2}(\mathbf{u}\cdot\nabla)^3 P_{N+1}(\mathbf{x}) -\\
\frac{h_{ij}^3}{3!}(\mathbf{u}\cdot\nabla)^4 P_{N+1}(\mathbf{x}) + ...\Big) = 0,
\end{aligned}
\tag{E.1}
$$

at each GLL point in the parent element. The left-hand side of this equation is a Taylor series expansion of (4.32) about the point $\mathbf{x}$. The polynomial $P_{N+1}(\mathbf{x})$ is defined by

$$P_{N+1}(\mathbf{x}) = (1-\xi^2)L'_N(\xi)(1-\eta^2)L'_N(\eta), \tag{E.2}$$

which is zero at all GLL nodes in the parent element, since

$$(1-\xi_i^2)(1-\eta_j^2) = 0, \qquad i = 0, N, \quad j = 0, N, \tag{E.3}$$

$$L'_N(\xi_i) = L'_N(\eta_j) = 0, \qquad 1 \le i, j \le N-1. \tag{E.4}$$

Now define the function $F(\omega)$ as

$$F(\omega) = (1-\omega^2)L'_N(\omega). \tag{E.5}$$

The function $P_{N+1}(\mathbf{x})$ can then be written as

$$P_{N+1}(\mathbf{x}) = F(\xi)F(\eta). \tag{E.6}$$

The convection terms in (E.1) can then be written in the form

$$\begin{aligned}
(\mathbf{u}\cdot\nabla)P_{N+1}(\mathbf{x}) &= uF^{'}(\xi)F(\eta) + vF(\xi)F^{'}(\eta), \\
(\mathbf{u}\cdot\nabla)^2 P_{N+1}(\mathbf{x}) &= u^2F^{''}(\xi)F(\eta) + v^2F(\xi)F^{''}(\eta) + 2uvF^{'}(\xi)F^{'}(\eta),
\end{aligned} \tag{E.7}$$

$$\begin{aligned}
(\mathbf{u}\cdot\nabla)^3 P_{N+1}(\mathbf{x}) &= u^3F^{'''}(\xi)F(\eta) + v^3F(\xi)F^{'''}(\eta) + \\
&\quad 3u^2vF^{''}(\xi)F^{'}(\eta) + 3uv^2F^{'}(\xi)F^{''}(\eta), \\
(\mathbf{u}\cdot\nabla)^4 P_{N+1}(\mathbf{x}) &= u^4F^{''''}(\xi)F(\eta) + v^4F(\xi)F^{''''}(\eta) + \\
&\quad 4u^3vF^{'''}(\xi)F^{'}(\eta) + 4uv^3F^{'}(\xi)F^{'''}(\eta) + 6u^2v^2F^{''}(\xi)F^{''}(\eta).
\end{aligned}$$

Since $F(\omega) = 0$ for $\omega = \xi_i$, $i = 0, ..., N$, we have

$$\begin{aligned}
(\mathbf{u}_N\cdot\nabla)P_{N+1}(\mathbf{x}_{ij}) &= 0, \\
(\mathbf{u}_N\cdot\nabla)^2 P_{N+1}(\mathbf{x}_{ij}) &= 2uvF^{'}(\xi_i)F^{'}(\eta_j), \\
(\mathbf{u}_N\cdot\nabla)^3 P_{N+1}(\mathbf{x}_{ij}) &= 3u^2vF^{''}(\xi_i)F^{'}(\eta_j) + 3uv^2F^{'}(\xi_i)F^{''}(\eta_j), \\
(\mathbf{u}_N\cdot\nabla)^4 P_{N+1}(\mathbf{x}_{ij}) &= 4u^3vF^{'''}(\xi_i)F^{'}(\eta_j) + 4uv^3F^{'}(\xi_i)F^{'''}(\eta_j) + 6u^2v^2F^{''}(\xi_i)F^{''}(\eta_j),
\end{aligned}$$

After division by $(\mathbf{u}_N\cdot\nabla)^2 P_{N+1}(\mathbf{x}_{ij})$, the expression Taylor expansion (E.1) reduces to the following quadratic equation in h_{ij}

$$\begin{aligned}
&\frac{h_{ij}}{2} - \frac{h_{ij}^2}{6}\frac{(\mathbf{u}_N\cdot\nabla)^3 P_{N+1}(\mathbf{x}_{ij})}{(\mathbf{u}_N\cdot\nabla)^2 P_{N+1}(\mathbf{x}_{ij})} \\
&\qquad + We\left(-1 + \frac{h_{ij}}{2}\frac{(\mathbf{u}_N\cdot\nabla)^3 P_{N+1}(\mathbf{x}_{ij})}{(\mathbf{u}_N\cdot\nabla)^2 P_{N+1}(\mathbf{x}_{ij})} - \frac{h_{ij}^2}{6}\frac{(\mathbf{u}_N\cdot\nabla)^4 P_{N+1}(\mathbf{x}_{ij})}{(\mathbf{u}_N\cdot\nabla)^2 P_{N+1}(\mathbf{x}_{ij})}\right) = 0,
\end{aligned}$$

where we have neglected higher-order terms. After rearrangement this equation becomes

$$\begin{aligned}
&-\frac{h_{ij}^2}{6}\left(\frac{(\mathbf{u}_N\cdot\nabla)^3 P_{N+1}(\mathbf{x}_{ij})}{(\mathbf{u}_N\cdot\nabla)^2 P_{N+1}(\mathbf{x}_{ij})} + We\frac{(\mathbf{u}_N\cdot\nabla)^4 P_{N+1}(\mathbf{x}_{ij})}{(\mathbf{u}_N\cdot\nabla)^2 P_{N+1}(\mathbf{x}_{ij})}\right) \\
&\qquad + \frac{h_{ij}}{2}\left(1 + We\frac{h_{ij}}{2}\frac{(\mathbf{u}_N\cdot\nabla)^3 P_{N+1}(\mathbf{x}_{ij})}{(\mathbf{u}_N\cdot\nabla)^2 P_{N+1}(\mathbf{x}_{ij})}\right) - We = 0.
\end{aligned}$$

Substituting the expressions in terms of $F(\xi)$ and $F(\eta)$ for the streamline derivatives yields

$$
\begin{aligned}
-\frac{h_{ij}^2}{6}\Bigg(&\frac{3}{2}u_{ij}\frac{F''(\xi_i)}{F'(\xi_i)} + \frac{3}{2}v_{ij}\frac{F''(\eta_j)}{F'(\eta_j)} + 2Weu_{ij}^2\frac{F'''(\xi_i)}{F'(\xi_i)} + 2Wev_{ij}^2\frac{F'''(\eta_j)}{F'(\eta_j)} \\
&+ 3Weu_{ij}v_{ij}\frac{F''(\xi_i)}{F'(\xi_i)}\frac{F''(\eta_j)}{F'(\eta_j)}\Bigg) \\
&+ \frac{h_{ij}}{2}\left(1 + \frac{3}{2}Weu_{ij}\frac{F''(\xi_i)}{F'(\xi_i)} + \frac{3}{2}Wev_{ij}\frac{F''(\eta_j)}{F'(\eta_j)}\right) - We = 0.
\end{aligned}
\tag{E.8}
$$

Using the property of the Legendre polynomials

$$(1-\omega^2)L_N''(\omega) - 2xL_N'(\omega) + N(N+1)L_N(\omega) = 0, \tag{E.9}$$

expressions for the factors $\frac{F''(\omega_i)}{F'(\omega_i)}$ and $\frac{F'''(\omega_i)}{F'(\omega_i)}$ can be found. In particular, we have

$$\frac{F''(\omega_i)}{F'(\omega_i)} = \frac{L_N'(\omega_i)}{L_N(\omega_i)} = \begin{cases} -\frac{1}{2}N(N+1) & i = 0, \\ 0 & 1 \le i \le N-1, \\ +\frac{1}{2}N(N+1) & i = N, \end{cases} \tag{E.10}$$

$$\frac{F'''(\omega_i)}{F'(\omega_i)} = \frac{L_N''(\omega_i)}{L_N(\omega_i)} = \begin{cases} \frac{1}{8}N(N+1)(N^2+N-2) & i = 0, \\ \frac{-N(N+1)}{1-\omega_i^2} & 1 \le i \le N-1, \\ \frac{1}{8}N(N+1)(N^2+N-2) & i = N. \end{cases} \tag{E.11}$$

For internal GLL nodes (ξ_i, η_j), $1 \le i, j \le N-1$, the quadratic equation from which h_{ij} is determined, is now found to be

$$\frac{2WeN(N+1)}{3}\left(\frac{u_{ij}^2}{1-\xi^2} + \frac{v_{ij}^2}{1-\eta^2}\right)h_{ij}^2 + h_{ij} - 2We = 0. \tag{E.12}$$

Substitution of the correct entries from (E.10) and (E.11) into (E.8) results in similar expressions for calculation of h_{ij} on edges of elements, and corners of elements. This however can sometimes result in a negative discriminant for the quadratic equation for h_{ij}. In this case the factors are calculated using a the Taylor series truncated one order lower, i.e.

$$\begin{aligned} &P_{N+1}(\mathbf{x}) - h_{ij}(\mathbf{u}\cdot\nabla)P_{N+1}(\mathbf{x}) + \frac{h_{ij}^2}{2}(\mathbf{u}\cdot\nabla)^2P_{N+1}(\mathbf{x}) \\ &+ We\Big((\mathbf{u}\cdot\nabla)P_{N+1}(\mathbf{x}) - h_{ij}(\mathbf{u}\cdot\nabla)^2P_{N+1}(\mathbf{x}) + \frac{h_{ij}^2}{2}(\mathbf{u}\cdot\nabla)^3P_{N+1}(\mathbf{x})\Big) = 0. \end{aligned} \tag{E.13}$$

Appendix F

Discretization with LUST

The discretization of one term in the weak formulation of the term $\mathbf{u} \cdot \nabla \boldsymbol{\tau}$ will be presented for the Galerkin and using LUST methods. This is an example of how all the terms in the constitutive equation can be discretized, as long as no integration by parts is performed on the weak formulation.

The weak form of the convection term $u\frac{\partial \tau_{xx}}{\partial x}$, after transformation from the physical coordinates (x, y) to the computational space (ξ, η) on the parent element, is given by

$$I = \int_D u(\xi, \eta) \left(\frac{\frac{\partial y}{\partial \eta}\frac{\partial}{\partial \xi} - \frac{\partial y}{\partial \xi}\frac{\partial}{\partial \eta}}{det(J)} \right) \tau_{xx}(\xi, \eta)\phi(\xi, \eta) \left| det(J) \right| d\xi d\eta. \tag{F.1}$$

When the first term $\frac{\partial y}{\partial \eta}\frac{\partial}{\partial \xi}$ is approximated by the Gauss-Lobatto-Legendre rule we find

$$\tilde{I} = \sum_{p=0}^{N}\sum_{q=0}^{N} f(\xi_p, \eta_q)\phi(\xi_p, \eta_q) \left| det(J) \right|_{pq} w_p w_q, \tag{F.2}$$

where $f(\xi_p, \eta_q)$ is given by

$$f(\xi_p, \eta_q) = u(\xi_p, \eta_q)\frac{\partial y}{\partial \eta}(\xi_p, \eta_q)\frac{1}{det(J)_{pq}}\frac{\partial \tau_{xx}}{\partial \xi}(\xi_p, \eta_q), \tag{F.3}$$

and when we substitute the spectral approximations for u and τ_{xx} we have

$$\begin{aligned} f(\xi_p,\eta_q) &= \sum_{m=0}^{N}\sum_{n=0}^{N} u_{mn}h_m(\xi_p)h_n(\eta_q)\frac{\partial y}{\partial \eta}(\xi_p,\eta_q)\frac{1}{det(J)_{pq}}\sum_{k=0}^{N}\sum_{l=0}^{N}\tau_{kl}^{xx}h_k'(\xi_p)h_l(\eta_q) \\ &= u_{pq}\frac{\partial y}{\partial \eta}_{pq}\frac{1}{det(J)_{pq}}\sum_{k=0}^{N}\tau_{kq}^{xx}h_k'(\xi_p). \end{aligned} \tag{F.4}$$

For a particular test function ϕ_{ij}, the expression (F.2) becomes

$$\tilde{I}_{ij} = \sum_{p=0}^{N}\sum_{q=0}^{N} f(\xi_p,\eta_q)\phi_{ij}(\xi_p,\eta_q)\left|det(J)\right|_{pq} w_p w_q. \tag{F.5}$$

This expression will now be written out for two different choices for the test function ϕ_{ij}.

GALERKIN

In the standard Galerkin formulation, the test function $\phi_{ij}(\xi,\eta)$ is given by

$$\phi_{ij}(\xi,\eta) = h_i(\xi)h_j(\eta) \tag{F.6}$$

The expression $\tilde{I}_{ij}$ can now be written as

$$\begin{aligned} \tilde{I}_{ij} &= \sum_{p=0}^{N}\sum_{q=0}^{N} u_{pq}\frac{\partial y}{\partial \eta}_{pq}\frac{1}{det(J)_{pq}}\left[\sum_{k=0}^{N}\tau_{kq}^{xx}h_k'(\xi_p)\right] h_i(\xi_p)h_j(\eta_q)|det(J)|_{pq}w_p w_q \\ &= u_{ij}\frac{\partial y}{\partial \eta}_{ij}\frac{1}{det(J)_{ij}}\left[\sum_{k=0}^{N}\tau_{kj}^{xx}h_k'(\xi_i)\right]|det(J)|_{ij}w_i w_j, \end{aligned} \tag{F.7}$$

or, when using $f(\xi_p,\eta_q)$

$$\begin{aligned} \tilde{I}_{ij} &= \sum_{p=0}^{N}\sum_{q=0}^{N} f(\xi_p,\eta_q)h_i(\xi_p)h_j(\eta_q)|det(J)|_{pq}w_p w_q \\ &= f(\xi_i,\eta_j)|det(J)|_{ij}w_i w_j. \end{aligned} \tag{F.8}$$

LUST

In the LUST method, the test function ϕ_{ij} is redefined as

$$\phi_{ij}(\xi,\eta) = h_i(\xi)h_j(\eta) + h_{ij}^{L}\mathbf{u}\cdot\nabla\left(h_i(\xi)h_j(\eta)\right), \tag{F.9}$$

where h^L_{ij} is the LUST shift factor at (ξ_i, η_j). After inserting the spectral approximation for $\mathbf{u}$, the test function ϕ is found to be

$$\begin{aligned}\phi_{ij}(\xi,\eta) = {} & h_i(\xi)h_j(\eta) \\ & + h^L_{ij}\left[\sum_{m=0}^{N}\sum_{n=0}^{N} u_{mn}h_m(\xi)h_n(\eta)\right]\left[\frac{\partial y}{\partial \eta}_{pq}\frac{h_i'(\xi)h_j(\eta)}{detJ_{pq}} - \frac{\partial y}{\partial \xi}_{pq}\frac{h_i(\xi)h_j'(\eta)}{detJ_{pq}}\right] \\ & + h^L_{ij}\left[\sum_{m=0}^{N}\sum_{n=0}^{N} v_{mn}h_m(\xi)h_n(\eta)\right]\left[\frac{\partial x}{\partial \xi}_{pq}\frac{h_i(\xi)h_j'(\eta)}{detJ_{pq}} - \frac{\partial x}{\partial \eta}_{pq}\frac{h_i'(\xi)h_j(\eta)}{detJ_{pq}}\right],\end{aligned} \tag{F.10}$$

which can be simplified to

$$\begin{aligned}\phi_{ij}(\xi,\eta) = {} & h_i(\xi)h_j(\eta) \\ & + \frac{h^L_{ij}u_{pq}}{detJ_{pq}}\left[\frac{\partial y}{\partial \eta}_{pq}h_i'(\xi)h_j(\eta) - \frac{\partial y}{\partial \xi}_{pq}h_i(\xi)h_j'(\eta)\right] \\ & + \frac{h^L_{ij}v_{pq}}{detJ_{pq}}\left[\frac{\partial x}{\partial \xi}_{pq}h_i(\xi)h_j'(\eta) - \frac{\partial x}{\partial \eta}_{pq}h_i'(\xi)h_j(\eta)\right] \\ = {} & h_i(\xi)h_j(\eta) \\ & + \frac{h^L_{ij}h_i'(\xi)h_j(\eta)}{detJ_{pq}}\left(\frac{\partial y}{\partial \eta}u - \frac{\partial x}{\partial \eta}v\right)_{pq} + \frac{h^L_{ij}h_i(\xi)h_j'(\eta)}{detJ_{pq}}\left(\frac{\partial x}{\partial \xi}v - \frac{\partial y}{\partial \xi}u\right)_{pq}.\end{aligned} \tag{F.11}$$

In analogy to (F.8) $\tilde{I}_{ij}$ can be expressed as

$$\begin{aligned}\tilde{I}_{ij} = {} & \sum_{p=0}^{N}\sum_{q=0}^{N} f(\xi_p,\eta_q)h_i(\xi_p)h_j(\eta_q)|det(J)|_{pq}w_pw_q \\ & + \sum_{p=0}^{N}\sum_{q=0}^{N} f(\xi_p,\eta_q)\frac{h^L_{ij}h_i'(\xi_p)h_j(\eta_q)}{detJ_{pq}}\left(\frac{\partial y}{\partial \eta}u - \frac{\partial x}{\partial \eta}v\right)_{pq}|det(J)|_{pq}w_pw_q \\ & + \sum_{p=0}^{N}\sum_{q=0}^{N} f(\xi_p,\eta_q)\frac{h^L_{ij}h_i(\xi_p)h_j'(\eta_q)}{detJ_{pq}}\left(\frac{\partial x}{\partial \xi}v - \frac{\partial y}{\partial \xi}u\right)_{pq}|det(J)|_{pq}w_pw_q \qquad \text{(F.12)} \\ = {} & f(\xi_i,\eta_j)|det(J)|_{ij}w_iw_j \\ & + \sum_{p=0}^{N} f(\xi_p,\eta_j)h^L_{ij}h_i'(\xi_p)\left(\frac{\partial y}{\partial \eta}u - \frac{\partial x}{\partial \eta}v\right)_{pj} sgn(detJ)_{pj}w_pw_j \\ & + \sum_{q=0}^{N} f(\xi_i,\eta_q)h^L_{ij}h_j'(\eta_q)\left(\frac{\partial x}{\partial \xi}v - \frac{\partial y}{\partial \xi}u\right)_{iq} sgn(detJ)_{iq}w_iw_q.\end{aligned}$$

Bibliography

[1] K. Atalik and R. Keunings. Non-linear temporal stability analysis of viscoelastic plane channel flow using a fully-spectral method. *J. Non-Newtonian Fluid Mech.*, 102:299–319, 2002.

[2] B. Bernstein, E. A. Kearsley, and L. J. Zappas. A study of stress relaxation with finite strain. *Trans. Soc. Rheol.*, 7:391–410, 1963.

[3] G. B. Bishko, O. G. Harlen, T. C. B. McLeish, and T. M. Nicholson. Numerical simulation of the transient flow of branched polymer melts through a planar contraction using the 'pom-pom' model. *J. Non-Newtonian Fluid Mech.*, 82:255–273, 1999.

[4] R. J. Blackwell, T. C. B. McLeish, and O. G. Harlen. Molecular drag-strain coupling in branched polymer melts. *J. Rheol.*, 44:121–136, 2000.

[5] A.N. Brooks and T.J.R. Hughes. Streamline upwind/Petrov-Galerkin formulations for convection dominated flows with particular emphasis on the incompressible Navier-Stokes equations. *Comp. Meth. Appl. Mech. Engng.*, 32:199–259, 1982.

[6] J. Cahouet and J. P. Chabard. Some fast 3D finite element solvers for the generalized Stokes problem. *Int. J. Numer. Meth. Fluids*, 8:869–895, 1988.

[7] E. O. Carew, P. Townsend, and M. F. Webster. Taylor-Galerkin algorithms for viscoelastic flow: application to a model problem. *Num. Meth. Part. Diff. Eqns.*, 10:171–190, 1994.

[8] W. Couzy and M.O. Deville. A fast schur complement method for the spectral element discretization of the incompressible Navier-Stokes equations. *J. Comput. Phys.*, 116:135–142, 1995.

[9] P. G. de Gennes. Reptation of a polymer chain in the presence of fixed obstacles. *J. Chem. Phys*, 5(2):572–579, 1971.

[10] M. Deville, P. F. Fischer, and E. Mund. *Higher order methods for incompressible fluid flow.* Cambridge, 2002.

[11] M. Doi and S. F. Edwards. *The theory of polymer dynamics.* Oxford University Press, Oxford, 1986.

[12] M. Dryja and O. B. Widlund. Domain decomposition algorithms with small overlap. *SIAM J. Sci. Comput.*, 15:604–620, 1994.

[13] X. Escriva, E. Leriche, and T. N. Phillips. Preconditioned uzawa algorithm for the velocity-pressure-stress formulation of viscoelastic flow problems. *J. Sci. Comput.*, 17:219–229, 2002.

[14] N. Fiétier. Numerical simulation of viscoelastic fluid flows by spectral element methods and time-dependent algorithms. *PhD thesis, Ecole Polytechnique Fédérale de Lausanne, Switzerland*, 2002.

[15] N. Fiétier and M. O. Deville. Time-dependent algorithms for the simulation of viscoelastic flows with spectral element methods: application and stability. *To appear in J. Comput. Phys.*, 2003.

[16] P.F. Fisher. An overlapping Schwarz method for spectral element solution of the incompressible Navier-Stokes equations. *J. Comput. Phys.*, 133:84–101, 1997.

[17] M. I. Gerritsma and T. N. Phillips. Discontinuous spectral element approximations for the velocity-pressure-stress formulation of the Stokes problem. *Int. J. Numer. Meth. Engng.*, 43:1404–1419, 1998.

[18] M. I. Gerritsma and T. N. Phillips. Compatible spectral approximations for the velocity-pressure-stress formulation of the Stokes problem. *SIAM J. Sci. Comput.*, 20:1530–1550, 1999.

[19] M. I. Gerritsma and T. N. Phillips. On the use of characteristic variables in viscoelastic flow problems. *IMA J. Appl. Math.*, 66(2):127–147, 2001.

[20] H. Giesekus. A simple constitutive equation for polymer fluids based on the concept of deformation-dependent tensorial mobility. *J. Non-Newtonian Fluid Mech.*, 11:69–109, 1982.

[21] R. Guénette and M. Fortin. A new mixed finite element method for computing viscoelastic flows. *J. Non-Newtonian Fluid Mech.*, 60:27–52, 1995.

[22] O. Harlen. Constitutive models for polymer melts obtained from tube theory - the pompom model. *Lecture Notes presented at University of Wales, Aberystwyth*, May 2003.

[23] T. C. Ho and M. M. Denn. Stability of plane Poiseuille flow of a highly elastic liquid. *J. Non-Newtonian Fluid Mech.*, 3:179–195, 1977/1978.

[24] M.A. Hulsen, A. P. G. van Heel, and B. H. A. A. van den Brule. Simulation of viscoelastic flows using Brownian configuration fields. *J. Non-Newtonian Fluid Mech.*, 70:79–101, 1997.

[25] N. J. Inkson, T. C.B. McLeish, O. G. Harlen, and F. J. Groves. Predicting low density polyethylene melt rheology in elongational and shear flows with 'pom-pom' constitutive equations. *J. Rheol.*, 43(4):873–896, 1999.

[26] D. D. Joseph. *Fluid dynamics of viscoelastic liquids*, volume 84 of *Applied mathematical sciences*. Springer Verlag, New York, NY, 1990.

[27] G. E. M. Karniadakis and S. J. Sherwin. *Spectral/hp Element Methods for CFD*. Oxford University Press, Oxford, 1999.

[28] A. Kaye. Non-Newtonian flow in incompressible fluids. *College of Aeronautics, Cranfield, England, Tech. Note*, 1962.

[29] R. A. Keiller. Numerical instability of time-dependent flows. *J. Non-Newtonian Fluid Mech.*, 43:229–246, 1992.

[30] R. G. Larson. Instabilities in viscoelastic flows. *Rheol. Acta*, 31:213–263, 1992.

[31] K. C. Lee and B. A. Finlayson. Stability of plane Poiseuille and Couette-flow of a Mawell fluid. *J. Non-Newtonian Fluid Mech.*, 21:65–78, 1986.

[32] A. Lozinski and R. G. Owens. An energy estimate for the Oldroyd B model: theory and applications. *J. Non-Newtonian Fluid Mech.*, 112:161–176, 2003.

[33] Y. Maday and A. T. Patera. Spectral element methods for the incompressible Navier-Stokes equations. In A. K. Noor and J. T. Oden, editors, *State of the Art Surveys in Computational Mechanics*, pages 71–143, New York, 1989. ASME.

[34] T. C. B. McLeish and R. G. Larson. Molecular constitutive equations for a class of branched polymers: the pom-pom polymer. *J. Rheol.*, 42:81–110, 1998.

[35] S. T. Milner, T. C. B. McLeish, and A. E. Likhtman. Microscopic theory of convective constraint release. *J. Rheol.*, 45:539–563, 2001.

[36] J. S. Mullen and P. F. Fischer. Filtering techniques for complex geometry fluid flows. *Comm. Numer. Meth. Engng.*, 15:9–18, 1999.

[37] I. Newton. *Philosophiae Naturalis Principia Mathematica, 1st Ed., Bk 2, Sect. IX.* London, 3rd Edn, 1726, translated by A. Motte, Cambridge University Press, 1934, 1687.

[38] R. G. Owens and T. N. Phillips. *Computational Rheology.* Imperial College Press, London, 2002.

[39] R.G. Owens, C. Chauvière, and T.N. Phillips. A locally-upwinded spectral technique (LUST) for viscoelastic flow. *J. Non-Newtonian Fluid Mech.*, 108:49–71, 2002.

[40] L.F. Pavarino. Indefinite overlapping Schwarz methods for time-dependent stokes problems. *Comp. Meth. Appl. Mech. Engng.*, 187:35–51, 2000.

[41] L.F. Pavarino. Overlapping Schwarz preconditioners for spectral element discretizations of convection-diffusion problems. *Int. J. Num. Meth. Engng.*, 53:1005–1023, 2002.

[42] L.F. Pavarino and T. Warburton. Overlapping Schwarz methods for unstructured spectal elements. *J. Comput. Phys.*, 160:298–317, 2000.

[43] M. G. N. Perera and K. Walters. Long-range memory effects in flows involving abrupt changes in geometry. Part I: Flows associated with L-shaped and T-shaped geometries. *J. Non-Newtonian Fluid Mech.*, 2:49–81, 1977.

[44] N. Phan-Thien and R. Tanner. A new constitutive equation derived from network theory. *J. Non-Newtonian Fluid Mech.*, 2:353–365, 1977.

[45] K. C. Porteous and M. M. Denn. Linear stability of plane Poiseuille flow of viscoelastic liquids. *Trans. Soc. Rheol*, 16:295–308, 1972.

[46] A. Quarteroni and A. Valli. *Domain decomposition methods for partial differential equations.* Oxford Science Publications, London, 1999.

[47] M. Renardy. Existence of slow steady flows of viscoelastic fluids with differential constitutive equations. *Z. Angew. Math. Mech.*, 65:449–451, 1985.

[48] M. Renardy. Recent advances in the mathematical theory of steady flow of viscoelastic fluids. *J. Non-Newtonian Fluid Mech.*, 29:11–24, 1988.

[49] M. Renardy. Mathematical analysis of viscoelastic flows. *Ann. Rev. Fluid Mech.*, 21:1–36, 1989.

[50] M. Renardy. Current issues in non-Newtonian flows: a mathematical perspective. *J. Non-Newtonian Fluid Mech.*, 90:243–259, 2000.

[51] M. Renardy, W. J. Hrusa, and J. A. Nohel. Mathematical problems in viscoelasticity. *Pitman Monographs and Surveys in Pure and Applied Mathematics, Longman, Harlow, England*, 35, 1987.

[52] Y. Saad and M. Schultz. GMRES: A generalized minimal residual algorithm for solving nonsymmetric linear systems. *SIAM J. Sci. Statist. Comput.*, 7:856–869, 1986.

[53] C. R. Schneidesch and M. O. Deville. Chebyshev collocation method and multidomain decomposition for Navier-Stokes equations in complex curved geometries. *J. Comput. Phys.*, 106:234–257, 1993.

[54] B.F. Smith, O. Bjørstad, and W.D. Gropp. *Domain decomposition: Parallel multilevel methods for elliptic partial differential equations.* Cambridge University Press, Cambridge, 1996.

[55] M. D. Smith, R. C. Armstrong, R. A. Brown, and R. Sureshkumar. Finite element analysis of stability of two-dimensional viscoelastic flows to three-dimensional disturbances. *J. Non-Newtonian Fluid Mech.*, 93:203–244, 2000.

[56] R. Sureshkumar and A. N. Beris. Linear stability analysis of viscoelastic Poiseuille flow using an Arnoldi-based orthogonalization algorithm. *J. Non-Newtonian Fluid Mech.*, 56:151–182, 1995.

[57] R. I. Tanner. *Engineering Rheology.* Clarendon Press, Oxford, 1985.

[58] H. van der Vorst. Bi-CGSTAB: A fast and smoothly converging variant of Bi-CG for the solution of nonsymmetric linear systems. *SIAM J. Sci. Statist. Comput.*, 13:613–644, 1992.

[59] R. G. M. van Os and T. N. Phillips. The prediction of complex flows of polymer melts using spectral elements. *J. Non-Newtonian Fluid Mech.*, 122:336–350, 2004.

[60] R. G. M. van Os and T. N. Phillips. Spectral element methods for transient viscoelastic flow problems. *J. Comput. Phys.*, 2004. Accepted for publication.

[61] W. M. H. Verbeeten, G. W. M. Peters, and F. T. P. Baaijens. Differential constitutive equations for polymer melts: the extended pom-pom model. *J. Rheol.*, 45(4):823–843, 2001.

[62] W. M. H. Verbeeten, G. W. M. Peters, and F. T. P. Baaijens. Viscoelastic analysis of complex melt flows using the extended pom-pom model. *J. Non-Newtonian Fluid Mech.*, 108:301–326, 2002.

[63] W. M. H. Verbeeten, G. W. M. Peters, and F. T. P. Baaijens. Numerical simulations of the planar contraction flow for a polyethylene melt using the XPP model. *J. Non-Newtonian Fluid Mech.*, 117:73–84, 2004.

[64] N. D. Waters and M. J. King. Unsteady flow of an elastico-viscous liquid. *Rheol. Acta*, 9:345–355, 1970.

[65] H. J. Wilson, M. Renardy, and Y. Renardy. Structure of the spectrum in zero Reynolds number shear flow of the UCM and Oldroyd B liquids. *J. Non-Newtonian Fluid Mech.*, 80:251–268, 1999.